

VTT SYMPOSIUM 265

**Keywords:** thermal power plant, nuclear plant, boiler, turbine, condition, life, fuel, maintenance, inspection, monitoring, risk, reliability, material, damage, corrosion, fatigue, creep, degradation

# **Baltica VIII**

## **Life Management and Maintenance for Power Plants**

### **Vol. 2**

Helsinki–Stockholm–Helsinki  
18–20 May, 2010

Edited by Pertti Auerkari & Juha Veivo

Organised by

VTT



ISBN 978-951-38-7593-2 (soft back ed.)

ISSN 0357-9387 (soft back ed.)

ISBN 978-951-38-7594-7 (URL: <http://www.vtt.fi/publications/index.jsp>)

ISSN 1455-0873 (URL: <http://www.vtt.fi/publications/index.jsp>)

Copyright © VTT 2010

JULKAISIJA – UTGIVARE – PUBLISHER

VTT, Vuorimiehentie 5, PL 1000, 02044 VTT

puh. vaihde 020 722 111, faksi 020 722 4374

VTT, Bergsmansvägen 5, PB 1000, 02044 VTT

tel. växel 020 722 111, fax 020 722 4374

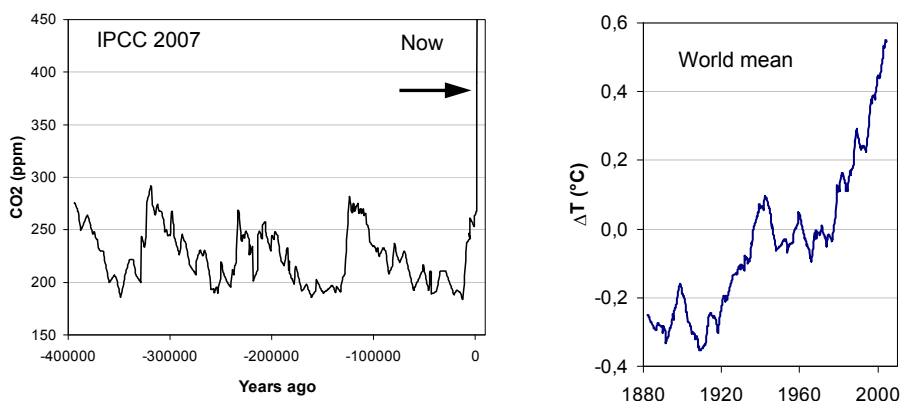
VTT Technical Research Centre of Finland

Vuorimiehentie 5, P.O. Box 1000, FI-02044 VTT, Finland

phone internat. +358 20 722 111, fax + 358 20 722 4374

## Preface

The Baltica Conferences have since 1988 witnessed a continuous change in the environment for the technology and business of power plants. Apart from the shift towards large actors and more unified practices, also grids and businesses are increasingly connected by the developments in the political landscape, technology, and the ability of people to contact each other anywhere. Meanwhile, some aspects may simply come around: the first Baltica Conference took place two years after Chernobyl, and new nuclear seems to be rising again. One driver of change is global warming, easy or not it is to remember after a hard winter in Europe and a decade of steady world mean temperature.



To start an ice age – something not everybody want – requires in air less than 300 ppm CO<sub>2</sub>. Hydro, wind, other renewables and nuclear can push, but the world is not easily or quickly weaned from coal, oil and gas, or taught to apply carbon capture. The current level is 390 ppm CO<sub>2</sub> and rising, and the countermeasures provide a background for BALTICA VIII.

The editors wish to thank all authors, referees, organisers and the Board of the Conference for their invaluable help in preparing for the event and the proceedings. Financial and other contributions by the supporting and sponsoring organisations are also gratefully acknowledged.

Espoo, 18 May 2010

Pertti Auerkari & Juha Veivo

Editors

# Contents

Preface	3
<b>Session 3. Combustion plant – Biomass &amp; waste boilers</b>	
Benchmarking for plant maintenance <i>Kari Komonen, Toni Ahonen and Susanna Kunttu</i>	6
Managing corrosion in biomass boilers: benefits and limitations of coatings <i>Satu Tuurna, Tommi Varis, Kimmo Ruusuvuori, Stefan Holmström, Jorma Salonen, Pertti Auerkari, Tuomo Kinnunen, Patrik Yrjas, Risto Finne, Matti Nupponen, Ulla McNiven, Hannu Ahonen and Ari Kapulainen</i>	22
Selecting the right material for recovery boiler superheaters <i>Esa K. Vakkilainen and Pekka Pohjanne</i>	37
Oxyfuel combustion: Oxidation performance of steels in simulated oxyfuel conditions <i>Satu Tuurna, Pekka Pohjanne, Sanni Yli-Olli, Tuomo Kinnunen and Petra Jauhiainen</i>	52
<b>Session 5. Combustion plant – Fossil &amp; co-fired boilers</b>	
Safety issues arising from the corrosion-fatigue of waterwall tubes <i>John M. Brear, Paul Jarvis and Stephen Scully</i>	63
Life assessment for vintage boilers <i>Pertti Auerkari, Jorma Salonen, Stefan Holmström, Leila Laaksonen, Ulla McNiven, Olli Lehtinen, Sari Mäkinen, Ville Väänänen and Reino Nikkarila</i>	78
<b>Session 7. Combustion plant – High temperature components</b>	
Italian standardization in the field of defect evaluation, fracture mechanics and fitness for service of pressure equipment <i>Corrado Delle Site, Carlo Fossati, Giuseppe Giannelli, Claudio Sampietri and Andrea Tonti</i>	90
Defect integrity in components subjected to cyclic loading at high temperatures <i>Stuart Holdsworth</i>	104
Life assessment and extension for gas turbine blades <i>Pertti Auerkari, Jorma Salonen, Juhani Rantala, Sari Mäkinen, Ilkka Karvonen, Heikki Tanttari, Pekka Kangas and Jukka Taattola</i>	117
Fire incidents in underground coal storage <i>Juha Sipilä and Pertti Auerkari</i>	128



Development and Implementation of <i>i</i> -LAS (indentation based turbine remaining life assessment system) <i>Woosung Choi, Geewook Song and Jaeraeyang Koo</i>	143
Creep damage and long term life of steam line components: case X20 <i>Stefan Holmström, Pertti Auerkari, Jorma Salonen, Anssi Laukkanen, Juhani Rantala, Reino Nikkarila and Jarmo Junttanen</i>	154
Remaining lifetime assessment of power plant steam boilers <i>Vaclav Liska and Vaclav Mentl</i>	167
Creep strain, damage and life prediction for welded 0.5CMV steel <i>Juhani Rantala, Pertti Auerkari, Stefan Holmström, Jorma Salonen and Anssi Laukkanen</i>	176
Different types of cracking of P91 steel weld joints after long-term creep tests <i>Dagmar Jandová, Josef Kasl and Eva Chvostová</i>	193
<b>Session 10. Cross-cutting issues – New methods &amp; tools</b>	
New mechanical testing equipment for testing in real and simulated service environments (HIPS) <i>Pekka Moilanen and Stefan Holmström</i>	209
Characterization of true stress-strain behavior using optical monitoring <i>Tom Andersson, Lauri Elers, Anssi Laukkanen and Pekka Nevasma</i>	221
Non-contact measurement of oxide thickness with a laser ultrasonic technique <i>Jonne Haapalainen, Joona Eskelinen, Tarja Jäppinen, Stefan Sandlin and Edward Hæggström</i>	233
On-line flaw growth monitoring in high temperature plant <i>Ian Atkinson, Stephen Kelly, Philip Lay and Colin Brett</i>	239
Experience on the periodic wet bar diagnosis of water-cooled generator stator windings <i>Hee-Soo Kim and Yong-Chae Bae</i>	253
A breakthrough in ultrasonic detection and sizing of partially closed cracks? <i>Stefan Sandlin</i>	270
Development of nondestructive techniques for fuel cladding evaluation in hot cell <i>Tarja Jäppinen and Stefan Sandlin</i>	294

# Benchmarking for plant maintenance

Kari Komonen, Toni Ahonen and Susanna Kunttu  
VTT Technical Research Centre of Finland  
Espoo, Finland

## Abstract

The product of the project, e-Famemain, is a new kind of tool for benchmarking, which is based on many years' research efforts within Finnish industry. It helps to evaluate plants' performance in operations and maintenance by making industrial plants comparable with the aid of statistical methods. The system is updated continually and automatically. It carries out automatically multivariate statistical analysis when data is entered into system, and many other statistical operations. Many studies within Finnish industry during the last ten years have revealed clear causalities between various performance indicators. In addition, these causalities should be taken into account when utilising benchmarking or forecasting indicator values e.g. for new investments. The benchmarking system consists of five sections: data input section, positioning section, locating differences section, best practices and planning section and finally statistical tables.

## 1. Introduction

The significance of the availability of the production equipment, from the competitive advantage point of view, has increased considerably during the last years. The stronger emphasis on the safety and environmental matters has also increased the importance of the maintenance function. In many industrial branches, the significance of the maintenance function has grown and it has become a factor, which makes the difference. The availability of production equipment is very often less than 90% and OEE (overall equipment efficiency) less than 80%.

According to the management of many industrial enterprises 'benchmarking' is a powerful tool for the development of the plant operations. However, among many problems concerning benchmarking a challenge is to make companies or plants comparable. This challenge is sometimes used as an excuse to explain away the worse ranking in comparison. In this paper, we describe the system of benchmarking, which aims to make various production units comparable with the aid of statistical methods based on many years' theoretical and empirical research. The positioning of the production systems is one of instruments introduced in this paper, and the other tools of the system lean on the results of the positioning tool.

The success of the maintenance function can be evaluated (simplifying) with the aid of three factors: the performance of production function, cost-effectiveness of the maintenance function and the quality of maintenance processes. The product of the maintenance activities can be measured e.g. with the aid of overall equipment effectiveness (OEE), availability, lost production due to maintenance or reliability of the machinery. Typical measures for the cost-effectiveness of the maintenance function are 'maintenance costs in relation to plant replacement value', 'maintenance costs in relation to production volume' or 'maintenance costs in relation to production capacity'. The quality of the maintenance processes can be evaluated with such indicators as planning rate, customer satisfaction, employee satisfaction, accident rate or hazard rate etc.

The objectives of this research and development project have required a lot of pre-work:

- Standardisation of concepts and key figures needed in benchmarking
- Data collection
- Research work in the area of causalities between various key performance indicators
- Methods to identify the best plants
- Research to specify relationships between the best practices and performance indicators
- Methods to transform the research results into the properties of this benchmarking system
- Design of system architecture and programming of the web-tool (Komonen 2006).

## 2. Web-tool for benchmarking

The benchmarking system consists of four sections or tools (Komonen 2005).

1. *'Data input section'* is an electronic form to insert the data of the plant in the database. An incorporated test tool will give the user a notice in the case of the most probable mistakes.
2. In the *'positioning section'* there is an option to evaluate the success of the plant's maintenance function branch-wise (by industrial sector) with the aid of several indicators such as OEE, availability of machinery, production losses due to maintenance, maintenance costs as a percentage of estimated plant replacement value and many other.
3. In the *'locating differences section'* it is possible to compare the plant's mode of operations with the successful plants, with the less successful plants and with the average plant in the industrial sector in question. Comparison can be made with the aid of several economic, technical and organisational indicators.
4. In the *'best practices and planning section'* the user of the benchmarking system may find more hints of, which kind of modes of operations lead to successful results. The structure of the tool is illustrated in Figure 1.
5. *Statistical tables* is a section where floating averages for all key performance indicators are presented.

The system is automatic and runs all the automatic calculations getting commands from the user-code and password entered in the system. All the needed calculations are carried out when changes occur or the user commands to execute any task. Simulations are also possible options, for example, for planning purposes. The determination of the variables, which should be taken into account when the system executes automatic multivariate analyses for the positioning, is an expert's job. The same applies to the determination of the impact (direction and strength) of the modes of operations on the selected objectives. The users of the system are able to see their own data only and statistical key figures concerning the industrial branch in question.

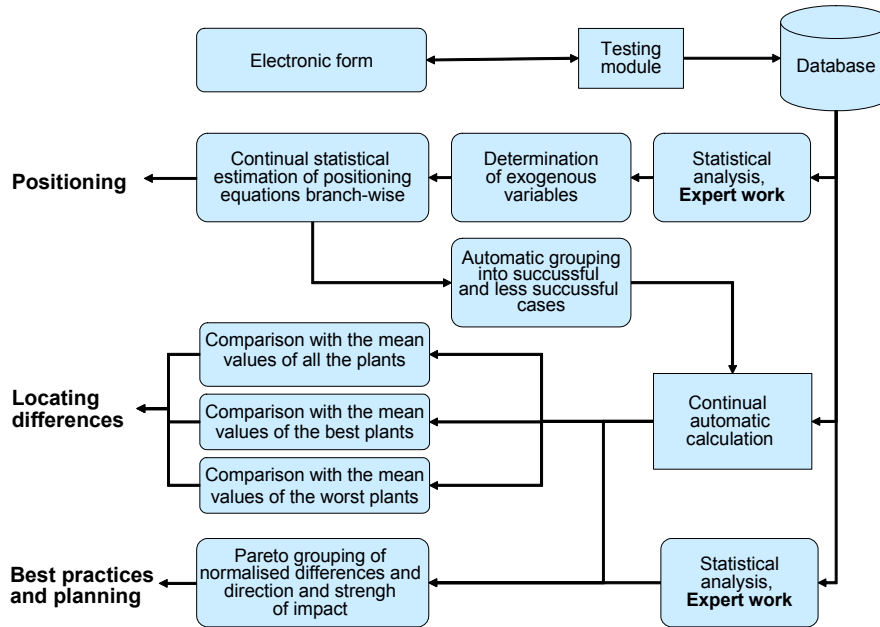


Figure 1. Schematic description of benchmarking system.

### 3. Features of benchmarking system

#### 3.1 Data input

‘Data input section’ serves the user an electronic form to insert data concerning the plant’s maintenance function. An incorporated test tool will give the user a notice in the case of the most probable mistakes. Data entered by the user is precondition for the broader use of this benchmarking system. A part of the data input sheet is illustrated in Figure 2.

All the entered data is confidential and no-one but the organisation which has entered the data in question can see it. The users of the system are able to compare branch-wise their own performance with the total figures and with the figures concerning their own country.

The successful use of this benchmarking system demands a high hit-rate of the most essential data. When this data has not been entered into the system, the program informs of missing data. The system informs the users also in the case of incorrect data input.

## Benchmarking for plant maintenance

For each indicator, there exists also the info-box, which gives additional information concerning the indicator in question. The users can see additional information, when pointing the word “info” with the cursor arrow. On the left of the input boxes, the plants can see the values, they have earlier entered into the database. It is possible to interrupt data input when needed and continue it later.

The screenshot shows a web browser window titled "E-FANEMAN - Microsoft Internet Explorer" with the address "http://www.e-faneman.com/gui/detainput/detain-plant02.php". The main content is a table for "Production (2)" with columns for "Unit", "Value", and "New value". The table lists various indicators such as "Electricity production technology", "Operating rate", "Overall availability", and "Production volume". Each row has an "Info" link. A tooltip is visible over the "Info" link for indicator 2.6, providing a definition of "Gross maintenance downtime".

	Unit	Value	New value	
2.1.1 Electricity production technology	code 1-7	0	<input type="text" value="Choose (0)"/>	Info
2.1.2 Pulp and paper production technology	code 1-4	0	<input type="text" value="Choose (0)"/>	Info
2.1.3 Manufacture of wood	code 1-4	0	<input type="text" value="Choose (0)"/>	Info
2.2 Operating rate	0%-100%	95,00	<input type="text" value="95,00"/>	Info
2.3 Operating time / (operating time + downtime related to failures)	0%-100%	93,00	<input type="text" value="93,00"/>	Info
2.4 Operating time / (operating time + net planned downtime due to maintenance)	0%-100%	90,00	<input type="text" value="90,00"/>	Info
2.5 Gross availability due to maintenance: Operating time / (operating time + gross planned downtime due to maintenance)	0%-100%	99,00	<input type="text" value="99,00"/>	Info
2.6 Maintenance related availability: Operating time / (operating time + net maintenance down time)	0%-100%	99	<input type="text" value="99"/>	Info
2.7 Overall availability: Operating time / (operating time + total down time)	0%-100%	87,00	<input type="text" value="87,00"/>	Info
2.8 Overall Equipment Effectiveness (OEE)	0%-100%	82,00	<input type="text" value="82,00"/>	Info
2.9 Lost production due to maintenance (% of plant turnover)	0%-100%	4,00	<input type="text" value="4,00"/>	Info
2.11.1 Shift work rate	1-5	1	<input type="text" value="1"/>	Info
2.11.2 Utilization rate of production equipment	0%-100%		<input type="text"/>	Info
2.14 Production volume	tons, M3, MWh		<input type="text"/>	Info

**Equipment and buildings (replacement value or fireinsurance value) (3)**

	Unit	Value	New value	
3.1 Production equipment: replacement value	M€	35,00	<input type="text" value="35,00"/>	Info

Figure 2. The illustration of the data input page.

## 3.2 Positioning

With the aid of the positioning results the sample of plants in the benchmarking data-base can be split down into two groups: successful plants and unsuccessful plants. These two groups can be used when trying to identify causes for successful or less successful performance in the case of the individual plant.

In the ‘positioning section’ the users are able to evaluate the success of their maintenance function branch-wise (by industrial sector) with the aid of several indicators such as availability of machinery, production losses due to maintenance, maintenance costs as a % of estimated plant replacement value and many other.

The above mentioned indicators are affected by several external influencing factors which are beyond the scope of the plant management or maintenance managers to determine. But still they have a considerable impact on the performance indicators. Examples of exogenous influencing factors are process severity, plant size, utilisation rate, age of the plant, technology. These factors are taken into account when evaluating one's success with the aid of multivariate statistical models. The conclusion page of the positioning is illustrated in Figure 2.

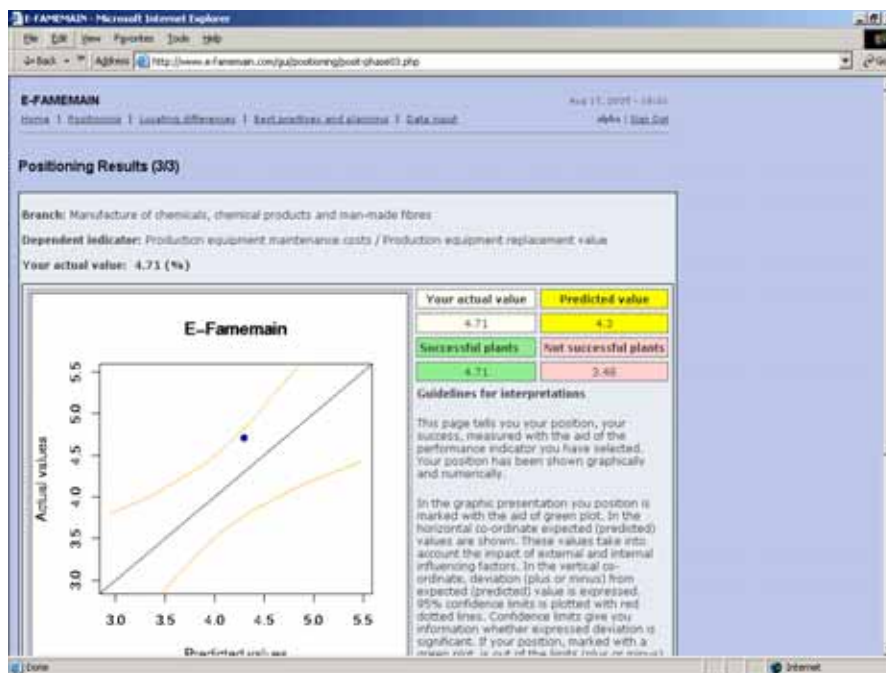


Figure 3. The conclusion page of the positioning.

As stated earlier in the positioning section, various plants are made comparable with the aid of exogenous factors. These factors should be taken into account when evaluating one's success. The benchmarking tool will take care of this analysis automatically for the user. The developed software calls the plants' data from the database, takes into account influencing factors and calculates for the users an expected, predicted value for each performance indicator the user has chosen. The users can also make simulations, how things would change if they were able to change factors which are or are not under their own control. This benchmarking software also groups all plants into successful and less successful subgroups (Komonen 2006).

The conclusion page tells the users their position, their success, measured with the aid of the performance indicator they have chosen. Their position has been shown graphically and numerically. In the graphic presentation the result of the positioning is marked with the aid of a green plot. In the horizontal co-ordinate predicted values are shown. These values take into account the impact of external and internal influencing factors (exogenous factors). In the vertical co-ordinate, the actual values of the plant are shown. The 95% confidence limits are plotted with red lines. The confidence limits give the plant in question information whether expressed deviation is significant or not. The position of the green plot marking plant's performance can be changed with the aid of the simulating tool introduced in the previous page.

### 3.3 Performance indicators

The simplified system of the key performance indicators can be classified in a hierarchical manner. The following structure is the modified version of those ones presented earlier by Komonen (e.g. 2002a).

- (1) business objectives
- (2) first level objectives of production
- (3) second level objectives of production
- (4) objectives for maintenance
- (5) exogenous factors for production and maintenance (external factors)
- (6) intermediate internal objectives for maintenance (follow-up variables)
- (7) action variables of maintenance function (means for improvement)
- (8) internal descriptive (explanatory) variables.

Some of the variables demand more explanation. **The maintenance objectives** are corresponding metrics for the performance of the maintenance function: e.g. availability of machinery due to maintenance, sum of unavailability costs and maintenance costs ("dependability costs"), maintenance costs as a % of estimated plant replacement value (PRV)). **Exogenous independent factors** are indicators, which help management to evaluate the state of technology or business environment and at the same time are beyond the scope of production or maintenance managers to determine, but which have a considerable impact on the other objectives. Examples of these kinds of factors are the utilisation rate of the production machinery, production volume, the amount of the production equipment, the integration level of the production process etc. **Intermediate internal**



**objectives** such as MTTF or MTTR are performance indicators, which should be measured and followed up, since they may give more information about the development needs. These variables are objectives, because production or maintenance managers cannot influence them directly. **The action variables of the maintenance function** are tools of production or maintenance managers, with the aid of which objectives are achieved. Preventive and improvement maintenance, outsourcing, operator maintenance etc. are good examples of these tools (e.g. Komonen 2002, 2002b).

Exogenous independent variables have the major role in the benchmarking system, because they offer an option to make various plants comparable, are basis for the positioning of plants and give a tool to divide the plants in the sample into the groups of successful and less successful production units. Therefore studies concerning causalities between the objective performance indicators and exogenous factors are valuable. The aim is to isolate two sources of variation in the objective indicators: exogenous factors and modes of operations. As mentioned above different kinds of production units or plants can be made comparable with the aid of exogenous factors. Thus, for example, objectives such as 'overall equipment effectiveness' (OEE) or availability are dependent on the external factors, which cannot be influenced in the shorter time span.

In the case of maintenance costs in relation to equipment replacement value exogenous factors may be the following:

- Integration level of production system (which has, in practice, often parallel impacts to maintenance costs as replacement value) (-)
- scale (replacement value of production equipment) (-)
- production volume / production equipment (replacement value) (+)
- shift work rate, operating rate (+)
- Industry –dummy variables (industry specific factors) (-, +).

In the case of maintenance costs in relation to capacity of the production line in question, the effect of exogenous factors may be the following:

- replacement value (-)
- capacity (-)
- capacity / replacement value (-)
- integration level (-)
- production volume (+).

Also other key performance indicators seem to be a function of exogenous factors. For example, 'breakdown hours in relation to plant size' is a function of the plant size. There is a straight scale effect present. This phenomenon is depicted in Figure 4. The causality between plant size and a number of breakdown hours is nonlinear and therefore we have used log transformation. We could present more empirical evidence for this kind of causalities, but in this paper we have to limit evidence in two examples.

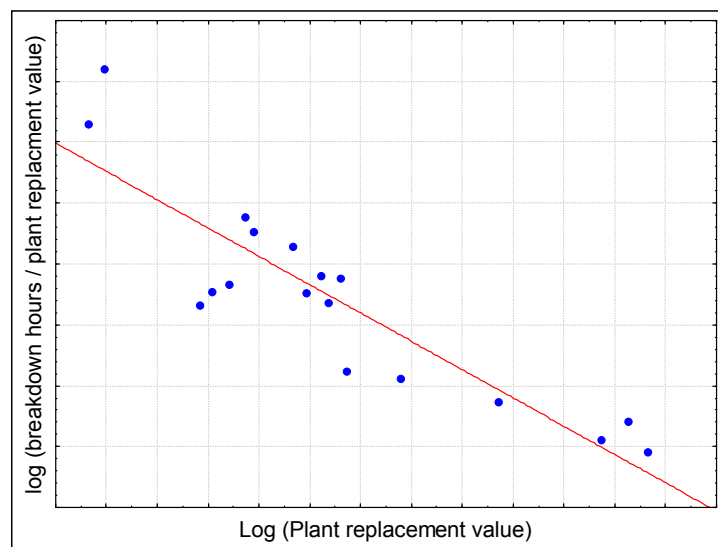


Figure 4. Example of causalities between key performance indicators: 'Breakdown hours in relation to plant size' is a function of the plant size.

In the case of the food industry as an empirical evidence, multivariate regression analysis was carried out in order to find out the impact of exogenous factors. It was interesting to notice that the variables having the most significant impact on the relative cost level were plant size and degree of integration (Table 1). The determining power of model was moderate (0,542), which is not bad taking into account the heterogeneity of the branch (Komonen 2006b).

Table 1. The variables having an impact on relative maintenance costs in the food industry.

Processing of food and liquid (N = 34)		
Dependent variable: Production equipment, Maintenance costs / Replacement value		
Adjusted R <sup>2</sup> = ,542	F(4,29) = 10,773	p < ,00002
	t(29)	p-level
Intercept	3,865	0,0006
Replacement value	-4,386	0,00014
Degree of integration	-2,275	0,030
Plant turnover / plant replacement value	1,859	0,073
Operating rate	1,331	0,193

The causal relationship between the relative maintenance costs and estimated variables is demonstrated in the scatter diagram (Figure 5), where predicted and observed values equal on the diagonal. Cases above the diagonal represent worse performance than expected (Komonen 2006).

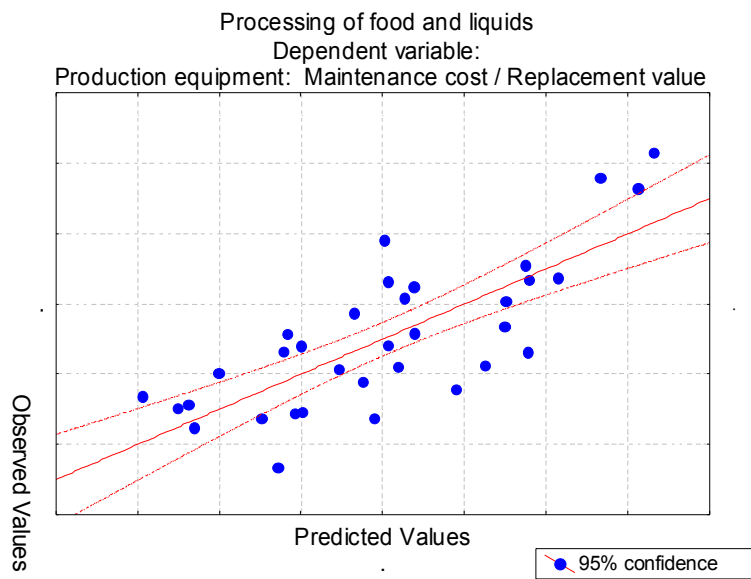


Figure 5. The predicting power of independent variables on relative maintenance costs in the processing of food and liquid.

### **3.4 Locating differences**

Applying positioning to all the cases in the sample it is possible to compare industry-wise the plant's mode of operations with the average plant or with the successful plants or with the less successful plants. Comparison can be made with the aid of several economic, technical and organisational indicators. Examples of the modes of operations are the amount of operator maintenance, preventive maintenance, contracting and improvements or the use of criticality analyses. Following the techniques introduced above it is possible to find some hints of which kind of modes of operations lead to successful results. Since the proper way to improvements depends on the plant's present positioning results and present mode of operations. The conclusion page of "locating differences section" is illustrated in Figure 6.

The objective of this analysis is to find probable causes for deviations from the expected (predicted) values in the positioning section. The benchmarking tool will take care of this analysis automatically for the user. The software calls all the needed data from data base and carries out positioning for each case and in this way groups all the cases into successful and less successful subgroups. Finally, the tool calculates means and deviations for the groups of all cases, successful plants and less successful plants and for each performance indicator the user has chosen. Plants' own actual values for the selected indicator is marked with a green plot. The user can also make simulations, how things would change if he were able to change factors which are or are not under his own control. As soon as the differences in modes of operations have been identified it is possible to investigate which modes of operations are effective and which are not.

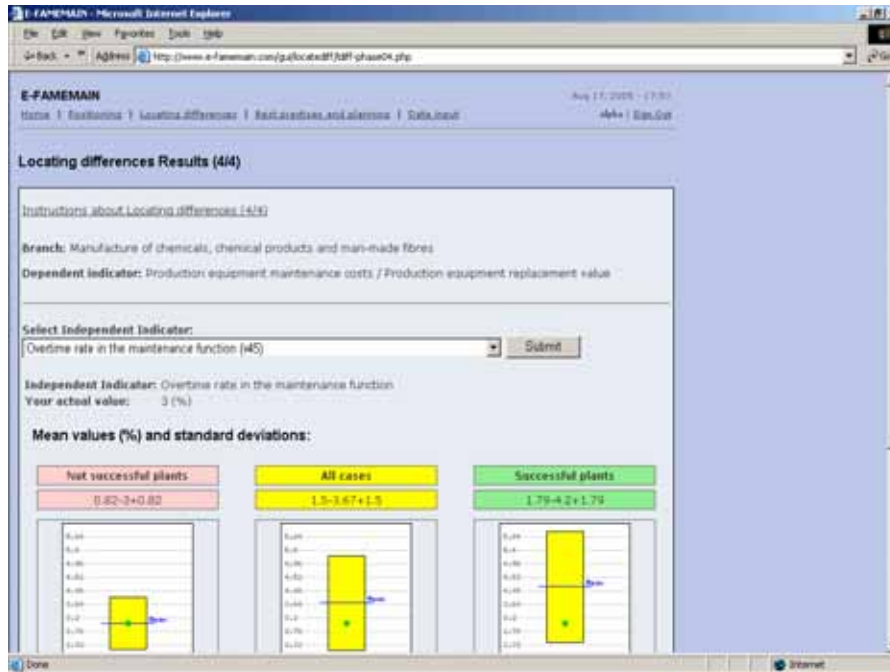


Figure 6. The conclusion page of locating differences.

### 3.5 Best practices and planning

In 'best practices and planning section' the user can find some hints of, which kind of modes of operations lead to successful results. Since the proper way to improvement depends on the user's present results and present mode of operations this section includes also management tool to help in the planning process.

The user is able to compare the plant's mode of operations with the successful plants. The comparison is the summary of the 10 largest deviations in the form of Pareto-diagram and the comparison can be carried out with the aid of several economic, technical and organisational indicators. The objective of this analysis is to find the course of actions which should be carried out in order to improve the performance of objective variables (e.g. OEE, availability or cost effectiveness). Deviations can be positive or negative values.

Since the statistical performance of the successful companies is based on the results of positioning, those results are presented here once again in order to make interpretation easier. Thus, the simulation tool is also available in this section. The differences between the mean values of the most successful plants

## Benchmarking for plant maintenance

and the users' own actual indicator values have been normalised. The graphical conclusions have been presented in Figure 7. The effect of the indicators in question on the dependent variables (e.g. OEE, availability or cost effectiveness) has been indicated in the same table (direction and strength). The causalities between independent and dependent variables have been studied with the aid of the sample entered into data base. Clear causalities could not always be identified (Komonen 2006).

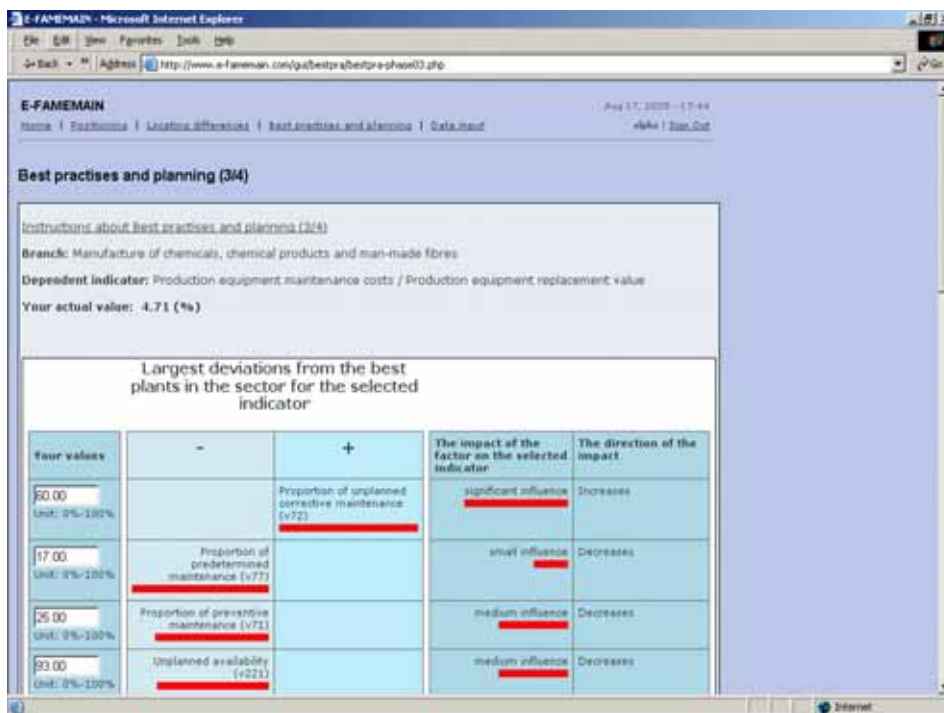


Figure 7. The first conclusion page of best practices and planning section.

The strength of impact has been presented with the aid of five levels: no impact, small influence, medium influence, significant influence and very significant influence. The direction of the effect denotes what happens to an objective value (e.g. availability) if the numerical value of an independent indicator (indicator which depicts the mode of operations) increases.

In the following page there is the summary of the largest deviations and their influence on the performance indicators presented in  $2 \times 2$  table (Figure 8). The greatest attention should be focused on the factors, which indicates the largest deviations and strongest impact. Further, less attention should be focused on the

factors having smaller deviations and smaller impact. If e.g. availability and maintenance costs are studied simultaneously, actions needed may be conflicting. In the case focus should be directed to those activities which have positive impact on both the factors (Komonen 2006).

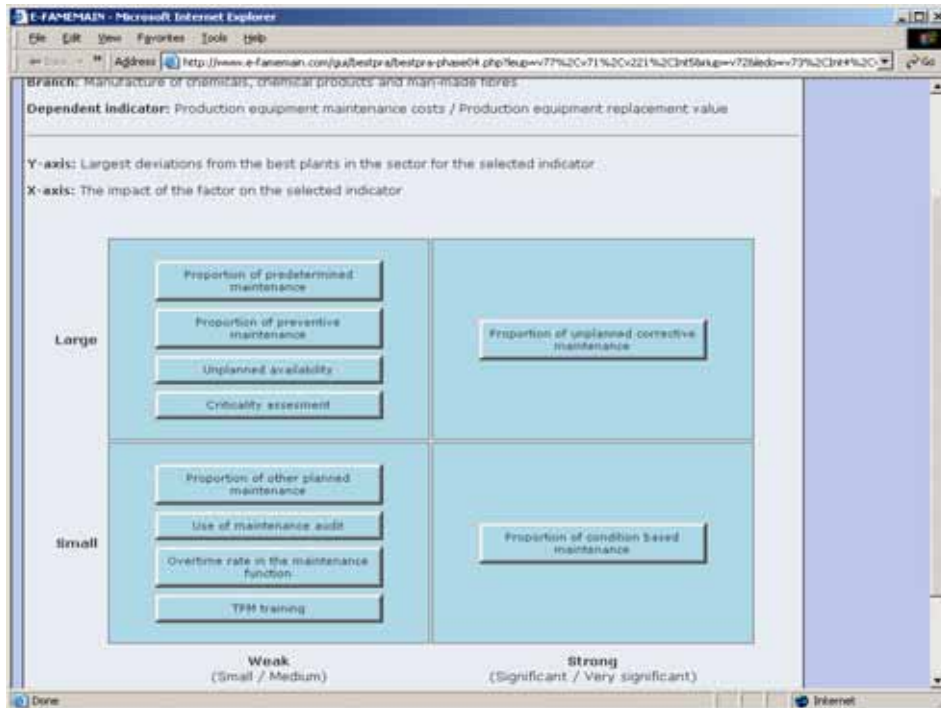


Figure 8. The second conclusion page of best practices and planning section.

## 4. Summary

Several studies during the last 17 years in Finnish industry have revealed clear causalities between certain performance objectives and exogenous variables (e.g. Komonen 1998). These causalities are valid in industrial maintenance, power plants as well as, in many cases, in logistics and operations. In addition, these causalities should be taken into account when utilising benchmarking or forecasting. The introduced web-based benchmarking tool is based on the above mentioned research activities concerning causalities between objective variables and exogenous influencing factors and on the research concerning causalities between the successful plants (determined with the aid of the positioning) and

modes of operations determined by action variables such as preventive maintenance or training of personnel. The results of the first mentioned causalities (objectives and exogenous factors) have been clear and the samples have been sufficiently large.

The needed actions to improve the benchmarking tool are identified. However, the most probable obstacle to improve the characteristics of the system is the lack data. The total number of the plants is surely large enough, but there is a lack of cases for the other than the most common indicators in a specific sector of the industry. In order to draw correct conclusions when using those indicators, more research concerning causal relationships between objectives and exogenous factors (and also action variables) should be carried out.

Regardless of the above mentioned problems some clear results have been achieved. In several industrial branches, the means which improve the product of maintenance activities such as OEE or availability increase the relative costs of the maintenance function and vice versa. Sometimes the results are opposite to expectations. Therefore, the optimisation of the improvement efforts is crucial. The quality of data and sufficient data are also crucial issues when improving benchmarking tools. In empirical research there is always trade off between the detailed data and the number of cases in sample. The ability of the companies to deliver data for a large number of sophisticated indicators is limited.

The introduced benchmarking system is quantitative in nature. There is surely a need to add qualitative features to the system. However, as soon as the scope of the tool is broadened to the qualitative field there is a need to change research strategies, and that means challenges in the architecture of the benchmarking tool and also problems with plants' willingness to deliver data.

## References

- Komonen, K. 1998. The structure and effectiveness of industrial maintenance. Espoo, Helsinki University of Technology, Department of Industrial Economics, Ph.D. Dissertation. (In Finnish).
- Komonen, K. 2002. A cost model of industrial maintenance for profitability analysis and benchmarking. *International Journal of Production Economics*, Vol. 79, pp. 15–31.
- Komonen, K. 2002b. Views on performance indicators and benchmarking in industrial maintenance. *Maintenance* 5, pp. 52–56.



Komonen, K. 2005. E-FAMEMAIN Benchmarking tool for industrial maintenance – a web based planning tool. Helsinki, Finnish Maintenance Society, p. 22 p. (In Finnish).

Komonen, K. 2006. E-FAMEMAIN: A new kind of web-based benchmarking tool. Conference Proceedings. Euromaintenance 2004, Basel.

Komonen K. 2006b. Availability guarantees and physical assets management: Empirical evidence of the impact of some underlying factors. Conference Proceedings. RAMS 2006. Newport Beach, CA, USA.

# Managing corrosion in biomass boilers: benefits and limitations of coatings

Satu Tuurna<sup>1</sup>, Tommi Varis<sup>1</sup>, Kimmo Ruusuvuori<sup>1</sup>, Stefan Holmström<sup>1</sup>,  
Jorma Salonen<sup>1</sup>, Pertti Auerkari<sup>1</sup>, Tuomo Kinnunen<sup>1</sup>, Patrik Yrjas<sup>2</sup>,  
Risto Finne<sup>3</sup>, Matti Nupponen<sup>4</sup>, Ulla McNiven<sup>5</sup>,  
Hannu Ahonen<sup>5</sup> and Ari Kapulainen<sup>6</sup>

<sup>1</sup>VTT Technical Research Centre of Finland, Espoo, Finland

<sup>2</sup>Åbo Akademi, Turku, Finland

<sup>3</sup>Kuopion Konepaja, Kuopio, Finland

<sup>4</sup>Turku Energia, Turku, Finland

<sup>5</sup>Fortum, Espoo, Finland

<sup>6</sup>Ekokem, Riihimäki, Finland

## Abstract

Oxidation and corrosion of materials in highly demanding applications is critical for longterm performance of materials used in power generation. Energy production in biomass fired boilers is increasing rapidly due to the advantages of CO<sub>2</sub> neutrality and renewability. Fluidised bed combustors and grate fired boilers have proved the most reliable technologies for burning biomass since its fuel characteristics are variable. The fly ash of biomass is relatively corrosive due to its composition containing high concentrations of chemically active compounds of alkali, sulphur and chlorine, and it also may contain erosive components especially in the case of fluidised bed boilers. Due to the potential for severe chlorine induced corrosion, plant operating temperatures and efficiency must be limited. To overcome material wastage more alloyed materials are needed. The high cost and sometimes hard to manufacture bulk materials could be replaced with coatings, which can be applied on the more economic low alloy steel having the proper mechanical properties. The paper discusses the benefits and limitations of thermal sprayed coatings in biomass boilers. The applied examples

have included iron and nickel based HVOF and arc sprayed coatings subjected to verification field testing in boiler testing under in aggressive biofuel conditions. The coatings have shown good corrosion resistance in long-term field tests.

## 1. Introduction

Thermal sprayed coatings have been used several years successfully as protective coatings against erosion in coal-fired power boilers. As the variety of dirty fuels used (waste, biomass) in power generation increases and the steam temperatures are increasing with higher efficiency demands, the need for better materials and protection become more important. The rate of corrosion in biomass combustion is much higher than in conventional coal fired power plants due to the heterogeneous fuel quality. Biomass deposits are usually rich of potassium, silicon and calcium, and chlorine and sulphur content can be also high. Chlorine can accelerate corrosion resulting in oxidation, metal wastage, internal attack, void formation and loose scales. HCl alone in the flue gas can not cause severe attack, but it may provide scale failure and enhance the corrosion rate. Severe corrosion may occur when chlorine is present in the deposits which are in contact with the metal scale. Alkali salt mixtures have low melting points and tend to melt on tube surfaces that increases the ash deposition on the tubes. The presence of alkali chlorides can cause enhanced corrosion already below the melting point of the deposit. The corrosion may be further accelerated by SO<sub>2</sub>, which can cause sulphation of alkali chlorides liberating HCl or Cl<sub>2</sub> gas near the metal surface. Fouling and slagging seem to be worsened by the presence of chlorine which increases the mobility of inorganic compounds. Many times the major mechanism of material wastage in biomass boilers has been detected as erosion stimulated corrosion and corrosion accelerated erosion, especially in the case of fluidised bed boilers [1–6]. Operating temperatures and efficiency are limited to maximise the lifetime of boiler components due to the potential for severe chlorine induced corrosion. In order to minimise material related risks, normally used low alloy steels have been replaced with high alloy steels in more aggressive conditions. These alloys normally contain high amounts of chromium and nickel for enhancing high temperature corrosion resistance. However, many times a combination of good mechanical properties and superior corrosion resistance is mutually exclusive. The high cost and sometimes hard to manufacture bulk materials could be

replaced with coatings, which can be applied on the more economic low alloy steel having proper mechanical properties.

In demanding corrosion environments it is not sufficient to just specify alloy and coating method. To obtain reliable coatings the whole coating production needs to be considered including alloy selection, spray parameters, surface preparation and base metal properties. The high velocity oxy fuel (HVOF) process, arc spraying, and spray with fuse are the most promising techniques to optimise both coating properties and economical aspects [7]. HVOF process is used in many industries due to flexibility, cost effectiveness and the superior quality of coatings [8]. The HVOF coatings are considered as relatively homogeneous and dense, but always contain some oxides and porosity (< 1%) at splat boundaries. These inhomogeneities affect the corrosion protection ability of the coatings. Aggressive elements from the surrounding environment can proceed through a coating causing the corrosion of coated component at least in some extent. The critical issue is to achieve high integrity coatings without significant particle oxidation during spraying. A cheaper option that is also more easily adaptable to on-site coating is arc spraying, although it will result in a higher porosity level (< 5%) [9, 10]. Thermal sprayed fused coatings are dense and very well adhered to substrate, but the applicability of these coatings in boiler plants is challenging and the production is mostly carried out in workshops. However, some companies are specialised on on-site manufacturing.

Nickel-chromium based alloys have been widely used as protective coating systems in environments with high temperatures [11]. To improve the erosion resistance, the standard practice is to add hard particles such as carbides (often chromium carbides) or borides to a metal matrix (e.g. nickel-chromium or iron-chromium) coating. For best erosion resistance the carbide content can exceed 50–70%, however high carbide content can reduce ductility and resistance to cyclic service [12, 13].

The corrosion behaviour of different HVOF and arc sprayed coatings were tested in long-term field tests. The results of these tests are represented. The overall benefits and limitations of coatings in biomass boilers are discussed.

## **2. In-service boiler testing**

Coatings were applied in three boiler applications. Boiler I was a fluidized bed boiler fired with solid biomass, mainly with peat mixed with wood-based fuels. The location of interest was selected within the economiser of the boiler, at a

position where ash blockages and tube failures have been recorded. The base material of the  $\text{Ø}48.5 \times 5.05$  mm (measured dimensions) test tube was 16Mo3. The HVOF thermal spray process using a DJ hybrid with hydrogen and Amperit 584.1 powder was applied to produce an about 200  $\mu\text{m}$  thick 75%  $\text{Cr}_3\text{C}_2$ -25% NiCr coating on the tube, Figure 1. The selected type of coating is mainly intended for applications against erosion, but with the high chromium and nickel contents (Ni-20%Cr) of the matrix also shows considerable resistance to corrosion. A maximum service temperature of 870°C is indicated by the powder manufacturer for  $\text{Cr}_3\text{C}_2$ -NiCr coating. A short section at each end of the tubes was left uncoated to facilitate appropriate tube attachment by welding. The coated length of the tube was about 1 m. The coated tube was installed in the economiser, Figure 2. The targeted time of exposure was set at about one calendar year.



Figure 1. An as-coated tube attached to a rotating fixture.

After about one year of exposure, the coated test tube was removed for post-exposure analysis. For post-exposure analysis, the coated sample tube was visually inspected and then cut to rings for more detailed cross-sectional investigation. The cross-section ring samples were prepared for metallographic inspection by grinding, polishing and etching, and for deposit analysis without aqueous media. The inspections were made by light optical (LOM) and scanning electron microscopy (SEM), and the external deposit was also analysed by using

energy dispersive X-ray spectroscopy (EDS). Similar procedures were also used for post-exposure analysis for the other two cases.



Figure 2. A coated tube installed into an economiser in boiler 2.

Boiler II was also a fluidized bed boiler with solid biomass, mainly wood-based fuels mixed with small amounts of peat. Test tubes were located at two positions, at cold and hot economiser, where tube failures have been recorded. The base materials of the test tubes were P235 in the cold end and P265 in the hot end of the economiser. The measured dimensions of the test tubes and applied coatings are presented in Table 1. Both the HVOF process using a DJ Hybrid and arc spray using a Smart Arc were applied to produce about 300  $\mu\text{m}$  and 400  $\mu\text{m}$  thick coatings, respectively, on the tubes. As in previous case, the targeted time of exposure was set to about one calendar year. After about one year of exposure, the coated test tubes were removed for post-exposure analysis.

Boiler III was a waste-fired grate boiler. The location of interest was selected within the superheater area of the boiler. The base material of the superheater tubes was 16Mo3 (nominal measures  $\text{Ø}38 \times 5$  mm). Both the HVOF and spray and fused coatings were about 300  $\mu\text{m}$  thick, Table 1. Also in this case the coated length of the tubes was about 1 m and a short section at each end of the tubes was left uncoated for welding. As in previous cases, the coated test tubes were removed for post-exposure analysis after one year of exposure.

Table 1. Summary of produced coatings for different boilers. AM = amorphous.

Coating type	Boiler appl.	Powder manufact.	Composition	Spray device	Tube material
<b>Cr<sub>3</sub>C<sub>2</sub>- (Ni20Cr)</b>	Boiler I	Sulzer, WOKA 7302	Cr <sub>3</sub> C <sub>2</sub> -25(Ni20Cr)	HVOF (DJ Hybrid)	16Mo3 Ø48.5×5.05
<b>NiCr 50-50</b>	Boiler II	Praxair, 1260F-10	Ni-46Cr-1.1Fe-0.5Si- 0.1CMnO	HVOF (DJ Hybrid)	P235 Ø38.3×4.2
<b>AM Fe-Cr</b>	Boiler II	Nanosteel, SHS7170	Fe-20Cr-10W-5Mo- 5B-5Mn-2C-2Si	HVOF (DJ Hybrid)	P235 Ø38.6×4.3
<b>NiCr 50-50</b>	Boiler II	Praxair, 1260F-10	Ni-46Cr-1.1Fe-0.5Si- 0.1CMnO	HVOF (DJ Hybrid)	P265 Ø38.7×5.1
<b>AM Fe-Cr</b>	Boiler II	Nanosteel, SHS7170	Fe-26Cr-5W-5B-4Mo- 4Mn-3Si-2C	Arc spray (Smart Arc)	P265 Ø39.5×5.5
<b>Fe-27Cr-2C</b>	Boiler III	Durum	Fe-27.2Cr-10.7Ni- 3.9Mo-1.4Si-2C	HVOF (DJ Hybrid)	16Mo3 Ø38×5
<b>AM Fe-Cr</b>	Boiler III	Nanosteel, SHS9172	Fe-25Cr-15W-12Nb- 6Mo-5B-4C-3Mn-2Si	HVOF (DJ Hybrid)	16Mo3 Ø38×5
<b>Ni-16Cr</b>	Boiler III	Sulzer Metco, Metco 19E	Ni-16Cr-4Si-4B- 4Fe-2.4Cu-2.4Mo- 2.4W-0.5C	Flame spray + fused	16Mo3 Ø38×5
<b>IN625</b>	Boiler III	Plasmalloy	Ni-23Cr-5Fe-10Mo- 4Nb-TiAlCMnSi	HVOF (DJ Hybrid)	16Mo3 Ø38×5
<b>Alloy 59</b>	Boiler III		Ni-24Cr-16.5Mo- 1.5Fe-0.5Al	HVOF (DJ Hybrid)	16Mo3 Ø38×5

### 3. Results of field testing

All the coated sample tubes were covered after a year exposure by a light brown deposit. In the first boiler application, no clear signs of significant wall thinning, defects of the coating or other damage were found on the external surfaces. The general appearance of a tube cross-section including the deposit and coating is shown in Figure 3. The coating seems to have suffered little if any wear, corrosion or other damage during service. Regarding the potential impact of corrosion, fireside element mapping of the coating showed only slight possible penetration of the deposit elements into the outer coating layers up to depth of

about 10  $\mu\text{m}$ . The results of EDS analysis taken from the deposit of the sample tube are shown in Figure 4. The results showed high contents of compounds like Ca, Al and Si, which are typical for deposit in peat and wood firing. The observed K content was higher than Na content, which is also typically for wood. Concentration of chlorine (more than 1%) is probably well compensated by the much higher S content.

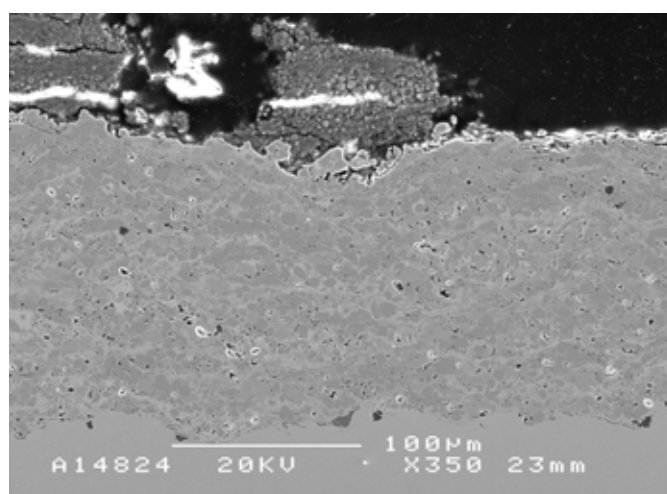


Figure 3. Cross-section of the  $\text{Cr}_3\text{C}_2$ -(Ni<sub>20</sub>Cr) coating (thickness 150–170  $\mu\text{m}$ ) below the fireside deposit.

The visual inspection of hot economiser tubes of the second boiler application revealed undamaged coating surfaces whereas corrosion pitting could be seen on un-coated tube surfaces. Coatings resisted conditions quite well in the conditions where uncoated tubes lost even 2 mm of their thickness. Deepest pits were found on the windward side at the positions of ten and two o'clock. Some differences between the coatings were observed in cross-sectional study, Figure 5. HVOF sprayed nickel-chromium coatings seemed undamaged after a one year service. Some cracking and spallation of amorphous iron-chromium coatings could be observed, especially in the case of arc sprayed coating. However, all coatings were still attached to the tube surfaces.



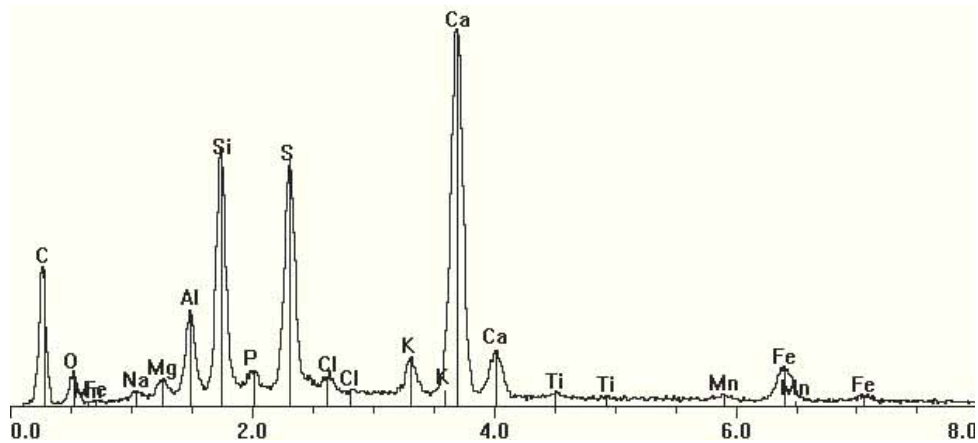


Figure 4. EDS spectrum of the deposit formed on the test tube in Boiler I. The peaks show presence and relative amount of the indicated elements.

The visual inspection of the external surfaces of the sample tubes in the third boiler applications did not reveal any signs of coating damages. The cross-sectional studies showed that all the coatings were principally in a good condition, Figure 6. At the inspection points, no peeling of coatings, no corrosion of the coating structure or tube below the coating was found. However, in some points a thin continuous oxide layer was formed at the coating-tube interface. This phenomenon was usually connected to the vertical cracking of the coating (Figure 6b) but not in all cases. Although cracks were found, no corrosion products were observed inside the cracks. Some minor cracks near the coating surface were also observed in the spray and fused coating. In all cases uncoated tube material was corroded and corrosion penetrated near the coating edge to around 100  $\mu\text{m}$ , Figure 6c. The typical thinning depth of tubes was around 100  $\mu\text{m}$ .

Managing corrosion in biomass boilers: benefits and limitations of coatings

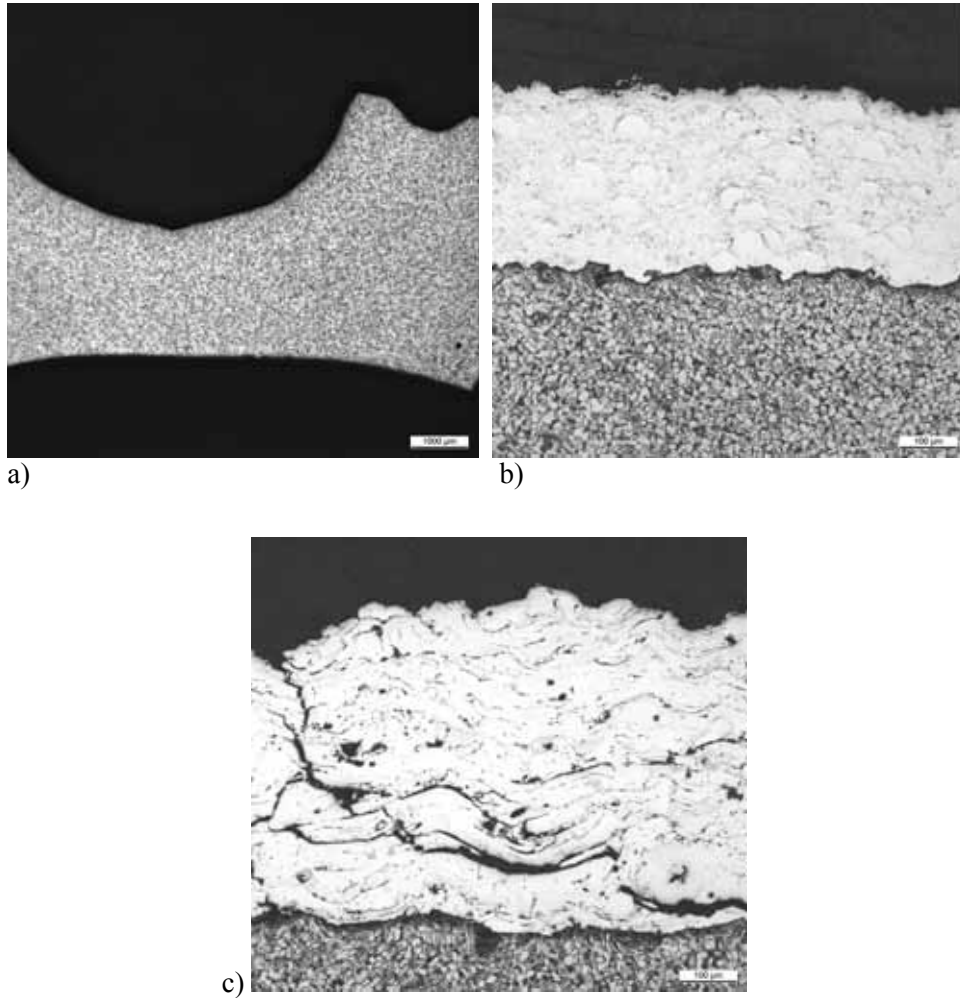


Figure 5. Tube cross-sections after one year service from Boiler II. a) Uncoated tube, b) HVOF sprayed nickel-chromium coating and c) arc sprayed iron-chromium coating.

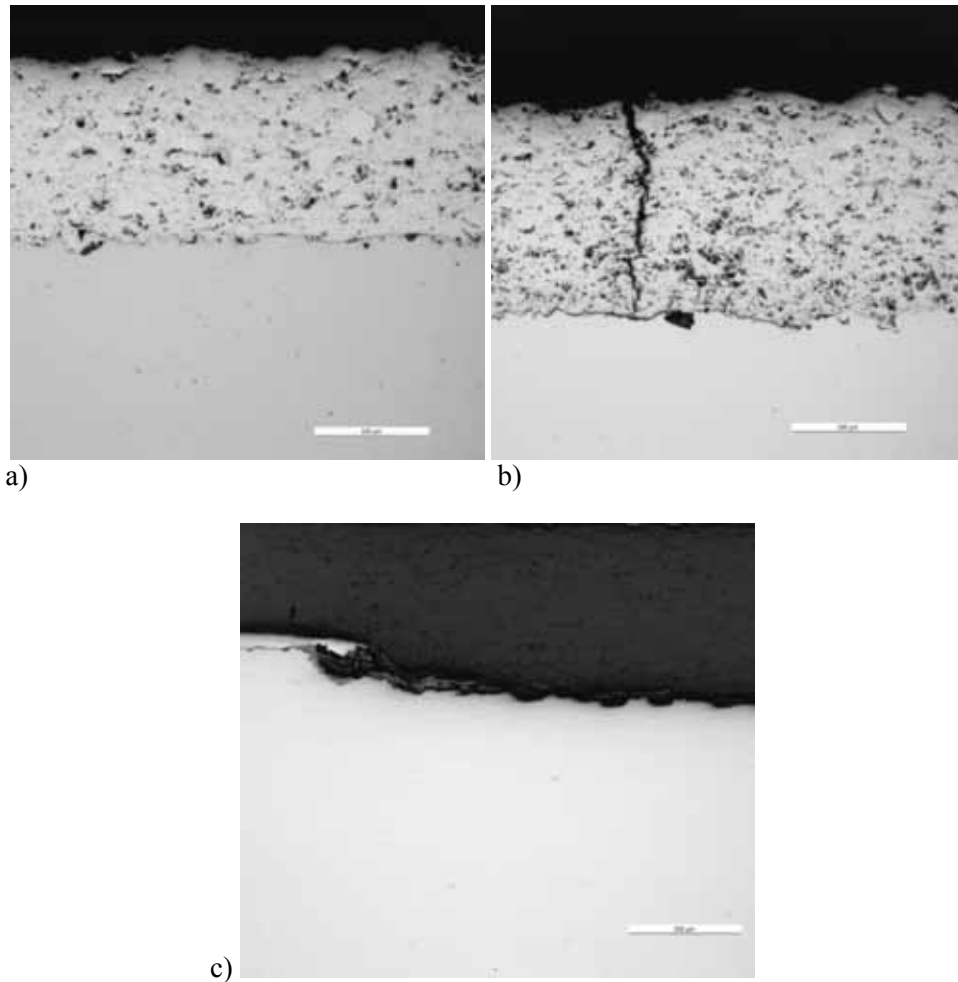


Figure 6. Cross-sections of the coated tubes from Boiler III. a) HVOF sprayed Ni-24Cr-16Mo, b) cracked HVOF sprayed Fe-25Cr and c) corroded tube surface near the coating edge.

## 4. Discussion

The service exposures were conducted in selected biomass and waste fired boilers where deposit formation or tube failures were observed in the past. In the case of boiler I, the applied coating performed well but the uncoated section was also not experiencing much damage or wall thinning. It was concluded that in this boiler the fuel and the process were sufficiently well controlled even without additional protection from coatings. In Boiler II, no appreciable corrosion or other damage was observed in the HVOF coated tubes under conditions where

uncoated tubes suffered severe material loss up to millimetres within one year of service. While fully protective for the test period, some cracking and spallation was observed in an amorphous iron-chromium coating, especially when produced with arc spraying. Similar cracks were also found on the amorphous coating from Boiler III. The importance of matching the CTE's in the coating and tube material is critical to avoid the tensile stress development in the coatings during the boiler heat up. Tensile stresses may easily break the coating having relatively brittle nature. The brittle nature of the thermal sprayed amorphous arc sprayed material is seen in Figure 7, where horizontal and through lamella cracks are visible even in the assprayed coating. Higher brittleness compared to HVOF coating (Figure 7a) may arise from the microstructure where arc sprayed coating typically has limited lamella cohesion due to the cracks between lamellas as shown in Figure 7. The brittle nature of the coating makes it also susceptible to failures in any kind of impacts during preparation. In particular Ni-50Cr HVOF coatings have performed well, without any detected symptoms of damage.

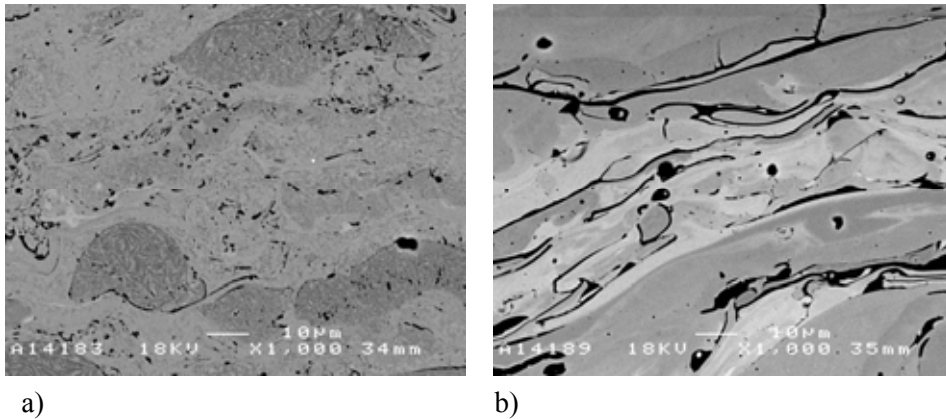


Figure 7. Typical microstructural features of a) HVOF sprayed and b) arc sprayed coatings.

The coatings in Boiler III performed well and no corrosion was observed in the coated areas. Some coatings, particularly amorphous coating and spray and fused coating, had some cracks, but no corrosion products were observed inside the coatings. Fusion treatment might form some stresses in the coating structure, which facilitate crack formation. The spray and fused coating composed of different phases and no clear lamellar structure which is typical for sprayed coatings was present. The cracks are suggested to facilitate the formation of

oxide layers at the coating-tube interface. The oxide layers were also observed below the sound coatings. This may be a result from the cracks situating nearby, but not in the exact inspection point, or from the coating structure and composition. Some structures may allow easier oxygen penetration although the microscopical observation does not reveal any significant differences.

The good results suggest that the benefit of coatings could be extended to boilers and locations with even more severe service conditions. Also, the observed good performance of the tested coatings may provide opportunities for cheaper coatings, and for this purpose further investigation with field testing is underway.

## **5. Benefits and limitations of coatings**

The advantages of thermal spraying are that it is relatively inexpensive, part size is not a concern and deposition rate is high. Relatively thin coating layers may show an economical benefit provided that they retain sufficient protective qualities. Unlike new bulk metals, coatings can be used as non-standard materials with highly alloyed tailored compositions that have not been established in the current material standards for pressure equipment. The experience on the practical value of fireside thermal spray coatings has been rather mixed, and the resulting operator attitudes sometimes reserved. However, improvements have been reported in the materials, processes and quality aspects of such coatings, e.g. [14–16]. And also the study related to this paper has shown that coatings can withstand conditions where bare tube materials suffer severe material loss. For successful service on the fireside, the coating should be thick and resistant enough not to wear off before a specified minimum period of boiler service. The coating should remain protective without peeling or exfoliation in the boiler environment up to a specified time, and should allow for fabrication at competitive cost so that the intended function (e.g. heat transfer) of the coated component remains at the specified level for the specified time.

The adhesion of thermal spray coating is mainly mechanical, thus coating removal and recoating are possible instead of replacement of whole component. The surface heat-up is quite limited (max 200°C) and the potential for the distortion and change of mechanical properties of tubes during coating process is very small.

The coating production is very sensitive for manufacturing parameters, and incorrect parameters produce porous structures with weak adhesion. Even though the coating material performance itself may be advantageous the chlorine penetration to the base material-coating interface or thermo-mechanical compatibility

can cause unexpected damages. Based on the experiments it became evident that the mechanical compatibility is one of the key issues in the material selection, thus most of the tested materials can withstand the corrosion conditions but suffered the cracking. Different kinds of surface modification techniques or post-spray treatments, e.g. laser melting or sealants, can be used to improve the coating quality and properties, such as density, hardness and toughness of coatings [17–19]. These, however, increase production costs in some degree. Coating selection should be based on life-cycle costs and the material selection is case specific. The benefit from the investment to the coated solution should be significantly larger than the cost of repeated replacement. Except perhaps in case of simple wall panels, the component should be probably designed as a coated system, to obtain maximum benefit from the attainable coating quality. In this way suitable coatings could facilitate the use of more aggressive fuels and firing conditions than what are the practical limits otherwise.

## 6. Conclusions

On-site experiments in three Finnish boiler plants for up to one year each at a time have demonstrated a range of coating materials that promise to improve the expected life of boiler tubes under corrosive/erosive service. Requirements of further development are seen in up-scaling the coatings from the test scale of about one square meter to that of thousands of square meters or more in plant, essentially without loss in quality.

The results can be applied for current and future boilers to improve the durability and life expectancy of the fireside heat transfer surfaces. For optimal benefit in many cases, such solutions are likely to require some design modification of the components. However, when the combustion conditions are severe and result in rapid loss of fireside material, the economical benefits from the coatings can be substantial by more than doubling the expected life.

## Acknowledgements

The valuable technical and financial support of Fortum (Espoo, Finland), Turku Energia (Turku, Finland) and Ekokem (Riihimäki, Finland) are gratefully acknowledged. The financial support by Tekes (Finnish Funding Agency for Technology and Innovation) and VTT is also acknowledged.

## References

1. Pettersson, R., Flyg, J. & Viklund, P. High temperature corrosion under simulated biomass deposit conditions. *Corrosion Engineering Science and Technology*, Vol. 43 (2008), pp. 123–128.
2. van Lith, S. C., Frandsen, F. J., Montgomery, M., Vilhelmsen, T. & Jensen, S. A. Lab-scale investigation of deposit-induced corrosion of superheater materials under simulated biomass-firing conditions. Part 1: Exposure at 560°C. *Energy & Fuels*, Vol. 23 (2009), pp. 3457–3468.
3. Nielsen, H. P., Frandsen, F. J., Dam-Johansen, K. & Baxter, L. L. The implications of chlorine-associated corrosion on the operation of biomass-fired boilers. *Progress in Energy and Combustion Science*, Vol. 26 (2000), pp. 283–298.
4. Ma, W. & Rotter, S. Overview on the chlorine origin of MSW and CI-originated corrosion during MSW & RDF combustion process. Second International Environment and Public Health Track Shanghai, China, 2008. IEEEXplore.
5. Montgomery, M., Vilhelmsen, T. & Jensen, S. A. Potential high temperature corrosion problems due to co-firing of biomass and fossil fuels. *Materials and Corrosion*, Vol. 59 (2008), pp. 783–793.
6. Wang, B.-Q. Erosion-corrosion of coatings by biomass-fired boiler fly ash. *Wear*, Vol. 188 (1995), pp. 40–48.
7. Heath, G. R., Heimgartner, P., Irons, G., Miller, R. & Gustafsson, S. An assessment of thermal spray coating technologies for high temperature corrosion protection. *Materials Science Forum*, Vols. 251–254 (1997), pp. 809–816.
8. Stokes, J. & Looney, L. Residual stress in HVOF thermally sprayed thick deposits. *Surface and Coating Technology*, Vols. 177–178 (2004), pp. 18–23.
9. Oksa, M., Kärki, J., Varis, T. & Turunen, E. Corrosion resistance of HVOF coatings in a biofuel boiler plant. *EUROCORR '05*, Lissabon, Portugal, September 4–8, 2005, 421.
10. Uusitalo, M., Vuoristo, P. & Mäntylä, T. High temperature corrosion of coatings and boiler steels below chlorine-containing salt deposits. *Corrosion Science*, Vol. 46 (2004), pp. 1311–1331.

11. Higuera Hidalgo, V., Belzunce Varela, J., Carriles Menéndez, A. & Poveda Martinez, S. High temperature erosion wear of flame and plasma-sprayed nickel-chromium coatings under simulated coal-fired boiler atmospheres. *Wear*, Vol. 247 (2001), pp. 214–222.
12. Totemaier, T., Wright, R. & Swank, W. Microstructure and stresses in HVOF sprayed iron alumide coatings. *Journal of Thermal Spray Technology*, Vol. 11 (2002), pp. 400–408.
13. Wang, B. Q. & Seitz, M. Comparison in erosion behavior of iron-base coatings sprayed by three different arc-spray processes. *Wear*, Vol. 11 (2001), pp. 755–761.
14. Singh, H., Puri, D. & Prakash, S. Some studies on hot corrosion performance of plasma sprayed coatings on a Fe-based superalloy. *Surface and Coatings Technology*, Vol. 192 (2005), pp. 27–38.
15. Sidhu, T. S., Prakash, S. & Agrawal, R. D. Hot corrosion studies of HVOF NiCrBSi and Stellite-6 coatings on a Ni-based superalloy in an actual industrial environment of a coal fired boiler. *Surface and Coating Technologies*, Vol. 201 (2006), pp. 1602–1628.
16. Sundararajan, T., Kuroda, S. & Abe, F. Steam oxidation resistance of two-layered Ni–Cr and Al APS coating for USC boiler applications. *Corrosion Science*, Vol. 47 (2005), pp. 1129–1147.
17. Oksa, M., Turunen, E. & Varis, T. Sealing of thermally sprayed coatings. *Surface Engineering*, Vol. 20 (2004), pp. 251–254.
18. Tuominen, J., Vuoristo, P., Mäntylä, T., Kylvälähti, M., Vihinen, J. & Andersson, P. H. Improving corrosion properties of high-velocity oxy-fuel sprayed Inconel 625 by using a high-power continuous wave neodymium-doped yttrium aluminum garnet laser. *Journal of Thermal Spray Technology*, Vol. 9 (2000), pp. 513–519.
19. Sidhu, B. S., Puri, D. & Prakash, S. Mechanical and metallurgical properties of plasma sprayed and laser remelted Ni–20Cr and Stellite-6 coatings. *Journal of Materials Processing Technology*, Vol. 159 (2005), pp. 347–355.



# Selecting the right material for recovery boiler superheaters

Esa K. Vakkilainen and Pekka Pohjanne\*  
Lappeenranta University of Technology  
Lappeenranta, Finland

\*VTT Technical Research Centre of Finland  
Espoo, Finland

## Abstract

The aim of this paper is to examine the selection of superheater materials for recovery boilers. Fireside wastage in recovery boilers is mainly caused by formation of corrosive deposits, typically with aggressive molten alkali phases. Fireside corrosion can also be caused by gaseous components and is then usually associated with a reducing atmosphere. This active oxidation can affect superheater tubes even at temperatures lower than the first melting temperature. There is a wide array of available superheater materials to choose from and a few newer materials to be considered. The operating conditions and deposit properties must be looked at when material selection is done. The material choice has a significant effect to the cost of the recovery boiler, as the selection of the final superheater material can change the price by a factor of 10.

## 1. Introduction

The recovery boiler is fired with evaporated black liquor that is the spent cooking liquor from the kraft process. The current average black liquor dry solids content in Finland is around 80% DS. The black liquor is a good fuel since it contains more than half of the energy content of the wood fed into the digester. Recovery boiler carries out several functions, it burns the organic material that is contained in the black liquor to generate high pressure steam and

## Selecting the right material for recovery boiler superheaters

nowadays also increasing amounts of electricity; it regenerates the used chemicals in black liquor, and reduces some waste streams in an environmentally friendly way [1]. The trend to increase electricity generation is forcing to increase steam values. If the steam pressure and temperature can be increased to 104 bar and 520°C from typical current values of 80 bar and 480°C the electricity generation capacity of the recovery boiler plant increases about 7% [2]. A typical new recovery boiler is shown in Figure 1.

A key issue for the recovery boiler is the high availability need. And when recovery boilers are designed one of the most difficult questions that arise is; what kind of materials should one use for different parts of the recovery boiler. In future this is expected to become even more complicated since the demand to increase steam value increase the corrosion risk especially in the superheaters.

When selecting superheater materials one needs to consider several factors [4, 5]. Set design conditions (pressure, temperature, corrosion, erosion) determine the boundary conditions. Tube material mechanical properties (strength) determine the tube thickness. Manufacturing properties (weldability, need for heat treatment) determine the required time to manufacture a piece of heat transfer surface. Cost of material and relevant manufacturing cost give the total cost for heat transfer surface. Often also material availability (time the material can be delivered for manufacturing) plays a significant role. One should not forget that variation of process values during operation (e.g. temperature spikes and liquor chemistry) can greatly affect corrosion rate and strength of some materials but not others.

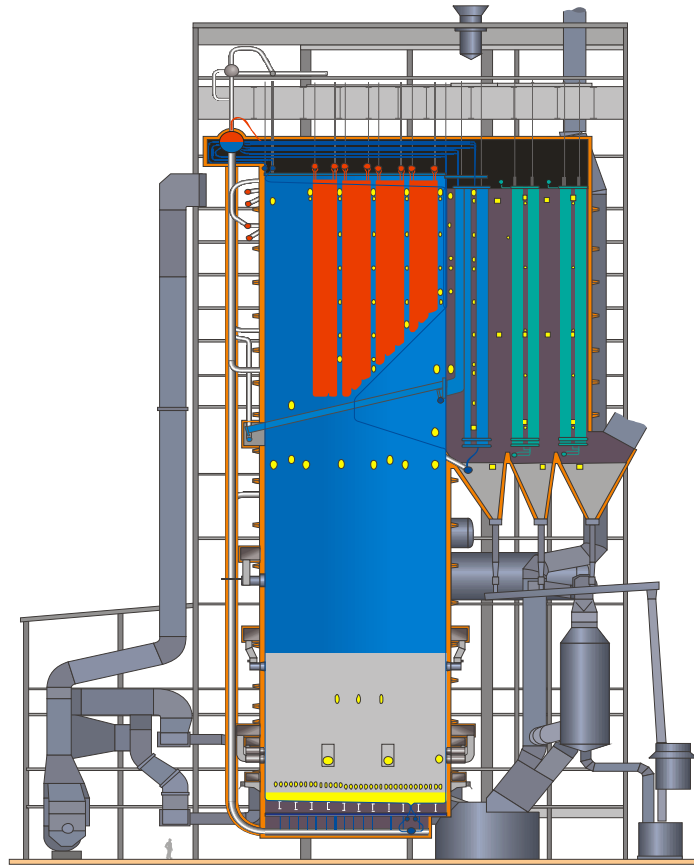


Figure 1. Typical modern recovery boiler. The superheater tubes are colored red. [3].

## 2. Recovery boiler processes

Recovery boiler processes efficiently inorganic and organic chemicals in the black liquor. Efficient inorganic chemicals processing can be seen as high reduction rate. The furnace also disposes of all organics in black liquor. This means stable and complete combustion. Reduction (removal of oxygen) and combustion (reaction with oxygen) are opposite reactions and it is difficult to achieve both at same unit operation, furnace.

Black liquors contain inorganic chemicals. During combustion and reduction reactions significant amounts of alkali compounds vaporize. Small char fragments and liquor particles may entrain to flue gas flow. These phenomena cause deposits on heat transfer surfaces that increase heat transfer resistance and

thus reduce boiler performance. Even with improved air systems and advances in recovery boiler design, fouling remains one of the big operating problems.

Corrosion is the main problem that limits the ability of kraft recovery boiler to produce electricity [4]. In e.g. coal fired boilers much higher superheater temperatures are typically used. In comparison to coal fired boilers kraft recovery boilers have higher rates of alkali metals, chloride in gaseous form and often highly reducing conditions caused by carryover particles. On the other hand levels of some high temperature corrosion causing elements like antimony, vanadium and zinc are typically low.

Fireside corrosion in recovery boilers is caused by formation of deposits, which have corrosive properties. Recovery boiler ash in contact with the tubes is normally solid. Main compounds affecting recovery boiler corrosion are alkali, chloride and sulfur (sulfidity). Sodium and potassium may enhance formation of ash deposits with low melting points 500–600°C. Contact of tube surface with molten alkali salts causes rapid corrosion. Active oxidation can affect superheater tubes even at temperatures lower than the first melting temperature. Therefore operating the recovery boiler without gaseous chlorine at superheaters is essential. As sulfidity increases the polysulfide content of deposits on the heat transfer surfaces can increase which increases corrosion [6].

### 3. Superheater failures

Recovery boiler superheaters suffer from corrosion, design issues and operation issues. Operation problems that cause superheater failure can be [7]

- Condensate blocked tubes during start up
- Water from hydrotest not being evacuated during start up
- Water carryover from the drum
- Desuperheater spray water quality control issues
- Sootblower action
- High temperature cycling caused by poor superheating control.

Table 1 shows reported BLRBAC data on significant superheater faults in American Recovery boilers. As can be seen there are several reasons for faults and this places significant difficulties on selection of proper material. The reason for large number of fatigue faults is the constant swinging caused by the recovery boiler Sootblowing equipment operation. The second biggest failure type is then hot corrosion.

Table 1. Typical recovery boiler superheater faults [8].

<b>Fault type</b>	<b>% fault</b>	<b>% boiler</b>
Fatigue	32.4	32.1
Hot corrosion	28.0	34.9
Tie in breakage	20.5	31.1
No fault given	12.5	23.6
Welding	9.2	15.1
Overheating	7.5	13.2
Roof sealing	7.1	12.3
Leak above the roof	4.6	7.5
Moisture	2.9	5.7

## 4. Superheater corrosion

The superheater corrosion behavior depends on three factors [9]: 1) The tube surface temperature, 2) the deposit chemistry and 3) the local atmosphere at the vicinity of tubes.

The main steam temperature is the main parameter that affects the choice of superheater materials, this because the corrosion rate increases as the superheater steam temperature increases, Figure 2. It should be noted that the superheater corrosion rates are not uniform, but depend strongly on the local conditions. However, the overall increasing effect of temperature to superheater corrosion is evident. Steam side heat transfer coefficients in typical recovery boiler superheaters are low. Superheater surface temperature can be tens of degrees higher than the bulk steam temperature, Figure 3. A rough estimate is that in areas where radiation is present the metal temperatures are about 50°C higher than the steam temperature [10]. This is taken into account when positioning superheaters. The corrosion risk of hottest superheaters can be reduced by placing behind the nose or protecting it by screen tubes.

The superheater panels can also be designed so that the steam temperature in the outer tubes is lower than in the middle to balance the high heat flux and higher corrosivity. This is achieved by using shorter routes for outside bends, which results to lower pressure loss, higher mass flow and lower end temperature, Figure 4. This procedure is in more detail described in [11].

Selecting the right material for recovery boiler superheaters

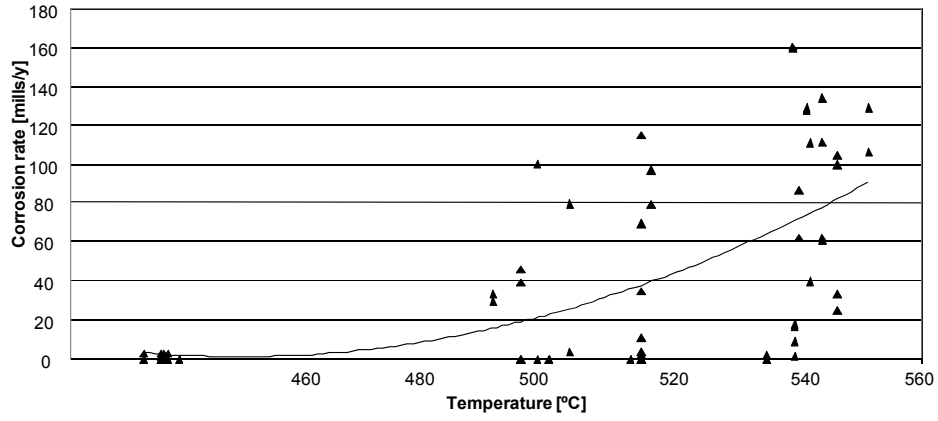


Figure 2. Effect of temperature on superheater corrosion rates [10].

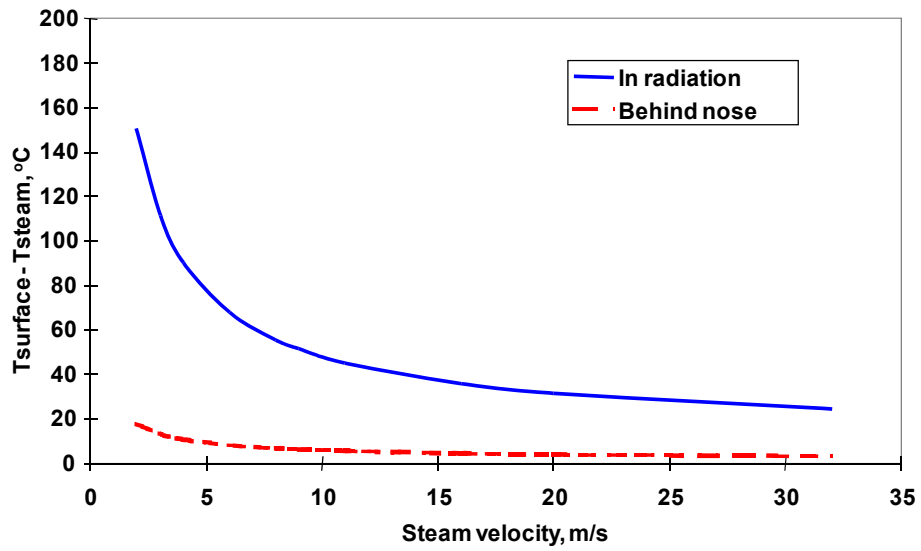


Figure 3. Effect of steam velocity on superheater surface temperature [1].

## Selecting the right material for recovery boiler superheaters

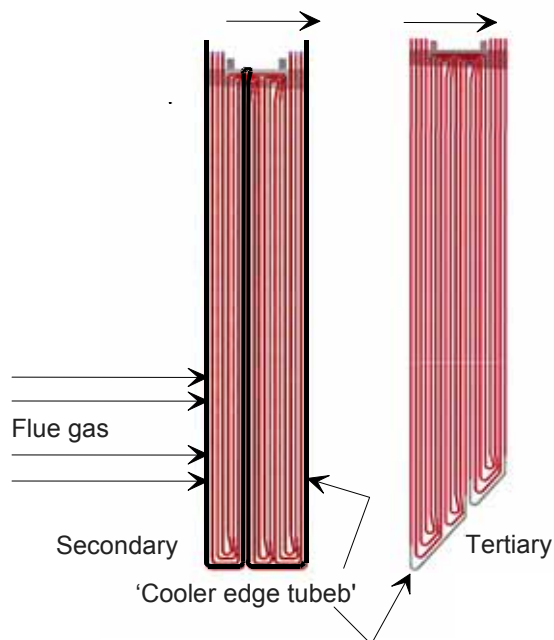


Figure 4. Cooler edge design to mitigate corrosion.

Melting behavior of deposits in kraft recovery boiler heat transfer surfaces determines many of the deposit properties. The first melting temperature  $T_0$  (FMT) is the temperature at which the melt appears in a recovery boiler deposit, Figure 5. The temperature where deposit melting appears marks also the region where fouling and corrosion problems occur. Understanding and predicting first melting temperature is particularly important in terms of superheater corrosion [12]. Sodium and especially potassium lower the first melting point. Also carbonate and sulfide may lower the FMT, but their effect is smaller than that of the potassium [9]. Hot corrosion failures occur typically at the lower bends of the hottest superheaters.

Recently it was noted that fast corrosion can occur even below the first melting temperature, Figure 8. Reason to this is active oxidation. Chloride in fuel forms NaCl,  $\text{Cl}_2$  and HCl in gaseous form. In active oxidation these gases react with iron to  $\text{FeCl}_2$  [13]. This when in contact with oxygen, reacts back to  $\text{Fe}_2\text{O}_3$  releasing gaseous chlorine. Reformed iron oxide layer is porous and does not offer protection from corrosion. Released chlorine can react with fresh iron oxide and the cycle repeats. This process needs continuous gaseous chlorine

Selecting the right material for recovery boiler superheaters

outside the metal surface to proceed. Other necessities for the process are high temperature and reducing conditions [10]. In recovery boilers process upset that produce high SO<sub>2</sub> levels may ignite oxidation [10]. Active oxidation has been studied a lot in connection with waste burning and recovery boilers. It can be identified from sharp chloride layer between deposit and the uncorroded tube [14].

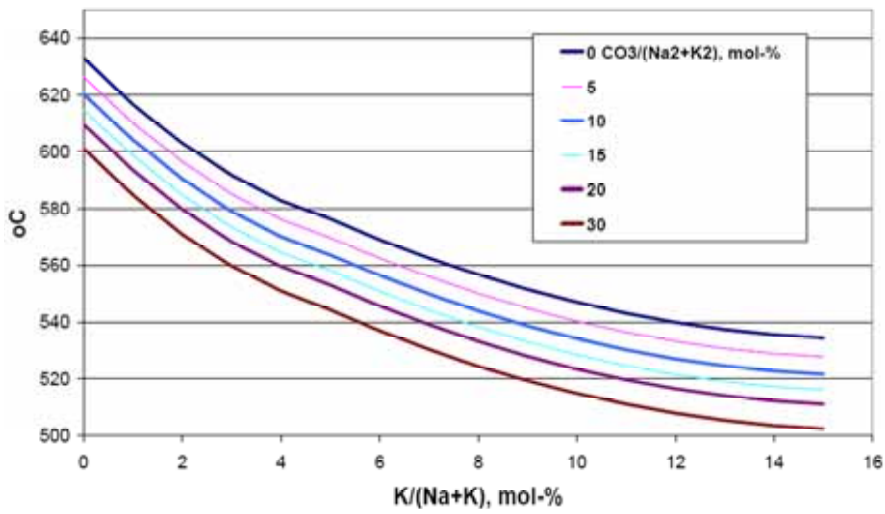


Figure 5. First melting temperature ( $T_0$ ) of recovery boiler superheater deposit.

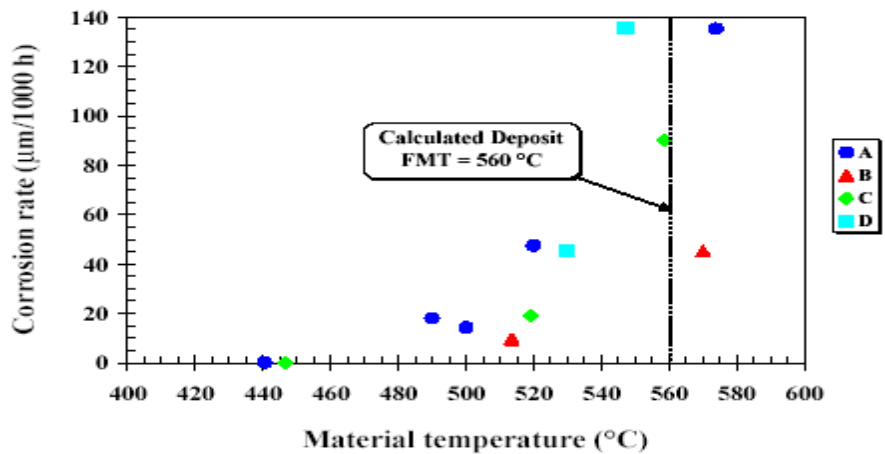


Figure 6. Corrosion rate as function of the first melting temperature ( $T_0$ ) of recovery boiler superheater deposit [15].



## 5. Selection of superheater materials

Typical primary superheater materials, when they are protected from direct furnace radiation are carbon steel (SA/A-210 Gr A-1, S235JRG2) which can be used up to 350–400°C. Secondary and tertiary superheater materials contain often 1 to 3% Cr to improve corrosion resistance. Examples from these are 13CrMo44 and T22/10CrMo910) which are used up to 400–480°C. Corrosion resistance is increased with chromium alloying and martensitic (X10CrMoVNb9-1, X20CrMoV11-1) and austenitic (X1NiCrMoCu31-27-4, NiCr22Mo9Nb) steels are used in hottest and most corrosive superheaters up to 500–520°C.

The material choice has a significant effect to the recovery boiler cost as the selection of the final superheater material can change the price in ratio of 1 to 10, Table 3. Usually this is solved by using the most corrosion resistant and expensive materials only in locations where needed, e.g austenitic stainless steels in the lower bends or at the outer tubes in the panels.

Selecting the right material for recovery boiler superheaters

Table 2. Materials used for recovery boiler superheaters.

	<b>Cr</b>	<b>Ni</b>	<b>Mo</b>	<b>Si</b>	<b>Cu</b>	<b>Al</b>	<b>Mn</b>	<b>C</b>	<b>Fe</b>	<b>Other</b>
15Mo3	0.3	0.3	0.3	0.26	0.3		0.65	0.16	97.6	
13CrMo44	1.0	0.3	0.3	0.26	0.3		0.55	0.14	97.1	
10CrMo910	2.3		1.00				0.50		96.1	
X10CrMoVNb91	9.0	0.3	1.00	0.40			0.50		88.7	V, Nb
HCM 12	12.0		1.00						86.9	V, Nb
X20CrMoV121	12.0	0.5	1.00	0.50			0.50	0.23	85.2	V
AISI 347	17.5	10.3		1.30		0.70	1.60	0.08	68.4	Nb, Ta
AISI 321	18.5	10.2		0.75			2.00	0.06	68.5	
AISI 309	23.0	14.5		0.70			1.50	0.10	60.2	P
HR2M	22.2	14.4	1.49	0.55			3.14	0.03	58.1	N
YUS170	24.4	13.2	1.50	0.78			0.58	0.02	59.5	N, P
AISI 310	25.0	20.5		0.50				0.08	53.8	
HR3C	25.0	29.5		0.42	1.28		1.10	0.06	42.6	N
AC66	27.0	32.0		0.25		0.02	0.8	0.06	39.2	Ce, Nb
Sanicro 28	27.0	31.0	3.50		1.00		0.05	0.01	37.3	
Sanicro 38	21.0	38.0	2.50	0.30	1.70		0.80		35.6	Ti
Alloy 825	22.0	39.0	3.50	0.36			0.50		34.5	Ti
HR11N	28.5	41.2	1.06	0.12			0.50	0.01	28.6	N
Super 625	21.0	52.7	8.97	0.21		0.28	0.20	0.01	15.8	Nb
Sanicro 65	21.0	61.0	8.40	0.35			0.38		8.8	
Alloy 625	21.0	58.0	9.0	0.50		0.4	0.50	0.10	5.0	Nb,Ti
Alloy 690	29.0	61.5				0.1		0.03	9	

## Selecting the right material for recovery boiler superheaters

Table 3. Recovery boiler superheater costs calculated for SHIII for boiler in Figure 1.

Material	Tube		Manufacturing		Total
	€/kg	k€	€/kg	k€	M€
SA/A-210	0.9	300	5	1 500	1.8
16Mo3	1	300	5	1 500	1.8
13CrMo44	1.2	400	5	1 500	1.9
10CrMo910	1.5	500	5	1 500	2
T24	1.8	600	5	1 500	2.1
X10CrMoVNb91 (T91)	4.2	1 400	8	2 500	3.9
AISI 347	6	1 900	9	3 000	4.9
AISI 310	9	2 900	11	3 500	6.4
HR3C	9	2 900	11	3 500	6.4
AC66	20	6 500	14	4 500	11
Sanicro 28	24	7 800	15	4 800	12.6
Sanicro 38	24	12 900	15	4 800	12.6
Sanicro 63	40		17	5 400	18.3

## 6. Future recovery boilers

Typical recovery boilers fire black liquor at a dry solid of 80% and operate at a steam pressure of 80 bar and a temperature of 480°C to reduce superheater corrosion and ensure boiler availability. In the future the situation is expected to change. Reason to this is the aim and need to increase CO<sub>2</sub> free, green electricity. This requires that the steam values are increased maybe even to a level of 160 bar and 550°C, which increase material temperatures to a level of 580–600°C. At present a number of modern boilers exist in Sweden, Finland and Japan that operate at more than 100 bar and 500°C. No current recovery boiler operates at higher pressure than 120 bar and higher temperature than 520°C.

Special attention is paid to the superheaters, whose corrosion resistance is the major concern. The traditional heat resistant CrMo-steels and austenitic stainless are not anymore applicable in these temperatures, because of their corrosion resistance is insufficient. Tests have shown that the corrosion rates of the austenitic stainless steel AISI 321, 347, 316 and even 310 increase to so high

## Selecting the right material for recovery boiler superheaters

level at temperature clearly beyond 500°C that their use should be avoided. New materials solutions to this are looked from the highly alloyed austenitic iron and nickel based alloys, which can be used either as mono or composite tube. Composite tubes are considered attractive, because they are not susceptible to steam/water side stress corrosion cracking, which is one of the Achilles heels of austenitic stainless steels.

### **Stainless steels:**

AISI 347 has been widely used in current superheaters typically as short pieces in most corrosive places. Parts manufactured from AISI 347 have no record of corrosion failure in Finland. In high temperature boilers, where improved intergranular corrosion resistance is needed alloys like 309 and 310, with higher amounts of chromium should be used. For this Sumitomo has developed new grades HR2M and HR3C [16, 17]. Nippon Steel answer to this is 25Cr14Ni (YUS 170) modified (low C and Si with small amounts of Mo and Ni) to resist intergranular attack (IGA) [18, 19]. Welding Service Inc (WSI) uses for recovery boiler superheaters Unifuse 310 weldoverlay coating. The experiences have been mainly positive. In example cases Unifuse 310 is reported to last more than two years without visible damage. In the same conditions the old steel (T11) corroded 3.9 mm/year [20].

### **High Cr – high Ni – Fe base alloys:**

Sanicro 28 is currently used in recovery boiler superheaters as compound tube. It has a good corrosion resistance because of high Cr- (27%) and Ni- (31%) content, other alloying elements being 3.5% Mo and 1.% Cu. AC66 (1.4877) is like Sanicro 28, but it doesn't contain Cu and it is Nb-stabilised because of the higher carbon content. This material has not been widely used in recovery boilers, but in comparable corrosion conditions at biomass boilers it has been proven as one of the best materials.

### **High Cr – high Mo – Ni base alloys:**

Materials belonging to this category are e.g. Sanicro 63, Sanicro 67, Super 625. These high molybdenum grades have excellent service records from waste incineration. When selection these materials special attention should be paid on manufacturing as well as on long-term stability and ageing at high temperatures

[21]. WSI has also developed and used Unifuse 52 type welded coating (28% Cr, 14% Fe with minor amounts of Al and Ti) for use in coal fired boilers [20]. Coating can be welded to carbon or austenitic steel tube.

## 7. Conclusions

Recovery boiler operation in a pulp mill is a complex process with several interrelated parameters and almost infinite variables. Therefore the selection of materials for long time trouble free service is not an easy task.

There is a wide array of available superheater materials to choose from. There are even a few newer materials that should be considered. The operation conditions and deposit properties must be looked at when material selection is done. The material choice has a significant effect to the recovery boiler cost as the selection of the final superheater material can change the price in ratio of 1 to 10.

Understanding and predicting first melting temperature is particularly important in terms of superheater corrosion. Contact of tube surface with molten alkali salts causes fast corrosion even with the best of materials. Chloride corrosion can affect superheater tubes even at temperatures lower than the first melting temperature. Therefore operating the recovery boiler without gaseous chlorine at superheaters is essential.

## Acknowledgements

Parts of this paper were from research funded by the Tekes – the Finnish Funding Agency for Technology and Innovation which is gratefully acknowledged.

## References

1. Vakkilainen, E. K. Kraft recovery boilers – Principles and practice. Suomen Soodakattilayhdistys ry. Helsinki, Finland: Valopaino Oy, 2005. 246 p. ISBN 952-91-8603-7.
2. Vakkilainen, E. K. Future of recovery boiler technology. 40th Anniversary International Recovery Boiler Conference. Finnish Recovery Boiler Committee, Haikko Manor, Porvoo, May 12–14, 2004. Pp. 51–58.

## Selecting the right material for recovery boiler superheaters

3. Tikka, M. UPM Kymin uusi talteenottolinja. (UPM Kymi new recovery line). Soodakattilapäivä, 29 October 2008, Finnish Recovery Boiler Committee. (In Finnish).
4. Bruno, F. Superheater corrosion in kraft recovery boilers (Korrosion hos överhettare i sodapannor. En översikt och diskussion). Stockholm, Sweden: Stiftelsen för Värmeteknisk Forskning, 1997. Technical Report SVF/602. 134 p.
5. Bruno, F. On the influence of chlorides and sulphurous compounds on the corrosion of superheater tubes in boilers with special consideration on Kraft recovery boilers. Värmeforsk Service AB, 1999. Technical Report VF-664. 36 p.
6. Yli-Olli, S., Pohjanne, P., Heikinheimo, L., Kinnunen, T. & Pankakoski, P. H. Sulphidation of advanced kraft recovery boiler materials. International Chemical Recovery Conference – Efficiency and Energy Management. Quebec City, Canada, May 29 – June 1, 2007. Pulp and Paper Technical Association of Canada. Pp. 273–278.
7. McMillan, J. Superheater problems, their causes & solutions. 2004 International Chemical Recovery Conference. Charleston, South Carolina, USA, June 6–10 2004. Pp. 953–964.
8. Grace, T. M. & Clement, J. L. Investigation of superheater design and performance, Part 2. 2009 TAPPI Engineering, Pulping & Environmental Conference. 13 p.
9. Salmenoja, K. Superheater corrosion in modern recovery boilers. 40th Anniversary International Recovery Boiler Conference. Finnish Recovery Boiler Committee, Haikko Manor, Porvoo, May 12–14, 2004. Pp. 103–113.
10. LaFond, J. F., Verloop, A. & Walsh, A. R. Engineering analysis of recovery boiler superheater corrosion. Tappi Journal, Vol. 75 (1992) 6, pp. 101–106.
11. Tran, H., Gonsko, M. & Mao, X. Effect of composition on the first melting temperature of fireside deposits in recovery boilers. Tappi Journal, Vol. 82 (1999) 9, pp. 93–100.
12. Tran, H. Recovery boiler corrosion. In: Adams, T. N. (Ed.). Kraft recovery boilers. Atlanta, GA, USA: Tappi Press, 1997. Pp. 283–324.
13. Grabke, H. J., Reese, E. & Spigel, M. The effects of chlorides, hydrogen chloride, and sulfur dioxide in the oxidation of steels below deposits. Corrosion Science, Vol. 37 (1995) 7, pp. 1023–1043.

## Selecting the right material for recovery boiler superheaters

14. Nishio, T., Matsumoto, H., Shinohara, M. & Arakawa, Y. Influence of ash composition on corrosion rate of superheater tubes. Proceedings of 2001 Tappi Engineering, Finishing & Converting Conference. Atlanta, GA: Tappi Press. 6 p.
15. Salmenoja, K. & Tuiremo, J. Achievements in the control of superheater corrosion in black liquor recovery boilers. Proceedings of 2001 Tappi Engineering, Finishing & Converting Conference. Atlanta, GA: Tappi Press. 9 p.
16. Sumitomo Metal Ind. Ltd. Comparison of new materials for boiler tube and pipe. Sumitomo, 904 F-No. 2878 Rev. 4, April 1998. 3 p.
17. Otsuka, N. Soodakattilapäivät 10.10.2002, Marina Congress Center, Helsinki, Finland.
18. Kaneko, S., Takatuka, H., Arakawa, Y. & Tanaka R. Mitsubishi-CBC high efficiency chemical recovery boiler power generation system. 31st Pulp and Paper Annual Meeting, ABTCP, Sao Paolo, Brazil, October 19–23, 1998. Pp. 693–704.
19. Matsumoto, H., Notomi, A., Nishio, T., Arakawa, Y. & Takatsuka H. Advanced technology for corrosion resistant materials for recovery boiler. 1998 International Chemical Recovery Conference. Pp. 51–60.
20. Lai, G. & Blogg, N. Unifuse cladding for surface protection against corrosion and erosion/corrosion in power boilers and waste heat recovery systems. 2003 Tappi Fall Meeting. 19 p.
21. Kawahare, Y. & Kaihara, Y. Recent trends in corrosion resistant tube materials and improvements of corrosion environments in WTE plants. Corrosion 2001. NACE, Paper No. 01173.

# **Oxyfuel combustion: Oxidation performance of steels in simulated oxyfuel conditions**

Satu Tuurna, Pekka Pohjanne, Sanni Yli-Olli, Tuomo Kinnunen  
and Petra Jauhiainen  
VTT Technical Research Centre of Finland  
Espoo, Finland

## **Abstract**

Carbon capture and storage (CCS) is shown to be one of the key technologies for CO<sub>2</sub> emissions reduction in numerous energy scenario analyses. In addition to moving towards emission free energy production, improved energy efficiency is essential in order to reach emission reduction targets. Oxyfuel combustion can be expected to differ from combustion in air by e.g. modified distribution of fireside temperatures, much reduced NO<sub>x</sub> but increased levels of fireside CO<sub>2</sub>, SO<sub>2</sub> and water levels due to extensive flue gas recirculation. Increased flue gas recirculation may increase the concentration of a number of contaminants in the deposited ash and promote fouling and corrosion. In the paper, the oxidation performance of superheater steels has been determined at 580 and 650°C under simulated oxyfuel firing conditions. The results are compared to corresponding results from simulated air-fired coal combustion conditions.

## **1. Introduction**

The demand for reduced emissions requires the development of efficient combustion technologies suited for carbon capture and storage (CCS) systems. Oxyfuel combustion is seen as one of the major options for CO<sub>2</sub> capture for future clean coal technologies. It can be in principle adapted to both new and



retrofit units with similar fuel flexibility as in conventional coal-fired plants [1, 2].

Compared to conventional air-fired combustion, the oxyfuel process will use oxygen or oxygen-enriched air to reduce the nitrogen in the flue gas and to increase the CO<sub>2</sub> content for easier capture. Much increased flue gas recirculation is used to avoid overheating. Even if the thermal conditions are similar in the oxyfuel and air fired systems, recirculation and reduced flue gas volume will increase the concentration of not only CO<sub>2</sub> but also other flue gas constituents and impurities such as CO, SO<sub>x</sub>, Cl, H<sub>2</sub>O, Hg, As, Se etc. in the oxyfuel process. The resulting concentrations naturally depend on the fuel and process details, but imply a potential challenge to the high temperature corrosion resistance of boiler surfaces. Volatile elements that often serve as bonding agents for ash deposits will increase the risk of fouling and corrosion. The higher O<sub>2</sub> concentration may also contribute to higher SO<sub>2</sub> to SO<sub>3</sub> conversion with significant effect on boiler corrosion. As the currently available information on the corrosion rates under oxyfuel conditions is very limited [3–5], corrosion testing of existing boiler materials under high CO<sub>2</sub> combustion environments with the relevant oxygen, water vapour and impurity concentrations is very much needed. This should be supported and complemented by field-testing preferably in a well characterised coal fired boiler before and after retrofitting to oxyfuel combustion, to investigate the potential risk of increased corrosion rates.

## 2. Materials and methods

The oxidation performance of alloys T22 (10CrMo9-10), X20 (X20CrMoV11-1), 347HFG (TP347HFG), and HR3C was investigated under simulated combustion conditions. The chemical compositions of materials are given in Table 1. Rectangle shape specimens with dimensions of 12 × 18 × 3 mm<sup>3</sup> were machined from thick walled tubes. The samples were bright polished with SiC paper and ultrasonically degreased in ethanol.

The multi-sample exposure tests were carried out under isothermal conditions at temperatures of 580 and 650°C in gases simulating oxy-fired and air-fired coal combustion. Steel T22 was tested only at 580°C, because 650°C is so much over its design values. High chromium steel HR3C was tested only at 650°C. The exposure tests were carried out in horizontal tube furnaces with premixed gases. The gas flow used was 10 l/h. The gases were passed through a humidifier unit at an appropriate temperature to obtain desired moisture content in the gas

mixture. Table 2 summarises the test conditions. The specimens were weighed to obtain mass changes. The thickness and microstructure of the oxide layers were evaluated by optical and scanning electron microscopy (SEM) combined with energy dispersive spectroscopy (EDS).

Table 1. Chemical composition (in wt.%) of the test materials.

Alloy	Fe	Cr	Ni	Mo	Other
T22	bal.	2.16	0.06	0.92	0.48 Mn, 0.26 Si
X20	bal.	11.2	0.48	0.86	0.2 C, 0.49 Mn, 0.3 V
347HFG	bal.	18.3	11.7	0.23	0.07 C, 1.64 Mn, 0.92 Nb, 0.33 Cu
HR3C	bal.	25.5	19.4	0.11	1.1 Mn, 0.39 Si, 0.45 Nb

Table 2. Test conditions for laboratory tests.

Simulated system	Vol. %					Temp.	Duration
	N <sub>2</sub>	O <sub>2</sub>	CO <sub>2</sub>	H <sub>2</sub> O	Ar	°C	h
Air-fired	73.7	1.8	16.0	8.5	-	580, 650	168, 500, 1 000
Oxyfuel	-	3.6	60.0	30.0	6.4	580, 650	168, 500, 1 000

### 3. Results

SEM/EDS analyses of cross-sections revealed that the oxide layer formed at 580°C on the T22 steels had a triple layer structure, Figure 1. The outermost layer composition corresponded to hematite (Fe<sub>2</sub>O<sub>3</sub>). A layer beneath that consisted of magnetite (Fe<sub>3</sub>O<sub>4</sub>). The inner scale growing inwards from the original sample surface consisted of magnetite type oxide, partly an iron-chromium spinel, probably mixture of Fe<sub>3</sub>O<sub>4</sub> – (FeCr)<sub>3</sub>O<sub>4</sub>. In addition, there was an internal oxidation zone at metal surface. After 1 000 h in the air combustion environment the thickness of hematite layer increased at the expense of magnetite layer compared to the oxide layers formed in oxyfuel combustion environment.

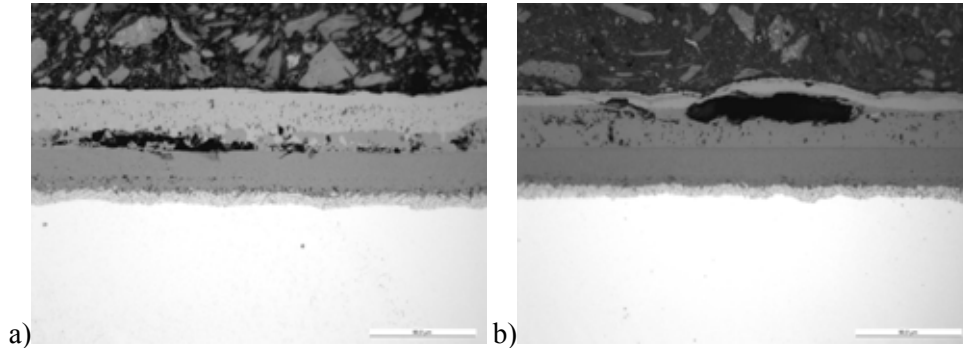


Figure 1. Optical micrographs of T22 cross-sections after exposure at 580°C in a) air combustion and b) oxyfuel combustion environment for 1 000 h.

From micrographs of X20 (Figure 2) it can be seen that also in this case oxide scales formed had a triple layer structure containing hematite, magnetite and mixed iron-chromium oxide with small amounts of alloying elements like molybdenum. An internal oxidation zone could be found at metal surface, but in this case it was discontinuous. The outer hematite layer was much thicker on samples exposed in air-fired coal combustion conditions than in oxyfuel conditions.

Oxide layers formed on steel X20 had a two layer structure at 650°C. No spallation was observed. The outward growing scale consisted of hematite with only local traces of magnetite. The inward growing layer consisted of the mixed oxide of iron and chromium with minor amounts of alloying elements from the alloy. Figure 4 represents the EDS analyses of formed oxide scales. Some carbon enrichment was found near the interface between inner and outer oxide layer, and also inside the inner layer after 1 000 h exposure in oxyfuel combustion environment (Figure 4b). The inward growing layers contained quite much porosity, Figure 3. There were no significant structural differences between oxides formed in air and oxyfuel combustion environments at 650°C. No internal oxidation zone was found beneath the oxide scale.

Oxyfuel combustion: Oxidation performance of steels in simulated oxyfuel conditions

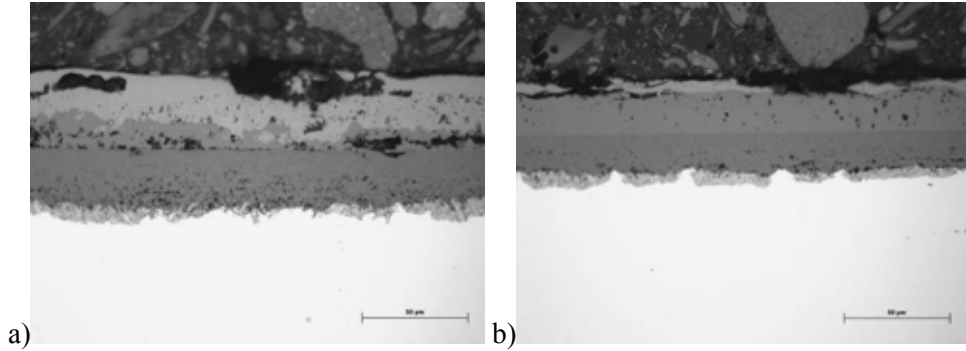


Figure 2. Optical micrographs of X20 cross-sections after 1 000 h at 580°C in a) air combustion and b) oxyfuel combustion environment.

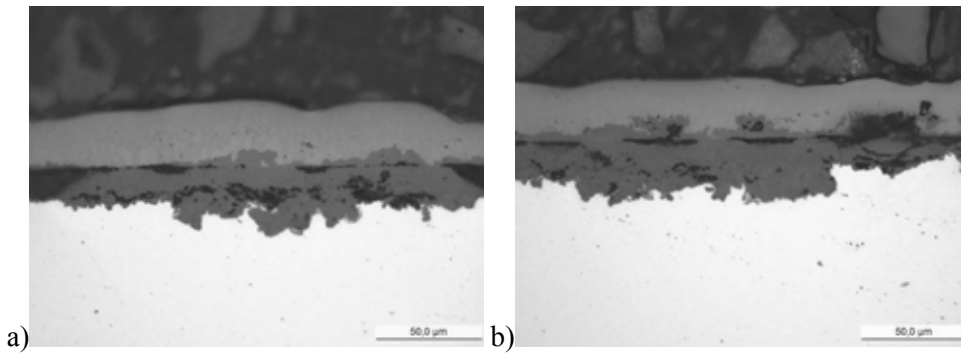


Figure 3. Optical micrographs of X20 cross-sections after 1 000 h at 650°C in a) air combustion and b) oxyfuel combustion environment.

With short exposure times only very thin or no oxide scale was formed on alloy 347HFG. After 1 000 h exposure at 580°C in air combustion environment the oxide layer was still relatively thin with a two-layer structure. The layer thickness increased when exposure temperature was increased up to 650°C. The oxides formed in oxyfuel conditions had a nodular structure; even at 650°C the oxide scale was uneven around the sample although a continuous scale was found some parts of the sample, Figure 5. EDS analyses showed that the outer layer was iron oxide whereas the inner layer contained mainly mixed oxide of iron, chromium and nickel.

Oxyfuel combustion: Oxidation performance of steels in simulated oxyfuel conditions

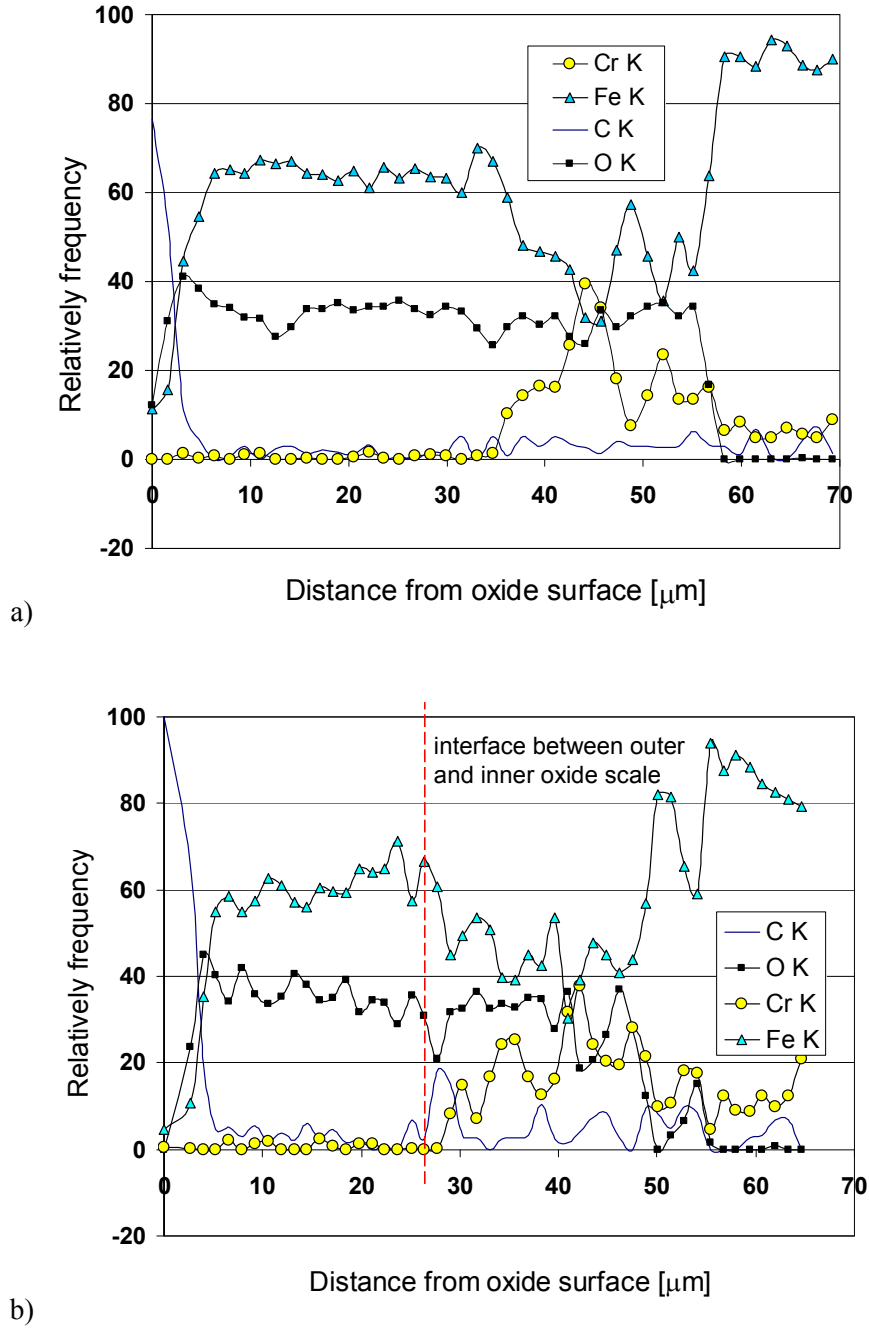


Figure 4. EDS line scan analyses representing main components of oxide scales formed on X20 after 1 000 h at 650°C in a) air combustion and b) oxyfuel combustion environment.

Oxyfuel combustion: Oxidation performance of steels in simulated oxyfuel conditions

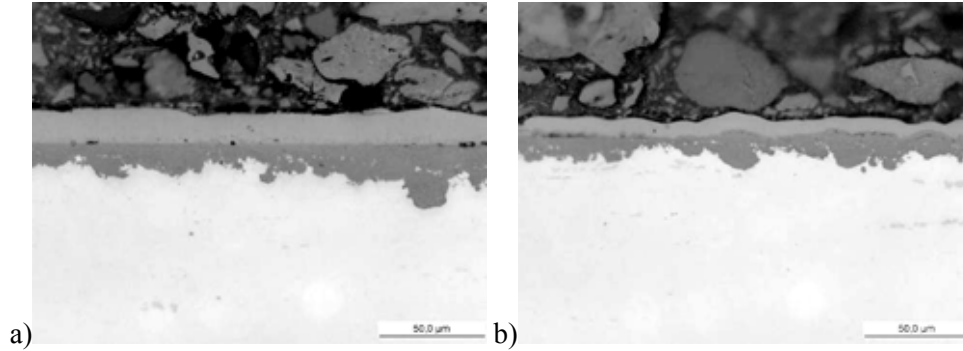


Figure 5. Optical micrographs of 347HFG cross-sections after 1 000 h at 650°C in a) air combustion and b) oxyfuel combustion environment.

Very thin oxides were formed on the surfaces of HR3C steel at 650°C. After 1 000 h exposure some nodule formation, Figure 6, was observed on the HR3C surfaces in both test conditions. Figure 7 shows the cross-sections of exposed HR3C samples. The oxide was composed of two layers, the outer layer contained iron oxide with small amounts of chromium and the inner layer contained mixed oxide of chromium, nickel and iron.

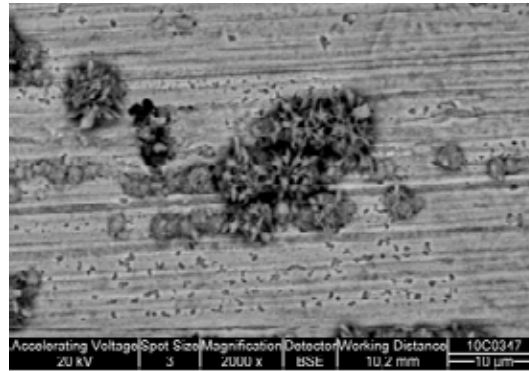


Figure 6. SEM image of HR3C steel surface after 1 000 h exposure at 650°C.

Oxyfuel combustion: Oxidation performance of steels in simulated oxyfuel conditions

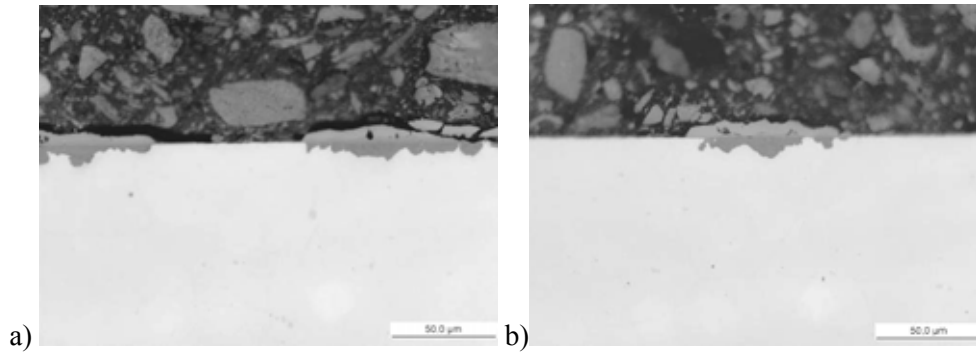


Figure 7. Optical micrographs of HR3C cross-sections after exposure at 650°C in a) air combustion and b) oxyfuel combustion environment for 1 000 h.

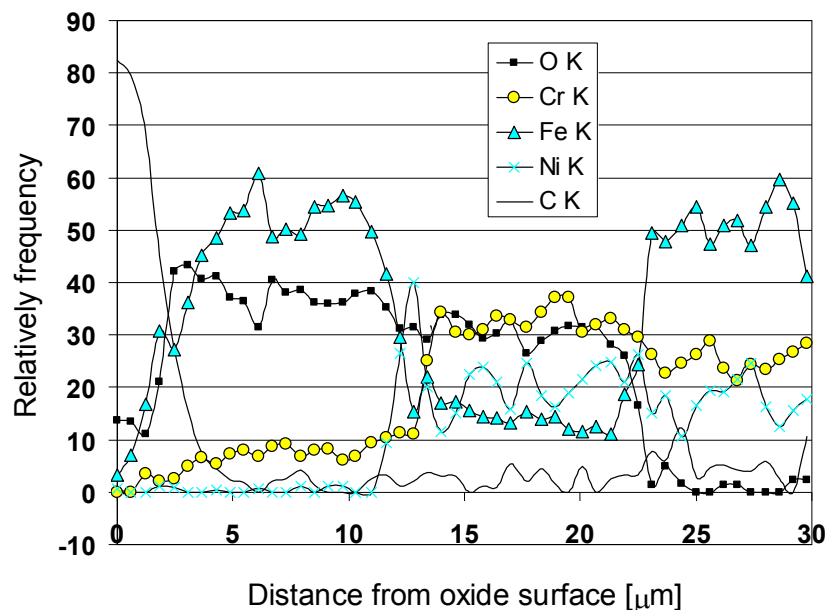


Figure 8. EDS analysis of oxides formed on HR3C after 1 000 h at 650°C in oxyfuel conditions.

Figure 9 summarises the weight gain data for each alloy after 1 000 h at 580 and 650°C in the both test conditions. The oxidation rate of steels T22 and X20 was substantially similar at 580°C. Both steels were heavily oxidised. Steels T22 and X20 were marginally less oxidised in simulated oxyfuel condition than in air condition. At 650°C the oxidation rate (weight gain) of steel X20 was

substantially similar than at 580°C, although it appears to be marginally better in air than in oxyfuel conditions. Steel 347HFG has approximately one order of magnitude less weight gain at 580°C, and it seems to be somewhat better in simulated oxyfuel conditions. At 650°C in air 347HFG is clearly more oxidised. However, in oxyfuel conditions the difference between 580°C and 650°C in oxidation is less. Alloy HR3C has clearly less weight gain than other test materials. The results show one order of magnitude less weight gain under oxyfuel condition in comparison with testing under air.

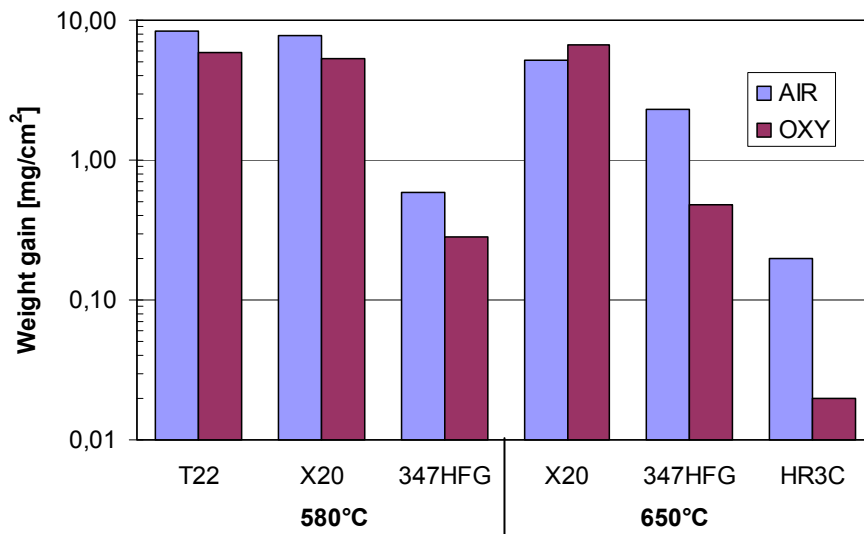


Figure 9. Weight gain of different samples exposed 1 000 h at 580 and 650°C in air-fired and oxyfuel conditions.

#### 4. Discussion and conclusions

Metallographical analysis of low alloyed samples showed that the exposure conditions have effect on the oxide scale formation and structure. In reference air-fired coal combustion conditions at 580°C the outermost hematite layer thickness increased and magnetite layer decreased as a function of exposure time as expected, Figure 2. The increase of hematite layer thickness in oxyfuel conditions was much slower. At 650°C the difference between test conditions was smaller. Oxidation rate at higher temperatures is higher and reactions occur much faster.



The oxidation rate of steels T22 and X20 was substantially similar at 580°C. Both steels were heavily oxidised. The oxidation rate of both steels X20 and 347HFG was somewhat lower in the simulated oxyfuel conditions than in the simulated air-fired coal combustion conditions at 580°C. At 650°C the oxidation rate of steel X20 was substantially similar than at 580°C, although it appears to be marginally better in air than in oxyfuel conditions. The significant difference of oxide structures of X20 formed at different exposure temperatures was the porous internal layer formed at 650°C (Figure 3). Porosity may weaken the protective behaviour of scale and accelerate breakaway oxidation. Oxide spallation of can also affect on the observed oxide thickness and mass change results. However, in this study clear spallation was not observed. These issues bring some uncertainty to the results, for a mass change and oxide thickness.

The oxidation of 347HFG steel was less than low alloyed steels. 347HFG seems to be somewhat better in simulated oxyfuel conditions. The oxidation started with nodule formation, which began from the grain boundaries. With longer exposure times and higher temperature the nodules grew together forming a continuous layer. This is typical behaviour for alloyed materials. The smaller grain size guarantees the easier formation of a protective oxide because of the slow bulk diffusion of chromium. The oxidation of HR3C samples in both atmospheres was very slow, especially under oxyfuel conditions, only some nodules were found on the exposed surfaces.

In this study the test conditions were purely oxidising. The situation is likely to change when some impurities, like SO<sub>2</sub> and HCl, are added to exposure gases. The metallurgical characterisation of samples revealed that some carbon enrichment inside the oxide layer had occurred after 1 000 h exposure in oxyfuel conditions.

## Acknowledgements

Financial support from VTT Technical research Centre of Finland and Tekes is gratefully acknowledged. The authors thank the skillful assistance of Arto Kukkonen, Taru Lehtikuusi, Marketta Mattila, Kirsti Nöjd and Päivi Varis.

## References

1. Kung, S. C, Tanzosh, J. M. & McDonald, D. K. Fireside corrosion study using B&W clean environment development facility for oxy-coal combustion systems. Proc.

Oxyfuel combustion: Oxidation performance of steels in simulated oxyfuel conditions

of the 5th International Conference on Advances in Materials Technology for Fossil Power Plants, 2008. Pp. 982–992.

2. Jordal, K., Anheden, M., Yan, J. & Strömberg, L. Oxyfuel combustion for coal-fired power generation with CO<sub>2</sub> capture – opportunities and challenges. *Greenhouse Gas Control Technologies*, 2005. Vol. 7, pp. 201–209.
3. Covino, B. B., Matthes, S. A. & Bullard, S. J. Effect of oxyfuel combustion on superheater corrosion. *Corrosion 2008 Conference & Expo*, March 16–19, New Orleans, LA, 2008. 9 p.
4. Hünert, D., Schulz, W. & Kranzmann, A. Corrosion of steels in H<sub>2</sub>O-CO<sub>2</sub> atmospheres at temperatures between 500°C and 700°C. *ICPWS XV*, Berlin, 2008.
5. Pirón Abellán, J., Olszewski, T., Penkalla, H. J., Meier, G. H., Singheiser L. & Quadackers, W. J. Scale formation mechanisms of martensitic steels in high CO<sub>2</sub>/H<sub>2</sub>O-containing gases simulating oxyfuel environments. *Materials at High Temperatures*, 2009. Vol. 26, pp. 63–72.

# **Safety issues arising from the corrosion-fatigue of waterwall tubes**

John M. Brear\*, Paul Jarvis\* and Stephen Scully<sup>+</sup>

\*Stress Engineering Services (Europe) Limited, Chichester, UK

<sup>+</sup>Electricity Supply Board, Dublin, Ireland

## **Abstract**

An incidence of waterwall tube failures, one leading to a significant steam release external to the boiler, has highlighted the need for rigorous risk assessment of such events. Initial review of the utility's experience revealed one of their boiler designs as having had a greater incidence of corrosion-fatigue issues in waterwall tubing than the others. These units were treated as a priority.

To address failure likelihood, fracture mechanics calculations were performed. These studies defined the necessary inspection coverage and sensitivity required to underwrite safe operation at various potential loads.

Personnel safety was considered the most important consequence of failure. Accordingly, potential steam releases were modelled to define safe exclusion zones within the boiler house. Standard calculations were found to be non-conservative; more exact formulae were needed to give realistic results.

Using the results of these studies, the utility was able to draw up a realistic inspection plan. Safe operating pressures and appropriate exclusion zones were defined for each boiler, and for a range of operational scenarios.

These tactics have allowed the utility to inspect the boilers in turn and to repair all significant defects in the waterwall tubes, whilst maintaining a good overall power output

In parallel, a root-cause investigation was performed to identify the factors contributing to the failures. Where possible, causative influences were reduced or mitigated so as to reduce the likelihood of failure whilst allowing increased flexibility of boiler operation.

## 1. Introduction

Historically, waterwall tube life has been predicted on the basis of a measured corrosion rate and the flow strength of the tube material. Provided this was referred to the area of maximum corrosion – often the ebullition zone – satisfactory results were obtained [eg 1, 2]. However, moves to increased cyclic operation have led to an increasing importance of less predictable processes, such as corrosion-fatigue.

Two sister once-through-type boilers, of 250MWe capacity, showed a higher incidence of corrosion-fatigue failures than did other units in the utility. Generally these manifested as leaks, but in 2005 a burst occurred, causing a significant steam release outside the boiler (Figure 1). The operating pressure was immediately reduced from 170 to 120 bar on the sister unit. A risk assessment was put in place, including investigation of failure likelihood, of failure consequence, of the variation of these with operational conditions, and of the root cause. Later, this exercise was extended to other boiler designs within the utility.



Figure 1. The 2005 tube-burst, showing window blow-out failure.

This paper highlights the salient features of this investigation, centring on the most critical units but including results from work on other boilers. It draws on work performed within the utility and collaboratively between the authors' two organisations.

## 2. Failure likelihood

### 2.1 Failure analysis

The failure was a window blow-out. Examination of the fracture surfaces indicated that there had been a pre-existing crack-like defect along the lower fracture surface, growing from the bore of the tube. The fracture was deepest where it was coincident with an old attachment weld, being effectively through-wall at this point. A section (Figure 2) confirmed that the defect was a corrosion-fatigue crack. The two circumferential cracks that allowed the tube material to tear away were relatively clean with some plastic deformation evident. Several sections through the top portion of the fracture found no evidence of a pre-existing defect, but rather signs of deformation consistent with the material being torn away due to overload.

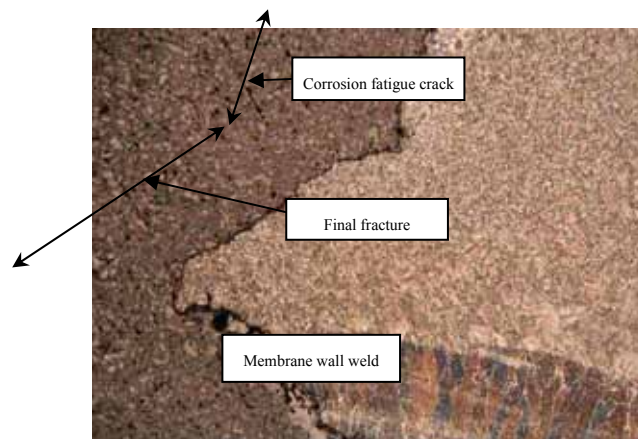


Figure 2. Section through the lower portion of the rupture.

### 2.2 Fracture mechanics

#### Stress analysis:

The tubes experience: the pressure stress, modified by the constraint of the membrane wall; local thermal stresses associated with heat transfer through the tube wall; long-range thermal stresses associated with the temperature distribution in the panel; and system loads associated with supports and attachments. Only the first is readily quantifiable.

The constraint effect of the membrane wall was investigated, but no suitable hand calculations were found to enable it to be quantified. As the analysis progressed, it was noted that the observed crack growth could be explained solely on the basis of the hoop stress, assuming lower-bound materials properties. The consequences after final fracture were influenced only by boiler pressure tube bore dimensions. It was not considered necessary, therefore, to perform a more elaborate stress analysis at this stage.

It should, however, be noted that the actual distribution of cracks and their growth and fracture behaviour will be affected by the other sources of loading identified above. This should be borne in mind when modifications are made to components of this type and age.

#### **Materials properties:**

The tube material is 15Mo3 (Material Number 1.5415) and materials properties have been taken from the most relevant standard contemporary with the construction of the boiler: DIN 17 177, May 1979 [3]. Physical properties were obtained from the corresponding Mannesmann data-sheet 405R [4].

Conservative fracture toughness values, appropriate to corrosive environments, have been taken from API 579 [5] and UK nuclear practice.

The assessment has been performed using lower-bound properties. Whilst it might be argued that actual properties are likely to be better, it is also recognised that there are additional sources of loading that have not been explicitly considered. The subsequent sections demonstrate that the failure can be explained under a combination of the pressure stress and minimum materials properties, thus other loads and material property variations can be taken to be in balance and do not need further consideration at present.

#### **Crack behaviour:**

Any longitudinal defect initiating at the bore of a tube will extend through-thickness and axially. A point will be reached where the remaining ligament ahead of the crack fails instantaneously and the crack penetrates the wall. Depending on the crack dimensions and the loading, subsequent growth in the longitudinal direction may be stable, resulting in a leak, or it might be unstable, leading to an instantaneous burst. The following sections address these various aspects of crack behaviour, in accord with recognised practice [5, 6, 7].

**Through-wall crack growth:**

The failure analysis confirms a corrosion fatigue mechanism. However, it appears that the process is corrosion dominated as the cracks are irregular and show alternating periods of crack growth and corrosion. At present, there are no data available to allow a predictive crack-growth analysis; however some estimates may be made from historical experience.

**Through-wall crack stability:**

A conventional fracture-mechanics analysis was performed to determine critical crack sizes for through-wall fracture. The load cases considered were based on the operating and test pressures of interest. A range of initial crack lengths from 4 to 240 mm was covered and a semi-elliptical crack geometry assumed. The surface behaviour is similar at both crack sizes, but instability at the deepest point becomes more brittle with increasing crack length, due to the decreasing constraint.

Instability of a 120 mm crack at the service temperature and an operating pressure of 170 bar is predicted at a depth of 2.86 mm, and the subsequent fast fracture through-wall is predicted to be by a predominantly ductile plastic collapse. These predictions are fully consistent with the observed failure.

**Leak-before-break**

A semi-elliptical crack of large aspect ratio will, once it penetrates the wall, assume an approximately rectangular geometry. Its stability with respect to longitudinal growth may now be assessed in exactly the same way as the through-wall behaviour was analysed.

At the service temperature and the operating and test pressures of interest, the lower constraint on growth in this scenario leads to a more mixed failure mode than was predicted in the through-wall direction. For the hydrostatic test pressures the increased flow stress and considerably reduced fracture toughness at ambient temperature lead to a predominantly brittle failure mode and a reduced critical crack length. Figure 3 defines the calculated leak-before-break boundary in terms of critical crack length as a function of service pressure.

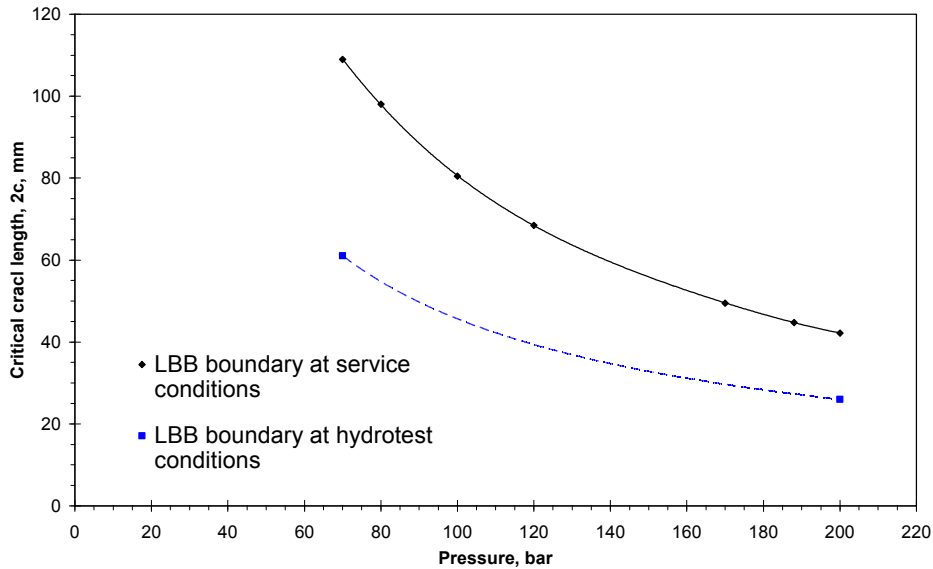


Figure 3. Leak-before-break boundary.

At the normal operating temperature and pressure, a crack of 50 mm or longer will, once it penetrates the wall, lead to a burst. This is consistent with the recent failure, where a 120 mm long defect led to a burst. The observed final failure mode, where a panel was blown out of the wall, is not uncommon in conditions of dynamic fracture and constrained displacements. The tubes are constrained by the membrane wall, and this will tend to inhibit the more usual ‘fish-mouth’ opening associated with ductile bursts. The adjacent 45° bends and the welded burner support stay will also have some influence. Under constrained dynamic fracture conditions, the 45° shear lip causes the fracture line to curve and become circumferential. High bending moments are then generated which cause the far edge of the panel to fail by ductile overload, as seen here.

These predictions are also consistent with the earlier failure history where all reported leaks appear to be associated with short crack lengths. It should be noted, however, that the majority of the earlier leaks appear to be located at welds, where microstructural effects may limit the crack size.

At service temperature and a reduced operating pressure of 120 bar, the critical crack length is predicted to be a little below 70 mm. To achieve a critical length of 100 mm would require the pressure to be reduced to below 80 bar.



**Combined results:**

Putting these parts of the analysis together allows the total stability behaviour of the cracks to be described, see Figure 4. The broadly horizontal lines are failure loci derived from the through-wall crack stability analysis; each represents a different operating or test pressure. A crack of dimensions below the appropriate failure locus is predicted to be stable: i.e. static or growing by a progressive mechanism such as corrosion fatigue. A crack of dimensions above the failure locus is predicted to be unstable and will penetrate the tube wall instantaneously. The leak-before-break boundary is derived from Figure 3. Any crack whose growth behaviour causes it to cross the appropriate failure locus at a point to the left of this boundary will generate a leak; any crack whose growth behaviour crosses the failure locus to the right of this boundary will generate a burst.

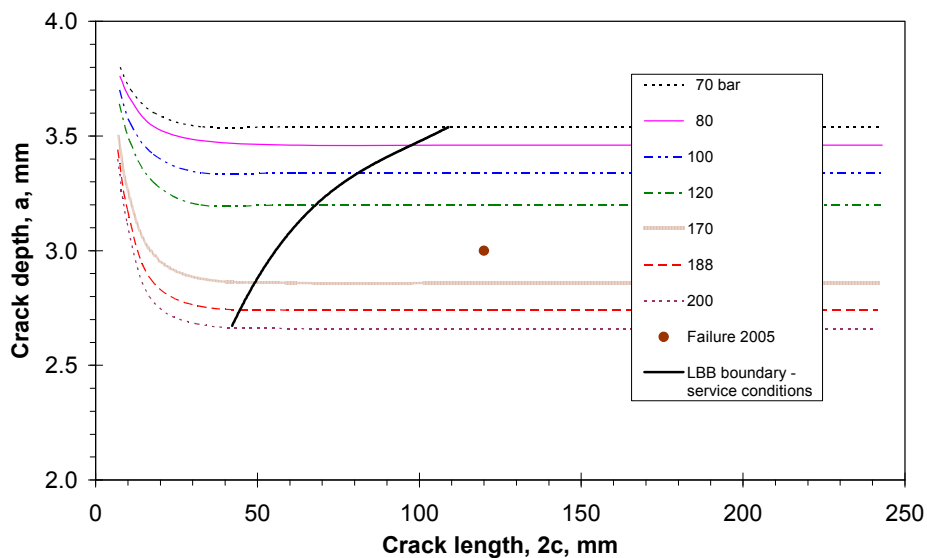


Figure 4. Total crack stability predictions at service conditions

**The significance of safety valve and hydrostatic tests**

The sister boiler was subject to a safety valve test, at the service temperature, in which the operating pressure was raised to 188 bar. No tube failures occurred. It is therefore reasonable to assume that no defect existed in the tubes, at that date, of dimensions above the 188 bar failure locus shown in Figure 4. In particular, considering the leak-before-break limit of 45 mm length at 188 bar:

Safety issues arising from the corrosion-fatigue of waterwall tubes

- Any defect present in the tubes of depth greater than 2.75 mm must have had a length less than 45 mm. At any operating pressure below 188 bar such a defect is predicted to generate a leak.
- Any defect of length greater than 45 mm present in the tubes must have had a depth less than 2.75 mm. At the current reduced operating pressure of 120 bar, such a defect needs to grow to a depth of 3.20 mm before it reaches a burst condition (and would also need to be of length greater than 68 mm).
- It is prudent to assume that the waterwall tubes of this sister boiler contain defects of depth close to 2.75 mm and length in excess of 68 mm. Such defects are predicted to generate bursts when they penetrate the wall. Regrettably there is no information available at present to predict the growth rate *a priori*.

Both boilers underwent hydrostatic tests at ambient temperature in the two years prior to the burst. The sister unit was tested in 2003 at 70 bar and 200 bar; the boiler in which the burst occurred in 2004 at 200 bar. In each case some leaks occurred during testing and some shortly after, generally in the range 1 600 – 3 700 h.

The calculated failure locus for hydrostatic testing at 200 bar is broadly comparable with that for normal service for cracks up to 100 mm length, but falls below it at greater crack lengths. Thus, despite the differences in failure mode predicted in the crack stability analysis, this test should provide a realistic screen for defects that would be immediately critical at the service condition. However, it will only become conservative and provide a margin for crack growth for defects above 100 mm in length.

Consideration of the burst event in the light of the previous hydrostatic test history does allow some estimate of crack growth behaviour in the potential burst regime. The failure locus for hydrostatic tests at 200 bar implies that any crack of 120 mm length must have been less than 2.80 mm depth at the time of testing, in comparison to a critical depth of 2.86 mm at the normal service condition. The crack that led to the failure must therefore have grown from no more than 2.80 mm to the predicted critical value of 2.86 mm in the 10 454 calendar hours between the hydrostatic test and the failure event. This gives a lower (non-conservative) bound to the crack growth rate.

A generally accepted conservative Paris law for fatigue crack growth in a corrosive environment gives the crack extension in metres per cycle as:

$$da/dN = 1.45 \times 10^{-12} \cdot \Delta K^{3.5} \quad (1)$$

where  $\Delta K$  is the cyclic stress intensity range. Assuming a 24 hour cycle from zero to the normal pressure stress, this law predicts a period of 9,576 hours for a 120 mm long defect to grow from 2.80 to 2.86 mm. This is within 10% of the observed time, indicating that this scenario is at least plausible, though not excluding the large number of other possible combinations of cycle length and stress range that would give similarly close results.

It is noted that, at the time of the tube burst, the sister boiler had served 15,120 hours from its comparable hydrostatic test without incident at the normal service condition. This would indicate that at the time of its hydrostatic test the most significant defect present in the sister boiler was smaller than the one which led to the tube burst.

Given that the above fatigue crack growth law is demonstrably compatible with the failure history, it may be applied to the sister unit. The previous calculations indicate that the reference defect condition is defined by the safety-valve test in 2005, at 188 bar and the service temperature, rather than by the hydrostatic test in 2003 at 200 bar and ambient temperature. Thus the crack growth regime to be considered is from 2.74 mm in 2003, at the service temperature and selected operating pressure. Predicted crack growth behaviour for this sister boiler is shown in Figure 5, which demonstrates the increase in crack growth time achieved by reduction of the operating pressure.

It must be stressed that these estimates of crack growth behaviour are illustrative, rather than indicative, let alone definitive. Many assumptions have been made from a relatively small amount of hard data. In particular, the irregular crack growth rates evidenced by the metallography have not been addressed. Nonetheless, reasonable assumptions on loading and materials properties have produced predictions of defect stability and development that are compatible with observation and experience.

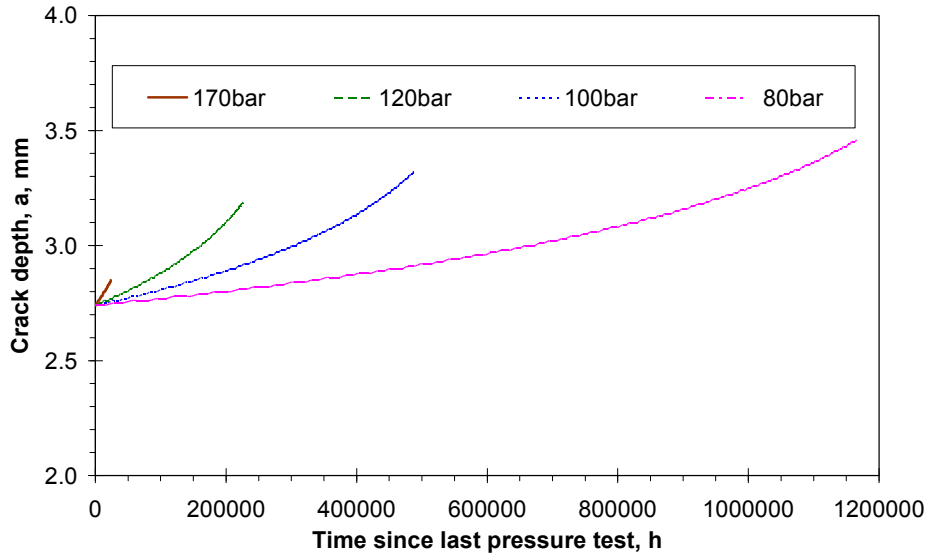


Figure 5. Predicted crack growth behaviour for the sister unit.

### 3. Failure consequences

Whilst there is a significant impact on availability due the frequency of waterwall failures, undoubtedly the danger to human life is the dominant consequence. It was therefore decided that a rigorous analysis of the potential steam release scenarios should be undertaken, in order to define safe exclusion zones around these and other boilers where tube failures had occurred.

#### Type of release:

As the failure situation addressed is that of a waterwall, it is necessary to consider possible water, steam and two-phase releases. Whilst the potential ballistic trajectory of a discharged water slug is considerable, it can readily be shown that instantaneous vaporisation would occur at the rupture point. Similar considerations apply to a two-phase release. It is therefore only necessary to examine a pure steam release in detail, as water and mixed discharges would immediately converge to that situation.

### **Characteristics of a steam release:**

At any realistic boiler operating pressures it can be shown that a steam release would be choked, i.e. sonic in nature (that is, the local velocity of escaping steam has reached the speed of sound at the local conditions). Calculations of sonic release rates were initially performed in a manner consistent with the methods given in recognised hazard assessment procedures [8, 9]. However the results were considered unrealistic in the light of known experience. It was noted that the formulae adopted by these procedures assume ideal gas behaviour; this is not appropriate for steam at these conditions. In particular such formulae implicitly underestimate the density of the steam, and thus the mass discharge rate. Accordingly, more accurate models have been used here, following standard texts on fluid dynamics [10, 11]. These take the density of the steam from standard steam tables, rather than calculate it on the basis of molecular weight, pressure and temperature. In all cases, a full rupture of the tube has been assumed.

### **Mass and temperature profile of the release:**

The release characteristics – mass release rate, velocity – were calculated for a range of operating pressures. As the models suggest, the mass release is approximately proportional to the operating pressure. At operating pressures above 60 bar, the mass released in three minutes exceeds the 10 000 lbs criterion of API 580 [8] and the releases are therefore classed as ‘instantaneous’. Assessment is thus based on the immediate effects of the release, rather than on subsequent dispersion of the released material. It should be noted, however, that the total fluid inventory in these drum-type boilers is large and therefore a considerable amount of material will be released after this three minute period.

The corresponding heat released from the steam to the air and the quantity of air required to cool the resultant mix to various temperatures were also calculated. Standard relationships have been used to determine the distances over which this occurs [9, 12, 13]. At a pressure of 120 bar, the exclusion zone size is calculated to be 12.5 metres. It is noted that this distance is insensitive to boiler pressure. This is a consequence of the significant contribution of the latent heat of vaporisation to the total heat of the released steam – particularly at lower saturation temperatures. Thus, in this range of operating conditions, the air/steam ratio required to achieve any given temperature below 100°C is only mildly affected by the release conditions.

In simple terms, therefore, the mass released (and therefore the heat released) is more-or-less proportional to the operating pressure, but the distance over which the temperature falls to a tolerable level is broadly constant.

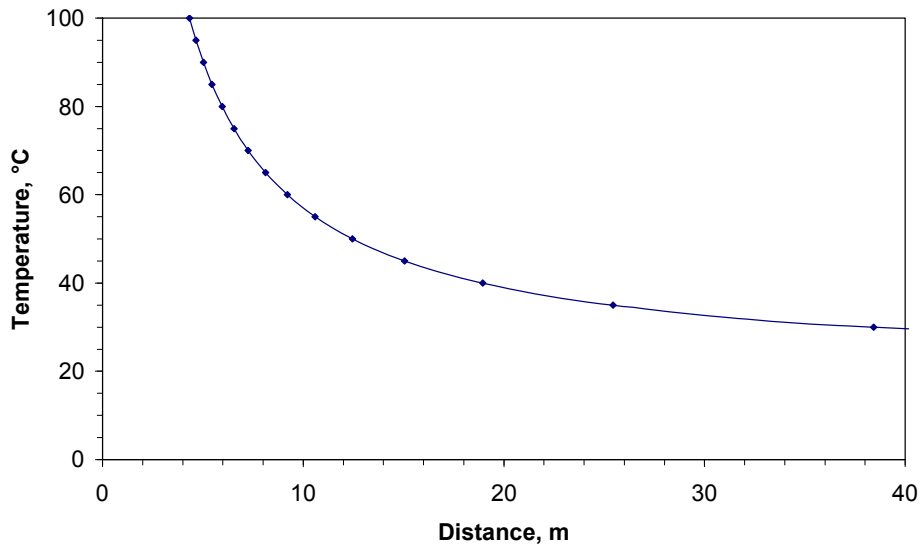


Figure 6. Decrease in temperature of the release with distance from the rupture

Figure 6 gives the variation in temperature of the steam/air jet as a function of distance from the release point, for an operating pressure of 120 bar. It is seen that below 10 metres the temperature rises rapidly and exceeds 60°C at 9 metres. Significant injury, even fatality, might be expected on such exposure. Brief exposure to a temperature of 50°C may be tolerable (12.5 metres) but for anyone involved in work, and therefore possibly restricted from rapid escape, a limit of 40°C (19 metres) is considered more appropriate. This last figure corresponds to the distance between the unit's boilers.

Exclusion zones should be planned recognizing that situations might arise where personnel are required briefly to move towards the rupture point in effecting their escape.

#### 4. Root-cause analysis

The root-cause analysis comprised a detailed review of operating, inspection and maintenance history in conjunction with a detailed failure analysis. This was followed by a programme of controlled operation with strain gauges, additional

thermocouples in place (Figure 7) along with potentiometers to monitor boiler movements. This enabled various operational modes to be studied and control procedures implemented that would allow the desired operational flexibility whilst minimising cyclic stresses within the waterwall.



Figure 7. Typical strain gauge installation.

The root-cause analysis identified a number of contributing factors. It was demonstrated that the problem is largely a legacy of a period of poor water chemistry and boiler operational difficulties during a period of high cycling and load following in the 1980s. This was rectified in the early 1990's but pitting and cracking had initiated in the tubes. Whilst the poor water chemistry contributed to the environmental influence on the corrosion-fatigue problem, the stress cycles were influenced by a number of elements. These were primarily generated during the periods when the feedwater flow was disrupted and there was a mismatch between the thermal input and flow. Flow disruptions can be caused by a number of issues, e.g. HP bypass openings, turbine trips and economiser steaming. Once the flow is disrupted, or reduced below what is needed for thermodynamic stability, the metal temperature rapidly rises. Thermal differentials give rise to high stresses in each affected tube and neighbouring

tubes. A further stress cycle is imposed when fluid flow is re-established and the tube cools. In conjunction with the pressure hoop stress these are the prime stress generators for the axial cracking as observed.

This resulted in marked reduction in the severity and frequency of these flow disruptions.

In the immediate period after the burst event, operation was kept as benign as possible. However, over time the data generated by the additional instrumentation identified the stress cycles, their causes were determined and efforts made to reduce or eliminate them. By carrying out controlled test programmes, it was possible to introduce increasingly flexible patterns without significantly increasing the number or severity of flow disruptions and resultant stress cycles.

## **5. Closure**

The work summarised in this paper has led to a much improved understanding of the corrosion-fatigue issue in these boilers, and thus to more confident and robust management plans.

The failure likelihood assessment established clear links between critical crack size, including leak-before-break behaviour, and operating conditions. Use of past inspection and test history enabled approximate crack growth behaviour to be predicted, and thus defined the timescales for inspection and the safe operating pressures to be maintained until such screening inspections could be performed.

The failure consequence assessment gave a rigorous basis for establishing exclusion zones around the boiler for normal operation, and pressure limits for times when it was necessary for personnel to be in closer proximity – eg when working on neighbouring units. It also demonstrated the non-conservatism of some standard release-rate formulae when applied to steam. Better formulae have been implemented and are recommended for steam-generating plant.

The root-cause assessment has identified both historical and current causative factors and allowed implementation of an investigation programme to address these in detail. Specific stress-raising events have been identified and control procedures have been put in place.

## **Acknowledgements**

The authors are grateful to many colleagues within ESB for their cooperation in the investigations, and to them, the utility's insurers and the UK Health and



Safety Executive for useful discussions. This paper is published with the permission of ESB Management and the Directors of SES Europe.

## References

1. CEGB, The Control of Fireside Corrosion – various editions.
2. American Petroleum Institute, Calculation of Tube Thicknesses for Fired Heaters. API Recommended Practice RP530 – various editions.
3. DIN Standard 17 177, May 1979. 15Mo3 Steel, Material Number 1.5415.
4. Mannesmann Steelworks Datasheet 405R, 1975. 15Mo3 Steel, Material Number 1.5415.
5. American Petroleum Institute, 'Fitness for service' API Recommended Practice 579, First Edition, 2000.
6. British Standard BS7910, Guide on Methods for Assessing the Acceptability of Flaws in Structures.
7. CEA Report DMT 96.096 A16: Guide for Defect Assessment and Leak-Before-Break Analysis.
8. American Petroleum Institute, Base Resource Document on Risk-Based-Inspection, Supplement to API Recommended Practice RP580/581.
9. Technica Ltd, Techniques for Assessing Industrial Hazards, World Bank Technical Paper WTP 55.
10. A.C. Walshaw and D.A. Jobson, Mechanics of Fluids, Third edition 1980.
11. G.F.C Rogers and Y.R. Mayhew, Engineering Thermodynamics Work and Heat Transfer, second edition 1967.
12. Albertson, Dai, Jensen, Rouse, Trans AMCE.
13. Hill, J Fluid Mech.

# Life assessment for vintage boilers

Pertti Auerkari, Jorma Salonen, Stefan Holmström  
VTT, Espoo, Finland

Leila Laaksonen\*, Ulla McNiven, Olli Lehtinen\*  
Fortum, Naantali\*/Jyväskylä, Finland

Sari Mäkinen, Ville Väänänen  
Helsingin Energia, Helsinki, Finland

Reino Nikkarila  
Inspecta, Espoo, Finland

## Abstract

The high temperature sections of power and combined heat and power (CHP) boilers are designed for some de facto expected but finite life. Several significant damage mechanisms must be taken into account, particularly in superheaters and reheaters that are designed for creep but also suffer from thermal degradation, external erosion and corrosion, and internal steam oxidation that will gradually increase the metal temperature. As rising temperature tends to accelerate all damage mechanisms, major effects can be expected from the internal oxide growth. The feedback loop is taken into account in procedures to predict superheater life from known tube dimensions, time in operation, and other initial data. The oxide effect can be mitigated by internal cleaning, but in-service spallation of a relatively thick internal oxide can also become significant in old plants. Spallation can create problems but extends the tube life by keeping the wall cooler than with an adherent oxide. Examples are shown for boilers with more than 150 000 h of service.

## 1. Introduction

Superheaters and reheaters experience the highest material temperatures of all boiler internals that operate as heat exchangers. The mechanical loading by internal pressure at high temperatures requires design for finite creep life, and the fireside and steam side environments also promote wall thinning through corrosion, oxidation and erosion. As the real service history will not be well known at the time of design, the differences in the design assumptions, manufacturing/assembly and later operation may offer potential for life extension, or for some surprises, when compared to the nominal “design life”. Typically, condition monitoring and maintenance actions are applied to support the life management so that the expected life (that itself may vary in time) will be achieved.

Two features can be assumed to dominate in the evolution of high temperature damage in superheaters and reheaters. First, increasing temperature will enhance the rates of practically all damage mechanisms that may be involved (creep, fatigue, erosion, external and internal oxidation/corrosion, material degradation). Secondly, the growing internal oxide will progressively increase the material temperature and thereby accelerate most damage mechanisms, shortening tube life. The design practices are usually based on creep life, with allowances for wall thinning due to the other mechanisms. As wall thinning can be significant in the hot end sections, the initial wall thickness is high and therefore the initial stress (and creep rate) is low, typically well below 30–50 MPa in older plants. When this stress with wall thinning arrives to a range of significant creep rate, the expected total damage rate also depends on the pressure level. In superheaters loaded by the pressure of live steam, relatively small additional wall thinning with the accompanied rise in material temperature can drive the creep rate relatively quickly towards the final failure. Together with operational fluctuations or events of overheating, this is thought to be one of the main reasons why creep failures in superheaters so rarely show creep cavitation damage of the type that is common in welded steam lines. Reheater tubes show cavitation damage more frequently, because the lower pressure level and initially thinner wall can result in longer times spent in the required stress range. Naturally, this can be also prevented by short term events like overheating.

In addition, the patterns of expected damage will also depend on material. This is partly due to the likely ranges of application and operating values, but also due to the composition, i.e. intrinsic features of the material type. Examples of such characteristic features are listed in Table 1 for a few classical super-

heater/reheater steels. The rate of internal oxidation in steam is much reduced with increasing chromium content of the steel, i.e. in the order of the steels shown in Table 1.

Table 1. Features of internal damage in some superheater/reheater steels.

Material type	Features of internal damage	EN designation
Mo-steel	Degradation, graphitization, (cavitation)	16Mo3
1Cr-0.5Mo	Degradation, (cavitation)	13CrMo4-5
2.25Cr-1Mo	Degradation	10CrMo9-10
11%Cr-steel	Degradation (but relatively resistant)	X20CrMoV11-1
Austenitic (316H)	$\sigma$ -phase formation, SCC <sup>1)</sup>	X6CrNiMo17-13-2

1) SCC = stress corrosion cracking

Consequently, any useful conclusions that may be drawn from the observed state of the material are also material specific. One of the major quantities sought in condition monitoring in this sense is the temperature history at the location of interest, since this will largely determine the rates of damage accumulation. With a rate model bounded by the initial, current and limit states of all influential damage mechanisms, tube life can be then predicted and modified also to future alternatives of the expected service history.

Apart from the model itself, this requires that:

- initial and current tube dimensions are reasonably well known/measured at worst locations
- initial and current operating pressures and temperatures are taken at the same locations, e.g. from operational records, and/or inferred from tube samples
- the rates of influential damage mechanisms are combined in the model.

As the true service conditions are not really known at the time of design, the implementation of design, fabrication and assembly is likely to include many conservative aspects that could on average translate into life extension. However, this is far from certain and only in-service measurements and inspections can confirm the actual state of the tubes. The long service life of typical plants also requires upgrading well before the end of life, although this may apply more on e.g. control systems than on the principal mechanical

components. Nevertheless, also superheater and reheater tubes are typical components that could be subject to maintenance operations such as internal cleaning (to remove scales and lower tube material temperatures) and local renewal. It is sometimes challenging to keep track on the changes so that tube sampling for condition and life assessment remains representative of the worst areas of the boiler.

Although creep design with relatively new steels has often used optimistic standard data [1, 2], more important sources of uncertainty are in the input data of life assessment. Examples are shown below on the impact of errors, uncertainties and material/boiler specific features in the assessed condition and life of superheaters/reheaters.

Also other comparable effects may appear when using guidelines based on shorter term data than the actual time in service. Here particular cases of low-alloy steels are taken as examples, with long term internal oxidation, micro-structural instabilities and operational data not necessarily agreeing for the assessment of the temperature history. Various sources of bias can be expected and have been observed for different approaches of assessment, with typical consequences in the predicted (creep) life. By properly accounting for the expected bias, it is believed that reasonable and safe but not overly conservative estimates of the residual life can be achieved. This also applies to cases where it is otherwise difficult to rely on one single source to indicate the actual temperatures or damage levels. Examples are given for cases where the time in service is approaching or exceeding 200 000 h.

## **2. Life of superheaters and reheaters**

The hottest sections of superheaters often have metal temperatures exceeding that of the steam by some 15–50°C. For a fixed steam temperature such a wide range of metal temperatures can cover a very large range in the expected tube life, as 10°C increase may approximately halve the tube life. It helps a little that the operating stress may be dominated by the fairly well controlled internal pressure, as superheaters and reheaters are made of relatively flexible small size tubing with low system constraints at least outside attachments. However, the tubes are subjected to the fireside environment, resulting in through-wall temperature gradients and non-constant material temperatures in addition to wall thinning by external oxidation, hot corrosion and wear (erosion) by the flue gas. Finally, the internal oxide layer is gradually growing and by its insulating effect

resulting in progressively increasing material temperature of the tube, if approximately constant heat flow is extracted from the superheater/reheater section. To counter the effect of the internal oxide, this layer may be removed by chemical cleaning, as has been done in the first example described below.

A reheater tube leak ( $\varnothing 70 \times 4$  mm, Figure 1a) was observed in a coal fired boiler after 185 000 h of service. Cross-section of the tube at this location showed through-wall creep cracking with abundant cavitation damage (Figure 1b). The differences in the microstructures of the tube (Figure 2) can explain how the measured steam temperature after reheater was only about 465°C, while the material temperature on the hotter side had apparently exceeded 500°C. For the material of the tube (16Mo3), this was sufficient to result in creep failure after fairly extensive time in service.

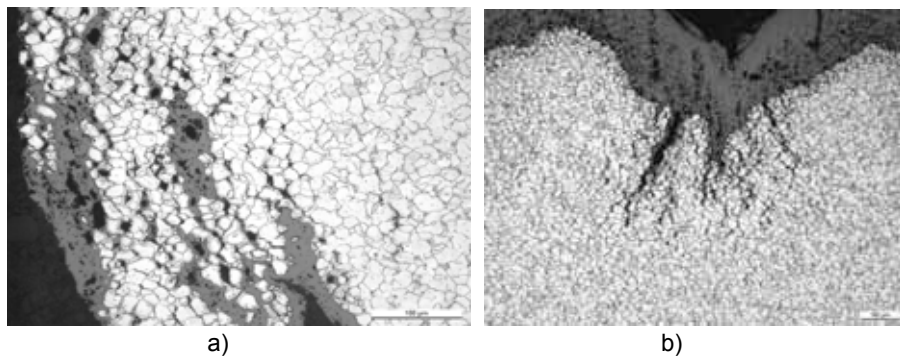


Figure 1. Cross-sections of the failed reheater tube; a) main failure surface; and b) initiating internally oxidised creep cracks on tube surface (scale bars 100  $\mu$ m).

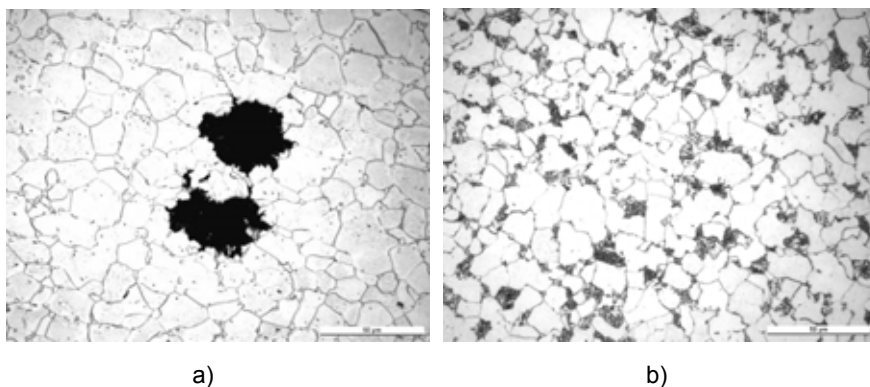


Figure 2. Microstructure of the tube material outside the immediate failure area: a) fireside, showing graphitization; b) opposite side (scale bars 50  $\mu$ m).

Further investigation of unfailed tube samples suggested that the remaining tubes were apparently subjected to less severe service conditions than the failed tube. Life prediction for the tubes was based on a simplified effective temperature history, essentially reducing the three past oxide cleaning episodes to a single effective cycle and then to a natural oxide growth prediction from the time of assessment onwards (Figure 3). An in-house software tool was used to combine the effects of stress, temperature and creep strength evolution to obtain a predicted life. In this case the tube temperatures were estimated from internal oxide thickness, which however fails to indicate the temperature history before the most recent tube cleaning (at 138 000 h of service). For the more distant past, the micro-structural evolution was used to assess the tube temperatures. An in-house study including 16Mo3 suggests that a Larson-Miller type of expression can describe the effects of time and temperature to a common master curve with constant features in the microstructures [2].

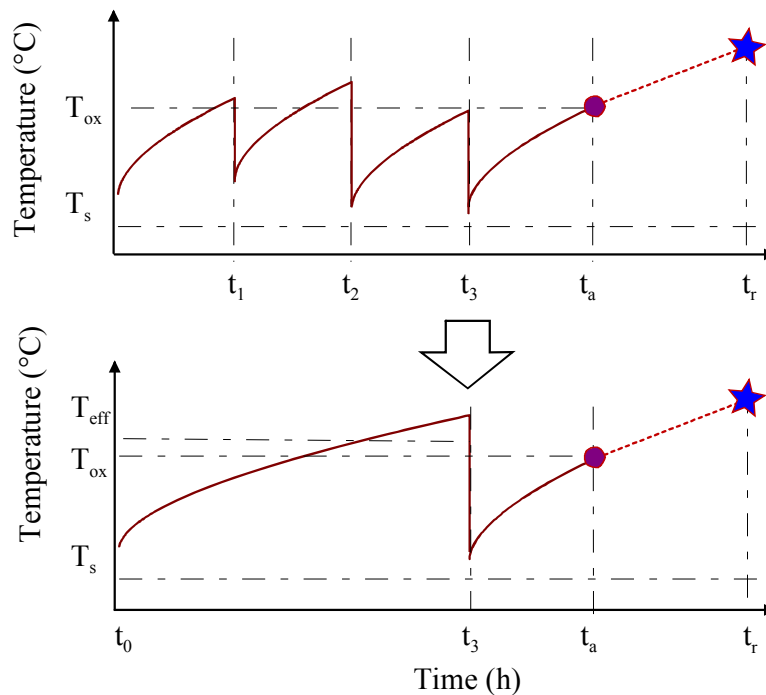


Figure 3. Reduction of service history to simplified cycles;  $T_{eff}$  = effective tube temperature in past service,  $T_{ox}$  = tube temperature from internal oxide;  $T_s$  = steam temperature;  $t_1$  to  $t_3$  = time to oxide removal,  $t_a$  = time of assessment,  $t_r$  = predicted end of life.

However, the microstructure (Figure 2) of the tube clearly indicated that graphitization of the material has taken place on the hotter side of the tube, resulting in a structure nearly completely lacking the eutectoid and grain boundary carbides. Due to somewhat faster transformation under creep loading and because such carbides are still present in the reference micrographs taken from shorter term laboratory annealing, direct comparison of the microstructural appearance (or hardness) can overpredict the effective service temperature. In this case the tube temperature must have been between the recent (oxide indicated) and higher, microstructure indicated level. The actual past effective temperature before the last tube cleaning was estimated to have been about  $520 \pm 5^\circ\text{C}$ .

The predicted minimum additional service life, taking also into account the other potential damage processes in addition to creep, was still several years (about 35 000 h). The predicted life should be inherently somewhat conservative due to e.g. assumptions made on the distribution of pressure in time. The reheater section was included in the inspection program for damage monitoring. For this purpose, a combination of replica inspections, diametral and wall thickness measurements have been applied at selected locations. The section was re-inspected after 15 000 h of additional service, with no indications to contradict the previous assessment of predicted life.

Another example was taken from the reheater of another coal-fired plant after about 180 000 h of service but no internal oxide cleaning. In this case the material is 10CrMo9-10, for which the microstructural state should work relatively well to describe the effective service temperatures (Figure 5). The oxide has grown to a considerable thickness of about 0.4 mm (Figure 6), but here it is the oxide based temperature assessment that is unreliable due to partial oxide spalling. Therefore, microstructure (and hardness) was used to establish the effective past service temperature at about  $575\text{--}600^\circ\text{C}$ . This is not far from the design temperature of  $579^\circ\text{C}$ . This can be compared with the measured mean steam temperature of  $530 \pm 12^\circ\text{C}$  from a one-year sample of in-service measurements. Using the same tools and principles as above, the minimum residual life of comparable tubes was predicted to be 50 000 h. The reheater section was included in a follow-up inspection program to monitor its performance. After more than 20 000 h of additional service, no incident has contradicted the predicted life.





Figure 4. Reheater tube sample (surface oxide removed), with indications of hot corrosion and thermal fatigue.

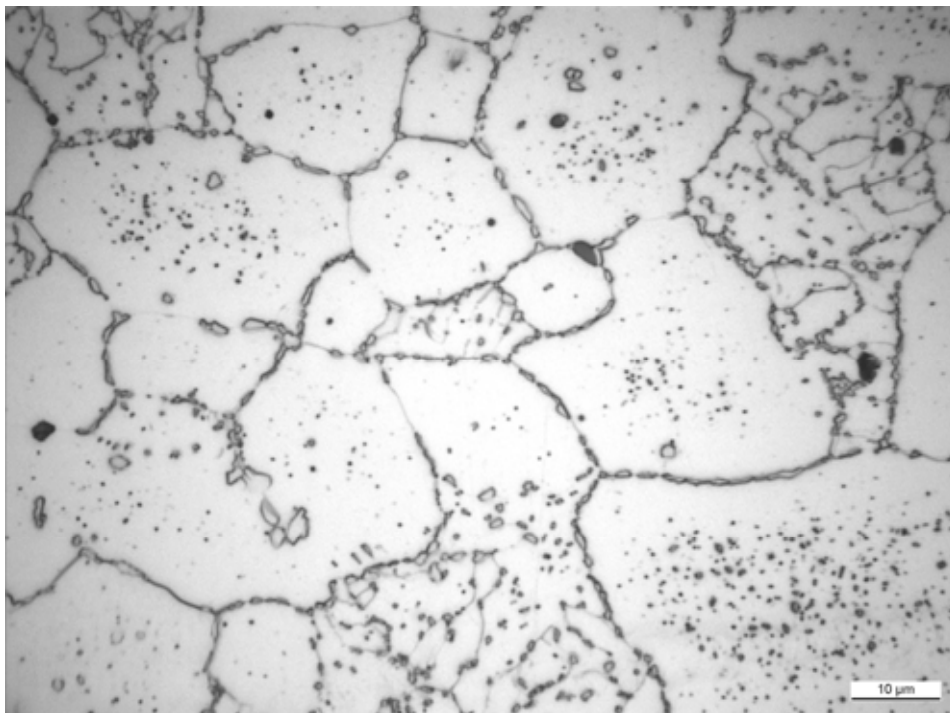


Figure 5. Microstructure of a reheater tube, scale bar 10  $\mu\text{m}$ .

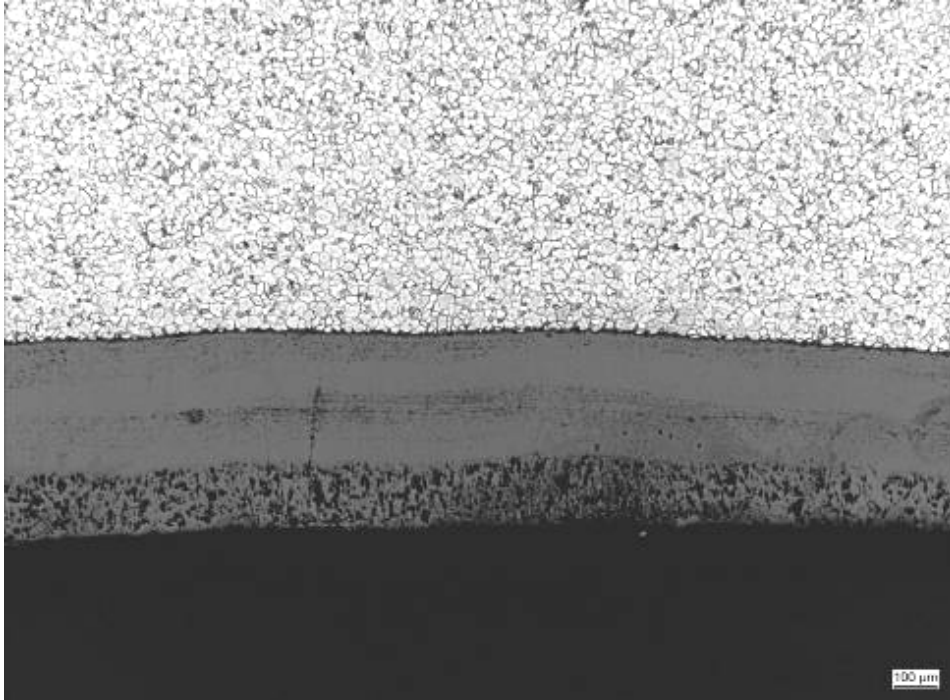


Figure 6. Sectioned internal oxide; scale bar 100  $\mu\text{m}$ .

### 3. Discussion and conclusions

While creep strength may provide the long-term integrity for superheater and reheater tubes, life of these tubes can be radically shortened by parallel damage mechanisms acting simultaneously and in combination with creep. Even mechanisms like thermal degradation that are included in the standard creep strength values are not explicitly accounted for by design, as internal oxidation will progressively increase the tube metal temperatures. Increasing metal temperature will accelerate all damage mechanisms such as creep, fatigue, and fireside and internal corrosion/oxidation/erosion of the tubes.

However, the effects of temperature can also be used to support life assessment by assessing the effective tube metal temperatures from the observed state of an extracted tube sample. This approach is fairly well established [3], but not without pitfalls as demonstrated above. Indications of the thermal history as the observed state of e.g. tube microstructure, hardness, oxide thickness or direct thermo-couple measurements can each suffer from various sources of error or

uncertainty. Some of the error sources are listed in Table 2. The above example of steel 16Mo3 graphitization and resulting loss of carbides in the microstructure is rather extreme, but it is common to see that microstructural features are different in long term service and in samples heat treated to a presumed similar state according to a time-temperature scaling parameter. This is partly because different features in the microstructure may show differences in their temperature dependence, and partly because by increasing the temperature to compensate for reduced time of exposure one may arrive at a different region of stability or different phase volume fractions. The other example on internal oxide spallation shows a common phenomenon that is generally indicated when the oxide is unrealistically thin, jagged or with a thinner outer than inner layer [4].

Table 2. Error sources in estimating the tube metal temperatures of superheater/reheater.

Method	Sources of error/uncertainty	Notes
Microstructure	Limited coverage of t-T range	E.g. graphitization of 16Mo3
Hardness	Not established for all materials	Widely used for 10CrMo9-10
Internal oxide	Oxide spalling, oxide variation	Indicated by layer imbalance
Thermocouples	Drift in service, installation limits	Often K-type (chromel-alumel)
Diffusion couples	Non-standard installation	e.g. PETIT couples

Such complexity is not uncommon in the measured data. Contradictory indications may exist of the actual service conditions, but it is often possible at least to rank them in order of credibility. Naturally, a single source of information will remove the contradictions but is still not ideal. Much attention should be paid to evaluating the temperature history, which will have a major influence in the resulting predicted life.

The examples from reheaters of coal fired plants also demonstrated the existing potential for material-specific features that can introduce bias in life prediction. Nevertheless, so far there are no indications to suggest that the predicted service life would be overly short or long in the example cases. Moreover, oxide spallation and possible worst case censoring in sampling are likely to extend life.

In the efficient supercritical boilers of future plant, superheaters will operate at considerably higher pressures (up to 300–400 bar) and steam temperatures (600–

750°C). The differences in operational values will be reflected in materials and relative roles of damage mechanisms, at least in some detail (Table 3).

Table 3. Expected differences in the damage mechanisms of end superheaters in vintage boilers (ferritic steels) and future boilers (austenitic to Ni-based materials, supercritical).

Mechanism	Vintage plant	Future plant	Notes
Creep	Steam $\leq$ 550–580°C	~600–720°C	Design base
Fatigue	Usually not critical	Cycling limits	Headers more limiting
Erosion (fireside)	High flow	High flow	Not temp. limiting
Corrosion (fireside)	Limits by fuel <sup>1)</sup>	Coal/gas only?	Often temp. limiting
Oxidation (internal)	Max ~ 0.5–1 mm	Max $\ll$ 1 mm <sup>2)</sup>	Increases tube temp.
Material degradation	Rarely limiting	Rarely limiting?	Reduced strength <sup>3)</sup>
Combined total	Mostly established	Limited experience	-

1) also through fouling

2) frequent spallation of external oxide layers

3) largely included in standard creep strength values except for overheating

While the operating temperature and pressure levels will continue to increase in the top-of-the-line coal-fired boilers, this will not happen to similar extent in future waste or biomass boilers that need to avoid excessive fireside fouling and corrosion. For the extreme cases of corrosive municipal or industrial waste incineration, the temperatures may remain so low ( $\leq$  400°C) that creep is of negligible importance. In spite of different materials and operating conditions that require adaptation in the tools of life assessment, and persistent conflicting damage information that is unlikely to disappear, the basic principles of superheater life assessment are likely to remain similar in the future. With gradually improving monitoring techniques and other new technology, the available background information can be expected to support the life assessments even better than today, independently of the boiler type.

Old plants will continue to operate under conventional service conditions widely in the world, while new comparable and modified plants will also mature to become new vintage plants. Consequently, the needs for long term life assessment will not fade quickly even for the conventional range of materials,

fuels, and boiler designs. The critical issues will also remain, such as the quality of data on long term material properties, accurately determined initial and current states of the components of interest, understanding of the dominant damage mechanisms, and their impact under the conditions of past and future service.

## References

1. Holdsworth, S. R. & Merckling, G. ECCO developments in the assessment of creep-rupture data. Proc. 6th Int. Charles Parsons Conf. on Engineering Issues in Turbine Machinery, Power Plant & Renewables. Trinity College, Dublin, 16–18 Sept, 2003.
2. Auerkari, P., Salonen, J., Rantala, J., Holmström, S., McNiven, U., Lehtinen, O., Pihkakoski, M. & Nikkarila, R. Experiences on lifing of boiler plants. EPRI International Conference on Advances in Condition and Remaining Life Assessment for Fossil Power Plant. Louisville, USA, 16–18 October, 2006.
3. Salonen, J. & Auerkari, P. Microstructural degradation of boiler tube steels under long term exposure to high temperature. Espoo: VTT, 1996. VTT Publications 280. 20 p. + app.
4. Knödler, R. & Straub, S. Growth of oxide scales during steam oxidation at 650°C. VGB Powertech, 2008. Vol. 88, No. 10, pp. 66–70.

# **Italian standardization in the field of defect evaluation, fracture mechanics and fitness for service of pressure equipment**

Corrado Delle Site, Carlo Fossati\*, Giuseppe Giannelli\*\*,  
Claudio Sampietri\* and Andrea Tonti  
ISPESL, Rome, Italy  
\*CSA/Exova, Milan, Italy  
\*\*ISPEL, Milan, Italy

## **Abstract**

Typically the design standards and codes (DIN, ASME, API, AFNOR ...) provide rules for the design, construction, inspection, testing and verification of new pressure vessels, pipes, tanks, components of machinery, other components. These codes often do not consider the fact that the component is subject to an inevitable degradation during service and that during inspections following manufacturing pressure test and putting into service problems can be found. Indeed defects in structural components of plant and machinery can arise both during construction but also during their lifetime (e.g. cracks, corrosion damage, exposure to fire, etc.). The Fitness for Service (FFS) Assessment procedures, developed as codes, standards, referenced guidelines periodically reviewed by committees of recognized experts, were born just to cover this aspect and are set to become increasingly important for analysis of component integrity. At the same time, the existence of clear procedures becomes essential because of two reasons: on one hand the growth of the competition between different plant operators and, on the other hand, the competition between the different providers of services (including FFS analysis, checks on plants, materials characterization, etc.).

Currently, the Italian working group “FFS” is conducting a comparative study of the major European and international standards and procedures in light of the industrial situation and national laws, in order to draft an appropriate guideline for the application of the “FFS” methodology in Italy. The principles of this guideline will be presented and discussed.

## 1. Introduction

Engineering structures may contain imperfections (pores, flaws, defects, local thin area or cracks) during the fabrication stage or during the service life [1]. The degradation of materials in components of plants necessitate procedures and data for assessing their service performance for safe operation and avoiding costly outages. If a flaw is found in a structural component during in-service inspection, an assessment is needed in accordance with a respective code whether the flaw should be removed (repaired) or component replaced or flaw is being left in the component to continue to use the component. In late years several procedures have been proposed to address this issue, avoiding any safety condition decrease. Therefore, engineering assessment procedures containing analytical expressions need to be further developed and unified – particularly in Europe – to assess (primarily to provide conservative estimation of the critical condition) the structural significance of the flaws or damages.

Damage of pressurized components may have several origins. Damage growth can be driven by different mechanisms. Several factors can affect the behaviour of the damaged component: application area, type of the component, loading conditions and others. Main failure mechanisms are fracture, fatigue, creep and corrosion. Also interactions among them need to be considered [2]. Industrial sectors like nuclear power, petrochemical, chemical, etc. have already established FFS procedures for their applications.

FFS procedures can be used to determine the size limits of defects due to above mentioned damage mechanisms. This issue can result in cost savings in operation. These procedures can lead to an assessment of component containing defect to ensure its structural integrity during its foreseen life and its re-inspection interval.

The outcome of the assessment is a decision to operate with or without monitoring, to repair or to replace the component under investigation. Even components manufactured by good manufacturing practices and procedures may develop cracks or may contain various kinds of defects; FFS assessment can

provide structural integrity information, a re-schedule of re-inspection intervals as well as actions for life extension.

Each module of FFS analysis include a stage about defect detection and thus non-destructive examination. Therefore it is important to establish a good maintenance program and periodical non destructive examination to find out defects as soon as possible. Non destructive examination is essential for fitness for service in the case size and shape of the defect is required as an input for the subsequent analysis. The level of inspection to comply with the whole procedure must be chosen considering that FFS procedures are applied first to reduce the costs, avoiding unnecessary repairs. So, in order to apply correctly a FFS procedure it is necessary to determine the flaw length, flaw height, flaw position, flaw orientation, whether the flaw cross section is planar or it is not planar. The defects needs to be identified as “surface breaking defects” and “embedded defects”. In order to find surface breaking defects the following methods can be used: visual testing, penetrant testing, magnetic particle testing, eddy current testing, potential drop, radiographic testing, ultrasonic testing. For embedded defects the following methods can be applied: radiographic testing, ultrasonic testing, eddy current testing, D.C. potential drop testing. Ultrasonic testing is useful to provide the height measurement. Eddy current and potential drop can provide the cross-sectional area of the flaw.

## 2. Methods

Defect stability, the growth mechanism, the evolution of the flaw are essential factors for the FFS procedure to apply. Activated flaws need to be carefully evaluated during service, because they can seriously affect the safety of plant working conditions. FFS procedures are established to provide better design rules, good practices for fabrication and advanced tools for prevention of in-service failures related to creep, fatigue, fracture and corrosion. These procedures are continuously updated, modelling procedures are also improved with new material properties and technology upgrading.

One of the latest procedure established in Europe is FITNET MK8 [2]. This procedure is based, according to above mentioned principles, to well known standards and good practices, like:

- SINTAP ‘Structural Integrity Assessment Procedures for European Industry’, Brite-Euram Project No. BE95-1426.



- BS 7910 ‘Guide on Methods for Assessing the Acceptability of Flaws in Metallic Structures’, 2005.
- R6 ‘Assessment of the Integrity of Structures Containing Defects’, British Energy Generation Report R/H/R6, Revision 4, 2001.
- API 579 ‘Recommended Practice for Fitness-For-Service’, Edition March 2000, American Petroleum Institute.

In case of using material properties in the assessment, a reference to a material standard is required. Testing of the material is not covered by the FITNET procedure.

Simplified models are needed to provide a standardized and reliable procedure to establish whether a defect is stable or not. This issue leads to a schematic approach and the use of flowcharts as much as it is possible. This can result in an improved reliability of the method.

National and international standards are widely applied. The rules and standards mentioned before are continuously tested, by application in the pressure components.

## **2.1 Most widely applied standards**

The Italian working group about fitness for service is mainly working on three main international standard: the American API 579, the British BS7910 and the European FITNET procedure MK8. The American API 579 was originally developed for petrochemical applications. Now it is applied also in other sectors, like power generation, with suitable modifications. The BS7910 was developed after the publication of British Energy R5 and R6, related to flaw assessment for high temperature conditions (R5) and flaw assessment in general conditions (without addressing of temperature issues). The FITNET procedure was developed by experts from 16 European countries, plus the contribution of experts from Japan, from USA and from Korea. It is conceived for the assessment of structures with welds, containing various kind of flaws.

### **2.1.1 API 579**

In API 579, life extension is regulated by residual lifetime and re-inspection interval, with a suitable safety factor. NDEs are relevant for flaw monitoring, indications for actions, health and safety for personnel [3]. The main damage

Italian standardization in the field of defect evaluation, fracture mechanics and fitness for service of pressure equipment

mechanism considered are: brittle fracture, corrosion, pitting, hydrogen blistering, welding misalignment, cracking, creep, firing, undercut and scaling. For each of the damage mechanism described above, there is a specific assessment procedure.

#### 2.1.1.1 Brittle fracture

API 579 provides procedures for evaluating the resistance brittle fracture of existing pressure equipment (vessels, piping and storage tanks) in carbon steel and low alloy steels. It also provides the testing procedure to determine the normal operation of starting and stopping.

#### 2.1.1.2 Corrosion

API 579 provides procedures for the evaluation of general corrosion. The thickness value used for the assessment may be to read in a "point" or in a detailed profile. It also provides a methodology to be used in case the reduction in thickness is treated as localized corrosion. This part also provides techniques for the evaluation of isolated or grouped defects made by thickness decreasing located in pressurized components. For evaluation the details of the thickness profiles are required. Procedures can also be used to assess individual craters of corrosion and "blisters".

#### 2.1.1.3 Pitting

The standard provides procedures for the evaluation of "pitting corrosion" extended and/or localized. Procedures can also be used to evaluate a network aimed to "blister".

#### 2.1.1.4 Hydrogen blistering

The standard provides procedures for the evaluation of isolated or grouped "blisters" and damage from hydrogen (HIC/SOHIC) including those located in the welding and structural discontinuities such as transitions in the shell, stiffening rings and flanges.

#### 2.1.1.5 Welding misalignment

Procedures are provided for the evaluation of efforts arising from geometrical discontinuities in the shell, including the misalignment of welding and/or distortion of a coating.

#### 2.1.1.6 Cracking

The Standard provides procedures for the assessment of cracks. Solutions for stress intensity factors and reference stress (load limit) are respectively in Annex C and Annex D. Methods to evaluate the residual stress as required by the assessment process are described in the Annex E. The characteristics of the material required in the evaluation are provided in Annex F. Recommendations for the assessment of the development of cracks, including attention to environmental conditions, are included in the procedure.

#### 2.1.1.7 Creep

The standard also include procedures for evaluating the remaining life of a component operating under creep conditions. The characteristics of materials required for the assessment are shown in the Annex F. The methods of analysis for the assessment of crack development are included, considering the attention to environmental conditions.

#### 2.1.1.8 Firing

This procedure provides the evaluation of equipment which have been damaged by fire. For the evaluation provides a methodology based on experimental values of heat exposure during the fire. For the damage assessment of components the procedures described in other parts of this norm are used.

#### 2.1.1.9 Undercut and bulge

The procedure provides techniques for the assessment of bulges, undercuts and combination thereof.

#### 2.1.1.10 Scaling

It provides procedures for the evaluation of stripping including those located in the welds and structural discontinuity in the shell, such as stiffening rings and flanges.

### 2.1.2 FITNET MK8

FITNET was a thematic networking project designed to develop a European Fitness-for-Service Procedure (FFS) for assessing the structural integrity of metallic welded or non-welded structures transmitting loads. It deals with defects known or postulated to be present in a structure together with the possible growth of such defects by a range of mechanisms (fracture, fatigue, creep and corrosion) and the assessment techniques required to evaluate failure risk. It is intended to provide a scheme into which results from European, national programmes and other contributions are harnessed to the aim of a fitness-for-service procedure based on European technology [1].

The FITNET Procedure covers four major failure modes for advanced design and safety in all industrial sectors. It also includes the recent advances in international, national standards as well as industrial codes such as API 579, BS 7910, British Energy R5 and R6 [1].

#### 2.1.2.1 Fracture module

The FITNET Fracture Module is based on fracture mechanics principles and the purpose of the analysis is to determine the significance, in terms of fracture and plastic collapse, of flaws postulated or present in structures and components. The procedure is based on the principle that failure is deemed to occur when the applied driving force acting to extend a crack exceeds the material's ability to resist the extension of that crack. This material 'property' is called the material's fracture toughness or fracture resistance.

The principles of the FITNET fracture analysis method are:

- A hierarchical structure based on the quality of available data inputs
- Decreasing conservatism with increasing data quality
- Detailed guidance on determination of characteristic input values such as fracture toughness

- Analysis in terms of a Failure Assessment Diagram (FAD) or Crack Driving Force (CDF)
- Method of incorporating the effect of weld strength mismatch
- Guidance on the treatment of constraint in fracture assessment
- Compendia of stress intensity factors, limit load solutions and weld residual stress profiles.

#### 2.1.2.2 Fatigue Module

The FITNET fatigue module provides a series of assessment routes, for evaluating the fatigue damage due to cyclic or fluctuating loads.

Two basic scenarios are foreseen:

- a) There is no pre-existing flaw, and the goal of the analysis is to determine the accumulation of fatigue damage at a critical location. In this case the basic approach is to determine the fluctuating stress range at the location in question and to relate this to appropriate fatigue life curves.
- b) A real or postulated flaw is present, and the goal of the analysis is to determine the fatigue life.

#### 2.1.2.3 Creep Module

The FITNET Creep Module specifies methods for assessing defects in structures operating at high temperatures and under creep-fatigue loading conditions. The information required to perform an assessment are:

- the operating conditions
- the nature of the defects
- materials data
- structural calculations to correlate materials data with the behaviour of complex structures.

The procedure includes the structural calculations required to assess whether a given defect will grow to an unacceptable size in a given service life under a given loading history. A step-by-step procedure is provided to perform these assessments and methods for following each step are specified.

There are 13 steps in the creep module of the FITNET Procedure, as follows:

- STEP 1 Establish Cause of Cracking and Characterise Initial Defect
- STEP 2. Define Service Conditions
- STEP 3. Collect Materials Data
- STEP 4. Perform Basic Stress Analysis
- STEP 5. Check Stability under Time-Independent Loads
- STEP 6. Check Significance of Creep and Fatigue
- STEP 7. Calculate Rupture Life based on the Initial Defect Size
- STEP 8. Calculate Initiation Time
- STEP 9. Calculate Crack Size after Growth
- STEP 10. Re-Calculate Rupture Life after Crack Growth
- STEP 11. Check Stability under Time-Independent Loads after Crack Growth
- STEP 12. Assess Significance of Results
- STEP 13. Report Results.

#### 2.1.2.4 Corrosion Damage Module

The corrosion damage module of the FITNET procedure provides guidelines on the appropriate steps to take when an environmental assisted, either by stress corrosion or corrosion fatigue, crack as well as when local thin area has been detected in service and an assessment of the implications for structural integrity has to be done. This module deals primarily with the Fitness-for-Service assessments of damage types due to:

- A) Environment assisted cracking (EAC):
  - a) Stress corrosion cracking
  - b) Corrosion fatigue
- B) Local Thinned Area (LTA).

#### 2.1.3 BS 7910

The fracture mechanics based fitness-for-purpose (FFP) approach enables the significance of flaws to be assessed in terms of structural integrity. The concept has been widely used by the British standards PD6493. The document has recently been revised and is now published as BS 7910 “Guide on methods for assessing the acceptability of flaws in metallic structures” [4].

BS 7910 includes the information required for assessment in terms of defect characteristics and dimensions, stresses and material properties. It gives also the procedures for assessment of fracture, fatigue, flaws under creep conditions and other modes of failure. The annexes contain normative procedures for dealing with certain situations: combined direct and shear stresses, determination of fracture toughness from variable materials data and informative data like residual stress distributions for welded joints, weld strength mismatch, proof testing and warm pre-stressing, etc.

BS 7910 gives procedures for assessing fatigue crack growth based on quality factors and crack growth calculation. A single procedure is given for assessing flaws at high temperature and corrosion. Further assessment is foreseen if initial results are not favourable. There are three levels for the assessment of fracture based on failure assessment diagram concept:

- Level 1 is a screening procedure and the most conservative.
- Level 2 is material specific and estimates the interaction between fracture and plasticity.
- Level 3 involves a direct calculation of plasticity effects.

A significant computation of stresses and fracture parameters is often necessary. BS 7910 is intended to apply to equipment manufactured by different design codes and materials, while API 579 is based around ASME design and materials. Specific stress and materials data is required even for level 1 fracture assessment. As a result, use of BS 7910 generally requires personnel experienced in FFS assessment with access to appropriate data and/or testing facilities. The code outlines methods for assessing the acceptability of flaws in all types of structures and components. The types of flaws which can be assessed are planar flaws, non-planar flaws and shape imperfections.

There are seven modes of failure:

1. Failure by fracture and plastic collapse
2. Damage by fatigue
3. Damage by creep and creep fatigue
4. Damage by leakage of containment vessels
5. Damage by erosion/corrosion
6. Damage by environment assisted cracking
7. Failure by instability.

### **3. Results, main differences among main standards**

The API are typical Anglo-Saxon standards which leave very little uncertainty to use them and do not necessarily require that the user is an expert in the various damage mechanisms. The BS even with very similar approach assumes that the user is a very experienced technician. BS 7910, like FITNET MK8, is intended to apply to equipment manufactured to different design codes and materials, unlike API 579 which is based around ASME design and materials.

While BS7910 and API 579 are national standards, FITNET Thematic Network (TN) has been prepared together by 62 experts from 16 European countries and 41 organisations. Additionally, experts from Japan, USA, Korea and Norway have provided in-kind contributions to the development of FITNET FFS Procedure. National programmes and in-kind contributions are harnessed to the common goal of a fitness-for-service procedure based on European advanced technology. Establishing an Italian national guideline, to be applied in Italian plants, all these differences need to be considered.

### **4. Discussion, Italian guidelines about Fitness For Service**

It is established that the Italian FFS evaluation of a pressure equipment will be conducted on the basis of the results of the following actions to perform:

- preliminary analysis that takes account of the project, history of exercise equipment, data of previous inspections, accident and/or repairs
- characterization of the defect
- identification of mechanisms of damage
- calculation.

#### **4.1 Preliminary analysis**

First there is preliminary assessments based on the following items which shall be available to the user and/or manufacturer.



#### **4.1.1 Original data project**

The original data needed for project evaluation FFS in general depend on the type of defect and/or damage mechanism identified in any case at least the following information must be available:

- project drawings and/or spreadsheet detailing the size (including tolerances and thicknesses of corrosion), materials used, the efficiency of welding and standard project,
- in the case of piping, isometric drawings,
- design loads under various conditions (including pressure, temperature, thermal loads under transient conditions, occasional loads such as wind, snow, earthquake, etc.),
- process fluids.

#### **4.1.2 Service data**

Service data are necessary for the assessment as they are linked to the damage mechanism and/or defect type; at least the following data need to be collected:

- Service history, pressure and temperature
- Working hours, number of start ups and shut downs, kind of process history, environmental conditions (last two issues are not always required)
- Suitable documentation about each relevant variation of service conditions during the life of the equipment
- Suitable documentation about each relevant variation of service conditions already scheduled for future life of the equipment.

#### **4.1.3 Maintenance data**

Maintenance data necessary for FFS assessment are generally related to the defect kind and/or damage mechanism; at least the following data are considered essential:

- Outcomes from manufacturing inspections
- Outcomes from previous inspection during service

Italian standardization in the field of defect evaluation, fracture mechanics and fitness for service of pressure equipment

- Outcomes from previous FFS assessment and/or life extension assessment
- Summary of corrective actions performed on the equipment (repairs, modifications and replacements).

#### **4.1.4 Defect characterization by NDEs**

Main parameters of each defect found in the pressure equipment need to be assessed. Size, orientation, position and possible causes need to be established before performing the damage mechanism characterization. All NDEs to be applied are evaluated before and during the inspection to apply the most suitable procedures for the case under investigation.

#### **4.1.5 Damage mechanisms**

The draft of this part is still under development, but in principle it is foreseen to individuate the cause of each damage mechanism. The guidelines for the preparation of this part are according to FITNET MK8, so there are no large constraints for the expert.

#### **4.1.6 Calculations**

On the basis of faults, the found mechanism of damage and the component under investigation, the method/rule/procedure more suitable for the FFS analysis among those provided for in paragraph 2 must be identified. If more damage mechanisms can coexist simultaneously, the FFS analysis must be performed for all mechanisms. The method/rule/procedure chosen must clearly show the limits of applicability and limitation. Where there is more than one level of study analysis, it should normally be performed starting from the lowest (most conservative approach) and it could go to the next level where the analysis is not satisfactory. The required input data necessary for assessing FFS in general depend on the method/rule/procedure and level of study chosen. The method/rule/procedure chosen must clearly show the list of all data input required, regarding the characteristics of the component (dimensions, materials, etc.), the design conditions, operation and proof that the component is subject (pressure, temperature, nature of fluids, etc.), running time, characteristics of materials with particular reference to those related to faults and the mechanism of damage found. Particularly, as regards the characteristics of the materials, it is

appropriate that the method/ rule/procedure adopted will show these characteristics or indicate explicitly how to obtain them.

## 5. Conclusions

The Italian working group “FFS” is conducting a comparative study of the major European and international standards and procedures in light of the industrial situation and national laws, in order to draft an appropriate guideline for the application of the “FFS” methodology in Italy. The principles of this guideline have been presented and discussed. The Italian procedure needs to integrate the European procedure FITNET MK8, with API 579, as the stake holders in Italy are from petrochemical application as well as from power plants. For petrochemical application they are more familiar with API and thus the transition needs to be smooth, without big jumps to the new procedure. This will lead to a better accepted procedure. The principle has been established to follow a single standard, once the working group has fixed the residual life, it is necessary also to fix a suitable safety factor to determine the appropriate inspection interval.

## References

1. FITNET Final Technical Report, Version 27th Nov. 06.
2. FITNET, Fitness for Service (FFS) Procedure. Revision MK8, Vol. 1, January 2008.
3. API 579. Recommended Practice for Fitness-For-Service. Edition March 2000, American Petroleum Institute.
4. Rastogi, R. An Introduction to BS 7910: The UK guide on methods for assessing the acceptability of flaws in metallic structures. Indian Nuclear Society Lecture on Welding, NDE and Integrity Assessment, September 18–22, 2006.

# Defect integrity in components subjected to cyclic loading at high temperatures


Stuart Holdsworth

EMPA: Swiss Federal Laboratories for Material Testing & Research  
Dübendorf, Switzerland

## Abstract

Cracks established during component manufacture or service subsequently propagate during high temperature duty due to the combined influences of thermo-mechanical transients and creep loading. As a consequence of the diverse loading conditions which can be responsible for high temperature crack propagation in service, the assessment of defect integrity in such circumstances is covered by more than one approach, each relying on a variety of material property input data. These approaches and the respective properties required for their implementation are reviewed. In addition, their application to the assessment of high temperature defect integrity is examined.

## Nomenclature

$a, \Delta a$	Crack length, crack extension
$A(T, \nu, t_h)$	Material constant in mid- $\Delta K$ fatigue crack growth rate laws; dependent on metallurgical condition, temperature, environment, frequency and hold time
$A_{20}$	Material constant for 20°C in mid- $\Delta K$ fatigue crack growth rate power law
$b$	Crack size exponent in short-crack creep-fatigue crack growth rate equations
$B'$	Constant in short-crack creep-fatigue crack growth rate equations (6,7)
$C^*$	Parameter characterising stress and strain rate fields at tip of crack in material deforming due to creep
$da/dN$	Crack growth per cycle
$(da/dN)_C$	Creep crack growth per cycle
$(da/dN)_F$	Fatigue crack growth per cycle
$(da/dt)_C$	Creep crack growth per unit time
	Creep damage accumulated at surface in single cycle

## Defect integrity in components subjected to cyclic loading at high temperatures

$D_C, D_C^{surf}$	Total creep damage, total creep damage at surface
$D(\epsilon_u)$	Constant in creep crack growth equation (5); dependent on material and temperature through dependence on creep rupture ductility
$E, E_T, E_{20}$	Elastic modulus, elastic modulus at temperature, $T$ , elastic modulus at 20°C
HSFCG	High strain fatigue crack growth
$J, \Delta J$	Parameter characterising stress and strain fields at tip of crack in material deforming plastically, cyclic $J$
$K, \Delta K$	Stress intensity factor, stress intensity factor range
$K_{min}, K_{max}$	Minimum, maximum stress intensity factor
$K_C$	Critical stress intensity factor responsible for unstable fracture
$\Delta K_{eff}$	Part of $\Delta K$ responsible for crack opening in transients involving a compressive component of loading [3]
$\Delta K_{eq}$	Equivalent cyclic stress intensity factor [3]
$\Delta K_{th}$	Fatigue crack growth threshold
LEFM	Linear elastic fracture mechanics
LSFCG	Low strain fatigue crack growth
$m$	Exponent in mid- $\Delta K$ fatigue crack growth rate power law equations
$N$	Number of cycles
$q$	Cyclic strain exponent in short-crack creep-fatigue crack growth rate equations (6,7)
$r_p$	Size of cyclic plastic zone
$R$	Load ratio ( $K_{min}/K_{max}$ )
$R_m$	Tensile strength
$t, t_h$	Time, hold time
$t_m$	Maximum allowable time at temperature
$T, T_{ref}$	Temperature, reference temperature
$\alpha_1, \alpha_2$	Empirical constants in equation (8)
$\epsilon, \Delta \epsilon$	Strain, strain range
$\dot{\epsilon}_C$	Instantaneous equivalent creep strain rate during the hold time
$\epsilon_{u, uniaxial}, \epsilon_{u, multiaxial}$	Creep rupture ductility, uniaxial and multiaxial
$n$	Exponent in creep crack growth equation (5)
$\sigma, \Delta \sigma$	Stress, stress range
$\sigma_m$	Mean stress
$\sigma_{ref}$	Reference stress
$\nu$	Frequency ( $dN/dt$ in Figure 4)

## 1. Introduction

Cracks established during component manufacture or service may subsequently propagate during high temperature duty as a consequence of the combined effects of cyclic and creep loading. The operating conditions responsible for crack growth at high temperatures are diverse, ranging from predominantly cyclic to mainly steady loading with infrequent off-load transients. The fatigue component of crack extension may be a consequence of high frequency (time

independent) or low frequency (time dependent) transients, applied in either load or displacement control. Moreover, cyclic loading can be linear-elastic, elasto-plastic or highly plastic. The creep component of cracking may be the result of primary (directly applied) and/or secondary (self-equilibrating) loading. As a consequence of the very diverse conditions which can be responsible for crack propagation at high temperatures, the assessment of defect integrity is currently covered by more than one approach, each with its own material property input data requirements (e.g. Table 1). These are reviewed in the following paper.

An important consideration in the characterisation of creep-fatigue crack growth rates and the assessment of high temperature components is the size of the crack relative to the size of the cyclic plastic zone at the surface. In the following review, long cracks are those whose size exceeds  $r_p$ , and short cracks are those whose size is less than that of  $r_p$ .

Table 1. Data requirements for the assessment of crack growth at high temperatures.

	<b>Higher Frequencies, Load Control</b>	<b>Lower Frequencies, Displacement Control</b>
Early (Short) Crack Growth ( $a < r_p$ )	$da/dN(\Delta J, R, T, \nu, t_h)$	$da/dN(\Delta \varepsilon, T, \nu, t_h)$
Long Crack Growth ( $a > r_p$ )	$da/dN(\Delta K_{eff}, R, T, \nu, t_h) + (1/\nu).da/dt(C^*, T); \Delta K_{th}(R, T, \nu, t_h)$	$da/dN(\Delta K_{eq}, T, \nu, t_h) + (1/\nu).da/dt(C^*, T)$

## 2. Long crack growth

### 2.1 General

Cyclic crack growth is conventionally considered in terms of three regimes (Figure 1). These are: *i*) a low- $\Delta K$  regime close to the fatigue crack growth threshold, *ii*) a mid- $\Delta K$  regime in which propagation rates are modelled by a power law (equation 1), and *iii*) a high- $\Delta K$  regime in which  $K_{max}$  approaches  $K_c$  (or  $\sigma_{ref}$  approaches  $R_m$ ), i.e. the condition(s) responsible for unstable fracture.

$$da/dN = A(T, \nu) \cdot (\Delta K)^m \quad (1)$$

In equation (1),  $A(T, \nu)$  and  $m$  are material constants dependent on temperature, environment and frequency (below a limiting value).

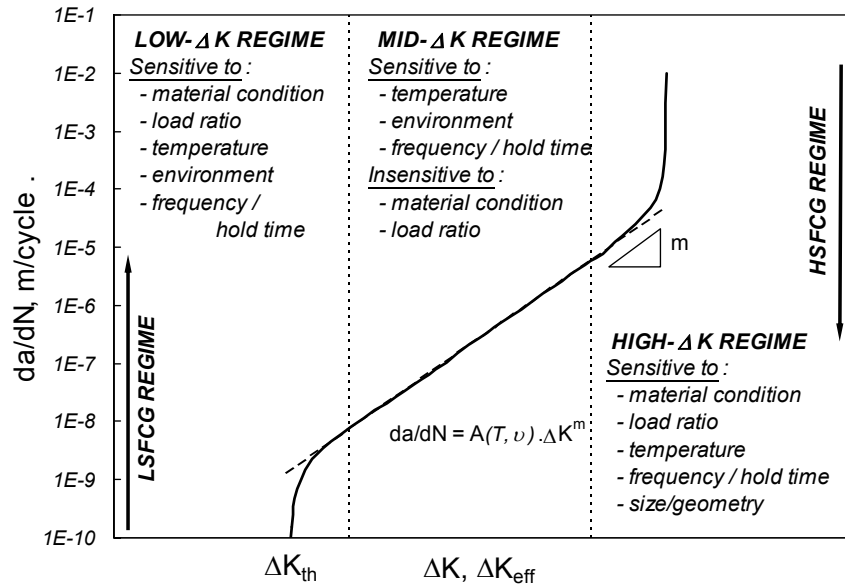


Figure 1. Cyclic crack growth rate regimes [1].

At low- $\Delta K$  levels close to  $\Delta K_{th}$ , the magnitude of  $da/dN$  is very sensitive to small increases in  $\Delta K$  and dependent on the same factors which influence  $\Delta K_{th}$ , these being: material, microstructure and yield strength, temperature, environment and load ratio ( $R$ ). Propagation rates in the mid- $\Delta K$  regime are less sensitive to microstructure and mean stress ( $R$ ) effects.

In the high- $\Delta K$  regime,  $da/dN$  becomes increasingly sensitive to the level of  $\Delta K$  and, in particular  $K_{max}$  (and/or  $\sigma_{ref,max}$ ) as  $K_c$  (and/or plastic collapse) is approached. Depending on the deformation and fracture characteristics of the material, crack growth rates can be strongly influenced by size and geometry. In these circumstances, a simple LEFM defined  $\Delta K$  is not the most effective correlating parameter and alternative energy based cyclic loading parameters such as  $\Delta J$  or  $\Delta K_{eq}$  are employed in equation (1) [2, 3]. In addition to the factors already mentioned,  $da/dN$  in the high- $\Delta K$  regime is strongly dependent on microstructure, mean stress, temperature, environment and frequency (strain rate).

At elevated temperatures, the  $da/dN(\Delta K)$  diagram may be alternatively split into two crack growth regimes (Figure 1) [1]. In the low strain fatigue crack growth (LSFCG) regime, load/displacement transients result in linear elastic loading cycles and low to mid- $\Delta K$  crack growth rates for which  $\Delta K$  (or  $\Delta K_{eff}$ ) still provides the most appropriate correlating parameter. Load/displacement

transients responsible for cyclic loading involving a degree of general yield (in particular in tension) are referred to as high strain fatigue crack growth (HSFCG) cycles. HSFCG rates are due to apparent  $\Delta K$ s and are influenced by whether deformation is load or displacement controlled, in particular in the material's creep regime. The overlap shown between the LSF CG and HSFCG regimes in Figure 1 is due to the fact that higher  $\Delta K$ s can be generated under linear elastic conditions with displacement controlled loading because of shakedown into compression.

Fatigue crack growth rates are increasingly sensitive to frequency with increasing temperature.

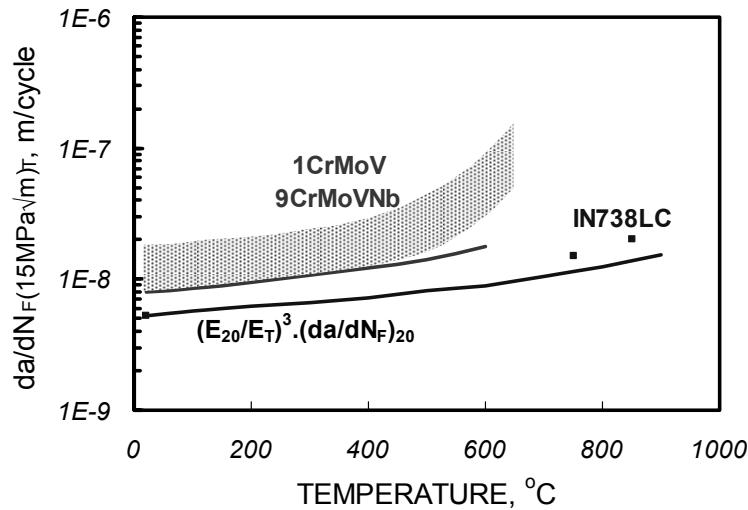


Figure 2. Effect of temperature on high frequency cyclic crack growth rate [4].

## 2.2 High frequency

At loading frequencies above those for which time dependent effects are influential (i.e. at elevated temperatures where oxidation is not responsible for significant crack tip oxide-wedging and/or creep damage enhancement), the factors affecting  $da/dN(\Delta K)$  behaviour are summarised in the previous section. For such conditions, the effect of temperature may be quantified in the mid- $\Delta K$  regime by rewriting equation (1) to give:

$$da/dN = A_{20} \cdot (E_T/E_{20})^m (\Delta K)^m \quad (2)$$



where  $A_{20}$  is equal to  $A(T, \nu)$  at ambient temperature in Equation 1. The effectiveness of this approximation is shown in Figure 2 for a number of high temperature materials [4]. It is clear that even at relatively high frequencies, there is a temperature (dependent on material) above which  $da/dN$  becomes increasingly influenced by time dependent thermally activated processes.

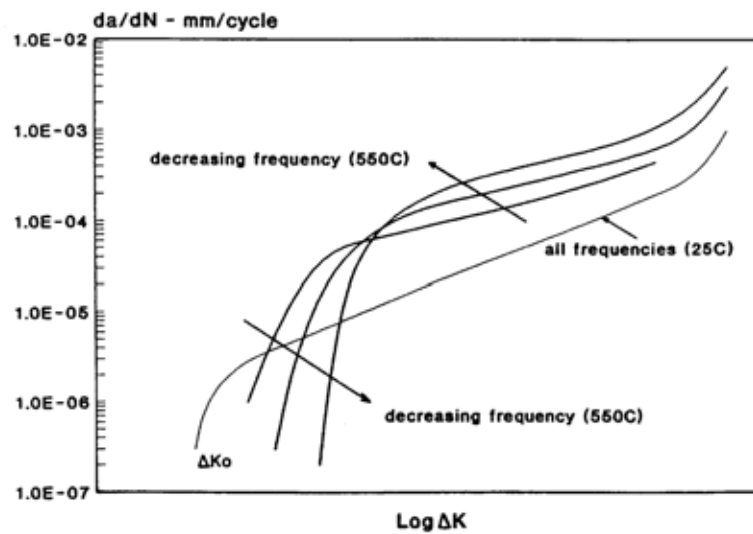


Figure 3. Effect of frequency on high temperature LSF CG rates in 1CrMoV steel [5].

### 2.3 Low frequency

At lower frequencies, oxidation and creep interaction effects become increasingly more influential at high temperatures (e.g. Figure 3). In load control, below a limiting frequency, crack growth rates may be regarded as being dominated by time dependent crack growth mechanisms (e.g. creep crack growth in Figure 4). The high temperature behaviour shown in Figure 4 is typical for many engineering alloys subject to load controlled cycling in the mid- $\Delta K$  regime.

In contrast, crack growth rates in the low- $\Delta K$  regime can reduce and  $\Delta K_{th}$  values increase with decreasing frequency due to oxide wedging and premature crack closure (Figure 3).

At high temperatures, the high growth rates associated with the high- $\Delta K$  or HSFCG regimes (Figure 1) can be generated either as a consequence of

relatively high magnitude cyclic loading applied remotely to a long crack (e.g. [3, 6]), or (more usually at an initial stage of thermal fatigue crack development) as high strain transients applied locally to a small crack contained in the cyclic plastic strain field (e.g. [7], see section 3). In the former case, cyclic crack growth rate behaviour is modelled using a modified form of equation (1), e.g.

$$da/dN = A(T, \nu) \cdot (\Delta K)^m \quad (3)$$

where  $\Delta K_{eq}$  is  $\Delta K_{eff}$  for purely elastic loading. Acknowledgement of the dependence of  $A$  on hold time reflects the potential dependence of this parameter on associated oxidation as well as creep damage [3].

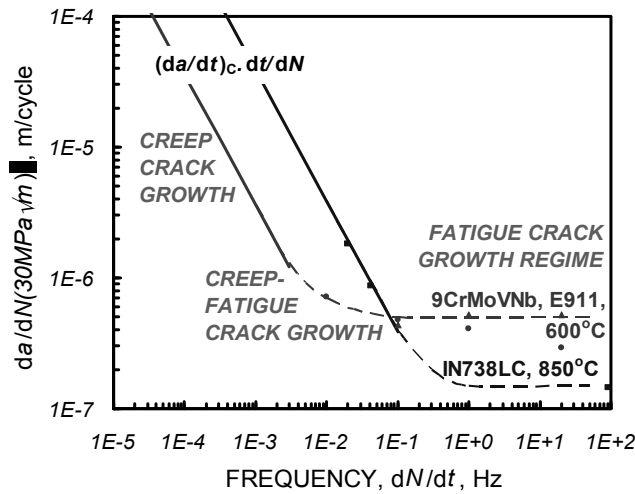


Figure 4. Effect of frequency on high temperature LSCFG rates in various alloys [4].

The high temperature crack growth properties required for the defect assessment of components subject to fatigue cycles involving hold (steady operating) periods may be derived from pure fatigue and pure creep crack growth rate data in a construction of the form given in Figure 4 when the loading is directly applied (i.e. load controlled). In such circumstances, the effective frequency may be simply determined from a knowledge of the total cycle time (i.e. transient + hold time). Alternatively, creep-fatigue crack growth behaviour is analytically modelled on the basis of fatigue and creep crack growth rate characteristics for the material, i.e.

$$(da/dN)_{total} = (da/dN)_F + (da/dN)_C \quad (4)$$

In equation (4),  $(da/dN)_F$  is given by equation (3), where  $A(T, \nu, t_h)$  may be influenced by creep and oxidation damage through its dependence on frequency and prior hold time [3] and  $(da/dN)_C$  is given by equation (5).

$$(da/dN)_c = \int_a^{a_0} D(\epsilon_{pl}) \cdot (C^*)^n \cdot dt \quad (5)$$

Any enhancement of the total growth rate per cycle due to creep-fatigue-oxidation interaction is covered by  $A(T, \nu, t_h)$  which is determined experimentally (e.g. Figure 5).

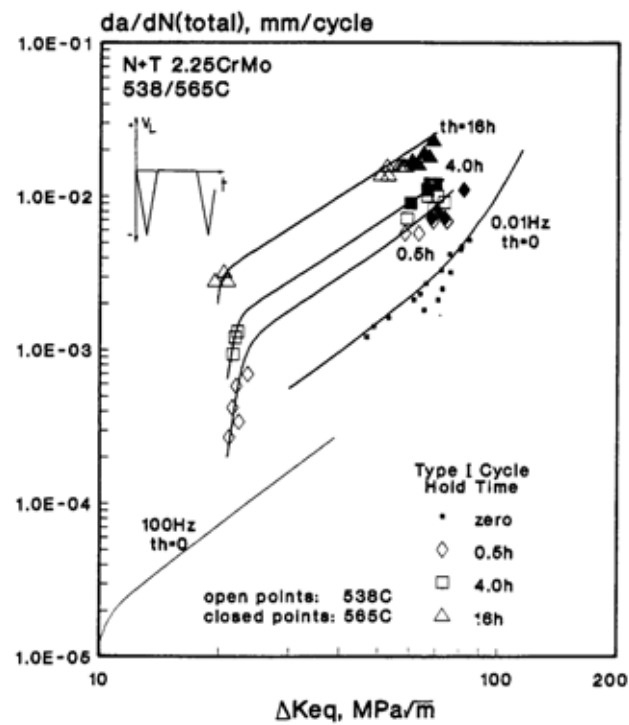


Figure 5. Long crack cyclic/hold creep-fatigue crack growth test data for 2¼CrMo cast turbine steel at 538/565°C [3].

### 3. Short crack growth

The HSFCG rates associated with small cracks contained in local cyclic plastic strain fields (typically  $a \leq 5$  mm) are most effectively modelled as a function of  $\Delta\epsilon$  [7–11] (e.g. Figure 6), i.e.

$$da/dN = B^t \cdot a^b \cdot (\Delta\epsilon)^c \quad (6)$$

For relatively short cracks contained in high cyclic plastic strain fields,  $(da/dN)_{total}$  is effectively modelled using a refinement of equation (6) [7, 10, 11],

$$(da/dN)_{total} = B^t \cdot a^b \cdot (\Delta \varepsilon)^q / (1 - D_C^{surf})^2 \quad (7)$$

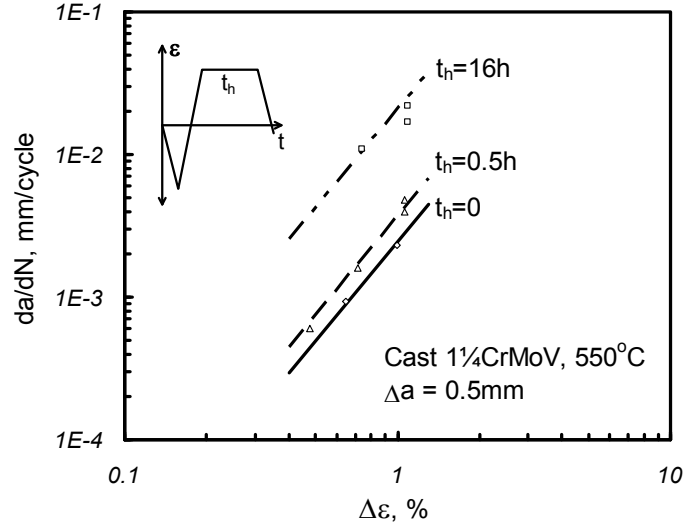


Figure 6. Comparison of crack growth rates after 0.5 mm crack extension from notch root in large SENB feature specimen creep-fatigue tests on cast 1¼CrMoV steel at 550°C [7].

The effect of hold time on HSFCG rate for a cast 1¼CrMoV steel at 550°C is shown in Figure 6. In this example,  $D_C$  was modelled as a function of hold time, i.e. equation (8), but in a formal assessment would be determined in terms of time fraction or ductility exhaustion (e.g. equation (11), section 4.3).

$$D_C = \alpha_1 \cdot (\ln(\alpha_2 \cdot t_h + 1)) \quad (8)$$

where  $\alpha_1$  and  $\alpha_2$  are empirical constants.

It is evident that the material property data required for the defect assessment of high temperature components subject to creep-fatigue loading can be strongly dependent on the specific operating conditions relating to the practical application under consideration. This means that the rigorous creep-fatigue defect assessment of a component can require a significant investment in the determination of appropriate material property data. It is therefore important to demonstrate that both creep and fatigue loading are significant at the critical feature to be assessed.

## 4. Defect assessment

### 4.1 Significant creep and fatigue

A creep-fatigue crack growth assessment is only necessary when both creep and fatigue are shown to be significant [12].

**Creep is significant** if the sum of the ratios of hold time to maximum allowable time at the reference temperature, for the total number of cycles, is greater than or equal to unity, i.e.

$$\sum_{i=1}^N [t_h/t_m(T_{ref})]_i \geq 1 \quad (9)$$

The values of  $t_m$  depend on material, crack size and temperature [13]. For materials with  $\varepsilon_u \geq 10\%$ ,  $t_m$  is taken to be the time required to achieve an accumulated creep strain of 0.2% at a stress level equal to the reference stress. Alternatively for  $\varepsilon_u < 10\%$ ,  $t_m$  is determined on the basis of a creep strain of  $0.2 \cdot \varepsilon_u$ .

**Fatigue is significant** if cyclic loading influences the development of creep damage. This is likely if the elastic range exceeds the sum of the steady state creep stress and the stress to cause yield at the other extreme of the cycle [12]. Fatigue is also considered significant if the estimated crack growth due to cyclic loading exceeds 10% of the calculated creep crack growth.

### 4.2 Creep-fatigue interaction

When both creep and cyclic loading are shown to be significant, the extent of creep-fatigue interaction should be determined. As a generality, the effect of creep damage on fatigue crack growth rates has little influence on the total crack growth per cycle provided the latter includes an explicit calculation of creep crack growth (i.e. equation (4)). In such circumstances, there is no creep-fatigue interaction and no requirement to enhance fatigue crack growth rates. It is only necessary to consider a creep-fatigue interaction when the effect of cyclic loading on creep is shown to be significant despite fatigue crack growth having been estimated to be only a small fraction of the total crack growth per cycle. For such conditions, the constants in equation (3) should be determined from tests with hold times relevant to the service application being assessed (e.g. [3]).

Similarly, in cases where cracks are propagated by fatigue through material heavily damaged by prior creep, propagation rates are likely to be increased. In these circumstances, a factor should be applied to the fatigue crack growth

constant to account for the amount of prior creep damage. This should be determined experimentally [13].

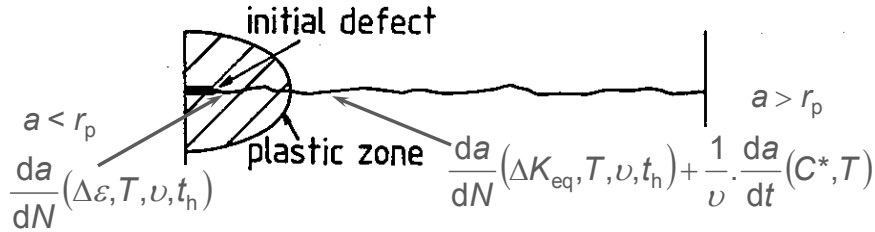


Figure 7. Crack growth regimes requiring Method-I and Method-II assessment approaches.

### 4.3 Assessment methods

The type of cyclic crack growth data required for high temperature defect assessment depends on the size of the defect relative to the cyclic plastic zone at the surface of the component. For cracks larger than the cyclic plastic zone (Figure 7), a power law modified for crack closure is used (e.g. equation (3) in conjunction with equation (4)). This approach is referred to as Method-I in [12]. For small defects embedded in the cyclic plastic zone (Figure 7), a strain based method for the calculation of crack growth is adopted. This approach is referred to as Method-II [12].

The **Method-I** approach is applied when the crack length exceeds the cyclic plastic zone size at the surface of the component (i.e.  $a > r_p$ ). In this regime, the total crack growth per cycle is determined using equation (4), Figure 7. The fatigue crack growth rate is given by equation (3) with the constants modified for hold time effects if creep-fatigue interactions are shown to be significant. If fatigue crack growth is shown to be insignificant, the high temperature defect assessment procedure focuses on the use of equation (4) without  $(da/dN)_F$  [12].

**Method-II** is applied to cracks growing inside the cyclic plastic zone at the component surface when creep is significant (Figure 7). In this regime, a high strain creep-fatigue crack growth law such as equation (7) is used.  $D_C^{surf}$  is the total surface creep damage (taking account of stress state if necessary) accumulated in the appropriate time from every cycle, and is:

$$D_C^{surf} = \sum_{i=1}^N (a_c^{surf})^n \quad (10)$$

where  $d_c^{surf}$  is the creep damage accumulated in the  $j$ th cycle and the summation is carried out over the appropriate time.  $d_c^{surf}$  is evaluated at the surface of the uncracked component, for example by a ductility exhaustion calculation, i.e.

$$(d_c^{surf})_j = \int_0^{t_{hj}} \dot{\epsilon}_c / \bar{\epsilon}_u(\dot{\epsilon}_c) \cdot dt \quad (11)$$

where  $\dot{\epsilon}_c$  is the instantaneous equivalent creep strain rate during the hold time and  $\bar{\epsilon}_u(\dot{\epsilon}_c)$  is the creep ductility at that strain rate, accounting for stress.  $\dot{\epsilon}_c$  is evaluated at the instantaneous stress during the hold time obtained from stress relaxation data.

When  $D_c^{surf} \rightarrow 1$ , equation (7) predicts an infinite crack growth rate. However, this should not be interpreted as predicting failure of the component. This corresponds to the exhaustion of creep ductility at the surface of the component and the instantaneous crack depth,  $a$ , should be set to the depth of the cyclic plastic zone,  $r_p$ . If  $r_p$  is greater than the crack depth that the structure can safely tolerate under service and overload conditions then remedial action should be taken. Cracks deeper than  $r_p$  are subjected to nominally cyclic elastic deformation and the Method-I approach should be followed.

## 5. Concluding remarks

The crack growth rate data used for the defect assessment of high temperature structures has been reviewed.

The material property parameters necessary for the defect assessment of such components subject to creep-fatigue loading can be strongly dependent on the specific operating conditions relating to the practical application under consideration. The rigorous creep-fatigue defect assessment of a component can therefore require a significant investment in the determination of appropriate material property data.

## References

1. Holdsworth, S. R. High temperature fatigue crack growth. In: Marriott, J. B. (Ed.) High Temperature Crack Growth in Steam Turbine Materials. CEC COST Monograph EUR 14678EN, 1994. Pp. 129–176.
2. Dowling, N. E. Crack growth during low cycle fatigue. In: Cyclic Stress-Strain and Plastic Deformation Aspects of Fatigue Crack Growth. ASTM STP 637, 1977. Pp. 97–121.

Defect integrity in components subjected to cyclic loading at high temperatures

3. Holdsworth, S. R. Factors influencing high temperature HSF crack growth rates in turbine casting steels. In: Ainsworth, R. A. & Skelton, R. P. (Eds.). Behaviour of Defects at High Temperatures.ESIS-15. MEP, London, 1993. Pp. 327–349.
4. Holdsworth, S. R. Material data requirements for assessing defect integrity at high temperatures. In: Strang, A. (Ed.). Materials for High Temperature Power Generation and Process Plant Applications. IOM, 2000. Pp. 177–197.
5. Skelton, R. P. & Haigh, J. R. Fatigue crack growth rates and thresholds in steels under oxidising conditions. Mat. Sci. Engng., 1978. Vol. 36, pp. 133–137.
6. Skelton, R. P., Beech, S. M., Holdsworth, S. R., Neate, G. J., Miller, D. A. & Priest, R. H. Round robin tests on creep-fatigue crack growth in a ferritic steel at 550°C. In: Ainsworth, R. A. & Skelton, R. P. (Eds.). Behaviour of Defects at High Temperatures.ESIS-15. MEP, London, 1993. Pp. 299–325.
7. Holdsworth, S. R. Creep-fatigue crack growth from a stress concentration. Materials at High Temperatures, 1998. Vol. 15, No. 2, pp. 111–116.
8. Skelton, R. P. Growth of short cracks during high strain fatigue cycling. In: Low Cycle Fatigue and Life Prediction. ASTM STP 770. ASTM, Philadelphia, 1982. Pp. 337–381.
9. Levailant, C. & Pineau, A. Assessment of high temperature low cycle fatigue life of austenitic stainless steels using intergranular damage as a correlating parameter. In: Ainsworth, R. A. & Skelton, R. P. (Eds.). Behaviour of Defects at High Temperatures.ESIS-15. MEP, London, 1982. Pp. 169–193.
10. Skelton, R. P. Application of small specimen crack growth data to engineering components at high temperatures: A Review. In: Low Cycle Fatigue. ASTM STP 942. ASTM, 1988. Pp. 209–235.
11. Skelton, R. P. Damage factors during high temperature fatigue crack growth. In: Ainsworth, R. A. & Skelton, R. P. (Eds.). Behaviour of Defects at High Temperatures.ESIS-15. MEP, London, 1993. Pp. 191–218.
12. R5, 2003. Assessment procedures for the high temperature response of structures. Procedure R5, Issue 3. British Energy, Gloucester, UK.
13. BS-7910. 1999. Guidance on methods for assessing the acceptability of flaws in metallic structures. British Standards Institution.



# **Life assessment and extension for gas turbine blades**

Pertti Auerkari, Jorma Salonen, Juhani Rantala  
VTT Technical Research Centre of Finland, Espoo, Finland

Sari Mäkinen  
Helsingin Energia, Helsinki, Finland

Ilkka Karvonen, Heikki Tanntari  
Lappeenrannan Energia, Lappeenranta, Finland

Pekka Kangas  
Neste Oil, Kilpilahti, Finland

Jukka Taattola  
FIAF, Tampere, Finland

## **Abstract**

Gas turbine blades operate under severe loading conditions, and for satisfactory service must be designed to withstand multiple damage mechanisms. On the other hand, if the assumptions on the future service are sufficiently conservative or actual service conditions more benign than foreseen, there is potential for blade life extension. This generally does not justify fully omitting intermediate inspections, as intervening damage by e.g. overheating or foreign objects is not excluded, and restoring coatings or other repairs could be needed. Nevertheless, a significant extension to the time of final replacement can be possible. In this work, example cases are used to highlight the technical challenges and results of blade life extension. Such aspects include assessment of in-service stress and temperature histories, interpretation of condition assessment, and materials performance. The example cases refer to ex-service blade samples extracted at the time approximately corresponding to the nominal blade life as defined by the engine supplier. Both land based and aircraft turbines are considered, and in

spite of the differences in design and service profiles, similarities can be pointed out. The results for the example cases generally suggest significant potential for life extension, for reasons related to the case-specific service histories.

## 1. Introduction

For the assumed service conditions, the design of gas turbines largely relies on the available information of type of service, fuels and customer expectations. As the actual service history will only be roughly known and the turbine will be in reality designed for a range of possible service histories, the machine and its major components could have considerable life extension potential if used under less severe conditions than assumed. On the other hand, new turbines tend to be “prototypes” in the sense of including new features even when compared to nominally similar “sister” machines. Also, during long term service some changes can be expected from the new opportunities created by the technical development during the life cycle of the turbine. Therefore, without additional effort the true remaining life of a particular component is not well established when approaching its (nominal) replacement limits. The first (hottest) rows of turbine blades will usually have the shortest cycles of reconditioning and renewal, with frequent priority in life assessment and maintenance. The last blade rows require less frequent attention but will also have a finite life. Although less intricate in geometry than in the first rows, blades of later rows are also not particularly cheap to replace as they are much larger in size than those in the first rows. There may be limited information on design, material and service history, and multiple damage mechanisms can affect the blade life. However, at this stage there is accumulated information on the service history, and also the blade condition can be evaluated in detail [1–3]. This work will review selected example cases on life assessment of ex-service gas turbine blades, particularly when approaching the nominal or suggested life limits. The examples cover different machine types, materials and design traditions, to explore the life extension potential.

## 2. Ex-service turbine blades

Principal features of the four example blade types are shown in Table 1.

Table 1. Features of example blades; eoh = equivalent operating hours.

Case/feature	1	2	3	4
Turbine type	W251	V64.3	F6A	(Aircraft)
Operation	CHP	CHP	CHP	Flights
Time in service	88 000 eoh	109 000 eoh	90 000 eoh	2 300 eoh
Row/no. of rows	2/3	4/4	3/3	1/2
Blade material	Udimet 500	Udimet 720 <sup>1)</sup>	GTD 111	Nimonic
Coating	None	None	Chromized	Aluminized
Cooling	No	No	No <sup>2)</sup>	Air

1) contradicting OEM documentation; 2) air cooling in blade root only

One to two blades from each turbine were sacrificed for detailed assessment. For reasonably conservative conclusions, sampling aimed to select blades that were dimensionally typical but otherwise by visual and other non-destructive inspection among the worst blades within each blade set.

### 3. Methods of assessment

The sample blades were subjected to non-destructive testing (NDT) including visual (VT), stereo microscopy, fluorescent penetrant inspection (FPI) and eddy current (ET) methods, to detect surface cracks or comparable defects. Surface roughness was measured with contacting line profiling for blade cases 1–3. The blades were sectioned to assess the internal condition, typically at the blade root, at 55–60% of the airfoil length, i.e. in the hottest region estimated from external colouring, and close to the tip of the blade. The sections were inspected by light optical and scanning electron microscopy (SEM). X-ray spectrum analysis and EDS were used for chemical analysis. The materials properties, like the as-new mechanical strength at the operating temperatures, were obtained for the case 1 blade (U500) from [4] and for case 2 blade (U720) from the materials database of TU Darmstadt [5]. For case 3, GTD 111 properties were assumed to comply with those included in [1]. For case 4, short term creep testing at 950°C and a selected test stress was used to support the assessment through comparison with the performance of new material. The blade and material condition was assumed to be sufficiently described by the service history, observations in the non-destructive and microstructural assessments, and other available information on

the blades and their damage. Life assessment was mainly based on simple life fraction (creep and fatigue) analyses on the results, although the likely impact of other potential damage mechanisms was also assessed.

## 4. Results

An overview of the results of non-destructive inspections and other surface assessment of the blades is shown in Table 2.

Comparison of ex-service and as-new (when available) blades showed that the differences between individual blades were sufficiently large to mask any possible systematic in-service change in the blade dimensions. Nevertheless, no obvious strain or distortion was observed in any of the blades. The chemical analysis of the blade materials confirmed the expected compositions. In general, most extensive service-related changes in the aerofoil cross-sections appear at or close to the leading and trailing edges. The observed features reflect the influence of the flue gas temperature, and in cool regions possibly also of the heat treatments.

Table 2. Observations in NDT and surface assessment of the blade cases.

Feature/case	Case 1	Case 2	Case 3	Case 4
Surface colour	Dark grey	Light greenish	Light grey	Blackish
Cracks <sup>1)</sup>	None (FPI, ET)	None (FPI, ET)	None (FPI, ET)	None (VT)
Roughness <sup>2)</sup>	Ra < 6 µm	Ra < 5 µm	Ra < 4 µm	-
Impact size <sup>3)</sup>	Max 1 mm	Max 0.5 mm	Max 0.5 mm	-
Tip condition	Modest wear	Small dent	Modest wear	Modest wear

1) As indicated in NDT; 2) surface at leading edge; 3) impacted particles

Where more than one blade was sectioned (cases 2 and 3), there was very little difference between the sample blades. No clearly defective features related to e.g. fabrication were observed in the blades or their inspected sections. Examples of the cross-section microstructures at the hot section of the case 3 blade airfoil are shown in Figures 2 and 3. The evaluated thickness of degraded surface and the mean size of the gamma' particles are summarised in Table 3.

Table 3. Features observed from the hot airfoil and root sections.

Feature	Case 1	Case 2	Case 3	Case 4
Surface layer <sup>1)</sup>	≤ 0.1 / 0.3 mm	≤ 0.1 / 0.2 mm	≤ 0.1 / 0.2 mm	< 0.05 mm
Size of $\gamma'$ <sup>2)</sup>	0.25 / 0.20 $\mu\text{m}$	0.3–0.4 $\mu\text{m}$ <sup>3)</sup>	Double peak <sup>3)</sup>	-

1) Oxidised + transformed material on leading/trailing edge, hot sections

2) Mean size, hot section / fir tree (root section)

3) As in the root section or otherwise in practically as-new state

Using the classical model for thermally activated coarsening of second phase particles ( $\gamma'$ ) with a radius growing from  $r_0$  to  $r$ :

$$r^3 - r_0^3 = \frac{B \cdot t}{T} \cdot \exp\left(-\frac{Q}{RT}\right) \quad (1)$$

where  $t$  is time,  $T$  absolute temperature,  $Q$  the apparent activation energy of coarsening,  $R$  the gas constant and  $B$  a material-dependent constant [1, 6]. From known time of exposure  $t$ , characteristic (mean) particle radius  $r$  and material specific constants  $Q$  and  $B$ , the effective temperature  $T$  can be solved, provided that there is sufficient change in  $r$ .

Comparison of the microstructures at the hot airfoil cross-section and at the blade root regions shows the extent of thermal coarsening that has taken place in the airfoil (Table 3). Applying the equation (1) on the  $\gamma'$  particles with the mean size from the aerofoil section as  $r$  and that from the root section as  $r_0$ , the resulting estimate of the effective material temperature at the hot section is obtained and shown in Table 4. For the blades of case 2, the microstructure at the 60% cross-section of the aerofoil showed no significant change between the airfoil and root section materials, indicating that the low service temperature has rendered the approach based on particle coarsening inapplicable. Therefore, the estimate of the blade material temperature was based on the measured flue gas inlet and outlet temperatures that must limit the temperatures of uncooled blades. For the blades of case 3, the microstructure of the airfoil cross-section showed only small differences between blade samples at equivalent sections, and in all airfoil sections the original two-peak size distribution and other as-new features of the  $\gamma'$  particles were still clearly observable. Again, the differences in particle coarsening were judged inadequate for assessing the effective material temperatures, the estimates of the blade material temperatures were based on the flue gas inlet and outlet temperatures.

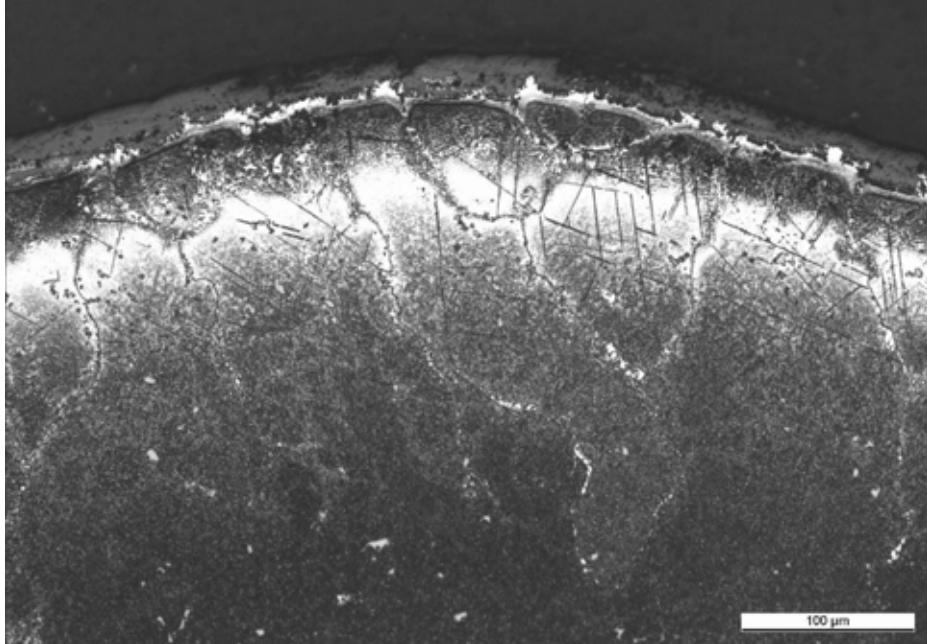


Figure 1. Cross-section of the airfoil leading edge (case 3).

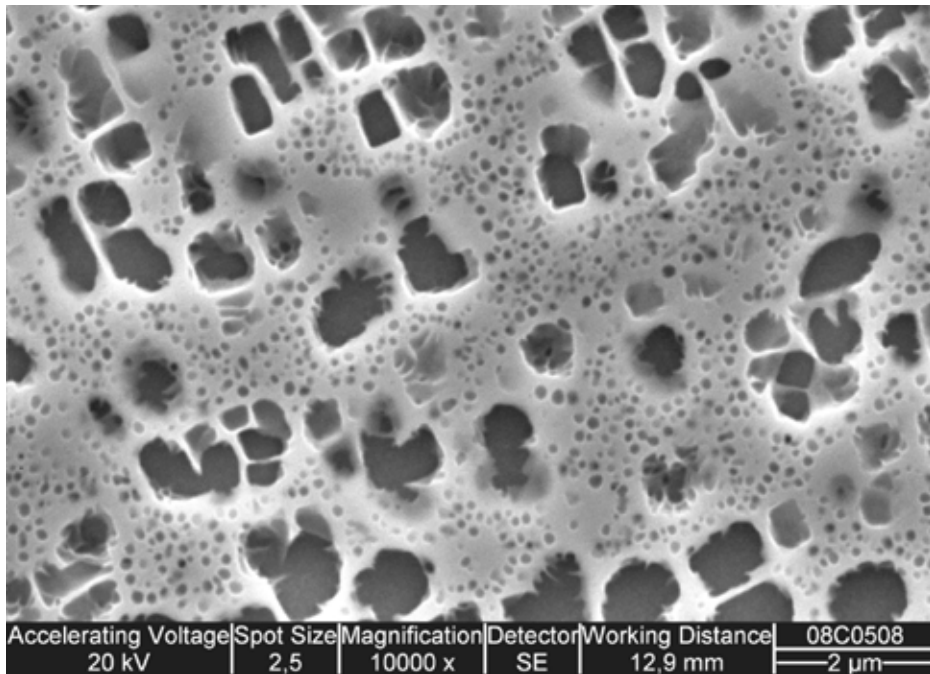


Figure 2. Blade microstructure, hot cross-section of the airfoil (case 3).

Table 4. Estimated maximum temperatures at the blade hot sections.

Feature	Case 1	Case 2	Case 3	Case 4
Location	60% lead edge	60% lead edge	55% lead edge	(Hot airfoil)
Max temp	765°C	≤ 600°C	≤ 700°C	< 900°C
Est. from	γ <sup>i</sup> coarsening	Flue gas temp	Flue gas temp	User info

Under steady base load service, the static tensile stress from the centrifugal mass loads of the blade may dominate. This stress at a blade radius  $r$  [2, 4]

$$\sigma_z = \frac{\rho \cdot \omega^2}{A} \cdot \int_r^{ra} A \cdot r \cdot dr \quad (2)$$

where  $ra$  is the tip radius of the blade,  $A$  the airfoil cross-section area at radius  $r$ ,  $\omega$  the angular velocity and  $\rho$  density of the blade material. As the level of this stress increases towards the root of the aerofoil, and material becomes weaker towards the location of the maximum temperature, it is the combined influence of mechanical loading and temperature-dependent material strength that determines the location of critical position along the airfoil. To account for the impact of the additional stress components and other uncertainties, a safe side approach could use a stress assessed for a cross-section towards the root of the airfoil and a temperature assessed for a location closer to the observed maximum. The estimates of the static stress levels are summarised in Table 5.

Table 5. Estimated static stress levels at the blade cross-sections of interest.

Feature	Case 1	Case 2	Case 3	Case 4
Rpm	4 918	5 400	5 150	-
Location	60%/root	60%/root	55%/root	Min. section
Stress <sup>1)</sup>	138/184 MPa	- /321 MPa	216/357 MPa	94 MPa <sup>2)</sup>

1) static, at the selected hot section / root of the airfoil; 2) test stress

## 5. Discussion

When evaluating the results from inspections, other measurements and assessments, it is important to consider all potential damage mechanisms that could significantly influence the blade life. Such an overview of the blade condition is shown in Table 6 for the example cases.

Table 6. Estimated impact of the potential damage mechanisms on the example blades.

<b>Mechanism</b>	<b>Case 1</b>	<b>Case 2</b>	<b>Case 3</b>	<b>Case 4</b>
Overheating	Minor	None	None	Minor
Overloading	None	None	None	None
Wear/erosion	Minor	Minor	Minor	Minor
FOD <sup>1)</sup>	Minor	Minor	Minor	Minor
Corrosion	None	None	None	None
Oxidation	Modest	Minor	Modest	Modest
Embrittlement	Minor	None	None	Minor
Fatigue <sup>2)</sup>	Minor	Minor <sup>2)</sup>	Minor <sup>2)</sup>	Modest
Creep <sup>3)</sup>	Life limiting	Minimal	Minimal <sup>3)</sup>	Life limiting

1) FOD = Foreign object damage

2) Potential lead mechanism for cases 2 and 3

3) Hot sections / high temperatures only

In general, only few indications of degradation were observed, mainly some modest oxidation, wear and impact traces on the blade surfaces, and some coarsening of the gamma' microstructure at the hot section, particularly in case 1 blade. Based on the evidence, it was judged likely that creep could be the life limiting damage mechanism for case 1 and 4 blades, and fatigue for case 2 and case 3 blades, although there was as yet no evidence of progressing fatigue damage or cracking. This would only apply if no short term mechanisms like foreign object damage (FOD), overheating or overloading, did not intervene. For the blades of case 2, it is also possible that attachment clearances and fretting can require mitigating action. The outcome of the resulting life assessment is summarised in Table 7, and for cases 1–3 in Figure 3.



Table 7. Comparison of the blade cases including the predicted safe additional life.

<b>Issue/prediction</b>	<b>Case 1</b>	<b>Case 2</b>	<b>Case 3</b>	<b>Case 4</b>
Location	60% / root	60% / root	55% / root	Airfoil
Lead mechanism	Creep	Fatigue?	Fatigue?	Creep
Added life	25 000 h	> 100 000 h	90 000 h	~2 000 h

The predicted residual life appears considerable in all cases, suggesting that the example blades can allow further operation while replacement had been recommended by OEM or the maintenance service provider. Particularly in cases where the operating temperature is low, the impact from most potential damage mechanisms seems to be modest or minimal after reaching the nominal (recommended) service life. Inversely, increasing temperatures will boost the rate of life consumption through several damage mechanisms. It is also to be remembered that the operator, control system and the maintenance procedures must remain alert to short term events and mechanisms that could intervene and in the worst case terminate the blade life abruptly. For example, overheating, verloading, foreign or internal objects, or control failure could result in dramatic loss of the residual life.

Nevertheless, the results from the example cases suggest significant potential for life extension and related savings, when the service conditions are not too severe. The benefits from base load operation, clean natural gas firing, and proper maintenance are likely to guarantee such benefits. The opposite may be true for new cheap fuels, increased cycling in service, and less vigilant attitudes towards operation and maintenance.

## 6. Summary

Four example cases of ex-service gas turbine blades have been subjected to life assessment at or close to the nominal or suggested life limit. The examples cover a range of machine types, materials, designs and service conditions with foreseen interest and potential in life extension.

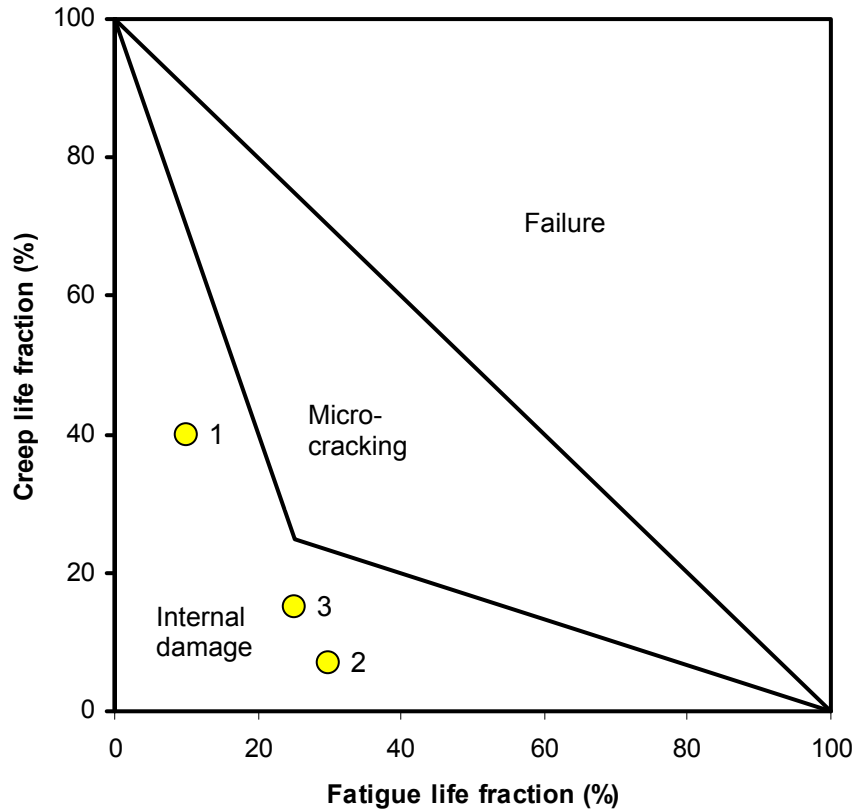


Figure 3. Approximate position of the blade cases 1–3 on a creep-fatigue life fraction map.

The results suggest that the life of the example blades can be significantly extended from the nominal or recommended limits in all cases. For land-based turbines, the likely reasons for the positive outcome include base load operation, clean natural gas fuel, modest operating temperatures, and relatively conservative design for these blades. In case of the aircraft turbine example, additional experimental support was needed to confirm the life extension potential. However, life extension will also require that to avoid intervening damage or cracking, proper condition monitoring, inspection and maintenance programs must be continued. Some vigilance is needed to monitor the progress of multiple damage mechanisms and their combinations that can threaten the blade life. This would be particularly important if the operational conditions were to be modified, e.g. by becoming more cyclic in future.

## Acknowledgement

This work was a part of the European COST 538 project, and the national project LC-Power/LifePower. The authors wish to acknowledge the financial and technical support by the Finnish Funding Agency for Technology and Innovation (Tekes), the national industry group of the projects, and VTT. The expert technical help by Alfred Scholz (TU Darmstadt, Germany) and Erica Vacchieri (Ansaldo Recherche, Italy) in the COST 538 project is also much appreciated.

## References

1. Viswanathan, R. Damage mechanisms and life assessment of high-temperature components. ASM International, 1989. 497 p.
2. Reed, R. C. Superalloys – fundamentals and applications. Cambridge University Press, 2006. 372 p.
3. Bohl, W. Strömungsmaschinen 2 – Berechnung und Kalkulation. Würzburg, Vogel Buchverlag, 2005. 286 p.
4. NRIM Creep Data Sheet 34B. NRIM, Tokyo, 1993. 62 p.
5. Auerkari, P., Salonen, J., Scholz, A. & Vacchieri, E. Intermediate report of COST 538 project, 2007. 8 p.
6. Auerkari, P., Salonen, J., Gustafsson, T. E., Karvonen, I., Tanttari, H. & Mäkinen, S. Evaluation of the operating conditions of gas turbine blades and vanes after long term service. Baltica VII – Life Management and Maintenance for Power Plants, Helsinki–Stockholm 12–14 June, 2007. VTT Symposium 247, Vol. 2, pp. 25–34.

# Fire incidents in underground coal storage

Juha Sipilä and Pertti Auerkari\*

Helsingin Energia, Helsinki, Finland

\*VTT Technical Research Centre of Finland

Espoo, Finland

## Abstract

Autoignition of coal in underground storage facilities is reviewed in the light of recent incidents of smouldering fires. The opportunities to prevent and extinguish closed-space fires are also considered considering the efficiency of the available alternatives. The challenges of such fires are highlighted by an example case, describing the observations and outcome of a smouldering coal storage fire. The principles of self-heating and most critical factors in spontaneous combustion such as the condition and quality of coal are fairly well known, but usually only provide partial help in fire prevention. The experience suggests that nitrogen injection can be useful for extinguishing controllable fires, while more extensive measures may be needed against uncontrolled fires. In general, efficient fire extinction during plant operation can be challenging, as any air ingress tends to feed the fire. Methods and indicators for predicting and detecting the ignition are discussed, and improvements are suggested to enhance the storage and plant availability. Also, new experience on dealing with frozen coal is discussed in brief.

## 1. Introduction: coal storage fires

Likelihood of autoignition, or self-initiated fire of coal without external heat source, depends partly on the coal properties (Tables 1 and 2). Also, the boundaries of coal from different origins tend to show increased sensitivity to autoignition in storage. This will not happen without oxygen, but air ingress is

often difficult to exclude. The heat from oxidation increases the local temperature and the reaction rate. Warm coal when entering storage will reduce the heating step to autoignition. Also, fractionation in transport and entrance to the storage, and leakage water may create air channels for easier oxidation. Mainly bituminous coals are considered here (Table 1).

Coal oxidation is slow, when temperature is below about 40–50°C. From about 50–80°C the reaction rate can remain relatively steady but is able to remove humidity. At still higher temperatures the reaction rate progressively increases, and finally at about 200–250°C, self-sustaining combustion can be expected. However, a layer of coal can be an effective obstacle for heat transfer, and then the critical temperature for self-sustained reaction can be 70–80°C for bituminous coal [1–3]. The factors affecting autoignition are described in brief in Table 2. Depending on coal type, the likelihood of such ignition is highest about 3–6 months after entering storage. Uncompacted coal containing coarse particles can ignite within 1 to 1.5 months. Complete oxidation of coal carbon to carbon dioxide will produce 252–504 kJ/mol of thermal energy. The oxidation rate of coal increases approximately by a factor of ten when temperature rises from 30°C to 100°C. The rate is reduced during oxidation that will form a partly protective (absorbed) layer on the coal particles. The final gaseous oxidation products are typically released as carbon dioxide, carbon monoxide and water or steam [4, 5].

Table 1. Typical ranges of properties for coal used in pulverised coal firing.

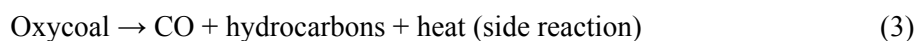
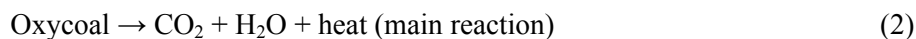
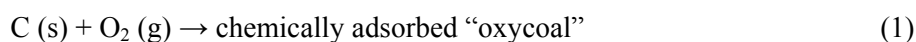
Property	Typical range	Notes
Water content	8–12%	-
Ash content	10–20%	Residual minerals etc. (unburnt fraction)
Volatiles	27–36%	E.g. hydrocarbons
Sulphur content	0.2–1.2%	Depends on local acceptance & cleaning system
Particle size	0–50 mm	As-delivered and in storage before coal mills
Heating value	~ 25 000 kJ/kg	Approximate basis level
Hardgrove index	0–90	Describes ease of crushing e.g. in coal mills

## Fire incidents in underground coal storage

Table 2. Factors affecting coal autoignition; V/A = volume to surface area ratio.

Factor	Effect on autoignition	Notes
Coal rank	Lower rank – easier autoignition	E.g. safer with anthracite
Petrography	High liptinite – easier autoignition	High inertite – less autoignition
Volatiles	More volatiles – easier ignition	Usually lower rank = more volatiles
Methane	More methane – reduced oxidation	No ambient oxidation at > 8 m <sup>3</sup> /t
Porosity	High porosity – easier autoignition	Lower thermal conductivity
Particle size	Small size – easier autoignition	Same V/A → similar ignition temp.
Water content	High content – easier autoignition	Easiest for large particles, young coal
Ash/minerals	High alkalis – easier oxidation	Ash, borates, CaCl <sub>2</sub> – less oxidation
Pyrite content	High content – easier autoignition	Significant only when > 2% pyrite

The oxidation process of solid coal can be divided into partial reactions:



The reaction (1) takes place at low temperatures, below 80°C. The reactions (2) and (3) are providing heat (33.4–35.1 MJ/kg) for autoignition, if sufficient amount of air is available and heating can be maintained to sustain the reactions. In addition to the fire risk, the adverse effects of oxidation include reduction of the heating value of the stored coal. With sustained heating the oxidising reaction can be intensive enough to maintain the fire, while opening and spreading the burning coal may result in cooling and self-extinction (Figure 1).



Figure 1. Digging out an open storage coal fire to spreading it for self-extinction.

The underground coal storage at the Salmisaari CHP power plant has been operational since 2004, and replaces the earlier above-ground storage. The storage has a total capacity of 250 000 tons, which corresponds to about half of the yearly fuel consumption of the plant. The storage consists of four silos,  $\varnothing$  40 m  $\times$  65 m each, with the silo bottom at a depth of -120 m (Figure 2). During the relatively short operational history, smouldering fires have occurred in the silos.

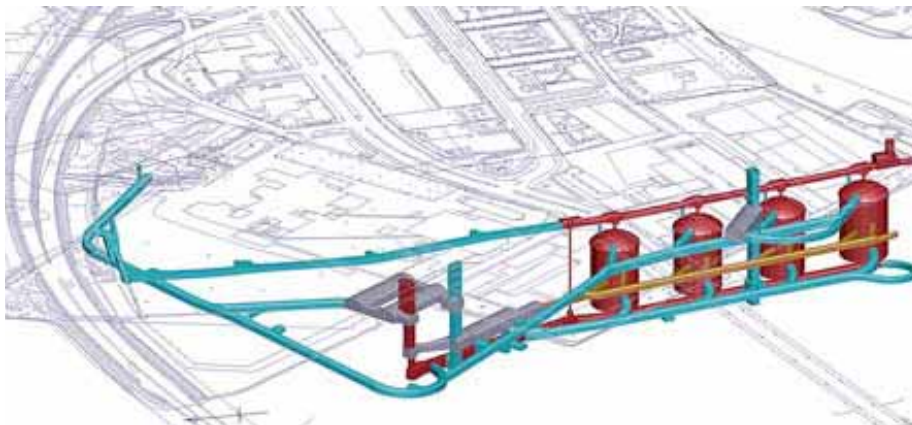


Figure 2. The underground coal storage at Salmisaari power plant.

Coal is discharged from the silos to the boiler plant on horizontal and vertical conveyors. These are critical components with maximum allowable operating temperature of 70°C; the delivery time of a new vertical conveyor is about 8 months. During yearly maintenance periods the plant may be out of service for the summer months. During this time the stored coal cannot be simply burned in the boiler, which is otherwise common way to discard heated batches of coal.

## **2. Detecting coal ignition and fires**

There are several (non-standard) methods to predict how likely self-heating and autoignition are for a given coal type [6, 7]. These methods typically take into account e.g. dry ash-free oxygen content, oxygen-carbon ratio, time of adiabatic heating to a given limit temperature, and content of inherent water and volatiles. The ignition can be detected from burning odours (coal tar and phenols), brown smoke, emerging gases and increasing temperature. A reasonable goal is an alarm of the elevated fire risk before attaining the critical temperature of 70–80°C. A fully safe storage requires that even local temperatures are not rising above 40°C. Symptoms of coal bed heating have been listed in Table 3. Self-heating of coal can be indicated by monitoring the gaseous reaction products that will emerge sequentially, with general stages of autoignition as shown in Figure 3. Normal carbon dioxide content in air (about 390 ppm) can be high enough to disturb early detection of coal oxidation, but carbon monoxide concentration is a more sensitive indicator. Carbon monoxide is a combustible gas that can spread evenly in air, and dangerous to humans at 30–300 ppm concentration depending on time of exposure. Significant amounts of CO are already formed at about 50°C, with rapid increase when approaching the critical regime of 70–80°C. Other gaseous products like methane and hydrogen are only produced in notable amounts above 100–150°C. These gases together with ethane, propylene and coal dust are also potential sources of explosions.



Table 3. Symptoms and indications of heating in a coal storage

Temperature	Indications	Notes
40°C	Limit temperature for autoignition	Safe storage below this limit
50°C	Acceleration of self-heating	Still relatively slow heating
60°C	Steam formation, burnt coal odour	—
> 60°C	Development of autoignition	Heating to ignition point expected
70–80°C	Alarm of autoignition	Elevated fire risk

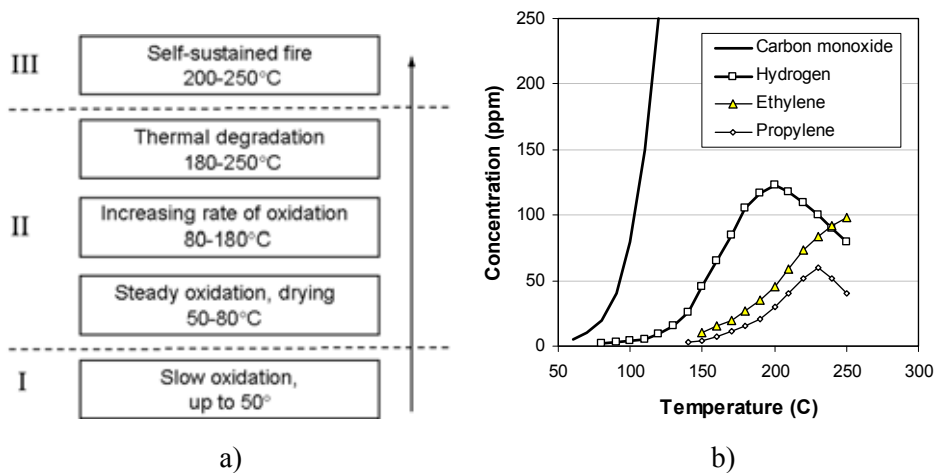


Figure 3. a) Stages in autoignition of coal; b) development of gaseous reaction products at low temperature oxidation of coal (adapted from [2, 3]).

For wide free areas of coal surface, thermal cameras can be used to determine the surface temperature gradients, and then to apply thermocouple sensors for more detailed information. Continuous temperature measurement of coal entering storage can be arranged from an even coal flow on belt conveyors. Any heated coal can be directed either to combustion or to a short-term storage with enhanced monitoring and prevention systems. On coal entering storage directly from ship, differences up to about 20°C have been shown in the same coal batch [1].

Measuring highest local temperatures for hot spots in the main storage is more difficult, although they are most likely to appear within 1–3 m from the surface providing air access. A sufficiently dense network of sensors can be a challenge in underground silos, and surface measurements may be too late to indicate deep hot

spots. Somewhat deeper measurements can be made using thermocouples attached to lances that are pushed through the surface layers (1–3 m) of the stored coal.

For analysing gas compositions to detect fires early, sufficient sensitivity to carbon monoxide and oxygen content must be available, with supporting information on the CO<sub>2</sub> content. Measurements of methane and hydrogen concentrations do not provide early information on coal heating, but should be available for assessment of the risk of dust (or hybrid) explosion. Increasing methane and hydrogen concentrations indicate a further extended stage of the fire as these gases appear at higher temperatures. Odour analysers could indicate an initiating fire even earlier than traditional CO and smoke sensors.

### **3. Approaches to coal fire prevention**

At early stages a fire can be prevented by cutting it off from access to oxygen. This is only possible in storage facilities that can be closed and sealed to interrupt the air flow. On the other hand, adding air flow by ventilation can remove the heat that is being produced by the oxidation process. In underground rock storage such advantages are unlikely, but efficient ventilation is needed for human access. Evaporation of water from the coal surface requires heat and this is taken from the coal. This will cool the coal bed, and increasing air flow for ventilation will lead to coal cooling and drying, in the best case increasing the heating value of coal.

The oxidation reaction can be stopped by preventing oxygen access so that air oxygen is replaced by an inert gas, such as nitrogen or carbon dioxide. For fire extinction, in practice the oxygen content must not be above 4%. The auto-ignition risk can be in principle reduced by ensuring that there are no other fire or heat sources in the vicinity, and that the storage is dry and clean. Emergency transfer of coal must be made possible, and no already heated coal should be brought to the storage. Coals with highly differing qualities and grain sizes should be stored separately, and strongly self-heating coals should be used first [9].

An explosion can occur in flammable gases like methane, CO, hydrogen and light hydrocarbons, in coal dust, or both together (hybrid explosion). Coal dust can ignite as a suspended dust bed in air, or as a precipitated dust layer, with differences in the igniting reactions. The igniting energy can be provided by a spark or even human static discharge.

Methane originates from coal deposits and can also be formed as a consequence of self-heating. Methane can explode at concentrations of 5–15% in

the presence of oxygen content higher than 12.4%. Typical coal dust with a mean particle size of 60  $\mu\text{m}$  can explode at concentrations of 40–5 000  $\text{g}/\text{m}^3$ , when oxygen content is at least 12%, at ignition energy below 10 mJ. For prevention, formation of coal dust can be controlled by appropriate process design. With typical water content of crushed coal of about 8–12% the amount of dust remains small. When necessary, water content can be increased e.g. on the conveyor belt in transport, and the effect can be enhanced by additives that lower surface tension. The explosion risk from methane can be much reduced by making the storage space inert immediately when the methane content increases to above 1%. The explosion hazard can also be reduced by monitoring CO content and starting the inert gas injection before significant methane formation. This approach could stop the autoignition process at the early stages before temperature can rise to the critical regime [2, 4].

#### **4. Fire control and extinction**

The process and spreading of fire requires fuel, oxygen and heat. Removal of any of these elements will end the fire. Extinction of coal fires in underground (or other closed space) storage is based nearly without exception on replacement of air (oxygen) by an inert gas [8, 10].

Carbon dioxide is not widely used for extinguishing coal fires because of the Boudouard reaction where carbon (coal) at high temperatures will reduce a part of carbon dioxide to flammable and toxic carbon monoxide. However, carbon dioxide is otherwise an efficient agent to extinguish fires and is applied as an extinguishing (flue) gas component. Nitrogen is easily available in liquid and gaseous form, and can be transported to fire sites in large quantities. If needed, nitrogen can also be produced locally using a nitrogen generator (pressure swing absorption or PSA equipment). Figure 4 shows nitrogen application at the Salmisaari power plant. Nitrogen is cold, dry and practically non-reactive in fire extinction, generally acceptable from safety point of view, and it can be evaporated from liquid phase up to 300  $\text{m}^3/\text{min}$ . Nitrogen is somewhat inconvenient to store for long periods, and can only be led to the silos with purpose-built pipelines. Nitrogen is cheaper (and more easily available) than  $\text{CO}_2$  but more expensive than GCP [8].

Gaseous combustion products (GCP) or flue gases mostly consist of nitrogen together with carbon dioxide. GCPs generally have low oxygen content (0–3%), and they are quite cost effective as GCPs can be made at the site at rates up to

Fire incidents in underground coal storage

1 800 m<sup>3</sup>/min. One potential limitation is the included steam that could produce flammable CO and hydrogen gas. Table 4 is comparing different inert gas systems for fire extinction. Sealing off can also be an effective approach for preventing or reducing oxygen access to a coal fire. Fly ash of coal fired plants mixed with water ( $\geq 1:1$  by weight) is a cost effective, easily available and well performing sealing material against oxygen ingress.

Table 4. Characteristics of selected inert gas fire extinguishing systems [1].

System	Flue gas generator <sup>1)</sup>	Jet blast <sup>2)</sup>	N <sub>2</sub> generator <sup>3)</sup>
Output	0.5 m <sup>3</sup> /s	7–30 m <sup>3</sup> /s	0.001–5.0 m <sup>3</sup> /s
Exit temperature	54°C	85°C	Ambient
Oxygen	2%	0.5–1.6%	0–3%
Nitrogen	82–84%	80–85%	97–100%
CO <sub>2</sub>	14–15%	13–16%	-
CO	0–15 ppm	3 ppm-0.4%	-
Steam	1.2%	1–2%	-
Water droplets	n/a	Can be abundant	-

1) Tomlinson boiler 2) e.g. Steamexfire or GAG 3) e.g. evaporators or pressure swing absorption



Figure 4. Nitrogen injection at the Salmisaari power station.

## 5. Case 1: smouldering fire in 2008

The case involves a smouldering fire in the Salmisaari underground coal storage in 2008, lasting for four months. The fire was first indicated by elevated CO levels 15th September in the silo no. 4, suggesting autoignition. This silo mainly contained Russian low sulphur coal, with an about one meter layer of old Polish coal at the bottom. Extinguishing measures were started by using nitrogen, but the effort was not fully successful before discharging the silo completely. Thermal images showed two hot spots on the silo surfaces, one next to a maintenance door and another on nearly opposite side of the silo. At the time of thermal imaging the fire status had already improved and the coal surface level was only at a height of 6.3 m. At discharging, relatively strong steam flow was observed next to the bottom maintenance door and the concrete wall [1].

Complaints from the inhabitants living in the vicinity of the plant were received, mainly about flue gas fan noise and smell of hydrogen sulphide. The inhabitants were asked to close doors and windows and wait for further instructions. At the early stages of the fire, the fire alarm was followed by a national level radio notification that turned out to be unnecessary. The complaints and general alarm were naturally not considered good for the public image of the plant.

No production limits were introduced during the incident, although personnel traffic in the storage was only allowed with oxygen breathing support. The completed fire extinguishing by alternate nitrogen filling and coal discharge took about 4 months. At the time of discharge coal was often heated but a thin layer of cool coal from another silo was used to protect the conveyor belt. Also, the belt was watered if hot coal was detected coming out of the silo. The water flow was sufficient to prevent significant formation of explosive gas mixtures.

The provider of the belt conveyor had noted that the rubber belt starts to harden at temperatures exceeding 70°C. Visual inspection of the belt conveyor showed no obvious damage. Rubber hardening is expected to shorten belt life, but although hardening cannot be excluded, it has not been confirmed.

Cracking and spalling of the sprayed concrete in the silo wall was observed on an area of about 2 500 m<sup>2</sup>, which is about one third of the silo wall area in contact with coal when the silo is full. An estimated temperature difference of about 120°C in the adjoining layers is enough to spall the porous sprayed concrete of the rock surface. Such a temperature difference is thought to arise already if the heated flue gas from the fire finds a channel along the silo walls or drains, i.e. the fire

does not need to touch the wall. The observed 20–30 mm wide cracks in a 120 mm thick fibre reinforced concrete suggest heavy thermal loads. The damage at the maintenance door at the silo bottom indicated that the smouldering fire occurred close to it (Figure 5). Partly burnt coal, ash and hard slag around the door opening suggest that this door provided air ingress during the fire. Also, several hollow areas with ash inside, indicated local fire against the silo wall. During fire the measured surface temperature was 50°C at the 1.1 m thick concrete wall, and 350°C on the steel door. This was hot enough to damage the fire seal of the door. The concrete surfaces near the silo also suffered damage near the discharge cone, at the nitrogen injection tubes and in the ceiling of the silo. Furthermore, the bellows of the discharge cone had nearly completely burnt away, resulting in additional ingress of air during the fire. The future improvement should aim to detect similar ignition earlier. There are studies suggesting that the smouldering fires (with indicative levels of gaseous reaction products) may extend quite slowly towards the upper surfaces and therefore real fires in silos may become extensive before being detected. The silos should be maintained in a condition that allows full discharging. More importantly, air tightness of the silos must be improved, and such action has been taken e.g. by sealing the maintenance door at the bottom of the silos. In addition, the density of nitrogen tubing should be increased in the silos, and an improved nitrogen system appears preferable at the discharge cones. Proper selection of coal that will be stored in the silos remains important. The causes and consequences of autoignition and fires in the underground coal storage, with simplified aspects of mitigation, are outlined in Figure 6.



Figure 5. Post-fire inside appearance of the bottom maintenance door opening [1].

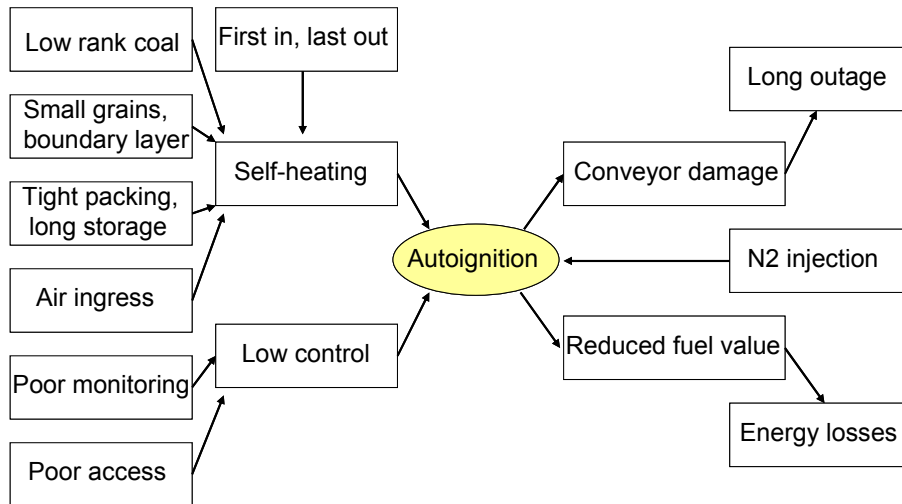


Figure 6. Causes and consequences of autoignition in underground coal storage, with mitigation (simplified); note that reduced access is also limiting efficiency of mitigation.

## 6. Case 2: challenge by cold coal

The first case was about problems that may occur with heated coal. An unexpected new challenge has been too cold frozen coal, when in February 2010 low sulphur Russian coal was received as 17 000 ton shiploads and stored into the silos 1 and 2. This coal was mined in Siberia (perhaps at  $-50^{\circ}\text{C}$ ) and transported first by rail to an intermediate storage in Vysotsk harbour (near Viborg), then by ship to Helsinki (Salmisaari) and finally (after crushing) by conveyors to the storage silos. At the time of offloading from ship, the temperature in Helsinki was about  $-15^{\circ}\text{C}$ . Because of relatively cold winter, coal was apparently frozen from the mine to the silos, and did not thaw even in the intermediate storage. The offloading was otherwise as usual but the deep frozen coal formed abundant dust that was colouring the nearby sea ice black. Offloading was also slow, because the coal batch in the ship was frozed solid and contained abundant impurities like wood and steel that frequently stopped the crusher conveyor.

When discharging the same coal from the silos, it was found to include ice blocks with variable amounts of coal in them. As such blocks were not introduced into the silos after coal crushing, this ice was apparently forming

from the groundwater seeping into the silos. During discharging from the silos, attempts were made to thaw the frozen coal from below by using electric heaters. In case of ice blockage at the discharge cone, automatic weighing control reacts by increasing the rate of coal discharge to maximum, so that uneven and at times a large amount of coal and ice was falling to the conveyor belt. A part of this fell on the floor, but the icy chunks on the conveyor belt could also cause yet another blockage at the discharge station of the next silo when the chunks were too large to pass through. Such a blockage swept the coal from the conveyor belt to the floor, so that both the blockages by ice chunks and the fallen coal required frequent manual clearing. As a result of blockages, not enough coal could be discharged from the silos 1 and 2, and manual clearing and cleaning work was required 24 h a day.

If frozen water can expand within the silo walls (leak water drains), freezing damage of the silo walls is possible although such a risk was considered small in this case. Thawing of frozen coal in the storage silos will take a long time, as the temperature in the silos is relatively low (+10...14°C), and the total mass of coal very large, with low thermal conductivity. External heating by e.g. steam has been considered but must be introduced with caution to avoid coal ignition.

Of the other silos at the time, no. 3 was out of service due to maintenance work that was estimated to take several weeks, and silo no 4 only contained a small amount of Polish coal corresponding to about 1–2 days consumption of the plant. Reserve fuel of the plant is heavy fuel oil that could not be pumped out of its storage tank due to low temperature (high viscosity). This was because the water based heating circulation did not work properly, apparently because its channels were blocked by falling rocks. To nevertheless operate the plant, four trucks were continuously transporting additional coal from Hanasaari (about 5 km away) to Salmisaari, so that the Salmisaari plant could be operated at more or less full rating. The situation was relieved at the end of February, after receiving a shipload of unfrozen Polish coal to the silo no. 4.

This already suggests future measures to avoid the problem with too cold coal: frozen coal batches should not be introduced to the storage, especially not to all operating silos in the same time, and the groundwater drainage of the storage could be better. Assuming gradually warming climate, the frozen coal problem may in any case fade away in future, if harsh winters like the one in 2010 will become increasingly uncommon.



## 7. Conclusions and recommendations

The closed space character of the underground silo storage has brought added emerging risk that is not comparable to that for above-ground open storage. There is no unique standard to predict the autoignition potential of given type of coal, even for open storage. The example case of the underground storage fire had one of the root causes in air leakage through the maintenance door frame at the silo bottom. As the fire was limited to the vicinity of this door, it is believed that similar events are reduced or prevented by gas tight sealing.

Some self-heating in the storage will probably occasionally occur, with sufficiently high temperatures for re-ignition. To reduce or avoid autoignition events, selecting and maintaining proper grade, grain size and temperature of the stored coal remains important. Complete air tightness may not be possible when discharging the silos but should be aimed at towards the lower parts of the silos. The condition of the storage will be continuously monitored at multiple sites using thermocouples and gas indicators. Nitrogen has been successfully used for extinguishing smouldering fires, but this can take a long time to complete when the silo is being used. From the consequences point of view, in the worst case the fire will damage the main conveyors, disabling the storage and the power plant during the critical winter months. The future monitoring systems must be compatible with the process control and sufficiently tolerant to the operational environment, to withstand corrosion, dust and humidity without requiring regular maintenance in the storage.

Unlike heated coal that in principle is only an enhanced problem in closed space storage, unexpected new trouble has occurred with too cold coal in the same storage. Compounded in this case by groundwater seepage to the storage, unavailability of coal from adjacent silos and unavailability of the alternative reserve fuel, the resulting trouble concentrated to the time of year when the power from the Salmisaari plant was most needed. With some difficulty, however, plant operation was secured by continuous manual effort at the silo discharge and conveyor systems and additional coal transport from the open storage of a neighbouring plant. Although the challenge by frozen coal is new, prevention and mitigation might be more straightforward than for heated coal.

## References

1. Sipilä, J. Preventing spontaneous combustion in an underground coal storage. Espoo: Helsinki University of Technology, 2009. Master's Thesis. 128 p. (In Finnish).
2. Anon. Understanding self-ignition of coal. Innovative Technologies for Exploration, Extinction and Monitoring of Coal Fires in North China. A literature study elaborated in co-operation of Deutsche Montan Technologie GmbH (DMT) and Federal Institute for Materials Research and Testing (BAM), 2000. 32 p.
3. Walker, S. Uncontrolled fires in coal and coal wastes. IEA Coal Research – The Clean Coal Centre. London, 1999
4. Grossman, S. L., Davidi, S. & Cohen, H. Explosion risks during the confined storage of bituminous coals. *Fuel*, 1995. Vol. 74, No. 12, pp. 1772–1775.
5. Wang, H., Dlugogorski, B. Z. & Kennedy, E. M. Coal oxidation at low temperatures: oxygen consumption, oxidation products, reaction mechanism and kinetic modelling. *Progress in Energy and Combustion Science*, 2003. Vol. 29, No. 6, pp. 487–513.
6. Smith, A. C. & Lazzara, C. P. Spontaneous combustion of U.S. coals. R19079, Washington, DC, USA, Department of the Interior, Bureau of Mines, 1987.
7. Smith, M. A. & Glasser, D. Spontaneous combustion of carbonaceous stockpiles. Part II. Factors affecting the rate of the low-temperature oxidation reaction. *Fuel*, 2005. Vol. 84, No. 9, pp. 1161–1170.
8. Ray, S. K., Zutshi, A., Bhowmick, B. C., Sahay, N. & Singh, R. P. Fighting mine fires using gases with particular reference to nitrogen. *The Journal of The South African Institute of Mining and Metallurgy*, 2000. Vol. 100, No. 4, pp. 265–272.
9. Fierro, V., Miranda, J. L., Romero, C., Andres, J. M., Arriaga, A. & Schmal, D. Model predictions and experimental results on self-heating prevention of stockpiled coal. *Fuel*, 2001. Vol. 80, pp. 125–134.
10. Tuomisaari, M., Baroudi, D. & Latva, R. Extinguishing smouldering fires in silos. Brandforsk project 745-961. Espoo: VTT, 1998. VTT Publications 339. 74 p.

# **Development and Implementation of *i*-LAS (indentation based turbine remaining life assessment system)**

Woosung Choi\*, Geewook Song and Jaeraeyang Koo  
Korea Electric Power Research Institute, KEPCO  
Daejeon, Republic of Korea

## **Abstract**

Steam turbine rotors are the most critical and highly stressed components of the steam power plant and have the highest capital cost among all the components. It requires not only a long outage for replacement and repairing, and also be major guideline to determine outage interval. Thus it is necessary to establish plans with which plants can be operated and managed effectively against damage problems. In this study, remaining life assessment tool *i*-LAS(indentation based turbine remaining life assessment system) has been developed for turbine rotor components. *i*-LAS is capable of evaluating remnant rotor life quickly considering actual in-service conditions. A modified damage model was established and successfully implemented to *i*-LAS system. A case study has been carried out to validate effectiveness and reliability of *i*-LAS for turbine rotor of 500 MW fossil power plants in Korea.

## **1. Introduction**

The number of unit of 500 MW Korean standard fossil power plant is 27 in Korea. Most of these facilities are facing a requirement for retrofit and expected to perform a feasibility study. Feasibility assessment is to determine replacement time and scope of facilities with consideration of the economic effects. Component life assessment and reliability evaluation of critical facilities are performed for

feasibility assessment. Thus, it is necessary to develop advanced technology to improve accuracy of life assessment method for more reliable feasibility study. In this regard, a lot of methods have been developed for this reason: accelerated degradation test, computer aided analytic method, and non-destructive technique. Some limitations, however, have been repeatedly reported in the listed methods. For example, accelerated degradation tests cannot be done in-situ condition because the test method is destructive and extraction of specimens from industrial facility in service is difficult. Computer aided analytic method such as finite element method may reduce the cost and testing time, however, there are uncertainties caused by various assumptions such as simplified geometry and operation condition. Indentation test method is a non-destructive technique and is useful to determine material properties of a component. This method can measure various mechanical properties such as elastic modulus, tensile strength, and residual stress by analyzing the indentation load-depth curve (Oliver & Pharr 1992, Lee & Kwon 2006).

Mechanical properties of low alloy ferrite steel for turbine facilities are degraded in long-term service under high temperature and rapid rotation operation condition. In order to estimate degradation status of a component, a portable indentation tester can be utilized for on-site measurements. Then, remaining life can be readily evaluated using *i*-LAS.

In this study, remaining life assessment tool *i*-LAS (indentation based turbine remaining life assessment system) has been developed for turbine rotor components. A modified damage calculation approach has been implemented to *i*-LAS making it capable of quickly evaluating rotor remnant life with actual in-service conditions considered. Furthermore, a case study has been carried out to validate the reliability of *i*-LAS for turbine rotor of 500 MW fossil power plants of Korea.

## **2. Indentation based turbine remaining life assessment system (*i*-LAS)**

Figure 1 describes how remaining life of a component can be evaluated using *i*-LAS. To obtain essential material parameters, measurements are carried out using portable indentation tester and hardness tester. Two testers measure parameters at two different locations: virgin area and aged area. Measured data are then transferred to calculation module and component damage consumption is calculated using the modified damage model. Ultimately, remaining life is

## Development and Implementation of i-LAS (indentation based turbine remaining life assessment system)

estimated based on previously calculated damage and actual operation history information.

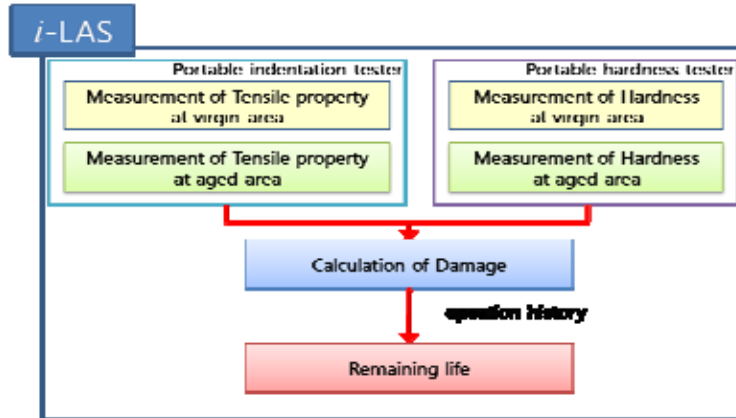


Figure 1. Architecture for simplified life prediction using *i*-LAS.



Figure 2. Introduction page of the *i*-LAS.

### 2.1 System structure

The *i*-LAS is constituted of information, measure, data, and life prediction menus as shown in Figure 3. All menu and functions are developed on Windows API basis. It is possible to import previous result from database after selecting plant information for database saving.

Development and Implementation of i-LAS (indentation based turbine remaining life assessment system)

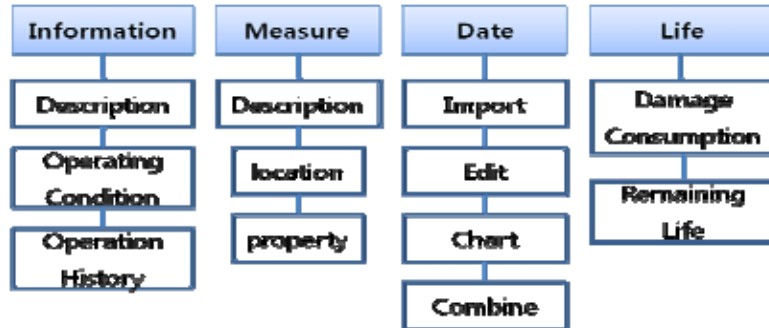


Figure 3. Overview of ATLAS Menu.

## 2.2 Detailed description of System

### 2.2.1 Information

Information module basically acquires plant specific data and material data. Basic information includes plant name, facility characteristics, and material information. In addition, plant specific operation history such as the number of start-up and operation hour is used in information menu. Recently, it has become relatively easy to obtain operation condition because most of the power plants have their independent plant information system. Obtained operation history information is relayed to the Life module for remaining life. Information menu window is shown in Figure 4.



Figure 4. Information menu window.

### 2.2.2 Measure

Measure module describes locations to be evaluated and mechanical parameters to be obtained and displays such information on screen. A portable indentation tester is used to achieve such data. Highly aged position and lowly aged position are indicated in this module. The locations can be found in the reference [5–6].

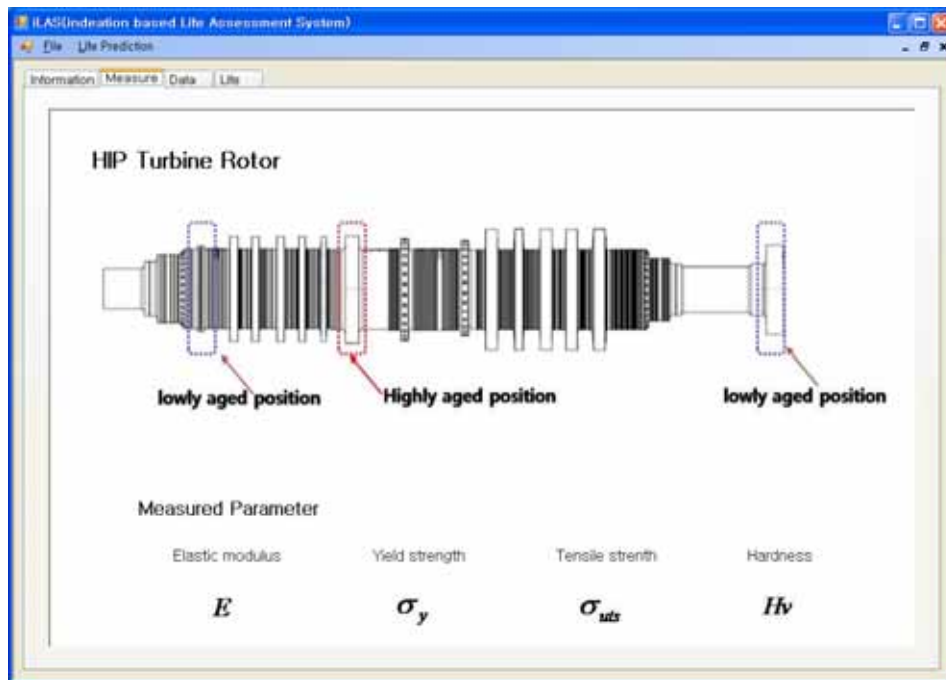


Figure 5. Measure menu window.

### 2.2.3 Data

In this menu, test results by portable indentation and hardness tester are imported. Elastic modulus, yield stress, and tensile strength are obtained from indentation tester and hardness is measured by hardness tester according to the aging states. Reference (or undamaged) values can be imported from indentation result for in-situ virgin states or for uni-axial tensile test where virgin material is used. Also, each value can be revised and used for stress-strain curve plotting. Using chart composition function, undamaged and damaged properties are compared on the chart at same scale.

Development and Implementation of i-LAS (indentation based turbine remaining life assessment system)

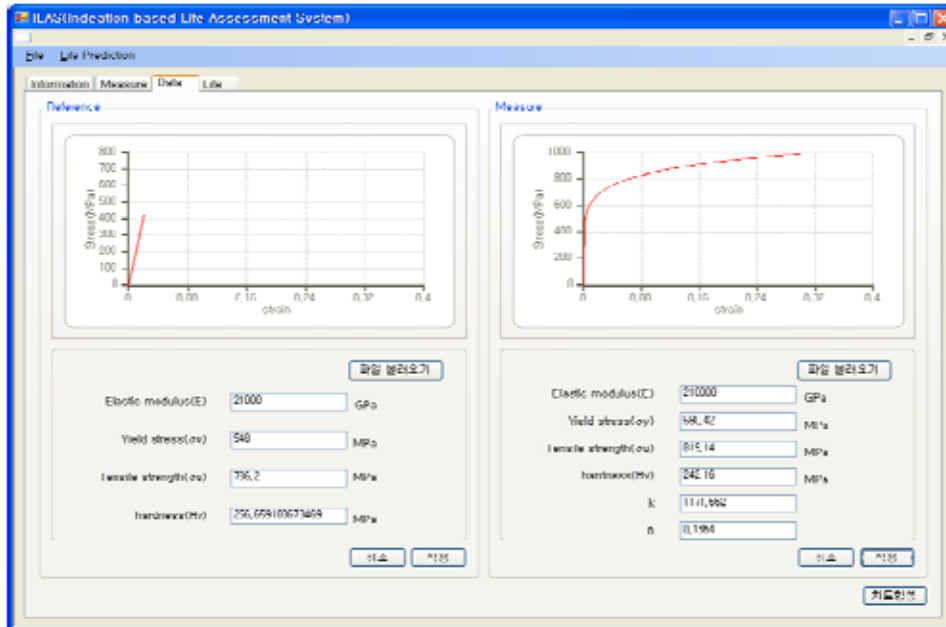


Figure 6. Measured value displayed in the Data menu.

### 2.2.4 Life

Life menu is comprised of damage consumption part and remaining life consumption part as shown in Figure 7. Generally, creep and fatigue damage should be considered in accurate remnant life assessment. *i*-LAS procedure is based on quantitative relationship between hardness and mechanical properties about damage. Detailed explanations on damage evaluation algorithm are described in reference [1–5]. In information menu, users are prompted to input plant data: operation hour and number of start-up considering cold, warm, hot states. In damage consumption part, total damage rates are calculated by embedded mathematical functions which use measured mechanical properties. According to the operation history, finally, remaining life is determined in the form of hour or cycle. Left on Figure 7 shows a HIP (High-Intermediate Pressure) turbine facility of 500 MW Korea standard fossil.



Development and Implementation of i-LAS (indentation based turbine remaining life assessment system)

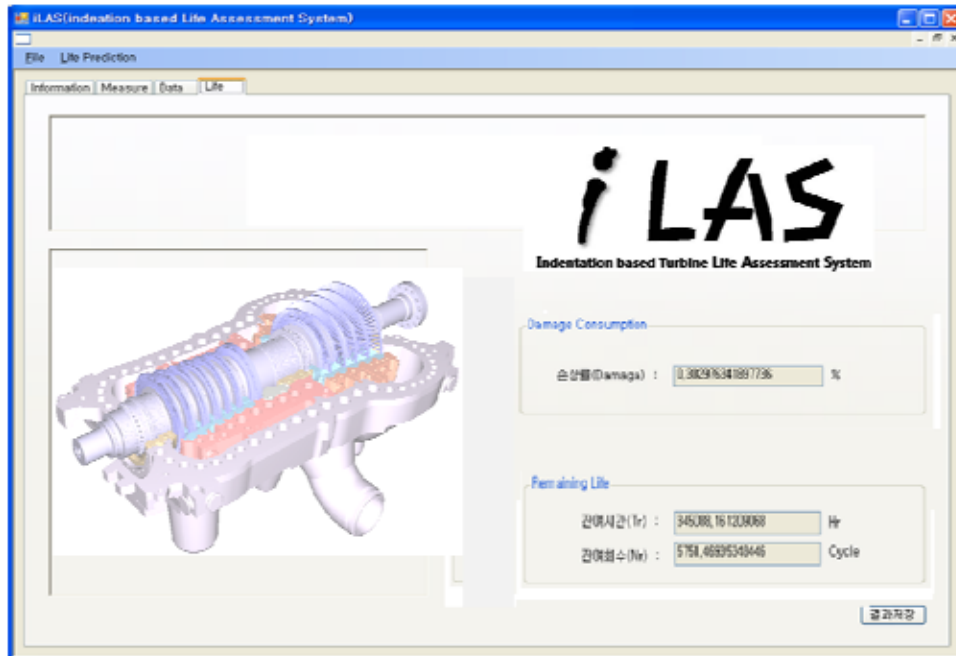


Figure 7. Windows of Life menu.

### 3. Case study

#### 3.1 Basic information

As of 2010, 27 standard fossil power plants of 500 MW are in operation in Korea and total power generated by the plants add up to 14 240 MW. Most of these facilities are faced with the need for improved performance and expected to perform a feasibility assessment. A retired 500 MW turbine rotor is selected for the case study and the remaining life is estimated by *i*-LAS. Table 1 shows a status of measured turbine facilities. This turbine facility begun its operation in 1983, and marked 141 000 hour operation and the recorded number of start-up is 191. Table 2 shows chemical composition of the turbine rotor material. Low-alloy ferritic steel, 1Cr-1Mo-1/4V, is widely used in high temperature applications.

Development and Implementation of i-LAS (indentation based turbine remaining life assessment system)

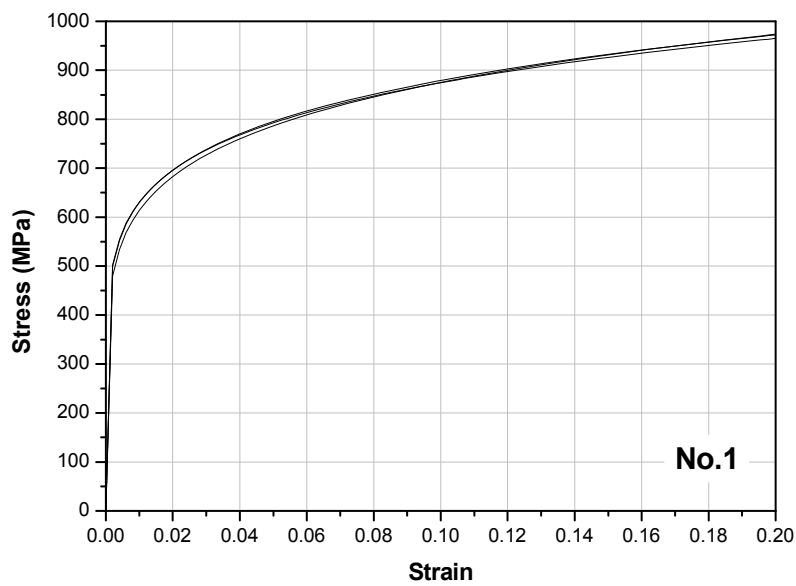
Table 1. Turbine facility status.

Completion date	Operating time (Hour)	The number of start-up (cycle)	Capacity (MW)
1983. 12	141 000	191	500

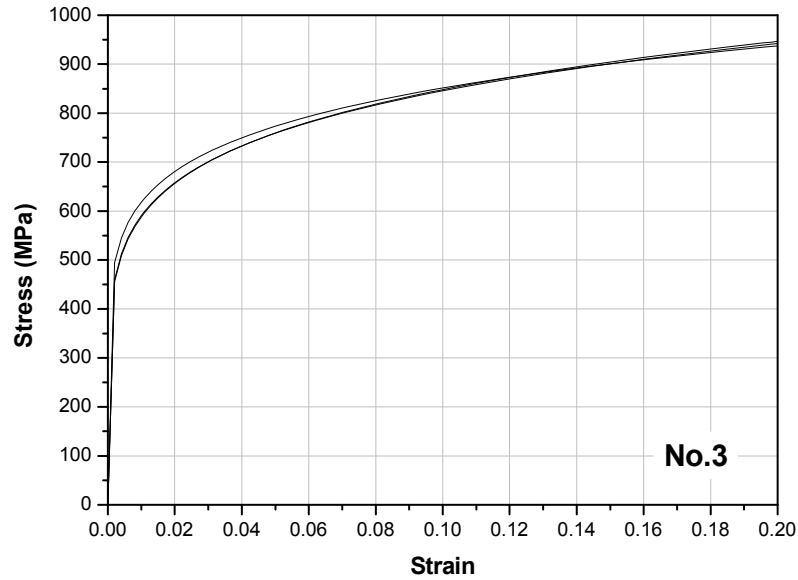
Table 2. Chemical composition (wt.%) of 1Cr-1Mo-1/4V.

C	Si	Mn	S	P	Ni	Cr	Mo	V	Sn
0.29	0.01	0.74	0.004	0.007	0.06	1.29	1.24	0.25	0.0047

Figure 8 shows stress-strain curve measured in the undamaged and damaged location of the rotor respectively using portable indentation tester. Measurements are done in different locations but in the same rotor. Detailed information is described in reference [5–6].



(a) Undamaged location



(b) Damaged location

Figure 8. Stress-strain curves by portable indentation tester.

### 3.2 Assessment result

The damage rate is obtained by measured tensile properties and hardness for turbine rotor of 500MW Power plant. Figure 9 shows damage rates at lowly aged and highly aged locations of turbine rotor. Remaining life is calculated from damage rate and operation history as shown in Table 3. According to the assessment results, the remaining lifetime of the 16-year-old turbine rotor is about 198 365 hour (22.6 year). When considering that the design lifetime of large turbine facility is approximately 30 years, this result (38.6 year) appears to be reasonable.

Development and Implementation of i-LAS (indentation based turbine remaining life assessment system)

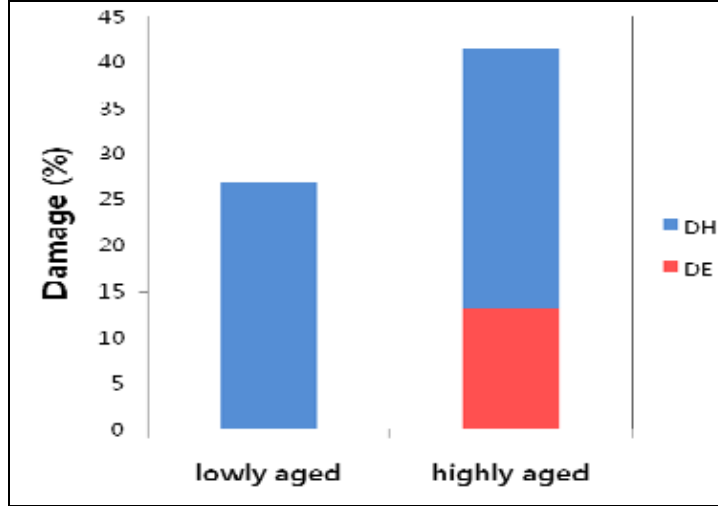


Figure 9. Damage rates from indentation test.

Table 3. Summary of result.

	Remaining Life	
	Lowly aged location	Highly aged location
Modified damage model	384 420 hour (43.9 year)	198 365 hour (22.6 year)

## 4. Conclusion

i-LAS (indentation based turbine remaining life assessment system) has been developed to calculate remaining lifetime of major turbine facilities such as rotor and casing. This system, called i-LAS, focuses on quickness, simplicity and accuracy based on material characteristic, operation condition. User can easily evaluate remaining life of turbine facilities and all information can be revised or saved in database. A modified damage model was successfully implemented to i-LAS system. Using developed program, a reliable life assessment result can be easily obtained. i-LAS is applied to one of 500MW fossil power plant in Korea. The damage rate of the 16-year-old turbine rotor is calculated by the modified damage model. Reasonable remaining lifetime when compared to general service time, is obtained by modified damage model.

## References

1. Lemaitre, J. & Desmorat, R. *Engineering Damage Mechanics*. Springer, 2004.
2. Tasan, C. C., Hoefnagels, J. P. M. & Geers, M. G. D. A critical assessment of indentation-based ductile damage quantification. *Acta Materialia*, 2009. Vol. 57, pp. 4957–4966.
3. Seok, C. & Koo, J. Evaluation of material degradation 1Cr-1Mo-0.25V steel by non-destructive method. *Materials Science and Engineering A*, 2005. Vol. 395, pp. 141–147.
4. Lee, K. et al. Safety assessment based on mapping of degraded mechanical properties of materials for power plant pipeline using instrumented indentation technique. *Journal of Loss Prevention in the Process Industries*, 2009. Vol. 22, pp. 868–872.
5. Song, G., Choi, W., Koo, J. & Jinseong. Investment reduction through the life extension of aged turbine. KEPCO TDR Report, 2009.
6. Choi, W. & Song, G. Life prediction system of turbine facilities for fossil power plant using portable indentation tester. Patent No.1020090087051, 2009.
7. Choi, W., Kim, B., Hyun, J. & Song, G. Development and Implementation of advanced turbine life assessment system. *Power Gen Asia Track 4*, 2008.
8. Choi, W. S., Fleury, E., Kim, B.-S. & Hyun, J.-S. A Life assessment for steam turbine components based on viscoplastic analysis. *Journal of Solid Mechanics and Materials Engineering*, 2008. Vol. 2, No. 4, pp. 478–486.
9. Allen, D.-J. & Fenton, S. T. A hardness based creep rupture model for new and service aged P91 steel. *Baltica VII*, 2004, pp. 156– 170.

# **Creep damage and long term life of steam line components: case X20**

Stefan Holmström, Pertti Auerkari, Jorma Salonen  
Anssi Laukkanen, Juhani Rantala  
VTT Technical Research Centre of Finland, Espoo, Finland

Reino Nikkarila  
Inspecta Oy, Espoo, Finland

Jarmo Junttanen  
Stora Enso Oyj, Varkaus, Finland

## **Abstract**

Hot steam lines operate at high temperatures and are designed against creep. In service they will consume the creep life at the highest rate in locations with the most adverse combination of material strength (weakness) and high stress (e.g. system loads). Adverse effects in stress state are promoted by features of geometry and discontinuities in the materials properties. In practice it is essential to find the areas of maximum damage, as these will determine the locations and timing to inspect and finally to repair or replace before failures or unplanned outages. The inspection experience from power plant steam systems have provided the established views on the expected locations of the early creep damage, and rules on timing the next inspection. The experience has also shown that optimal timing is materials dependent, and that the steel grade X20CrMoV11-1 (X20, 11% Cr steel) performs particularly well in the inspection statistics. This paper describes a case with observed creep cavitation and cracking in a branch weld of a X20 steam header that was replaced after 135 000 service hours. The characteristics of the observed damage and its evolution are discussed.

## 1. Introduction

During creep of pipes and tubes under pressure, stresses will redistribute to retain the maximum equivalent stresses and strains at the inner surface, while the maximum principal stress will shift to outer surface. This is the classical explanation for long term creep cavitation and cracking starting from the external surface, together with damage models where the maximum tensile principal stress will largely dominate the formation of long term creep cavitation damage on the grain boundaries of polycrystalline metals.

Modified by details in geometry and variation in creep properties of welds, the established principle is to inspect only the likely weakest spots (“mechanical fuses”) of large structures from outside for condition and life assessment. In this context life assessment really means setting the optimal time for the next inspection, after defining possible needs (and timing) for repairs or replacements. It has turned out that the hot steam lines of conventional thermal power plants are designed in such a similar way that the observed damage level together with the expired time in service is a good (albeit somewhat rough) indicator of life or the suitable and safe time to the next inspection. This naturally assumes that the plant and the steam line is operated and maintained to retain its preceding characteristics, or that at least any future changes can be sufficiently quantified. Simple guidelines exist for inspectors to classify the damage and make conclusions based on the observations. The original guidelines for this purpose [1] were material independent and quite conservative, but after collating more evidence from inspection statistics, the later guidelines have been made to include material-dependent recommendations [2]. Such guidelines that are based on long term inspection statistics suffer from lack of similarly established rules and recommendations for steels that only recently entered the accepted range of standard materials and service in plant.

However, even well established steels can be considered new for long term inspection experience. A good example is the steel X20CrMoV11-1, or X20 for short, which is an 11%Cr steel that has been used in high temperature components in Europe since 1960's. The available inspection statistics suggests that this steel and its welds suffer less creep damage after e.g. 100 000 service hours than common low alloy steels. The reasons for this are not entirely obvious, as the design to the same code and nominal life should be able to compensate for the differences in creep strength between the alloys.

The good service and inspection experience with X20 is also of interest and possible significance for the martensitic steels such as P91 (X10CrMoVNb9-1) and P92 (X10CrWMoVNb9-2) that are used in new steam plants and share many basic microstructural features with X20. For these steels no similar extensive operational and inspection experience is yet available, but instead some reported surprises on early creep damage [3]. A comparison of selected steels for hot steam lines is shown in Table 1.

Table 1. Comparison of steel X20 with older low-alloy and newer 9%Cr steels [4].

Alloy (EN 10216-2)	Cr wt %	Other alloying elements	Rp0.2 RT MPa min	R <sub>n/100 kh</sub> , MPa 550/600°C
10CrMo9-10	2.0-2.5	Mo	280	53 / 20
14MoV6-3	0.3-0.6	Mo,V	320	87 / 41
X20CrMoV11-1	10-12.5	Mo,V	490	128 / 59
X10CrMoVNb9-1	8.0-9.5	Mo,V,Nb,N	450	166 / 94
X10CrWMoVNb9-2	8.0-9.5	W,Mo,V,Nb,N,B	440	187 / 113

Below a case is described on a X20 header that was replaced after 135 000 h of service due to creep cracking at a branch weld. As creep cracking so early is not common in steam line components made of this material, a fairly detailed study was launched to clarify the case. This paper will report results on characterising the damage originally detected in the in-service inspections of the steam line.

## 2. Header case: operation and inspection history

The header was designed in 1989 to the Finnish standard SFS 2618 that is in practice compatible with e.g. the former German (TRD 300-series) design rules. The dimensions of the main body of the header are  $\varnothing 508 \times 32$  mm and those of the branch to the boiler  $\varnothing 310 \times 40$  mm. The nominal design creep life was 200 000 h, i.e. against mean stress corresponding to 200 000 h creep rupture at 540°C (129 MPa). The allowable stress was 102.3 MPa for the branch to the boiler, at the design pressure of 12 MPa. The relative safety margin in time was 3.1 (base material mean strength). The observed maximum creep damage was in the weld of the branch to the boiler, in the saddle point position (Figure 1).



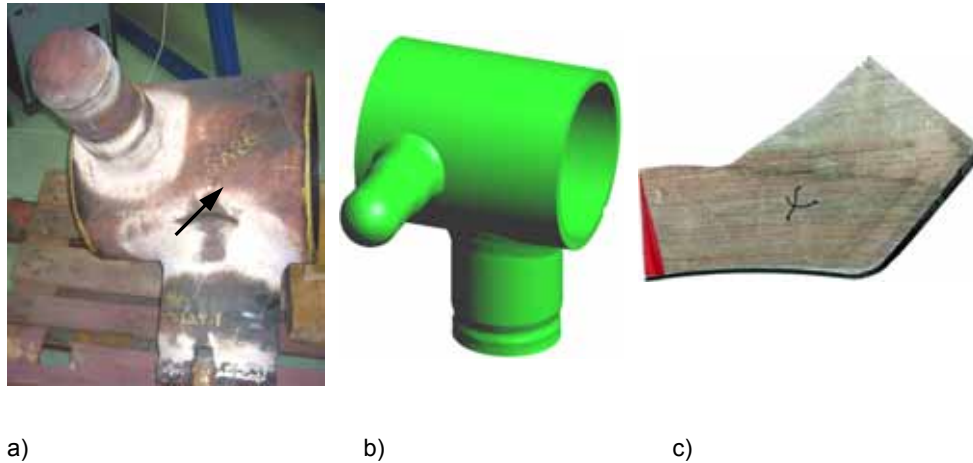


Figure 1. a) Section of the steam header with the main boiler branch, b) a 3D tracking image of the header section; and c) cross-section of the damaged saddle point location (arrow shows the location of maximum damage).

The in-service inspections were performed in 2002–2007 by the same person of Inspecta Testing, mainly with fluorescent magnetic particle and replica testing. The damage indications and follow-up actions are summarised in Table 2.

Table 2. Inspection history of the branch weld of the header (saddle point, fine grained heat affected zone of the side of the header body side).

Year	Observed HAZ indications	Action
2002	Cavitation & microcracking (class 4)	None
2003	Macroscopic cracking (50 mm max)	Repair by grinding 2 mm <sup>1)</sup>
2004	Microcracking (class 4)	None
2006	Macroscopic cracking (4 mm max)	None
2007	Macroscopic crack (10 mm max)	Header replacement

1) class 3 damage still present after grinding

The first indications of creep cavitation and microcracking were found in the weld (HAZ) of interest after 103 000 service hours. The end of the header service after 135 000 service hours corresponds to 68% of the nominal design

(creep) life. The maximum total grinding depth at the cracked site was about 3 mm on the base material side of the header body.

### **3. Predicted creep strain**

Of creep properties, standards such as EN 10216-2 only list mean stress to creep rupture for a range of temperatures. To assess expected damage, creep strain can be of more interest, to reflect the likely events well before failure. Although creep strain is not the same as (cavitation) damage, it is thought to be generally increasing with it. Therefore creep curves were constructed using X20 materials data from [5–9] for the X20 parent material. The strain model used was the logistic creep strain prediction tool (LCSP) based on time to rupture and creep curve shape functions [10, 11]. At the design limiting stress and temperature (about 100 MPa/540°C) the predicted base material creep behaviour is shown as the lower curve in Figure 2. It is (as usual) assumed that the weld is 20% weaker (in stress terms) than the parent material, and the resulting predicted creep behaviour of the weak part of the weld (HAZ) is shown as the upper curve in Figure 2. It is seen that at the design limit of loading, by the time of the 2002 inspection or after 103 000 h of service, the predicted creep strain at the weak HAZ is still below 1.5%, and that this level of strain would require some 300 000 h of service for the parent material. However, the general experience from other materials suggests that such a low strain level would not be enough for the observed damage (microcracking or class 4 creep damage).

Therefore, either the material has been clearly weaker than average X20, or loads (and/or temperatures) significantly higher than those assumed in design. Since the design stress levels already include the usual safety factors, the actual deviation from the usual operational conditions or material state have been more extensive than those usually covered by the design and manufacturing practices.

Further insight into the indicated damage was therefore sought by a more detailed characterisation of the cracked weld region.

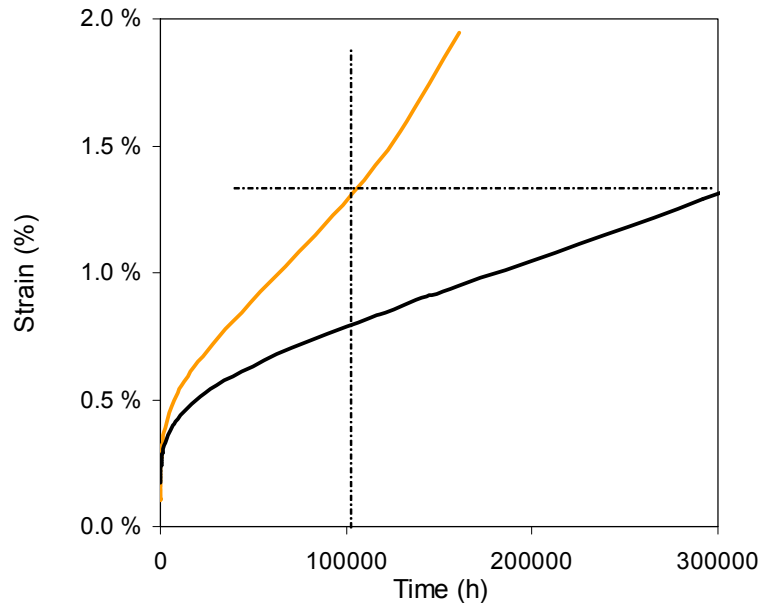


Figure 2. Predicted creep strain history for X20 parent material (lower curve) and outer heat affected zone (Type IV position, upper curve) at the design limit of the branch to the boiler; the vertical line shows time of first inspection.

#### 4. Features of the saddle point damage

The cross-section of the saddle point crack location is shown in Figure 3. The corresponding location and the crack from the weld surface side is shown in Figure 4. It is seen that the crack is here clearly a discontinuous “toilet paper” crack, with actual short cracks and inter-crack ligaments on roughly the same plane along the HAZ. Note that at this stage the original pipe surface of the cracked location has been ground to a depth of more than 2 mm due to preparation for inspections and earlier repair grinding.

Metallography of a cross-section of the main crack (Figures 5–8) shows the appearance of the crack and cavities in front of it. The cavitation is extending at least to a depth of 6 mm from the crack tip. All cavities are multidirectional and jagged in shape (Figures 7 and 8). The crack tip is not strongly blunted and appears to grow by joining creep cavities that surround the tip.

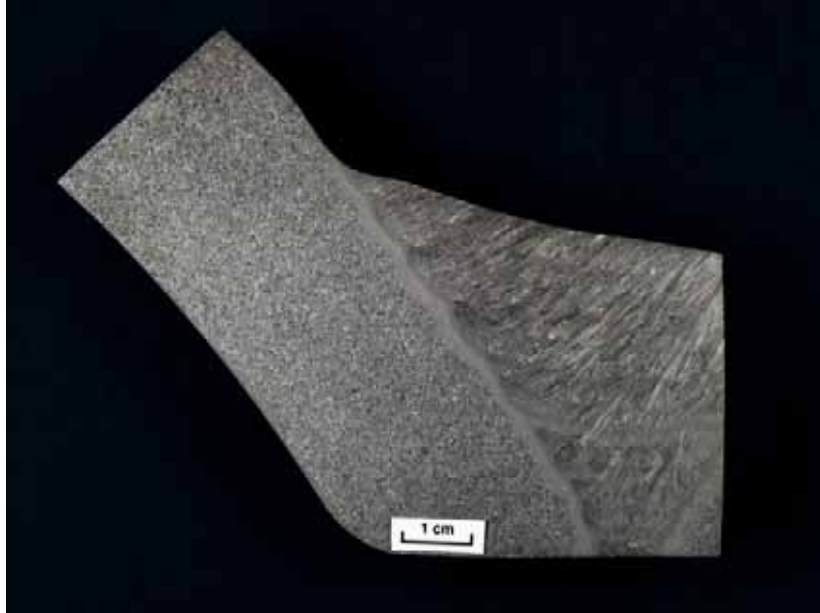


Figure 3. Cross-section of the saddle point crack location.

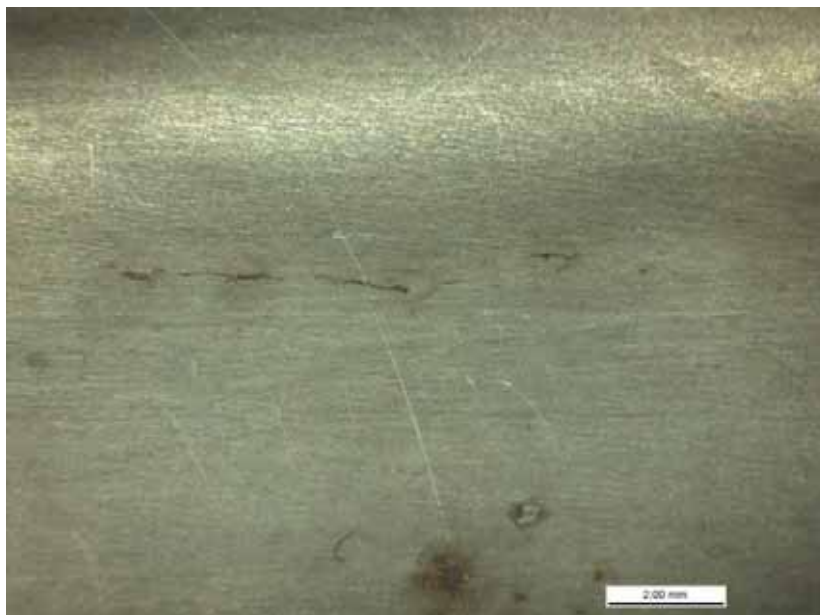


Figure 4. Appearance of the "toilet paper" crack on the header surface (axial direction of the header body horizontal).

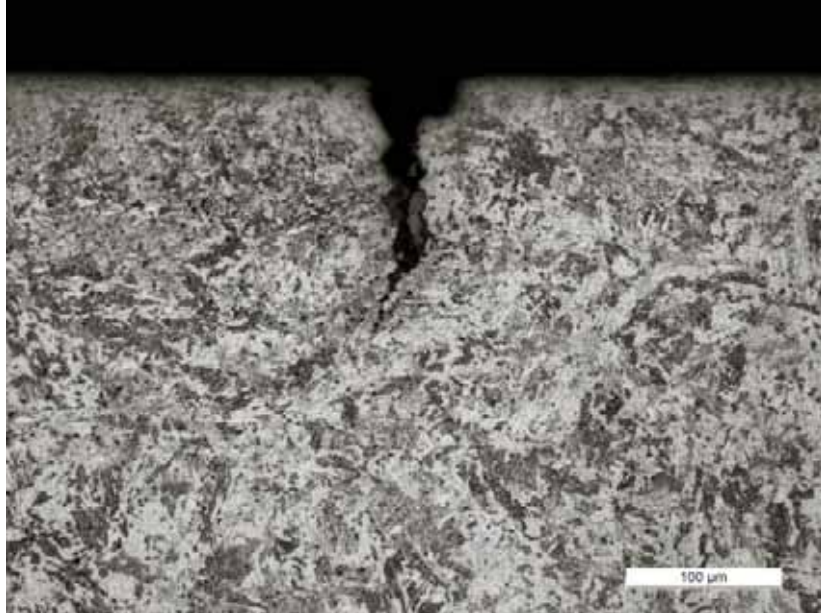


Figure 5. Cross-section of the surface crack.

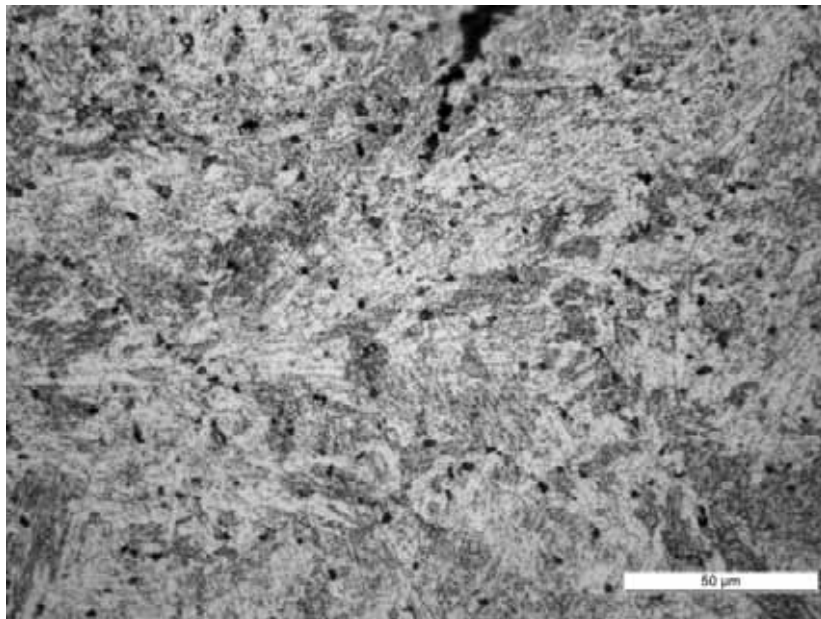


Figure 6. Creep cavitation in front of the crack tip.

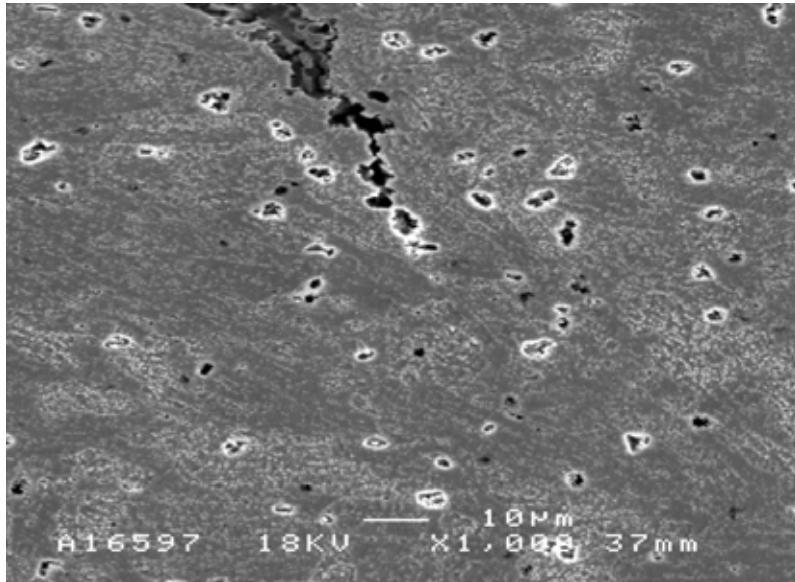


Figure 7. Creep cavitation ahead of the crack tip.

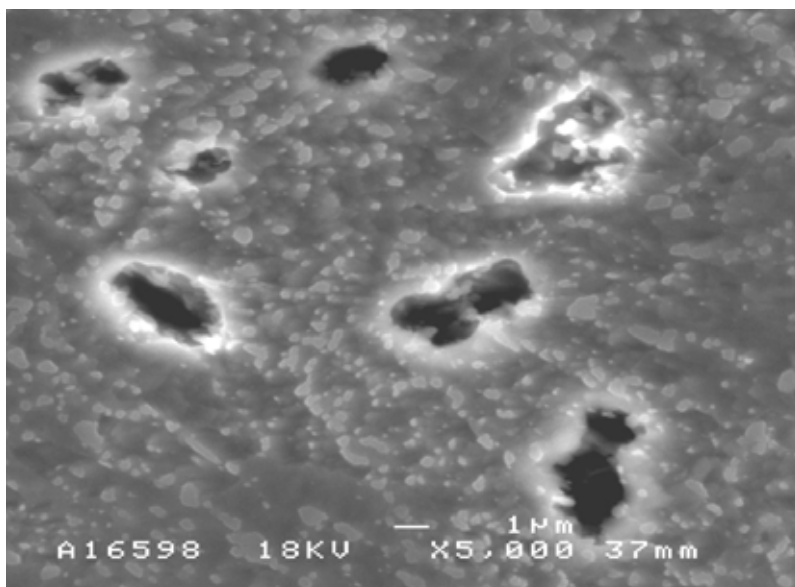


Figure 8. Creep cavities near the crack tip.

Such appearance of creep cavitation has been reported previously in welds of ferritic-martensitic 9%Cr steels in addition to X20; however, most such reports refer to observations from shorter term studies in the laboratory.

At least one reason why X20 components show relatively better performance in resisting creep damage than low alloy steels is the intrinsic complexity of the microstructure in the grain interior. The lath, block and packet boundaries are likely to distribute strain and damage more effectively than simple grain boundaries of conventional low alloy steels, even after suffering depletion of the strengthening particles in the HAZ of welds. The intrinsic strength appears as jagged, multidirectional shape of the cavities and as intermittent or bridging cracks (“toilet paper cracking”), where ligaments of metal are holding the material together at the site that was in the surface inspection interpreted as a single unified long crack.

The shape of the crack together with the inspection history and the already relatively long time in service indicate that the crack has been growing quite slowly and would not have accelerated quickly if left in place for about one year.

However, the fact remains that the weld did show genuine creep cracking after only 135 000 hours of service. The review suggests that this is not directly because of the design of the header vessel or the welded branch. In principle reasons for the early damage could be related to operational conditions, e.g. additional system stresses (moments) from the thermal movement of the piping. As no similar cracking was found on the corresponding opposite saddle point position, asymmetry in such thermal loading is possible. However, 90° from the saddle point position, both sides of the same HAZ showed some initial surface cracking (about 2 mm single cracks only). The remaining possibility is that the material was not typical average welded X20. Some deviation in heat treatments of the base material or the weld is possible but not proven. Further studies may clarify the remaining aspects of uncertainty, but the case can nevertheless be used as a benchmark for interpretation of observed creep damage in welded components after long term service. Factors that could reduce the creep life of the component and an assessment on their significance are shown in Table 3. Apart from the effects of single factors, also combined effects of e.g. system stresses and material weakening are possible. This would reduce the deviation needed in individual factors for the same impact.

Although the observed creep damage was relatively early for X20, it can be considered long-term damage so that its growth rate can be used to support the decisions on safe condition-based timing of inspections.

Table 3. Summary of potential factors resulting in relatively early header cracking

Cause	Assessment results	Notes
1. Design error	None in the review	Not common
2. Fabrication	None found in dimensions	Not excluded in heat treatment
3. High temp.	No evidence	Uncommon far from boiler
4. High pressure	Unlikely	Uncommon in steam lines
5. System loads	Possible, extent unknown	Thermal piping movement
6. Weak steel	Possible but not to the extreme	Evidence in microstructure
Combined	Possible (e.g. 2, 5, 6)	-

## 5. Conclusions

A X20CrMoV11-1 (X20) steam header has been retired after 135 000 hours of service due to creep cracking of a branch weld. The expired time to cracking (68% of the nominal design life) was considered relatively short in comparison with the general inspection experience with X20 steam pipe welds.

The observed creep damage occurred in the saddle point HAZ (type IV) and showed an appearance thought to be characteristic to 9–11%Cr steels with tempered martensitic microstructure. The shape of cavities and crack bridging suggest residual microstructural resistance to damage growth that would not proceed similarly in e.g. low alloy steels. These features are thought to be due to the microstructure where multiple small angle boundaries of the laths and blocks can distribute strain and damage wider than when only grain boundaries offer opportunities for cavity nucleation and growth. The observed relatively early cracking is probably due system stresses and/or weaker than average material rather than design, dimensions or operating temperature/pressure. In spite of relatively early creep damage for X20, the observed damage growth rate can be used to support recommendations for safe condition-based timing of inspections.

## Acknowledgement

The authors wish to acknowledge the financial support of the Academy of Finland, Decision no. 117700 (by Prof. Kim Wallin), the Värmeforsk project on



Creep damage development in welded X20 and P91 components, and the industry financed Finnish project LifePower.

## References

1. Neubauer, B. & Wedel, U. Restlife estimation of creeping components by means of replicas. In: *Advances in Life Prediction Methods*. New York: ASME, 1983. P. 307.
2. Auerkari, P., Holmström, S., Salonen, J., Borggreen, K., Storesund, J. & Rui, Wu. Evaluation of creep damage from replica inspection results. Nordtest Project No. 1306-96. Espoo: VTT, 1997. Report VTT VALB211. 33 p.
3. Brett, S. J. The creep strength of weak thick section modified 9Cr forgings. *Baltica V – Condition and Life Management for Power Plants, Vol1*. VTT Symposium 211, 2001. Pp. 35–44.
4. EN 10216-2, European Standard, Seamless steel tubes for pressure purposes. Part 2: Non-alloy and alloy steel tubes with specified elevated temperature properties, 2007.
5. Storesund, J., Borggreen, K. & Weilin, Z. Creep behaviour and lifetime of large welds in X20 CrMoV 12-1 – results based on simulation and inspection. *Int. Journal of Pressure Vessels and Piping*, 2006. Vol. 83, pp. 875–883.
6. Hua-Tang, Yao et al. A review of creep analysis and design under multiaxial stress states. *Nuclear Engineering and Design*, 2007. Vol. 237, pp. 1969–1986.
7. Bürgel, R. et al. Schädigungsentwicklung an X20CrMoV121 nach Langzeitbeanspruchung und Zuordnung von Restlebensdauer von Komponenten im Kriechbereich. VDEh und Arbeitsgemeinschaft für Hochtemperaturwerkstoffe, 13. Vortragsveranstaltung, Düsseldorf, 1990. Pp. 94–107.
8. Standard Data Tables, Vol. 2, Ferritic steels. SPRINT Specific project SP-249, Implementation of Power Plant Component Life Assessment Technology using a knowledge-based system, 1995.9. Entwicklung von Zeitstands Schäden in den Stählen X10CrMoVNb9-1 (P/T 91) und X20CrMoV 12-1. Untersuchungsbericht 35/1999, Bericht zum Forschungsvorhaben VGB-Nr. 160.14.

- 10 Holmström, S. & Auerkari, P. Robust prediction of full creep curves from minimal data and time to rupture. *Energy Materials; Materials Science and Engineering for Energy Systems*, 2006. Vol. 1, No. 4, pp. 249–255.
11. Holmström, S., Laukkanen, A., Rantala, J., Kolari, K., Keinänen, H. & Lehtinen, O. Modeling and verification of creep strain and exhaustion in a welded steam header. *Journal of Pressure Vessel Technology*, 2009. Vol. 131, 5 p.

# Remaining lifetime assessment of power plant steam boilers

Vaclav Liska<sup>1</sup> and Vaclav Mentl<sup>2</sup>

Skoda Research Ltd.<sup>1</sup>, Accredited Labs., Plzen, Czech Republic

University of West Bohemia<sup>2</sup>, Dept. Material Science and Technology,  
Plzen, Czech Republic

## Abstract

The energy producing power plants are designed for operational period of 20, 30 years. During this period, inspections are realized to investigate the operational capability of the respective components and the plant as a whole, and when the designed time is approaching its limit, the crucial questions are raised with respect to the following possible operation, its safety and risks that stem from the fact that the continuous degradation of material properties occurred during the longtime service as a result of service conditions, e.g. high temperatures, fatigue loading etc.

In opposite to the non-destructive techniques, accelerated creep to rupture tests of high temperature boiler components, e.g. high temperature headers, can give quantitative results as far as the remaining lifetime of the component is concerned.

Several steam turbine boilers were inspected according to the customer's demand to evaluate the remaining lifetime of the boilers that were operated more than 160 000 and 200 000 hours respectively. The evaluation was based on an extensive NDT inspection and the measurement of mechanical properties (including creep test data) of high temperature components. Making use of the Larson-Miller parameter in comparison with replica testing made it possible to evaluate quantitatively the lifetime exhaustion, to make an assessment of the remaining lifetime and to make a recommendation as far as the future inspection intervals of the boilers are concerned.

On the basis of accelerated creep test data performed on the degraded materials, the remaining lifetime hours were calculated for the three „safety“ situations :

1. „ZERO SAFETY“ ( neither recommended  $k = 1,5$  safety coefficient for working stress nor  $+70^{\circ}\text{C}$  increase of working temperature were taken into consideration ).
2. „STRESS SAFETY“ (1,5 safety coefficient for working stress and real working temperature were taken into consideration).
3. „FULL SAFETY“ (both 1,5 safety coefficient for working stress and working temperature +  $70^{\circ}\text{C}$  were taken into consideration).

At the Baltica VII conference, an example of this procedure was presented [1]. This paper summarizes the results of several more boilers and the results of the remaining lifetime calculation are discussed.

*Keywords: service degradation, remaining lifetime assessment, steam turbine boilers*

## 1. Introduction

The creep degradation was again taken into consideration as the decisive damaging factor in case of primary and secondary superheaters. Metallographic investigation and basic mechanical tests were performed.

To receive quantitative results, accelerated short-term creep tests were carried out of the creep samples machined of the during the in-site inspection selected super-heater tubes. The creep test conditions (stresses and temperatures) were chosen in order that the resulting times to rupture were reached within the relatively short time to be able to evaluate the results in time according to the requirement of the customer.

Two more real cases of creep test results and remaining lifetime evaluation in addition to that one discussed during Baltica VII are presented. For the CASE „1“, see [1].

## 2. Case „2“

### 2.1 Boiler description and technical details

- Steam output 350 t/h
- Steam pressure 6.2 MPa
- Steam temperature 485°C
- Fuel Natural Gas/Oil
- Year of Production 1976
- Service Hours 204 871

Boiler was made of common steels used in boilers produced 30–40 years ago in 1970s. The St35.8III steel was used for the tubes of water walls, economizer and inlet primary superheater, 15Mo3 steel was used for inlet secondary superheater tubes, 13CrMo44 for outlet primary and secondary superheater tubes.

Table 1. Creep test results.

Steel	Specimen designation	Temp. [°C]	Stress [MPa]	Hours to Rupture	Result	Location
13CrMo44	10.1	590	110	373	Rupture	Primary SH
	10.2	590	90	817	Rupture	
	14.1	590	160	2,5	Rupture	Secondary SH
	14.2	590	110	92	Rupture	
	14.3	590	70	1 754	Rupture	
	15.1	590	90	543	Rupture	
	15.2	590	110	135	Rupture	
	15.3	590	80	1 317	Rupture	
15Mo3	12.1	580	140	2	Rupture	Secondary SH
	12.2	580	90	187	Rupture	
	12.3	580	60	1 559	Rupture	
	13.1	580	80	755	Rupture	
	13.2	580	100	60	Rupture	
	13.3	580	70	716	Rupture	
St35.8III	11.1	500	110	984	Rupture	Primary SH
	11.2	500	140	197	Rupture	

## St 35.8

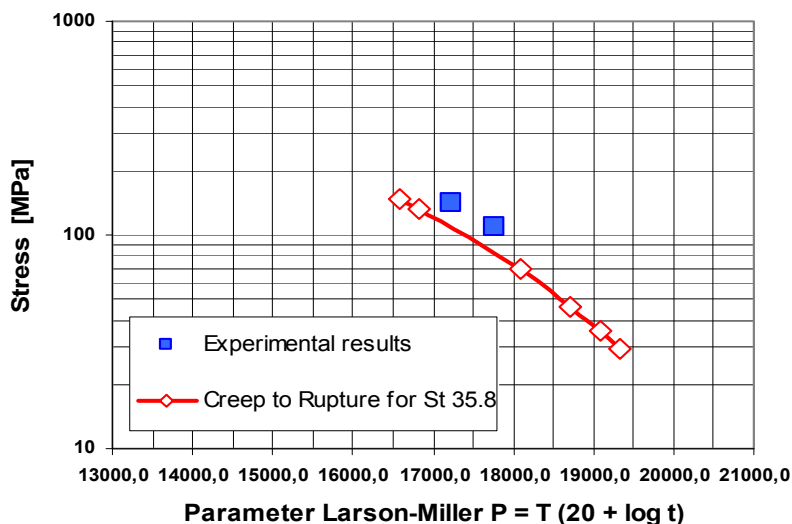


Figure 1. Comparison of tube creep results of the St 35.8 III steel after 205 000 hrs of service and creep-to-rupture properties of this steel. (For the creep-to-rupture properties of this steel see Taschenbuch : Stahl und Rohrenwerk Reisholz GmbH, einschliesslich 23. Nachtragslieferung, abgeschlossen im November 1971, Teil II).

## 13CrMo 44

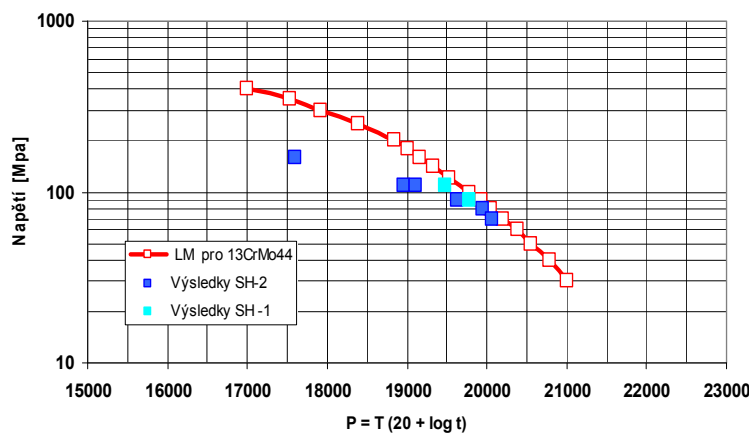


Figure 2. Comparison of tube creep results of the 13CrMo44 steel after 205 000 hrs of service and creep-to-rupture properties of this steel. (For the creep-to-rupture properties of this steel see "Warmfeste Werkstoffe für Kraftwerksanlagen", VEB WTZ Kraftwerksanlagenbau Pirna 1965, Autorenkollektiv: H. Seidel (Federführung), G. Arndt, R. Elze, R. Hennig, B. Melzer, K.-H.Patzer, W. Rossner, H.-K. Shiller).

### 15Mo 3

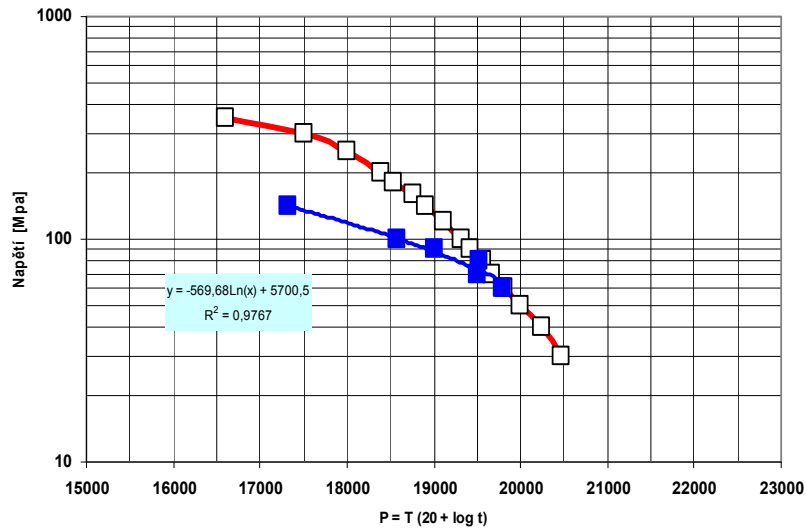


Figure 3. Comparison of tube creep results of the 15Mo3 steel after 205 000 hrs of service and creep-to-rupture properties of this steel. (For the creep-to-rupture properties of this steel see "Warmfeste Werkstoffe für Kraftwerksanlagen", VEB WTZ Kraftwerksanlagenbau Pirna 1965, Autoren: H. Seidel (Federführung), G. Arndt, R. Elze, R. Hennig, B. Melzer, K.-H.Patzer, W. Rossner, H.-K. Shiller).

For the purposes of this evaluation, the regression lines were constructed through the experimental points. These regression equations were then used to calculate the respective values of the Larson-Miller Parameters for the three abovementioned „safety“ situations what resulted in the remaining operational hours given in the Table 2.

Table 2. Remaining lifetime of the tested tubes resulted in the following results (only „FULL SAFETY“ is given).

Component	Material designation	Working temperature, °C	Remaining lifetime, years
Primary superheater (inlet)	St 35.8 III	385	51,9
Primary superheater (outlet)	13CrMo44	440	15 867,5
Secondary superheater (inlet)	15Mo3	450	261,7
Secondary superheater (outlet)	13CrMo44	485	311,2

## 2.2 Conclusions (Case „2“)

Taking into consideration even the full operational safety of the boiler, i.e. the abovementioned item No.3 „Full safety“, the remaining lifetimes of the tubes tested is sufficiently long in order that the components are operated safely till the next inspection. It can be thus assumed that all other high temperature components of this boiler in question made of these steels possess the similar quality.

## 3. CASE „3“

### 3.1 Boiler description and technical details

- Nominal steam output: 730 t/hr
- Steam temperature: 515°C
- Steam pressure: 9.2 MPa
- Operational hours (approx.): 177 000

Table 3. Results of the creep tests – steel 15 CD2.05 (A213T2), HTSH outlet.

Larson-Miller Parameter	Stress [MPa]	Temperature [°C]	Hours to rupture	Test sample	Result
20001	75	580	3400	26	rupture
19849	90	580	1098	26F *)	rupture
20001	75	580	3218	66	rupture
19849	90	580	1159	66F *)	rupture

\*) tube flame side

Table 4. Remaining lifetime calculation – 15 CD 2.05 (T2) steel, tubes 26,66. \*) maximum radius and minimum thickness measured during testing included.

Pressure [MPa]	Tube radius [mm/*]	Tube thickness, [mm/*]	Stress [MPa]	Temp. [°C]	Remaining lifetime [years]
9,2	24,4	5	44,9	515	1 506,15
13,8	24,4	5	67,3	515	79,33
13,8	24,4	5	67,3	585	0,618



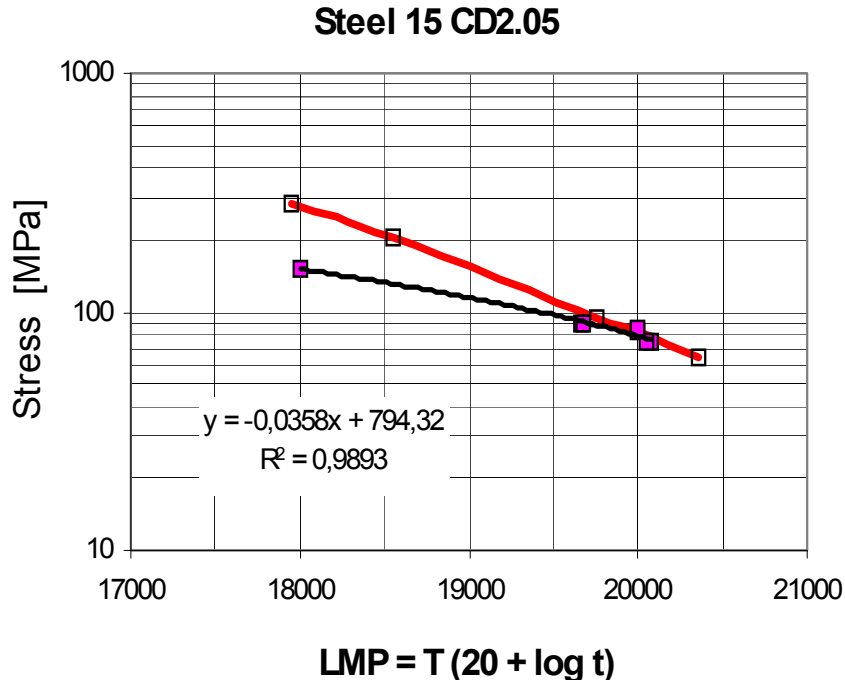


Figure 4. Creep to Rupture Curve and accelerated Creep Test Results, steel 15 CD2.05 (A213 T2).

Table 5. Remaining lifetime calculation – 15 CD 2.05 (T2) steel, tube 26. (Temperature determined according to the scale thickness after cleaning).

Pressure [MPa]	Tube radius [mm/*]	Tube thickness [mm/*]	Stress [MPa]	Temperature [°C]	Remaining lifetime [years]
9,2	24,4	5	44,896	511	2 071
13,8	24,4	5	67,344	511	107
13,8	24,4	5	67,344	581	0,799

Table 6. Remaining lifetime calculation – 15 CD 2.05 (T2) steel, tube 66. (Temperature determined according to the scale thickness after cleaning).

Pressure [MPa]	Tube radius [mm/*]	Tube thickness [mm/*]	Stress [MPa]	Temperature [°C]	Remaining lifetime [years]
9,2	24,4	5,1	44,017	509	2 810
13,8	24,4	5,1	66,024	509	144
13,8	24,4	5,1	66,024	579	1,038

### 3.2 Conclusions (Case „3“)

The HTSH tubes creep tests and remaining lifetime calculations revealed a considerable exhaustion of the remaining lifetime capacity, so that when taking into consideration the full operational safety of the boiler, i.e. the abovementioned item No.3 „Full safety“, the remaining lifetime has been (nearly) exhausted and the respective components should be replaced as soon as possible.

Till that time, the boiler will be operated with limited safety what should result in the precise keeping the service pressures and temperatures within the designed limits. The present situation of the HTSH tubes is also the result of the steel grade and tube dimensions used in the construction.

## 4. Final summary and conclusions

Two further examples (in addition to [1]) of boiler HTSH components remaining lifetime evaluation were presented. Making use of Larson-Miller parameter made it possible to perform accelerated creep tests of the tube material and quantify the remaining lifetime of the structure. The acceleration of the creep tests can substantially shorten the outage time and improve the economy. Together with the other common metallographic, chemical and mechanical tests, this procedure makes it possible to improve the overall assessment of the remaining lifetime of structures. Nevertheless, the number of service hours and the year of production should be taken into consideration when making decisions on the frequency of the subsequent inspections. The creep phenomena are of cumulative nature and accelerate close to the end of the lifetime exhaustion. It should be also taken into consideration, that only creep (as surviving phenomenon

in case of high temperature components) was considered in the remaining life calculation. Cyclic loading causing material fatigue and corrosion that can cause the geometry changes of the components and thus increase the stresses can thus contribute to the material damage and accelerate the process of material degradation.

## References

1. Mentl, V. & Liška, V. Remaining life assessment of steam turbine boilers. In: Veivo, J. & Auerkari, P. (Eds.). Proc. of International Conference on Life Management and Maintenance for Power Plants, BALTICA VII, Helsinki–Stockholm–Helsinki, 2007. VTT Symposium 246, Vol. 1. Pp. 106–112. ISBN 978-951-38-6315-9.
2. Liška, V., Koc, J., Chocholoušek, M. & Mentl, V. Hodnocení stupně degradace vysokoteplotních komponent, Sb. konf. „Kotle, energetická zařízení a kogenerace 2008. Praha, 3/2008.
3. Mentl, V. & Liška, V. Failure risk assessment and remaining lifetime evaluation of power plant steam boilers. 3rd Int. Conf. on Engineering Failure Analysis ICEFA III. Sitges, Spain, 7/2008.
4. Liška, V., Koc, J., Chocholoušek, M. & Mentl, V. Evaluation of degradation extent and remaining lifetime assessment of steam turbine boilers. Int. Conf. “Optimizing Operational Outages”. Budapest, Hungary, 9/2008.

# **Creep strain, damage and life prediction for welded 0.5CMV steel**

Juhani Rantala, Pertti Auerkari, Stefan Holmström,  
Jorma Salonen and Anssi Laukkanen  
VTT Technical Research Centre of Finland  
Espoo, Finland

## **Abstract**

Creep damage as cavitation and cracking has historically occurred somewhat earlier in the inspections of steam lines made of 0.5CMV steel, when compared to other low alloy steels. The difference has been attributed to modest creep ductility of 0.5CMV steel, and has resulted in attention paid to inspection and maintenance. As the steel is still being used in vintage plants, it is of interest for users while also serving as a model material that can show some essential features of long term creep in much shorter laboratory testing. Particularly challenging service can combine welded thick-wall components with pre-existing fabrication defects, resulting in an unfavorable combination of high stresses, multi-axial loading, and locally weak material. Examples are shown of the observed damage evolution in welded 0.5CMV steam line material in front of a crack-like defect. Long-term multi-axial loading does not necessarily result in type IV failure of welds, but can also induce creep damage and cracking close to the fusion line. This particularly applies to welds with undermatching weld metal such as those made with consumables corresponding to 2.25Cr-1Mo steel. With the LICON approach, it has been shown that this IIIa type of damage can be reproduced in about 5 000 h of multi-axial creep testing, while in plant such damage may require more than 100 000 h of service. The microstructural features of the observed damage and a comparison of uniaxial and CT test data suggest that the LICON approach of life prediction could be applied also for

welded components where the location of maximum damage deviates from the type IV position.

## 1. Introduction

Ageing power plants make use of some vintage materials that are no more applied in new plant. However, even for old materials new issues can arise, for example on the need, timing and procedures of repairs of aged components with indicated creep damage. As the on-condition maintenance according to the observed state is often based on earlier experience, it may not be self-evident whether such practices are prudent or overly conservative, e.g. for the reason of the experience based on worst cases, suboptimal technical practices or on conservative attitudes towards early damage [1, 2].

A well known vintage material in power plant applications is 0.5CMV steel, also known as 14MoV6-3 by its European standard designation, for example in the most recent edition of EN 10216-2 [3] on seamless tubes and pipes. This steel type has been widely used from 1960's to 1970's in hot live and reheat steam lines of thermal power plants. Considering its low alloy content (nominally 0.5% Cr, 0.5% Mo and 0.25% V) it has high creep strength due to MX-type precipitation strengthening, when properly heat treated. However, it can have relatively modest creep ductility, and also susceptibility to reduced cross-weld creep strength similar to other ferritic steels. Ductility issues and the emergence of competitive newer steels (such as X20CrMoV11-1 and X10CrMoVNb9-1) made the steel redundant in new plants from late 1970's to early 1980's onwards. Nevertheless, limited ductility and weld behaviour make this material of interest for those plants that are still operating with pipings made of it, and also as a model material for exploring the evolution of creep damage.

This paper aims to contribute to the high temperature life assessment knowledge on creep damage evolution and creep of welded 0.5CMV steel (14MoV6-3). The work aims to provide a qualitative and quantitative description of creep damage and crack initiation in a weld prepared with undermatching consumables, as a test case for the LICON approach of accelerated creep life assessment [4], and creep strain and rupture modeling for a COST case study material (also 0.5CMV).

## **2. Materials and methods**

### **2.1 Creep (CT) testing of 0.5CMV steel**

Cross-weld CT specimens ( $W = 25$  mm) were extracted from an ex-service 0.5CMV steam line material that had been re-heat treated to correspond as well as possible to as-new steel, and then welded with an undermatching consumable corresponding to that for welding  $2\frac{1}{4}$ Cr-1Mo steel (10CrMo9-10). The welding was performed to a special groove to provide a straight HAZ for subsequent testing. The welded 0.5CMV material and its pedigree data was provided by British Energy (UK). All CT creep testing for crack initiation was performed under constant load with monitoring of temperature, mouth opening at load line and crack growth (by DCPD). The testing conditions were set so that the longest testing time to crack initiation (to at least 0.5 mm) would be about 5000 h at 540°C. A narrow (0.14 mm) EDM tip was machined into the middle of the HAZ of each CT specimen notch for creep crack initiation from the HAZ.

### **2.2 Creep strain and rupture modeling**

Creep strain was modeled using the logistic creep strain prediction (LCSP) methodology, described in detail elsewhere [5]. The model requires a time to rupture model as base and two shape functions. The two presented rupture models were fitted to average strength values from standard rupture data tables of EN 10216-2 and from ISO data (1978) evaluated in the SPRINT 249 project [6]. The strain model is based on SPRINT 249 / ISO data time to strain tables enhanced with rather high temperature creep curves of a COST case data. The COST case data consisted of 6 tests in the stress range of 40-55 MPa at temperatures of 600-650°C. For modeling the procedures were in accordance to the ECCC Recommendations [7].

The COST and the EN/SPRINT/ISO rupture data values overlap at 600°C / 40 MPa with a time factor of about 2.7 calculated as SPRINT over COST data rupture times. The corresponding stress reduction factor is 0.63 in comparison to models based on data from both [3] and [6].

The temperature range for the EN 10216-2 based rupture model is from 490 to 560°C, SPRINT/ISO data (both rupture and time to strain tables) have a temperature range of 480–600°C. The stress ranges are 59–279 MPa (EN standard rupture values) and 8–299 MPa for the SPRINT/ISO data. Since the

bulk of the data is describing times to rupture (or strain) at durations from 10 000 h to 250 000 h, applicability of the rupture and strain models may not be well established for short term predictions.

The logistic creep strain prediction (LCSP) approach [5] was used to model time to strain using the average stress to given strains of 0.1% to 5% as shown for the 550°C isotherm in Figure 1.

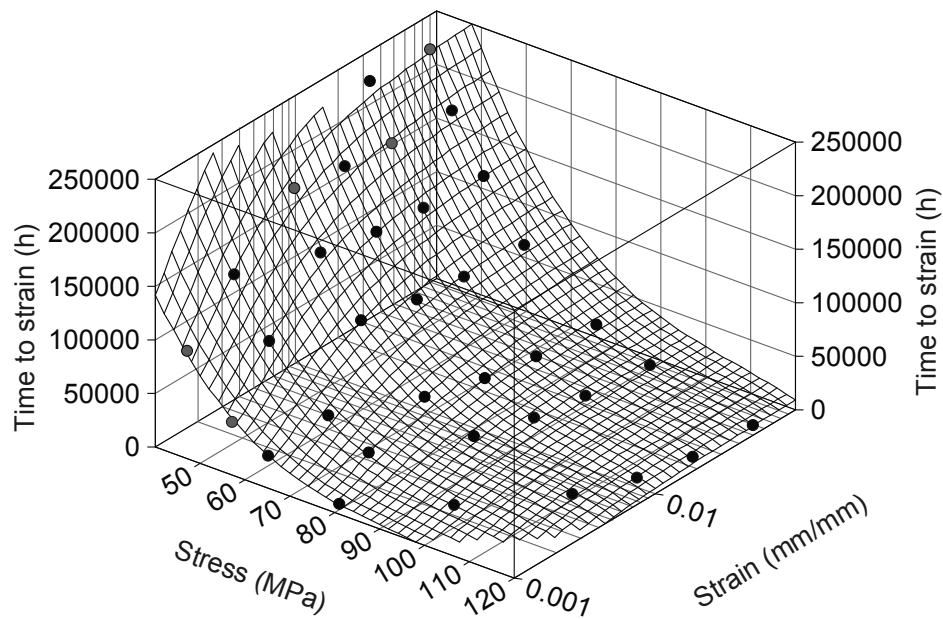


Figure 1. The 550°C isotherm for time to specified strain (SPRINT/ISO data).

### 3. Results

#### 3.1 Creep (CT) testing of 0.5CMV steel

The CT specimen testing results with the observed time to creep crack initiation are shown in Table 1. The longest test has practically achieved the intended maximum duration of 5 000 h at the time of interruption. The crack appearance after interruption is shown in Figures 3 and 4. The emerging creep crack was growing intergranularly in the coarse grained heat affected zone (CGHAZ), but in the shortest tests also straining in the main tensile stress direction, at least as

crack tip opening (Figure 5). When extensive enough, all tests resulted in type III cracking along the fusion line. More details of the crack in the longest test (CT5) are shown in Figures 6–9.

Table 1. Results of CT specimen testing (time to crack initiation; here Sref1 = plane strain Mises stress; Sref2 = plane stress Tresca stress.

Specimen	K (MPa√m)	Sref1 (MPa)	Sref2 (MPa)	Time (h)
CT1	15.0	85.1	135.2	198
CT2	13.5	76.5	121.6	434
CT3	12.0	67.8	107.8	888
CT4	11.0	62.3	99.0	2705
CT5	9.0	51.0	81.1	4673
CT6	8.0	45.6	72.4	11453

### 3.2 Creep strain and rupture modeling

A good description of the rupture data was found using the DESA software of TU Darmstadt. The COST data required a stress correction factor of 0.63 for minimal residuals in comparison with the models based on values given in [3] and [6]. The time to rupture at specified stress and temperature can be described by the Manson-Brown master curve

$$P_{MB} = \frac{\log_{10}(t_u) - \log_{10}(t_a)}{\left[ \frac{T + 273 - T_a}{1000} \right]^R} = \sum_{i=0}^N B_i f(\sigma)^i \quad (1)$$

where  $t_u$  is the time to rupture,  $T$  the temperature in °C and  $\log(t_u)$ ,  $T_a$ ,  $R$  and  $B_i$  are fitting parameters. Fitting resulted in a scatter factor [7] of  $Z = 1.06$  for the EN 10216-2 values, and  $Z = 1.04$  for the SPRINT values. For the SPRINT model the stress dependence was better described with a stress function in the form of  $\sigma^n$  instead of  $\log(\sigma)$ .



The LCSP model for the whole creep curve is defined as [7]

$$\log(\varepsilon_t) = \left( \frac{\log(t_u) + C}{\log(t_\varepsilon) + C} - 1 \right)^{1/p} \cdot x_0 \quad (2)$$

where  $\varepsilon_t$  is the predicted strain at time  $t_\varepsilon$ , and  $t_u$  is the rupture time that can be taken from the master curve for creep rupture. The  $p$  and  $x_0$  parameters are temperature and stress dependent, and  $C$  is a constant.

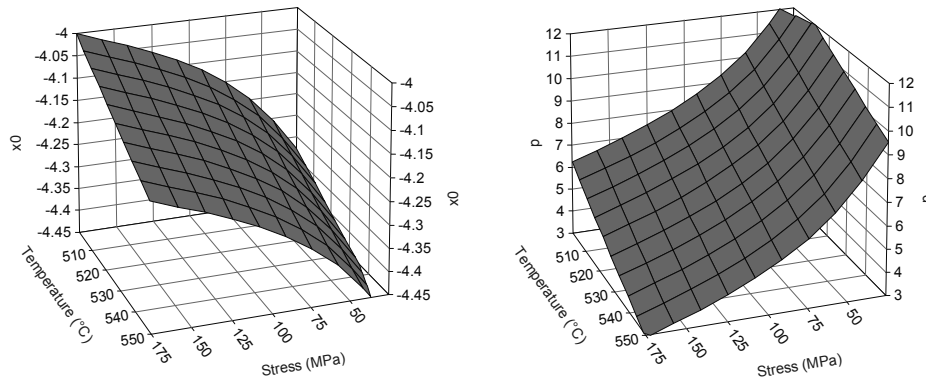


Figure 2. Temperature and stress dependence of the shape parameters for 0.5CMV steel.

A comparison of predicted vs. measured/table values of time to specified strain is shown in Figure 10. The predicted evolution of creep strains and strain rates as a function of life fraction at 550°C and 70 MPa (= 100 000 h life from SPRINT/ISO data) using the LCSP model is shown in Figure 11.

Creep strain, damage and life prediction for welded 0.5CMV steel

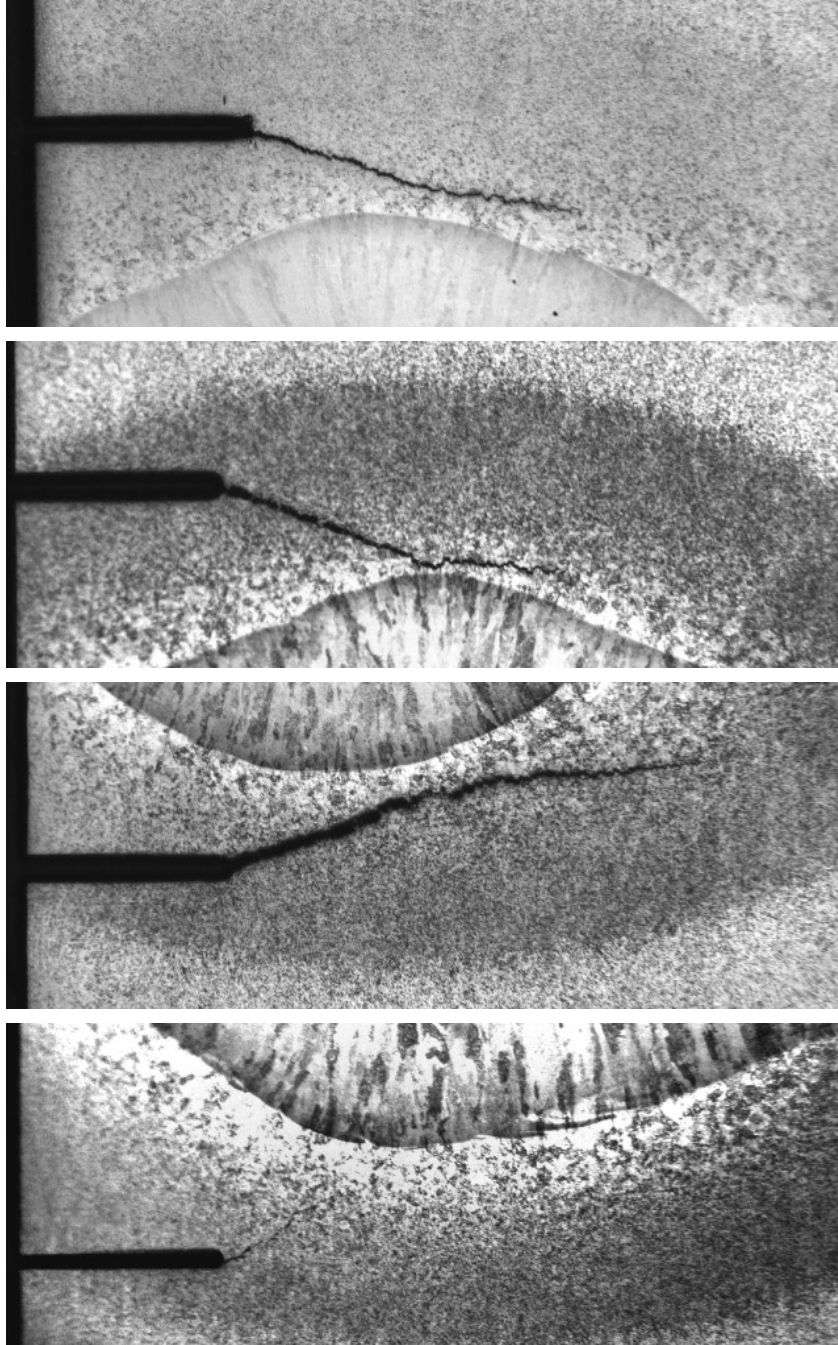


Figure 3. The crack of specimens CT1-CT4: crack has grown to CGHAZ close to the fusion line. Scale as in Figure 4.

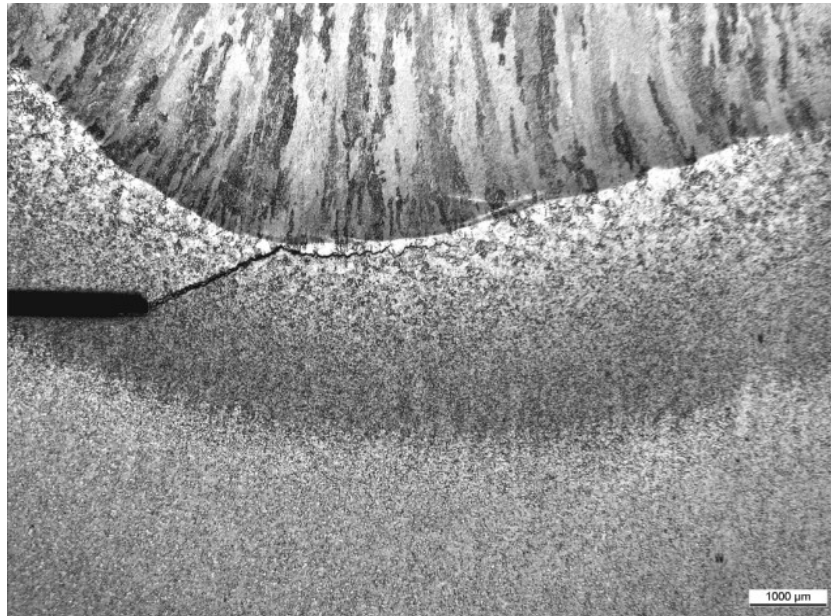


Figure 4. The crack of specimen CT5: crack has grown through CGHAZ to region close to the fusion line (type III crack).

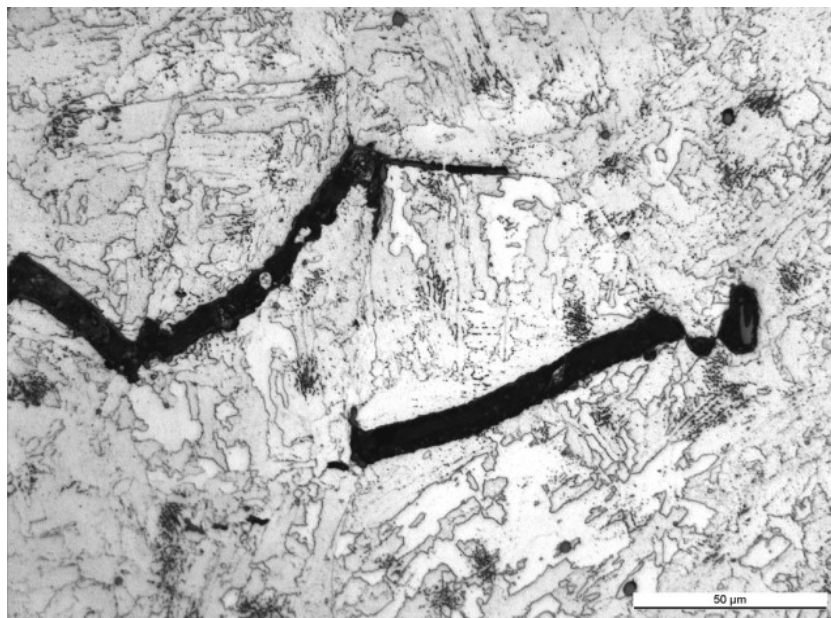


Figure 5. The crack tip of specimen CT2: note opening of intergranular cracks in the vertical (loading) direction.

Creep strain, damage and life prediction for welded 0.5CMV steel



Figure 6. The end section of the crack of specimen CT5 close to the fusion line.

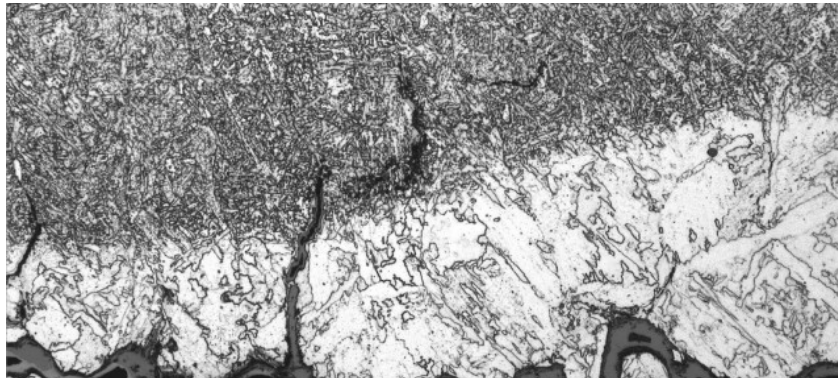


Figure 7. A detail of Figure 4; crack of specimen CT5 extending to weld metal.

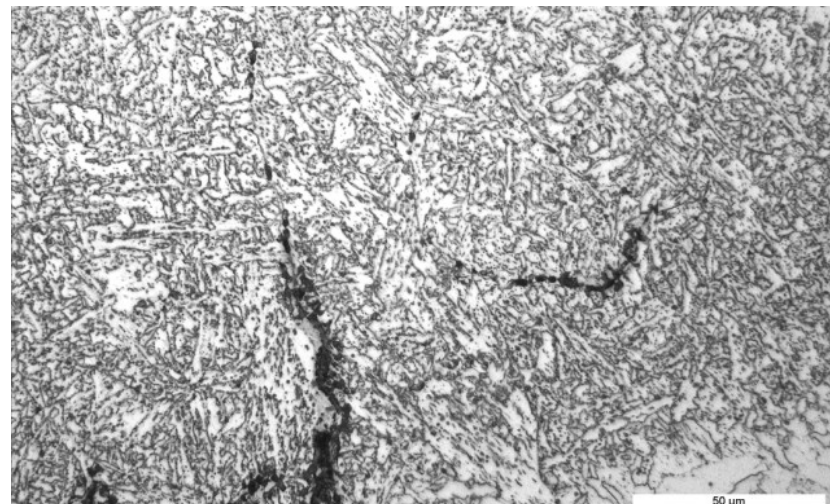


Figure 8. A detail of Figure 7; crack of specimen CT5 in weld metal.

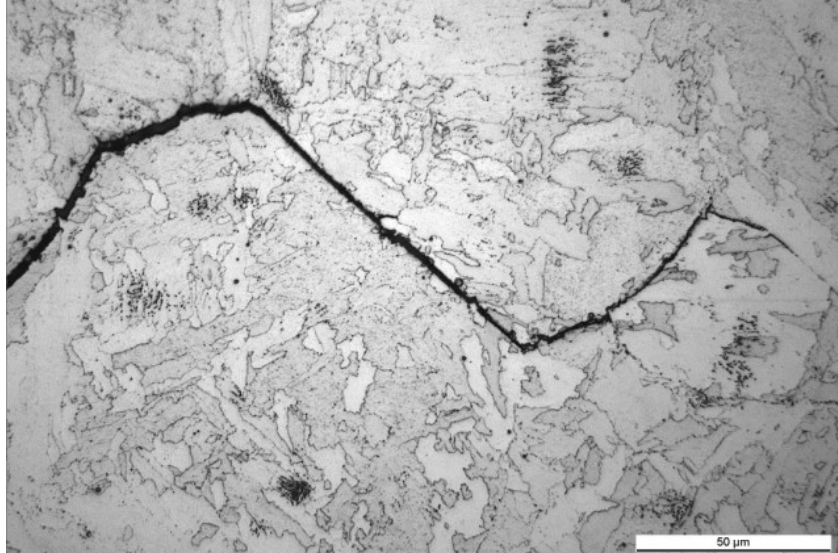


Figure 9. A detail of Figure 6; crack tip of specimen CT5.

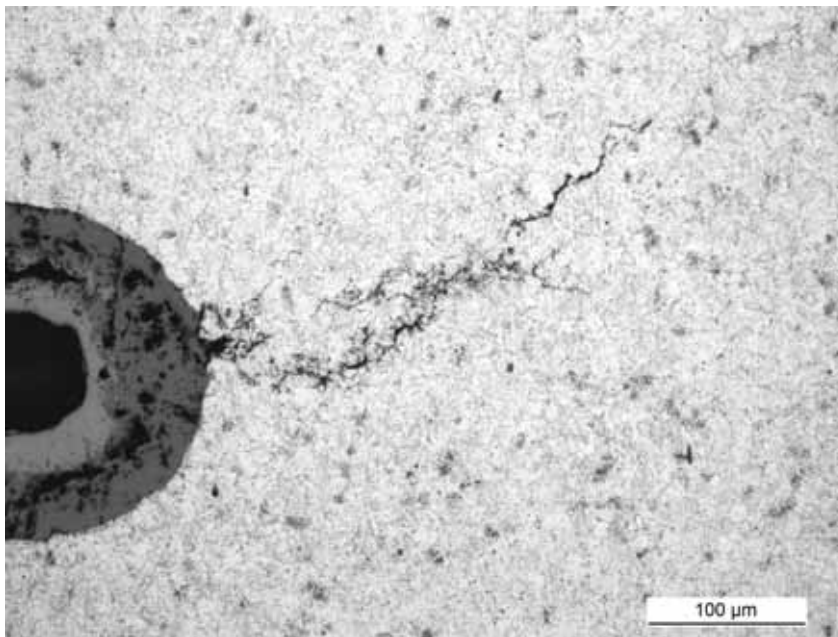


Figure 10. Specimen/test CT6: the crack is growing towards the CG-HAZ.

Creep strain, damage and life prediction for welded 0.5CMV steel

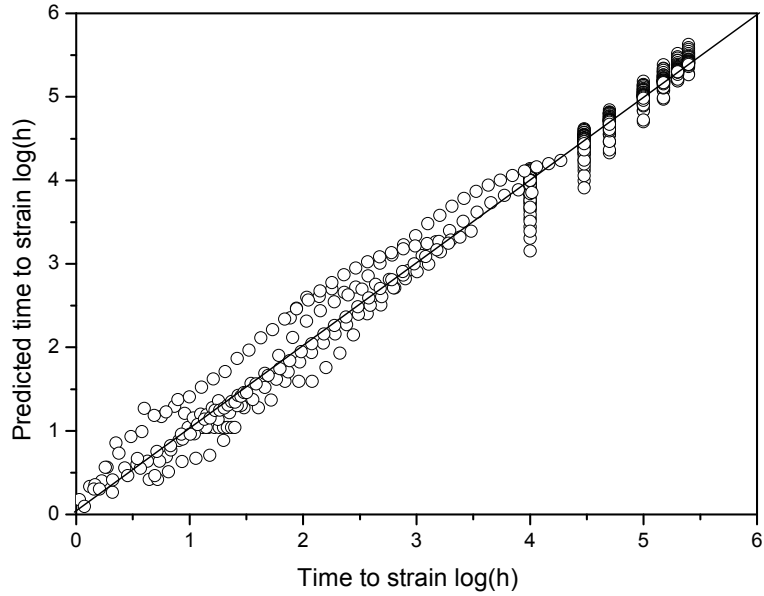


Figure 11. Predicted vs. measured/table values of time to specified strain (continuous curves from tests, vertically aligned data from [6];  $Z = 2.1$ )

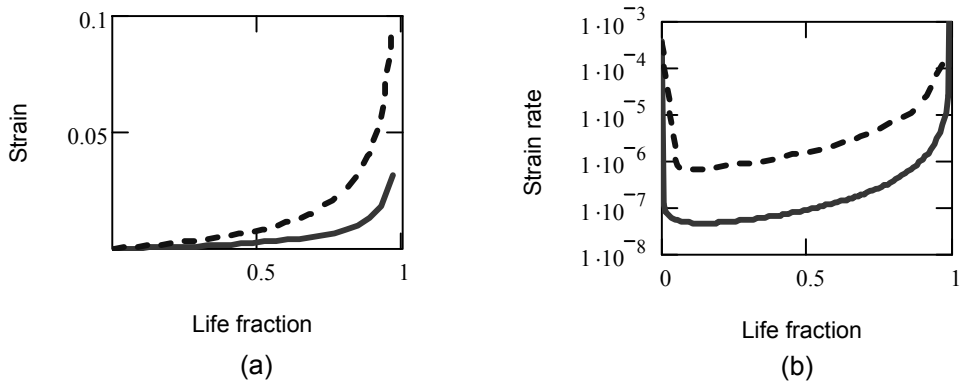


Figure 12. a) Normalised creep strain and b) creep strain rate at 550°C / 70 MPa (continuous line, 100 000 h life from [6] and at 600°C/58 MPa (dashed line, a simulated creep test).

## 4. Discussion

### 4.1 Creep strain and rupture modeling

The accuracy of the creep strain model mainly relies on the mean stress values to given strain as reported in [6]. The model has been validated by calculating minimum creep rates from the LCSP model and comparing these to values from [8] at 565°C for both short and long term tests (Figure 13). The LCSP shape functions from the data predict minimum creep rates with a scatter factor  $Z = 4.5$ , and with a very satisfactory slope. The results suggest that the LCSP approach is not only robust and easy to apply in the sense of requiring minimal data, but that the model predicts creep strains and strain rates surprisingly accurately (Figures 11 and 13).

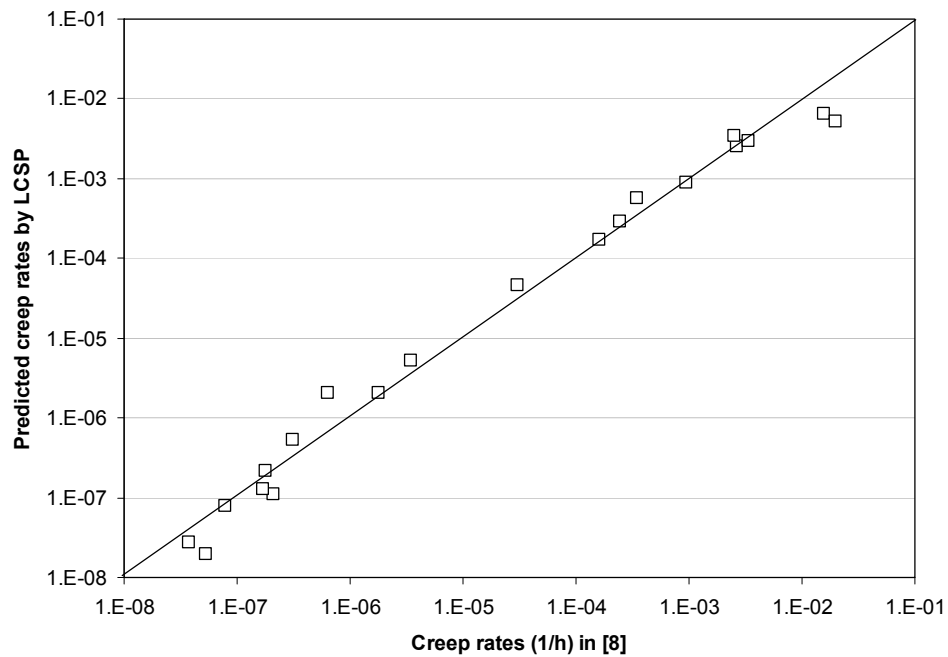


Figure 13. LCSP predicted minimum creep rates for 0.5CMV steel in comparison to rates given in [8], with time to rupture calculated using SRF = 0.7 in relation to EN-10216 model; for strain rate  $Z = 4.5$ .

## 4.2 Creep (CT) testing of 0.5CMV steel

In the LICON approach of life prediction, the stress multi-axiality at the tip of a notch or crack of a CT specimen is applied to accelerate creep crack initiation [4]. The approach aims to reduce the risk of unwanted mechanism changes that could result in non-conservative predicted life (Table 2). By definition, the approach requires that intergranular creep cavitation appears at the initiating crack to indicate classical long term damage. For welds of ferritic steels, this was typically interpreted as distributed dense creep cavitation at the fine grained or intercritical HAZ.

Table 2. Comparison of methods to accelerate creep and creep failure

Elevated quantity	Advantages	Limitations/disadvantages
Temperature	Simple, strong acceleration	Mechanism change possible <sup>1)</sup>
(Effective) stress	Simple, strong acceleration	Mechanism change possible <sup>1)</sup>
Stress multi-axiality	Damage enhancement	Control of stress level <sup>2)</sup>

1) with little or no enhancement of creep cavitation damage

2) complex testing geometry, requires finite element analysis (FEA)

However, in the present example the observed damage is not at this type IV position, but rather lies on the inner side of HAZ, either within the CGHAZ (specimens CT1 to CT3) or close to the fusion line (CT5). There is no indication of the damage deviating towards the type IV position, although the initial notch position would easily allow this as the crack first initiates close to the central region of HAZ (Figures 4–9). It also seems that towards longer times approaching 5 000 h of testing, the crack stays very close to the fusion line (Figures 6–9). The distance from the apparent fusion line is up to few grain boundaries only, and in one location the crack even branches to the weld metal side (Figures 7 and 8). The crack position appears roughly consistent of type IIIa damage, where carbon diffusion to the higher chromium weld metal creates a carbon depleted weaker zone in the HAZ next to the fusion line. Under typical plant conditions this may typically take some 200 000 h at similar or higher temperatures [9].

Another suggested indicator of long term damage is gb cavitation on the grain boundaries orientated against the highest tensile stress (Figure 14). While similar densities of creep cavitation damage as in type IV damage are not likely,



it is concluded that the observed mode of creep damage is expected to remain within the applicability limits of the LICON approach. Comparison of CT test results to uniaxial standard rupture stress also suggests potential for life prediction when using the LICON principle (Figure 15). Note that here a better – though still not perfect – compatibility of the slopes is obtained by taking the uniaxial correspondence to the weld metal (2.25Cr-1Mo) than to parent metal (0.5CMV). This may make sense as the crack is following the fusion boundary and also explores the weld metal side (Figures 7 and 8).

Further confirmation is sought from additional FEA of the case.

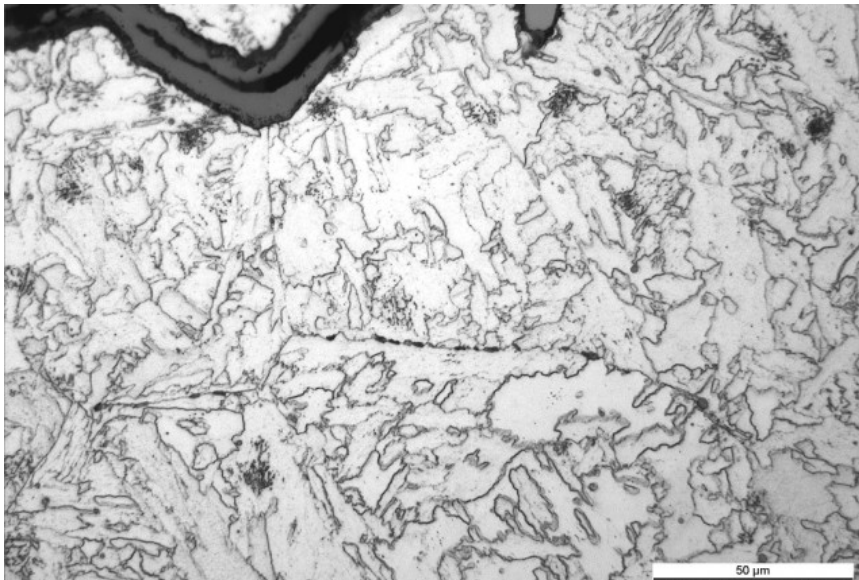


Figure 14. Grain boundary cavitation parallel to crack growth in CGHAZ of specimen CT5.

Creep strain, damage and life prediction for welded 0.5CMV steel

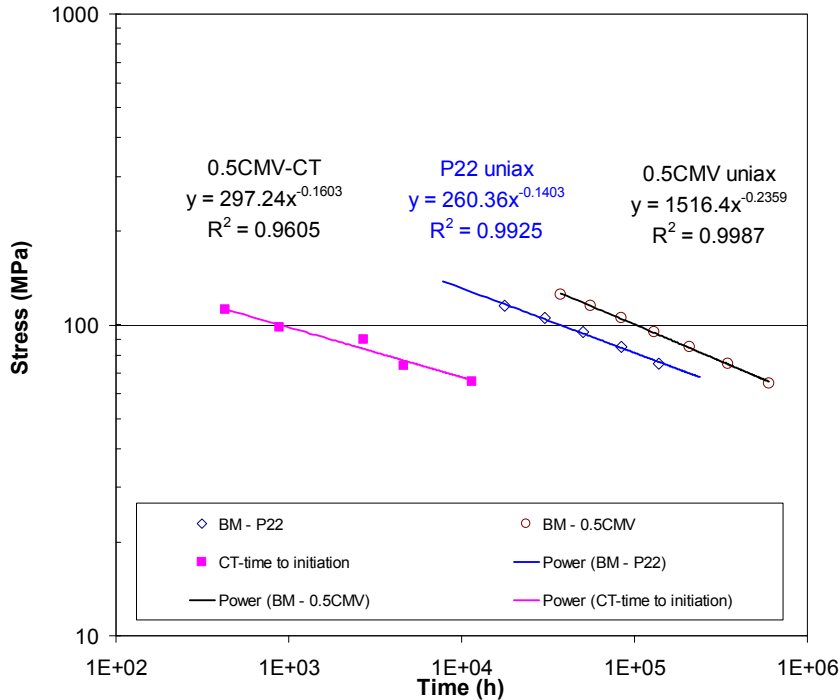


Figure 15. Comparison of CT (multi-axial) testing results and uniaxial data for 0.5CMV and 2.25Cr-1Mo steel (weld metal) using the LICON approach.

There remain some questions of interest in the performance of the LICON approach. When isothermally applied, it is not immediately clear how well does the method account for the presumably differing kinetics of long term thermal degradation (e.g. growth, coarsening and dissolution of strengthening precipitates) and stress activated damage such as transport and coalescence of vacancies and grain boundary cavities. In determining the long term standard creep properties by uniaxial testing the problem is circumvented by testing up to the time-temperature-stress range of the expected applications. When this is too slow and accelerated creep testing must be used, increasing the test temperature rather than stress is often recommended to avoid non-conservative life prediction [7]. While increased stress multi-axiality is not very similar to increased stress level in this respect, disregarding the possible additional impact of thermal degradation is not automatically justified. Against this background it appears of some consolation that multi-axial (CT) creep testing of 0.5CMV welds has been shown to reproduce the expected type of long term damage in a surprisingly short time.

## 5. Summary

To characterize creep crack initiation in the HAZ of 0.5CMV steel welded with an undermatching P22 consumable, creep testing of CT specimens with the notch tip in the HAZ has been performed up to 4700 h at 540°C. The observed creep crack tip in the longest test resided on the inner side of HAZ, close to the fusion line (type III or IIIa damage). The damage was characterized by intergranular crack growth preceded by creep cavitation mainly on the same and parallel grain boundaries approximately perpendicular to the principal loading direction. It was concluded that in spite of relatively low overall creep cavitation density, the observed damage is of the true long term type for the case and is expected to remain within the applicability limits of the LICON approach. Approximately 5000 h of testing time seems therefore sufficient to achieve the desired stable characteristics of long term damage.

A Manson-Brown type of expression was optimized to describe creep rupture of 0.5CMV steel. The reference material from an ex-service component required a stress correction factor of 0.63 in comparison with the standard mean values of EN 10216-2. The creep strain model mainly relies on the data from the European SPRINT 249 project. The model has been validated by calculating minimum creep rates from the LCSP model and comparing these with values from literature. Good agreement was observed with a scatter factor of  $Z = 4.5$ , and also with a very satisfactory slope. The results suggest that the LCSP approach is not only robust and easy to apply in the sense of requiring minimal data, but that the resulting models can accurately predict creep strains and strain rates.

## Acknowledgement

David Dean from British Energy is acknowledged for providing the welded CMV test material and related background information. The Academy of Finland is acknowledged for funding the work under Decision no. 117700 (prof. Kim Wallin).

## References

1. Salonen, J., Auerkari, P., Lehtinen, O. & Pihkakoski, M. Experience on in-service damage in power plant components. 2nd Int. Conf. on Engineering Failure Analysis (ICEFA-II), Paper O8.1. Toronto, Canada, 12–15 Sept 2006.

Creep strain, damage and life prediction for welded 0.5CMV steel

2. Auerkari, P., Salonen, J., McNiven, U. & Jovanovic, A. Classification of damage and prediction of its development in high temperature components of the power industry. *Failures '96*. A. A. Balkema (1996), pp. 269–280.
3. EN 10216, 2002. Seamless steel tubes for pressure purposes. Technical delivery conditions. Part 2: Non-alloy and alloy steel tubes with specified elevated temperature properties. CEN, Brussels.
4. Auerkari, P., Bendick, W., Holdsworth, S., Rantala, J. H., Hurst, R., Coussement, C. & Hack, R. Predicting long-term creep behaviour using the LICON methodology. *Proc. of the Conf Advances in Materials Technology for Fossil Power Plants*. University of Wales, Swansea, 1–6 April 2001.
5. Holmström, S. & Auerkari, P. Robust prediction of full creep strain curves from minimal data and time to rupture. *Materials Science and Engineering for Energy Systems 1* (2006), pp. 249–255.
6. Standard Data Tables, Vol. 2, Ferritic steels. SPRINT SP 249, 1995.
7. ECCC Recommendations, Vol. 5: Guidance for the assessment of uniaxial creep data, 2005.
8. Evans, R. W. & Wilshire, B. *Introduction to Creep*. Institute of Materials, London, 1993, p. 91.
9. Brett, S. (RWE npower, UK), 2006. Personal communication.
10. Holdsworth, S. & Mazza, E. Exploring the applicability of the LICON methodology for a 1%CrMoV steel. *Materials at High Temperatures*, Vol. 25, No. 4, pp. 267–276.
11. Hales, R. The role of cavity growth mechanisms in determining creep rupture under multiaxial stresses. *Fat. Fract. Eng. Mater. Struct.*, 1994. Vol. 17, 579–591.

# Different types of cracking of P91 steel weld joints after long-term creep tests

Dagmar Jandová, Josef Kasl and Eva Chvostová  
ŠKODA VÝZKUM s.r.o.  
Plzeň, Czech Republic

## Abstract

The paper deals with creep testing and microstructural investigation of trial weld joints prepared of wrought and cast 9Cr-1Mo-V steels using GTAW & SMAW method. Creep testing was carried out at temperature range from 525°C to 625°C, the longest time to rupture of 45 811 hrs was achieved. The creep strengths of weld joints for 100 000 hrs were calculated. Different types of cracking were observed in dependency on conditions of creep test and the type of weld joint. Type I and Type II fractures occurred at high applied stresses at relatively low temperatures in the tube weld joint and also in two specimens of the cast plate weld joint after creep test at the lowest temperature and the highest temperature. All other fractures were of the Type IV. Causes of different fracture location in tested weld joints were elucidated on the base of substructure evolution in individual zones – the weld metal, the heat affected zone and the base material. Two processes occur simultaneously, which result in the creep damage: i) softening of solid solution as a result of Laves phase precipitation and ii) formation and coalescence of cavities in the soft fine grained parts of heat affected zone.

## 1. Introduction

Grade 91 steel is widely used for production of components for fossil fuel power plants, which operate under severe service conditions for many years. A great attention was paid to investigation of creep properties of this grade and a lot of creep data were collected. Nevertheless experience has shown that some difficulties

persist in production and operating of components made of P91 steel. A number of unexpected in-service failures of grade P91 components correctly fabricated with desirable tempered martensitic structure demonstrates that study of long-term properties and failure development is still of a great importance. Type IV cracking of welds, which occurs in the fine grained region towards the parent side edge of the heat affected zone, belongs to the most often observed failure [1].

The paper deals with a study of trial weld joints prepared in conditions of real production of piping and cast components of steam turbine. Fracture mechanism after long-term creep exposures is correlated with microstructural processes taking place in individual parts of weldments. Partial results of performed experiments have already been presented in several conferences [2, 3, 4].

## 2. Experimental procedures

Two trial weld joints were fabricated from wrought or cast P91 steel using GTAW & SMAW methods. The first weld joint (C) was produced by joining cast plates  $500 \times 150 \times 25$  mm in size and the second one (C1) by joining tube segments with an outer diameter of 325 mm, a wall thickness of 25 mm and a length of 400 mm. The plates and the tube segments were joined in PA and in PC position respectively. The same conditions of welding process were kept for both weld joints [2]. The chemical composition of the base materials and the weld metals was verified using XRF method (Table 1). Both base materials were austenitized at  $1050^{\circ}\text{C}$  for 1.5 hrs, then oil quenched and tempered at  $750^{\circ}\text{C}$  for 3.5 hrs. The post-weld heat treatment (PWHT) was applied as follows:  $(740\div 750)^{\circ}\text{C}/2.5$  hrs for the C weld joint and  $760^{\circ}\text{C}/2.5$  hrs for the C1 weld joint. Smooth cross-weld specimens underwent long-term creep testing to rupture. Fractographic analysis was carried out using scanning electron microscopy (SEM). Metallographic samples were prepared in longitudinal section, macro and microstructures were revealed using Vilella's reagent, location of fracture was specified and structure was observed using light microscopy and SEM. Cross-weld Vickers hardness profiles of as received weld joints in conditions after PWHT and after creep tests were measured. Transmission electron microscopy (TEM) was used for study of microstructural changes taking place during creep exposures. Carbon extraction replicas were prepared from the weld metals and the base materials. Thin foils were prepared from the weld metal (WM), the coarse prior austenitic grain heat affected zone (CG HAZ), the fine prior austenitic grain heat affected zone (FG HAZ) and the

base material (BM). Foils were jet electropolished in a 6% solution of perchloric acid in methanol at a temperature range from -60°C to -40°C. Secondary phases were identified using energy dispersive X-ray microanalysis (EDX) and selected area electron diffraction (SEAD).

Table 1. Chemical composition of base materials and weld metals (wt%).

	<b>C</b>	<b>Mn</b>	<b>Si</b>	<b>Cr</b>	<b>Mo</b>	<b>V</b>	<b>Ni</b>	<b>Nb</b>	<b>Al</b>	<b>N</b>	<b>P</b>	<b>S</b>
<b>BM-t</b>	0.12	0.49	0.29	8.6	0.96	0.21	0.30	0.07	0.011	0.06	0.011	0.004
<b>BM-p</b>	0.12	0.41	0.21	8.8	0.92	0.22	0.10	0.09	0.004	0.06	0.014	0.008
<b>WM-t</b>	0.12	0.70	0.21	9.1	1.05	0.21	0.73	0.05	0.003	0.04	0.010	0.006
<b>WM-p</b>	0.12	0.71	0.23	9.1	1.05	0.20	0.68	0.05	0.005	0.04	0.012	0.009

t ...tube weld joint, p...plate weld joint

### 3. Results

#### 3.1 Creep testing

The long-term creep rupture testing was carried out at the air at stresses in a range from 40 MPa to 240 MPa and at temperatures ranged from 525°C to 625°C. Results are summarized in Table 2 and graphically represented in Figure 1 and 2. The stress is plotted vs. the Larson-Miller parameter  $P = T \cdot [C + \log \tau]$ , where T represents temperature given in kelvin, C = 25 for P91 steel and  $\tau$  means time to the rupture in hours. Full lines in graphs represent creep strength of the base materials for 100 000 hrs according to ECCC Data Sheets (X10CrMoVNb 9-1 steel for the tube weld joint and GX12 CrMoVNbN 9-1 steel for the plate weld joint). Fractures occurred in different parts of weldments in dependency on conditions of the creep test: in WM (Type I), in WM and HAZ (Type II), in FG HAZ (Type IV) or in BM unaffected by welding. Fracture location is specified in Table 2 and in graphical representations (Figures 1 and 2).

The creep strength of the weld joint for a definite temperature and time to rupture was calculated using interpolation and extrapolation and two different equations: (1) the standard regression equation [5] and (2) Larson-Miller equation.

$$\log \tau = A_1 + A_2 \cdot \log \left| \frac{1}{T} + \frac{1}{A_5} \right| + A_3 \cdot \log \left| \frac{1}{T} + \frac{1}{A_5} \right| \cdot \log \sinh(A_6 \cdot \sigma \cdot T) + A_4 \cdot \log \sinh(A_6 \cdot \sigma \cdot T) \quad (1)$$

Different types of cracking of P91 steel weld joints after long-term creep tests

Symbol  $\sigma$  represents applied stress, T is temperature in kelvins and  $A_i$  are materials constants, which were calculated using the least square method. Then creep strengths for 100 000 hrs and selected temperatures were calculated. The second relation (2) was obtained if Larson-Miller parameter P substitute  $\tau$  in equation (1) and  $T = 873$ . New constants  $A_i$  were calculated and the creep strengths were determined. The creep strengths of weld joints for 100 000 hrs and temperatures from 500°C up to 600°C were compared with the creep strength of the base materials according to ECCC Data Sheets (Table 3 and 4).

Table 2. Results of creep tests.

Temp. [°C]	Stress [MPa]	Specimen		Time [hrs]		A [%]		Z [%]		Fracture type	
		tube	plate	tube	plate	tube	plate	tube	plate	tube	plate
525	240	2C1	C16	3,772	9,309	14.6	11.9	72.4	51.0	II	IV,BM
525	220	3C1	C1	11,546	49,611	9.6	6.9	29.7	14.4	I	II
550	200	6C1	-	1,183	-	14.3	-	72.4	-	II	-
550	180	7C1	C4	9,853	31,920	6.3	2.5	14.2	14.4	I	IV*
550	160	-	C5	-	33,189	-	1.6	-	4.9	-	IV*
575	200	11C1	-	134	-	20.2	-	84.9	-	II	-
575	180	25C1	C6	960	2,853	15.8	7.6	84.9	19.2	BM	IV
575	160	12C1	C15	4,704	3,793	7.8	4.3	37.8	12.1	IV	IV
575	140	8C1	C7	9,608	10,031	3.0	3.0	18.8	4.9	IV	IV
575	120	9C1	C8	12,624	19,289	2.1	1.1	19.0	7.4	IV	IV
600	140	16C1	C3	981	1,797	20.4	4.8	59.3	12.3	IV	IV
600	120	15C1	C12	2,242	2,610	5.0	1.8	4.9	14.7	IV	IV
600	100	13C1	-	6,080	-	2.4	-	12.1	-	IV	-
600	90	26C1	-	8,165	-	0.5	-	11.9	-	IV	-
600	80	14C1	C10	10,181	25,818	2.1	1.1	18.8	9.8	IV	IV*
600	70	24C1	C11	27,471	45,811	1.6	1.4	4.9	4.9	IV*	IV*
625	100	18C1	C2	1,777	1,061	3.6	3.2	18.8	16.7	IV	IV
625	80	17C1	C9	3,970	2,291	2.0	1.1	16.7	5.2	IV	IV
625	60	19C1	C13	13,673	19,210	1.8	1.2	2.2	7.4	IV	IV*
625	50	20C1	C14	29,962	29,312	3.4	9.9	9.5	35.2	IV*	I*

A...elongation, Z...area reduction, I, II or IV...type of fracture, \*...cavities not only in HAZ, but also in WM and/or BM.



Different types of cracking of P91 steel weld joints after long-term creep tests

Table 3. Creep strength of tube weld joint for 100 000 hrs in comparison with that of the base material.

Temp.	Tube weld joint			X10CrMoVNb 9 1	Difference
	Creep strength			Creep strength	
	Regres.	Lars.-Miller.	Average	ECCC Data Sheet	
	A	B	$C=(A+B)/2$	D	$(C-D)/D$
[°C]	[MPa]	[MPa]	[MPa]	[MPa]	[%]
500	216	211	214	213	0,4
510	193	193	193	195	-0,9
520	172	175	174	177	-1,9
530	152	158	155	162	-4,2
540	134	141	137	148	-7,1
550	117	124	121	136	-11,2
560	101	109	105	124	-15,2
570	87	94	90	113	-20,0
580	74	80	77	102	-24,6
590	61	67	64	92	-30,7
600	49	56	53	82	-35,7

Table 4. Creep strength of plate weld joint for 100 000 hrs in comparison with that of the base material.

Temp.	Plate weld joint			GX12CrMoVNbN9-1	Difference
	Creep strength			Creep strength	
	Regres.	Lars.-Miller.	Average	ECCC Data Sheet	
	A	B	$C=(A+B)/2$	D	$(C-D)/D$
[°C]	[MPa]	[MPa]	[MPa]	[MPa]	[%]
500	229	246	238	223	6,5
510	208	221	215	206	4,1
520	187	198	193	190	1,3
530	167	175	171	175	-2,3
540	147	153	150	160	-6,3
550	130	134	132	146	-9,6
560	113	115	114	132	-13,6
570	98	98	98	119	-17,6
580	84	83	84	106	-21,2
590	72	70	71	95	-25,3
600	61	57	59	86	-31,4

Different types of cracking of P91 steel weld joints after long-term creep tests

The creep strengths of both, tube and plate weld joint, fall into the usually permitted  $\pm 20\%$  scatter band of the creep strength of the corresponding base material at temperatures up to 570°C. At higher temperatures it decreases below the bottom of that scatter band (Figures 1 and 2). Nevertheless creep strength of the plate weld joint is marginally higher than that of the tube weld joint within the whole tested temperature range.

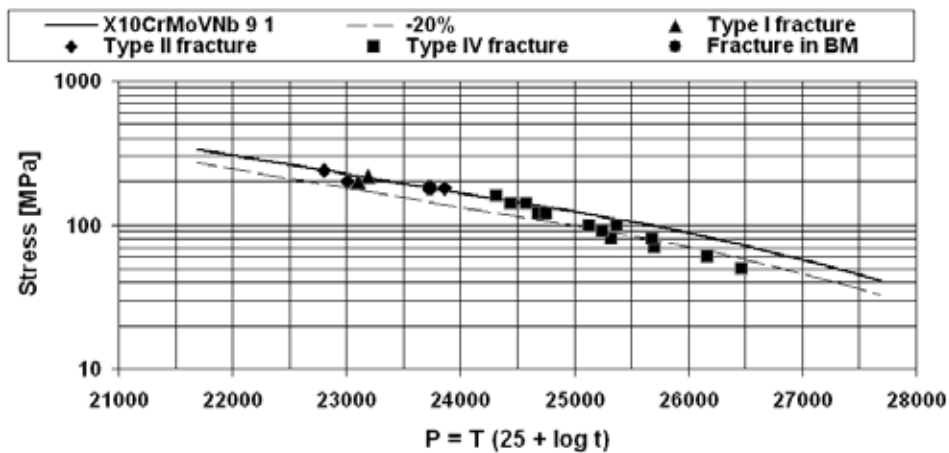


Figure 1. Stress vs. Larson-Miller parameter for the tube weld joint in comparison with a creep strength for 100 000 hrs of X10CrMoVNb steel. Type of fracture is specified.

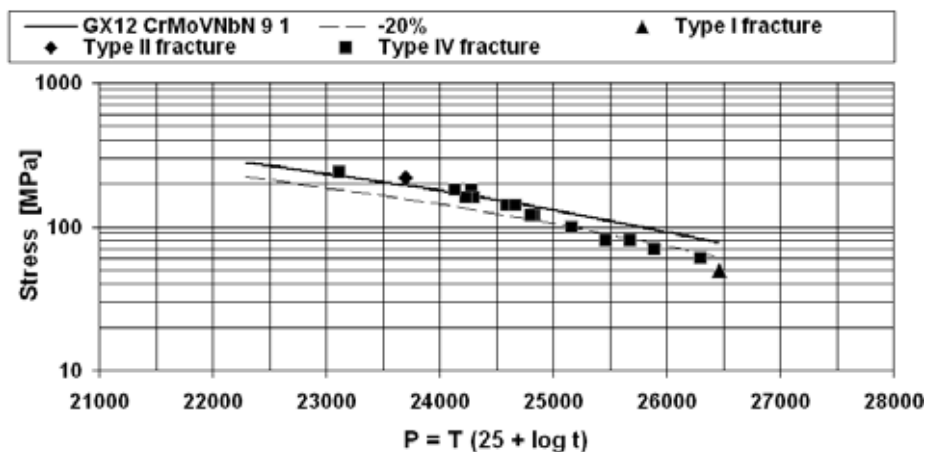


Figure 2. Stress vs. Larson-Miller parameter for the plate weld joint in comparison with a creep strength for 100 000 hrs of GX12CrMoVNBn steel. Type of fracture is specified.

### 3.2 Fractographic analysis

Fracture analysis of cross-weld crept specimens revealed some differences in creep failure between both trial weld joints exposed at the same conditions.

Fractures of the tube weld joint were located in WM at high stresses and relatively low temperatures and in BM and HAZ at higher temperatures and lower stresses. Cracks propagated in the weld metal close the fusion line at highest stress for a given temperature in a temperature range from 525°C to 575°C (Type II) and in the central part of the weld metal at lower stresses at 525°C and 550°C (Type I). A decrease in applied stresses for specimens tested at 575°C resulted in the crack propagation in the base material near the edge of HAZ. Elongations and area reductions were relatively high; elongation of specimens of Type II fracture and also the specimen, which ruptured in BM, ranged from 14% to 20% and their area reduction from 72% to 85%. The fractures occurred by ductile transcrystalline mechanism and fracture surfaces revealed a dimple morphology (Figure 3). The elongation and area reduction of specimens of Type I fracture ranged from 6% to 10% and from 14% to 30% respectively.

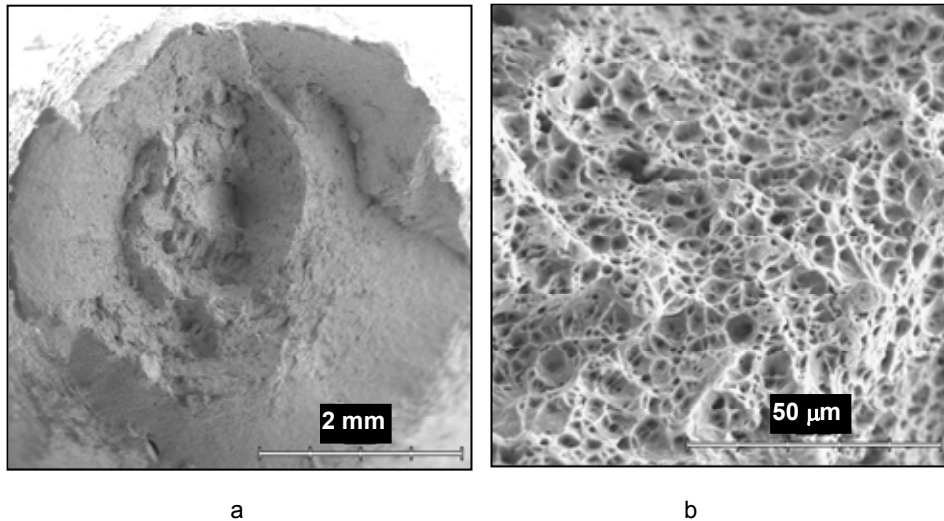


Figure 3. Fracture surface of the tube weld joint crept at 525°C/240 MPa/3 772 hrs: a) general view, b) detail of the central part. Specimen 2C1, SEM micrographs.

The transgranular creep fractures of the tube weld joint occurred in the fine prior austenite grain heat affected zone (Type IV). Elongation and area reduction were

Different types of cracking of P91 steel weld joints after long-term creep tests

usually low; elongation of a few percent and area reduction below 20%. Only one specimen (16C1), which was exposed at the highest stress at 600°C, showed remarkable macro-plastic deformation. Fracture surfaces covered with oxide layers showed some evidence of dimple morphology (Figure 2). Cavities were observed at fracture surfaces after long exposures at high temperature (Figure 4b).

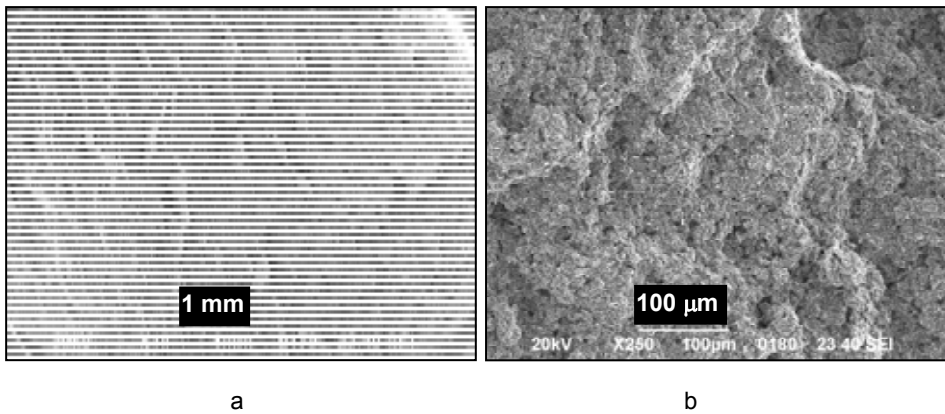


Figure 4. Fracture surface of the tube weld joint crept at 600°C/70 MPa/27 471 hrs: a) general view, b) detail of the central part. Specimen 24C1, SEM micrographs.

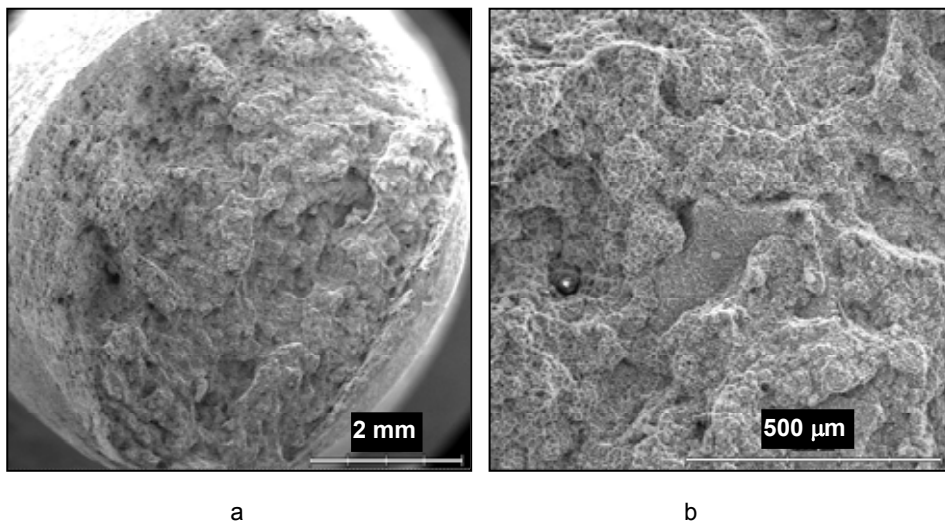


Figure 5. Fracture surface of the plate weld joint crept at 575°C/160 MPa/3 793 hrs: a) general view, b) detail of the central part. Specimen C15, SEM micrographs.

The crept test-pieces of the plate weld joint ruptured generally in the low temperature HAZ region, near to the base material (Type IV); exceptions were detected after creep tests at the lowest and the highest temperatures. Surfaces of Type IV fractures revealed the dimple morphology similar to the tube weld joint and, in addition, some intercrystalline facets were detected in C6 and C15 specimen (Figure 5). The fracture of C16 specimen loaded with the highest stress at 525°C was initiated in FG HAZ and occurred partly in HAZ and in unaffected BM, while fracture of C1 specimen exposed at lower stress at the same temperature partly occurred in WM and partly in the HAZ (Type II). The lowest loading at the highest temperature caused the fracture in the central part of WM (Type I). Some cavities were observed on the fracture surface of this specimen, especially along previous austenite grain boundaries (Figure 6).

Elongation of specimens with Type IV cracking was usually a few percent and area reduction did not exceed 20%. Only C16 specimen showed significant macro-plastic deformation after test at the highest stress and the lowest temperature. Plastic deformation was also evident in C14 specimen of Type I fracture after test at the lowest stress and the highest temperature.

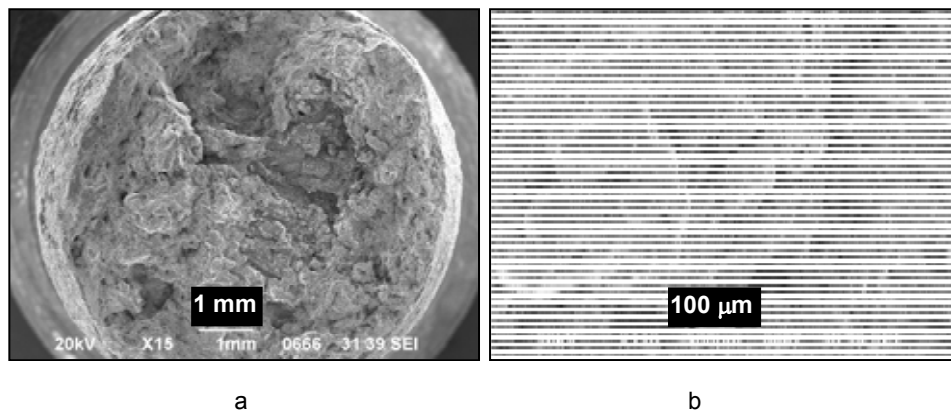


Figure 6. Fracture surface of the plate weld joint crept at 625°C/50 MPa/29 312 hrs: a) general view, b) detail of the central part. Specimen C14, SEM micrographs.

### 3.3 Hardness measurement

Before creep testing both weld joints showed typical crossweld hardness profile with higher hardness in the weld metal than in the unaffected base material, with local maxima in the coarse prior austenite grain heat affected zones close the fusion line and local minima in the fine prior austenite grain heat affected zones.

Different types of cracking of P91 steel weld joints after long-term creep tests

After creep tests some changes in hardness were found out in dependency on the creep conditions.

Hardness across the tube weld joint before creep testing varied from about 180 to 232 HV10. Hardness of unaffected base material was 200 HV10, hardness of the weld metal ranged from 207 to 224 HV10. Creep exposures at temperatures ranging from 525°C to 575°C did not significantly influence the hardness. Changes were found only in the plate weld joint after the exposure of almost 50 000 hrs at 525°C – hardness of WM and regions along the fusion line decreased, but still exceeded the hardness of BM. On the contrary long-term exposure at 600°C resulted in apparent increase by about 10 HV10 in the weld metal and also in the base material. Exposures at 625°C resulted in hardness decrease in the weld metal by about 20 HV 10. Cross-weld hardness profiles after PWHT and after creep tests at 600°C and 625°C are shown in Figure 7a.

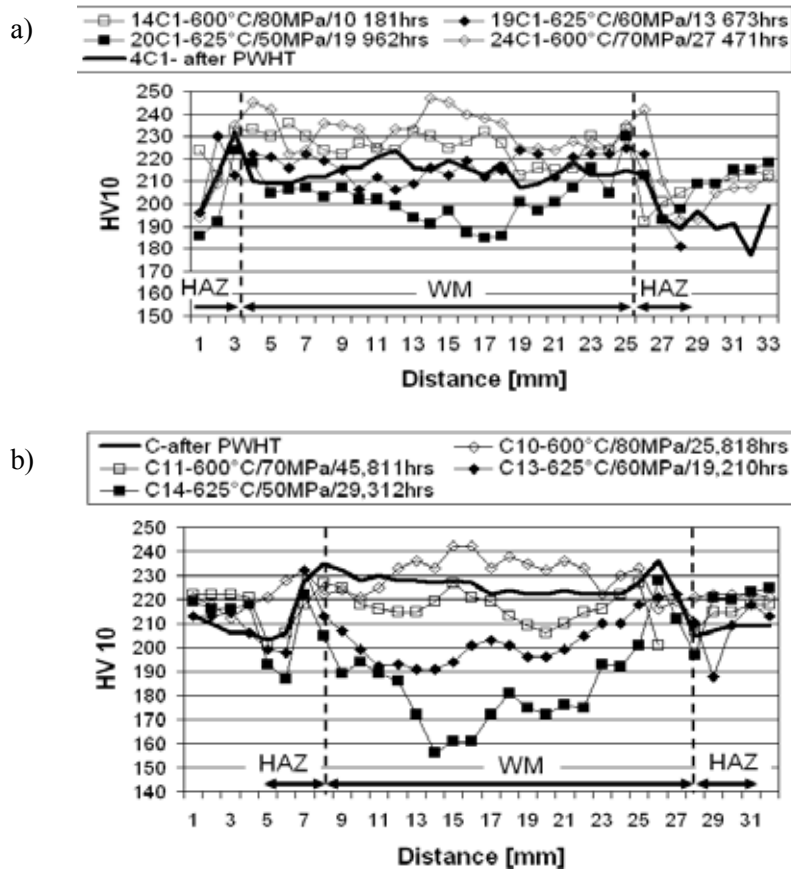


Figure 7. Cross-weld hardness profiles: a) the tube weld joint, b) the plate weld joint.

Hardness of the plate weld joint before creep testing was rather higher than that of the pipe weld joint as a result of lower temperature of post-weld heat treatment. Hardness of the base material and the weld metal were 210 HV10 and 226 HV10 respectively. During creep tests at temperatures from 525°C up to 600°C hardness slightly increases in the base material and also in the weld metal, while after tests at 625°C hardness of the base material increased and hardness the weld of metal remarkable decreased, especially after test at 625°C/50 MPa/ 29 962 hrs (Figure 7b).

### 3.4 Microstructural analyses

Microstructure of both the tube and the plate weld joints fully consists of tempered martensite. Neither polygonal ferrite nor fresh martensite was observed after PWHT. No defects were detected near the fusion line or in the weld metal, which could cause a premature fracture. Characteristic acicular structure was evident in WM, BM and CG HAZ, while fine featureless structure was present in the FG HAZ.

Substructure before creep exposure was lath-like tempered martensite, laths were divided into subgrains. Coarse  $M_{23}C_6$  carbides occurred at boundaries of prior austenite grains, ferritic laths and subgrains. Non-uniform distribution of fine vanadium carbonitride was observed within laths. Globular silicon oxide particles were present in the weld metal. Some differences were observed in size and distribution of secondary phases in individual zones of weld joint. Density of coarse particles was relatively low in WM and in CG HAZ and high in FG HAZ. On the contrary density of fine vanadium carbonitride was higher in the CG HAZ and lower in FG HAZ. A high dislocation density occurred in subgrains with relatively high density of fine precipitate. Subgrains in the FG HAZ were almost free of dislocations.

During creep tests cavities appeared in FG HAZ on the both sides of weld joint. Size and density of cavities increased with increasing temperature and time to rupture. Coalescence of cavities results in Type IV cracking. Cavities were observed only exceptionally in specimens of the tube weld joint, which revealed Type I and Type II cracking and in specimen ruptured in the base material. Individual cavities were also observed in other parts of weld joint – in the base material and/or in the weld metal after creep exposures longer than 30 000 hrs at 550°C and 20 000 hrs at temperatures above 600°C.

Precipitation reaction taking place during creep exposures strongly depended

on conditions of the creep loading [6]. Precipitation of Laves phase occurred at 550°C and higher and also several Z-phase particles were observed in both weld joints after long creep exposures at 625°C. Laves phase corresponded to the largest particles in the areas investigated. Sporadically observed Z-phase were a plate-like shape with dimensions of about 100 nm.

In the tube weld joint no important changes in size and distribution of secondary phases was observed after creep test at 625°C/60 MPa/13 673 hrs, nevertheless a growth of subgrains was evident in FG HAZ. After creep exposure at 625°C/50 MPa/29 962 hrs subgrains in FG HAZ were significantly coarser than those in BM and WM. Laves phase was not identified while some particles of Z-phase were observed on replicas prepared from WM and HAZ.

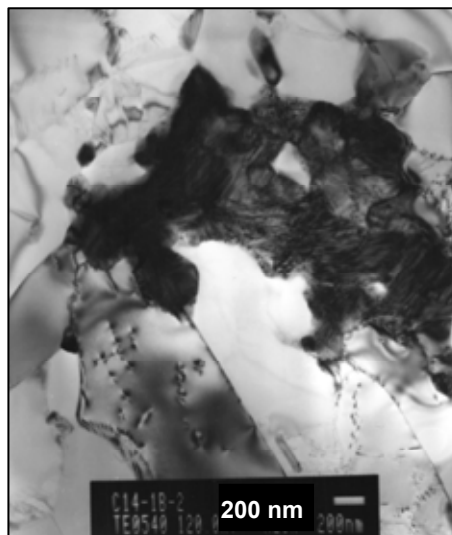


Figure 8. Cluster of particles in WM of the plate weld, 625°C/50 MPa/29,312 hrs, C14 specimen. TEM micrograph.

Significant changes in substructure were observed in the plate weld joint after exposures at 550°C and 625°C for about 30 000 hrs and at 625°C for about 14 000 hrs. In WM coarse particles of Laves phase were identified after test at 550°C/160 MPa/33 189 hrs using SAED and EDX microanalysis. Iron and molybdenum were prevailing in Laves phase, while chromium predominated in  $M_{23}C_6$  carbides. Changes in density of vanadium carbonitrides were not found out. Laves phase was not observed in other regions of the plate weld joint.

After creep exposure at 625°C/50 MPa/29 312 hrs massive particles of Laves phase (exceeded 1µm in size) were observed in the weld metal, apparently smaller ones in other regions of the weldment (Figure 8). A significant growth of subgrains occurred in WM. Massive particles often formed clusters with carbides and inclusions and drew atoms of molybdenum from ferritic matrix. Depletion of solid solution about molybdenum resulted in increase in size of subgrain and remarkable softening of the weld metal. Substructures of the weld metal in the tube weld joint and the plate one are shown in Figure 9.



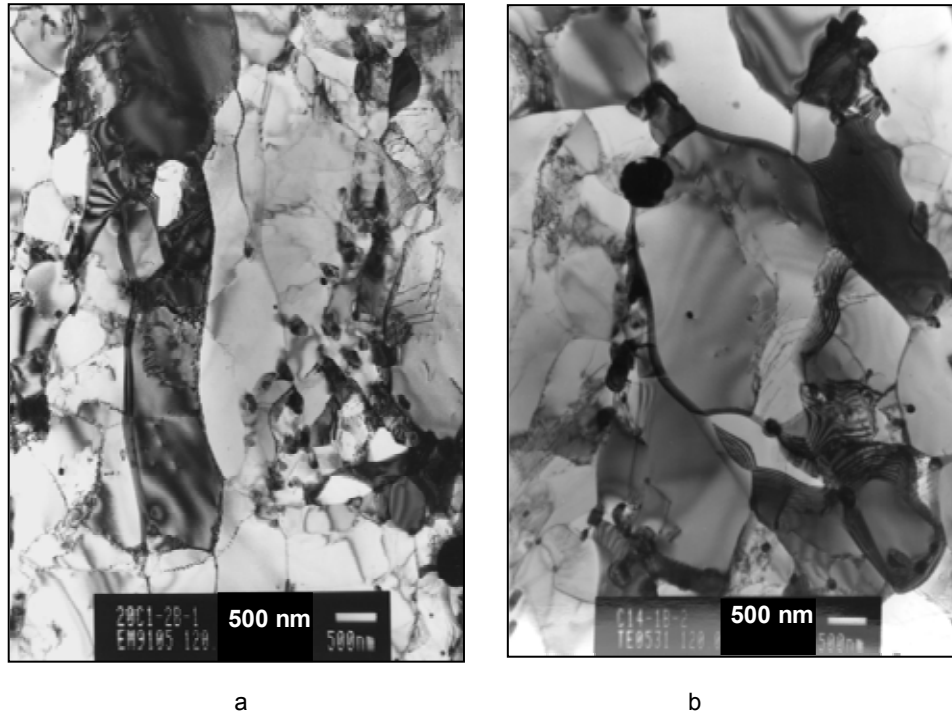


Figure 9. Substructure of WM after creep tests at 625°C and 50 MPa: a) the tube weld joint, 20C1 specimen, b) the plate one, C14 specimen. TEM micrographs.

## 4. Discussion

Creep testing demonstrated that creep strength of the plate weld joint is rather higher than that of the tube weld joint, although the welding process and geometry of weld joint were identical. The attention has been paid to the (Mn +Ni) content because it can influence  $A_{c1}$  temperature. The welded tube segments and cast plates contained 0.8 and 0.5 wt.% of (Mn +Ni) respectively, while (Mn +Ni) concentration was 1.4 wt.% in weld metal. It has been shown that increasing (Mn +Ni) content in P91 base material between 0.60 and 1.25 wt.% resulted in a decrease in the  $A_{c1}$  temperature of about 45°C [7]. In spite of this fact the temperature of applied PWHT of the tube weld joint was 760°C; it means from 10°C to 20°C higher than that of the plate weld joint and simultaneously 10°C higher than the temperature of tempering of the base material. Although  $A_{c1}$  temperature was not apparently exceeded during PWHT, a temperature of 760°C seems to be too high and caused drop in creep strength of the tube weld joint in

comparison to the plate one. The PWHT resulted in decrease in hardness of the tube weldment and Type I and Type II fracture, if relatively low temperatures and high stresses were applied. Fracture occurred by ductile transcrystalline mechanism similar to that at room temperature. At these conditions the cast material is more susceptible to fracture than the wrought one.

At relatively high temperatures and low stresses cavitation failure in FG HAZ causes Type IV fracture of both weld joints. In these zones lath-like structure is replaced by soft equiaxed grains and subgrains with low dislocation density and with coarser secondary phase particles at boundaries. Dislocation creep results in formation of steps at grain/subgrain boundaries and nucleation of cavities. Cavities can be also formed as a result of interaction between dislocations and coarse particles at grain boundaries. The growth of cavities is promoted by the grain boundary diffusion and coalescence of cavities results in crack propagation. Subgrain boundaries form also channels of relatively high speed diffusion similar to high angle boundaries, therefore intercrystalline facets are observed on Type IV fracture surfaces only exceptionally.

Precipitation of Laves phase occurs predominately in the weld metal during long exposures at a temperature of 550°C and higher and also in other parts of weldments. Occurrence of fine Laves phase particles has a positive influence on strength; hardness increases after creep exposures at 600°C up to about 30 000 hrs. However with increasing time and temperature of the creep exposure growth of Laves phase particles causes softening of matrix as a result of depletion of solid solution about molybdenum. Relatively soft weld metal can be easily deformed and at massive Laves phase particles and their clusters with silicon inclusions and chromium carbides cavities often nucleate. It is interesting that a higher temperature of PWHT probably retarded the Laves phase precipitation in the tube weld joint.

At temperatures above 550°C both processes occur: cavitation failure in FG HAZ and softening of solid solution mainly in the weld metal. Usually Type IV cracking occurs, however at 625°C softening of the weld metal can predominate and then Type I fracture is realized.

Precipitation of Z-phase seems to be of a secondary importance in comparison to precipitation of Laves phase. It can be expected, that detrimental influence of Z-phase, which causes dissolution of vanadium nitrides and decrease in precipitation strengthening, could be shown after creep exposures exceeding significantly 30 000 hrs at temperatures above 600°C.

## 5. Conclusions

The submitted study of weld joints prepared in conditions used in the industrial practice showed that small differences in chemical composition and PWHT can result in different kinetics of precipitation processes in individual zones of weldments. At high temperatures failure is concentrated in FG HAZ and Type IV fracture occurs, however at specific conditions failure in the weld metal can be dominant and then Type I fracture is realized.

## Acknowledgements

This work was supported by Grant projects SMS 4771868401 and OC09041 from the Ministry of Education, Youth and Sports of the Czech Republic.

## References

1. Brett, S. J. UK experience with modified 9Cr (grade 91) steel. In: Proc. BALTICA VII – Life Management and maintenance for Power Plants, Vol. 1. J. Veivo & P. Auerkari (Eds.). Espoo: VTT Technical Research Centre of Finland, 2007. Pp. 48–60.
2. Jandová, D., Kasl, J. & Kanta, V. Long-term creep testing and microstructure evaluation of P91 steel weld joints. In: Proc. BALTICA VII – Life Management and maintenance for Power Plants, Vol. 1. J. Veivo & P. Auerkari (Eds.). Espoo: VTT Technical Research Centre of Finland, 2007. Pp. 143–155.
3. Jandová, D., Kasl, J. & Kanta, V. Influence of substructure on creep failure of P91 steel welds. In: Proc. 2nd ECCO Creep Conference Creep & Fracture in High Temperature Components – Design & Life Assessment Issues. I. A. Shibli & S. R. Holdsworth (Eds.). Lancaster, PA, USA: DEStech Publications, 2009. Pp. 177–188.
4. Jandová, D., Kasl, J. & Kanta, V. Creep failure in welds of cast and wrought P91 steel after long-term creep testing. In: Proc. IIV International Conference on Advances in Welding and Allied Technologies. Z. Sun Eds. Singapore Welding Society, Singapore, 2009. Pp. 149–154.

Different types of cracking of P91 steel weld joints after long-term creep tests

5. Bina, V. & Hakl, J. Relation between creep strength and strength for specific creep strain at temperature up to 1 200°C. *Mater. Sci. Engn.*, 1997. Vol. A234–236, pp. 583–586.
6. Jandová, D., Kasl, J. & Chvostová, E. Influence of precipitation on dislocation substructure and creep properties of P91 steel weld joints. *Materials at High Temperatures* (in print).
7. Seifert, J., Alexandrov, B., Lippold, J., Sanders, J., Tanzosh, J. & King, B. Examination of phase transformation during PWHT of steel P91. In: *Proc. IIW International Conference Safety and Reliability of Welded Components in Energy and Processing Industry*. P. Mayr, G. Posch & H. Cerjak (Eds.). Graz: Graz University of Technology, 2008. Pp. 75–80.

# **New mechanical testing equipment for testing in real and simulated service environments (HIPS)**

Pekka Moilanen and Stefan Holmström  
VTT Technical Research Centre of Finland  
Espoo, Finland

## **Abstract**

This paper aims to introduce the application areas of the multifunctional high precision pneumatic loading system (HIPS), based on VTT developed and patented technology. The HIPS has been utilized in a number of different challenging environments, among others laboratory simulated nuclear power plant water environments such as the BWR, PWR and SCW, high temperature gas environment and actual nuclear reactor inpile testing. The test palette is also large, i.e. tensile testing, stress corrosion cracking, fatigue, creep fatigue, radiation impact on tensile and fatigue, and many variants with combined environmental impact. The HIPS has also successfully been used as mover system in a version of the contact electrode resistance measurement. The wide spectrum of tests enabled by the flexible concept is shortly described together with some test results from the different types of tests. The technological development path from single bellows tensile loading devices towards the more demanding double bellows fatigue and combined tension/compression/internal pressure system is described.

## **1. Introduction**

The primary goal of this paper is to present the multitude of possibilities offered by the high precision pneumatic loading system (HIPS). The first successful

New mechanical testing equipment for testing in real and simulated service environments (HIPS)

testing devices were published in the dissertation work of the first author [1] of this paper. Since then the HIPS has been developed from the basic 3-point bending type loading frame to a multipurpose testing platform capable of performing a multitude of materials testing types in demanding simulated and actual service environments. The HIPS variants covered to date is presented in Figure 1.

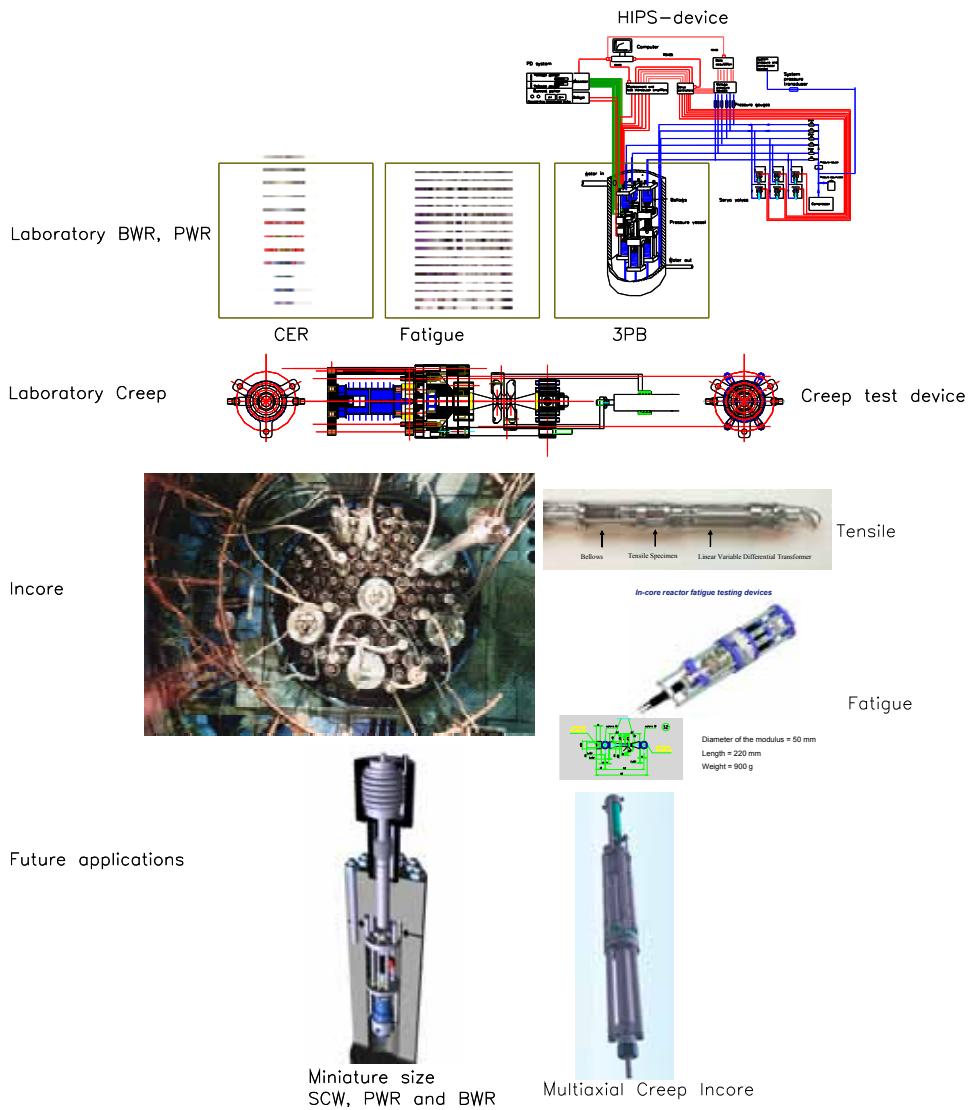


Figure 1. HIPS testing device variants, including test environments Flow diagram of a “basic” HIPS test- rig (one directional loading).

The patented basic control setup presented is the heart of the HIPS and is the same for all the applications give a few small modifications demanded by the selected environments. The main benefit of the loading system is that there are no moving loading lead throughs, only pressure line and electrical feedback connections. The testing device itself can be far away from the control units and servo valves (over 30 m and a Ø1.6 mm has been successfully implemented). This feature is a must for instance in nuclear reactor in-pile testing. A list of the testing environments and testing types performed to date is presented in Table 1.

Table 1. HIPS test environments, testing types and references.

Environment	Test types	Test specification	Reference
In-pile (BR2 test reactor)	Tensile test constant displacement rate 10e-7 1/s	2 sample rig, axial loading, stagnant water at 90°C	[2]
In-pile (BR-2 test reactor)	Creep fatigue	2 sample rig, creep fatigue loading (holding 10 and 100 s), stagnant water 90°C	[3]
In-pile (Osiris reactor)	Multiaxial creep internal pressure + tensile/compressive load with diametral strain measurement	under construction	[4]
BWR water chemistry (autoclave)	Stress corrosion cracking (SCC)	6 spec. autoclaves displ.rate $2 \times 10^{-8}$ mm/s, 288°C, 90 bar	[5, 6]
PWR water chemistry (autoclave)	Fatigue	Sinus wave 0.1 Hz (HLWR environment) 350°C / 160 bar	[7, 8]
PWR water chemistry (miniature autoclave)	Crack initiation and growth (K) testing	Miniature autoclave (Ø 64 mm)	ongoing
SCW environment 650°C / 350 bar	Crack initiation and growth (K) testing	Miniature autoclave (Ø 64 mm) double bellows loading unit	ongoing
High temperature (air)	Creep, creep fatigue	Tension and compression with 2 bellows - 600°C	ongoing

New mechanical testing equipment for testing in real and simulated service environments (HIPS)

One of the main features of the HIPS is the level of accuracy both in displacement (strain) and force (stress) in the various testing environments. The calibration of each system requires naturally thorough test runs with instrumented pressure, load and temperature feedback. The sensitivity of control realized by the pneumatic servo control enables excellent accuracy of the measured displacement, as the displacement fluctuation ( $< \pm 2 \mu\text{m}$ ) easily surpassed the limits set by the ASTM-1152-87 standard. An example of a rising load test (load as a function of displacement) is presented in Figure 2. The load accuracy also easily fulfils the same ASTM standard requirements.

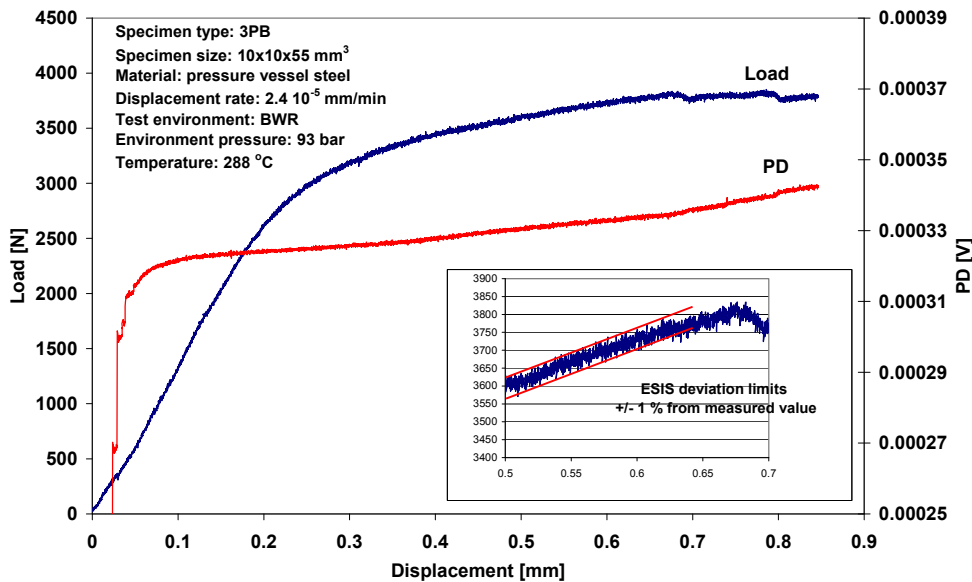


Figure 2. Displacement accuracy of HIPS in a rising load test

The HIPS control configuration enables loading using any of the available test parameters as inputs, i.e. pressure, force, displacements, strain and of course time. The usual modes are pressure (or load) as a function of time for creep and displacement as a function of time for tensile and fatigue testing.

The HIPS technology can also be utilized for applications where movement in itself is the essential feature. A good example of this is the HIPS powered contact electrode resistance (CER) [9] measuring device. In the CER prototype tests, an accuracy of  $\pm 0.1 \mu\text{m}$  can be accomplished for the electrode movement in air [9].



## 2. Power plant water environments

For the challenging water environments of the nuclear light water reactors, i.e. boiling water reactors (BWR), pressurized water reactors (PWR) and the future envisaged supercritical water reactors (SCWR), the simulated test environments are crucial for validation of the structural materials. Testing in these conditions has traditionally been conducted with hydraulic or electrical step motor systems with lead throughs for the loading rod. The HIPS technology is improving the integrity and the reliability of the tests by introducing a system without parts moving through the pressure boundaries. As shown in Table 1, the wide range of nuclear water chemistries, pressures and temperatures have been covered, as well as different test types including fatigue, tensile and crack initiation/growth testing. An example of a fatigue test is given in Figure 3.

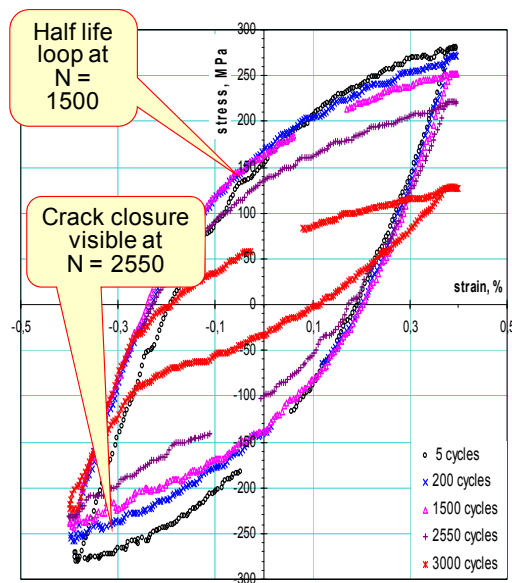


Figure 3. Fatigue cycles (0.1 Hz) for AISI 316 at 350°C / 160 bar (PWR environment).

An example of a typical load-displacement curve of Inconel 182 with the effects of sulphate intrusions is shown in Figure 4. The load starts to decrease quickly after sulphate is injected into the autoclave inlet water because of crack growth. When the sulphate intrusion is finished, the load decrease rate begins to slow down immediately. The lowest crack growth rates were measured in pure water

New mechanical testing equipment for testing in real and simulated service environments (HIPS)

prior to the first sulphate transient. The injection of a small amount of sulphate, producing a minor increase in the conductivity of the outlet water, affected the measured crack growth rate considerably in this alloy.

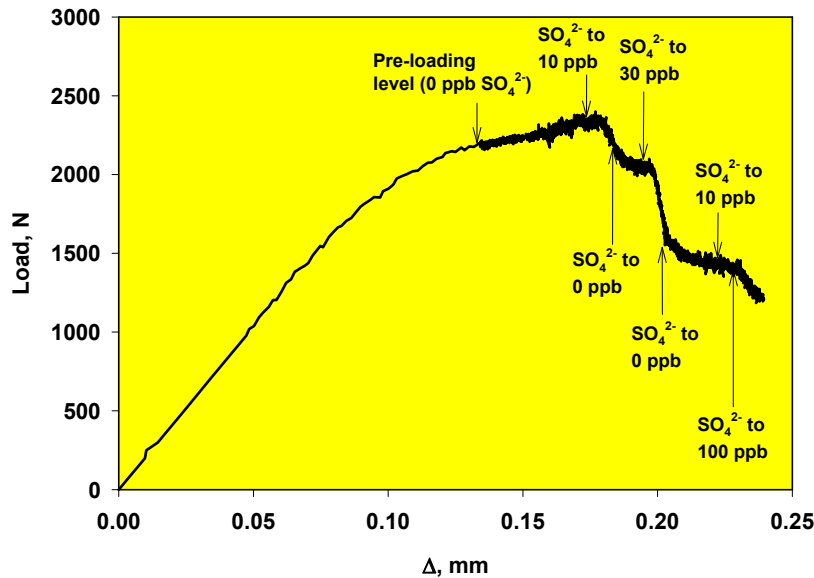


Figure 4. Example of a typical load-displacement curve of Inconel 182 with the effects of sulphate intrusions [1].

### 3. Nuclear reactor in-pile environments

It has been demonstrated that it is technically feasible to carry out well defined and controlled in-reactor dynamic tensile tests. This makes it possible to investigate the intrinsic role of the applied stress and the displacement damage acting concurrently in determining the global deformation behaviour of the material under dynamic irradiation conditions. The HIPS device has been used to determine stress and strain curves for pure Cu and Cu-alloy specimens in the BR-2 reactor in Belgium. The reactor pool water temperature was 90°C, neutron flux  $\sim 0.3 \cdot 10^{14}$  n cm<sup>-2</sup>s<sup>-1</sup>s (E > 1 MeV) and damage rate  $\sim 2 \cdot 10^{-4}$  h<sup>-1</sup>. The test was a constant displacement rate test with a strain rate  $\sim 10^{-7}$  1/s. The most significant feature of the results was that during the dynamic in-reactor test, the material deforms uniformly and in a homogeneous fashion without showing any signs of yield drop and plastic instability (i.e. low temperature embrittlement) as

commonly demonstrated by post-irradiation experiments. However, the fact that the material under the present irradiation and test conditions only shows a uniform elongation of about 12% is still a matter of concern, particularly since it remains unknown as to what causes this reduction in the uniform elongation. Further investigations are necessary to determine and understand the factors responsible for the reduction in the uniform elongation due to irradiation. The same pure copper tensile tested at 100°C in the unirradiated condition yields, for example, a uniform elongation of about 56%. New experiments have been done addressing this issue. An example of the test series with OFHC copper is presented in Figure 5.

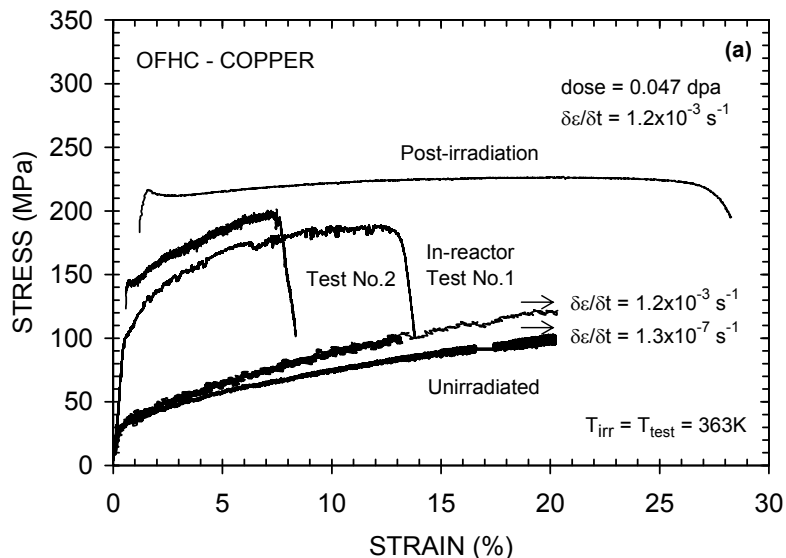


Figure 5. In-pile and post irradiation tensile tests of copper in BR2-reactor

The copper alloys components in ITER are expected to be exposed to thermal and mechanical loads (both static and cyclic) at the same time as being bombarded with a neutron flux. At the present time it is not known what the dynamic effect of the applied stress will be on the damage accumulation and thus on the mechanical performance of the copper alloy. It has already been shown that copper alloys are sensitive to the dynamic interaction between fatigue and creep. These effects could significantly affect the lifetime of components. The next step in the in-pile testing of these materials includes creep fatigue testing. An example of the creep fatigue HIPS is shown in Figure 6, and

New mechanical testing equipment for testing in real and simulated service environments (HIPS)

the creep fatigue strain controlled signal with stress response is presented in Figure 7.



Figure 6. HIPS probe for in-pile fatigue testing

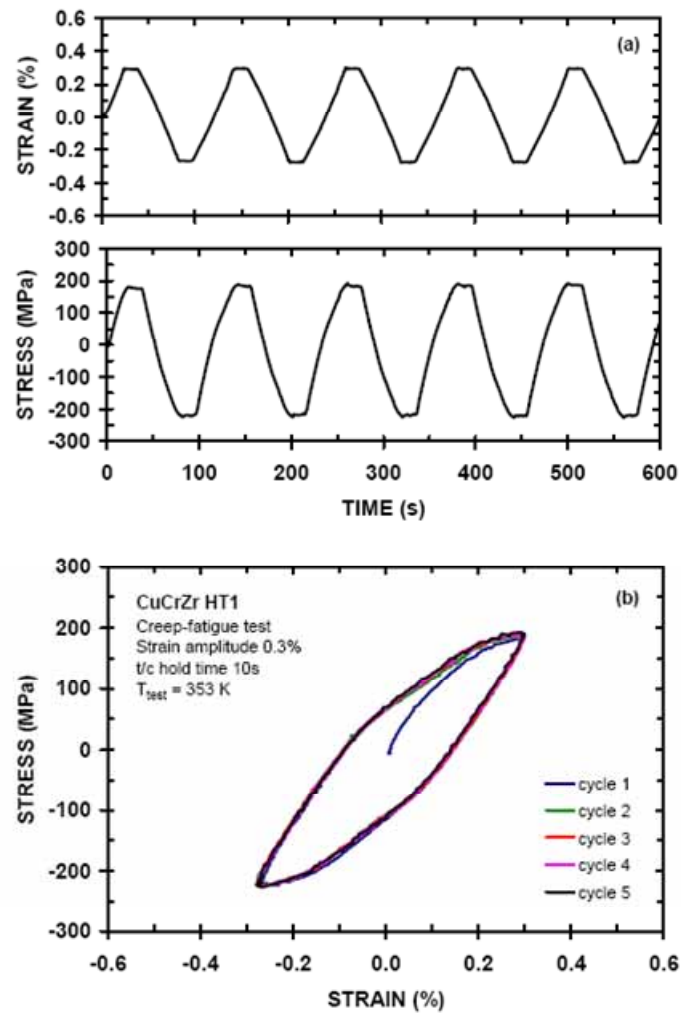


Figure 7. In-situ fatigue stress and strain curves and selected loops for a Cu-alloy

## 4. High temperature environments

For the high temperature applications where creep is an active damage mechanism the HIPS technology opens opportunities for most of the creep related testing types. To date the experience of the high temperature HIPS has been collected from constant load tests performed with a prototype single bellows (tensile load only) system and from the recently developed second generation push/pull bellows version where creep-fatigue tests have been performed. An example of a 600°C creep-fatigue test data set is shown in Figure 8. The loading frame with the bellows is shown in Figure 9.

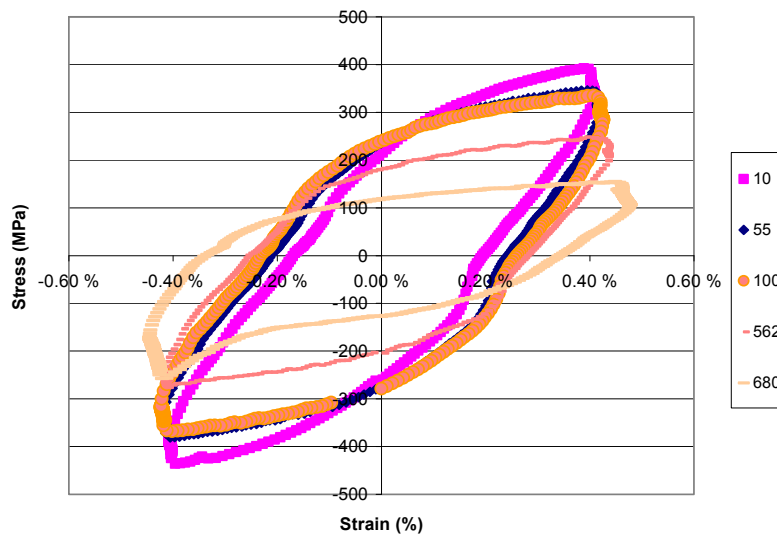


Figure 8. Creep fatigue loops for P24 steel at 600°C.

New mechanical testing equipment for testing in real and simulated service environments (HIPS)



Figure 9. The high temperature HIPS in front of the furnace.

## 5. Discussion and future plans

It is evident that the HIPS technology enables many different options for materials testing, also in difficult environments. The HIPS technology is also being developed towards smaller dimensions. The best example for this development is the miniature autoclave concept under construction both at VTT and JRC Petten (Netherlands). This testing system is enabling effective adaptation to the space limitations in supercritical conditions. The compact unification of the testing / loading frame with the autoclave itself will make the testing in flowing media (like difficult Gen IV coolants) within reach. One of the more advanced developments towards miniature autoclaves for the SCW (350 bar / 650°C) conditions is shown in Figure 10 (left side), together with another in-situ device or the MELODIE testing system (right side) for multiaxial loading developed in cooperation with CEA (France). The multiaxiality is here controlled by combined tensile loading and internal pressure of the specimen.



Figure 10. Double bellows SCW (left) and MELODIE (right) testing devices.

## References

1. Moilanen, P. Pneumatic servo-controlled material testing device capable of operating at high temperature water and irradiation conditions. Espoo: VTT, 2004. VTT Publications 532. 154 p. ISBN 951-38-6384-0; 951-38-6385-9.
2. Singh, B. N., Tähtinen, S., Moilanen, P., Jacquet, P. & Dekeyser, J. In-reactor uniaxial tensile testing of pure copper at 90 °C. *Journal of Nuclear Materials*, 2003. Vol. 320, No. 3, pp. 299–304. (TENSILE IN PILE).
3. Singh, B. N., Johansen, B. S., Tähtinen, S., Moilanen, P., Saarela, S., Jacquet, P., Dekeyser, J. & Stubbins, J. F. Final report on in-reactor creep-fatigue deformation behaviour of a CuCrZr alloy: COFAT 2 2008. Risø National Laboratory for Sustainable Energy, Roskilde, Denmark. Riso-R-1629. 41 p.
4. Guimbal, Ph., Auclair, M., Carassou, S., Moilanen, P., Tähtinen, S. & Villard, J.-F. MELODIE, an advanced device for study of the irradiation creep of LWR cladding with online biaxial control of stress and strain. IGORR International Group on Research Reactors. 12th Conference, Beijing, China, 28–30 October 2009. 5 p.

New mechanical testing equipment for testing in real and simulated service environments (HIPS)

5. Karjalainen-Roikonen, P., Moilanen, P., Toivonen, A. & Aaltonen, P. Method development for studies of environmentally assisted cracking (EAC). In: Solin, J. et al. (Eds.). RATU2, The Finnish Research Programme on the Structural Integrity of Nuclear Power Plants: Synthesis of Achievements 1995–1998. Espoo: VTT, 1998. VTT Symposium 190. Pp. 105–123.
6. Toivonen, A., Moilanen P., Pyykkönen M., Tähtinen S., Rintamaa R. & Saario T. The feasibility of small size specimens for testing of environmentally assisted cracking of irradiated and materials under irradiation in reactor core. Nuclear Engineering and Design, 1999. Vol. 193, pp. 309–316. (PSCFM device)
7. Solin, J., Karjalainen-Roikonen, P., Moilanen, P. & Marquis, G. Fatigue testing in reactor environments for quantitative plant life management. 2nd International Conference on Fatigue of Reactor Components. Snowbird, UT, 29–31 July 2002. EPRI OECD USNRC. 16 p. (FATIGUE)
8. Solin, J. Fatigue of stabilized ss and 316 NG alloy in PWR environment. Proc. PVP2006-ICPVT-11. ASME Pressure Vessels and Piping Division Conference. Vancouver, BC, Canada, 23–27 July 2006. American Society of Mechanical Engineers, ASME. 11 p.
9. Moilanen, P., Arilahti, E., Bojinov, M., Laitinen, T., Mäkelä, K., Mäkelä, M., Mäkinen, R., Saario, T., Sirkiä, P. & Toivonen, A. Pneumatic servo-controlled fracture resistance measuring device (PSFM-Device) and contact electric resistance measuring device (CER Device). Enlarged Halden Programme Group Meeting, Loen, Norway, 24–29 May 1999. 16 p.



# Characterization of true stress-strain behavior using optical monitoring

Tom Andersson, Lauri Elers, Anssi Laukkanen and Pekka Nevasmaa  
VTT Technical Research Centre of Finland  
Espoo, Finland

## Abstract

The present paper discusses the development and validation of miniature specimen techniques for the characterization of inherent strength properties of local microstructural regions of the weldment. The technique is based in in-situ optical monitoring of the specimen deformation behavior, particularly the localization of deformation, during the entire tensile test event using optical monitoring system. Also post-processing techniques are developed and documented for the system output. Examples of weldment characterization using  $1 \times 2 \times 8$  mm<sup>3</sup> size specimens and determination of the associated true-stress-strain-curves are given.

## 1. Introduction

Availability of true-stress-strain data and quantitative depiction of local state of deformation is vital in structural and fitness-for-services (FFS) analysis [1], in order to reliably assess fracture mechanism and failure behavior in externally loaded welded structures. This is particularly important in the case of new thermomechanically processed and mechanically strain hardened steel grades, since welding inevitably results in local softening and/or hardening phenomena in their 'metastable' microstructure. As a result, the mechanical properties can often vary substantially between the parent steel, the heat-affected zone (HAZ) and the weld metal. Moreover, a material property gradient also exists across the HAZ microstructure with the distance from the fusion boundary. Due to the

possibility to apply very small-size specimens, optical monitoring gives an opportunity to capture and study the tensile behavior of the different local, narrow microstructural regions within the weldment HAZ. This way, the inherent stress-strain characteristics of these microstructures can be quantitatively determined.

The optical monitoring system studied here can be used to test several different types of materials ranging from structural steels and stainless steels to copper alloys. The challenges relating to the use of specimens of different size and geometry (e.g., flat-bar, round-bar), however, are not yet satisfactorily known. This requires systematic study of the monitoring event and possible monitoring errors arising from the detection failures caused by specimen geometry related aspects.

## 2. Objective and Materials

The aim was to develop and validate tensile testing technique that uses miniature-size, i.e.,  $1 \times 2 \times 8 \text{ mm}^3$  flat-bar tensile specimen geometry for the characterization of different metallic materials and weldments both in parallel and transversal directions in relation to the weld. In conjunction with continuous optical monitoring of the specimen during the entire test event, the particular intention was to measure and monitor the localization of deformation in a specimen, with material's true-stress-strain curve and the associated strain-hardening parameters as awaited outcome of the test. The work also aimed at defining the capabilities, potency and limitations of the optical monitoring system in this respect.

As candidate material, multiple-pass GMAW weldments were made onto austenitic stainless steel grade EN 1.4318 (AISI 301 LN) in 5 mm plate thickness and mechanically strain-hardened by cold rolling into C850 delivery condition (i.e., the ultimate tensile strength of 850 MPa). The applied filler metal was grade 308 LSi. Welding was made using three different levels of heat input: 2.4, 3.3 and 4.8 kJ/cm; consequently, three series of specimens: M3, M4 and M6 were tested, respectively. An example of macrosection of the investigated GMAW weldment is presented in Figure 1, together with the marked locations from where the  $1 \times 2 \text{ mm}^2$  size miniature flat-bar tensile specimens were extracted within the narrow HAZ region of the welded joint [2]. The intention here was to sample both the grain-coarsened HAZ microstructure at the immediate vicinity of the weld fusion boundary, and the fine-grained/inter-

critical HAZ microstructure further off the fusion boundary. In the former case, sampling also some amount of weld metal could not be avoided, see Figure 1.

As reference material, direct-quenched & tempered (DQT) bainitic-martensitic extra-high strength structural steel plate HT80 manufactured by Sumitomo Metal Industries, Japan, was adopted [3]. As only base material was investigated here, round-bar tensile specimen geometry of  $\varnothing 6$  mm diameter size was used instead of flat-bar specimen type.

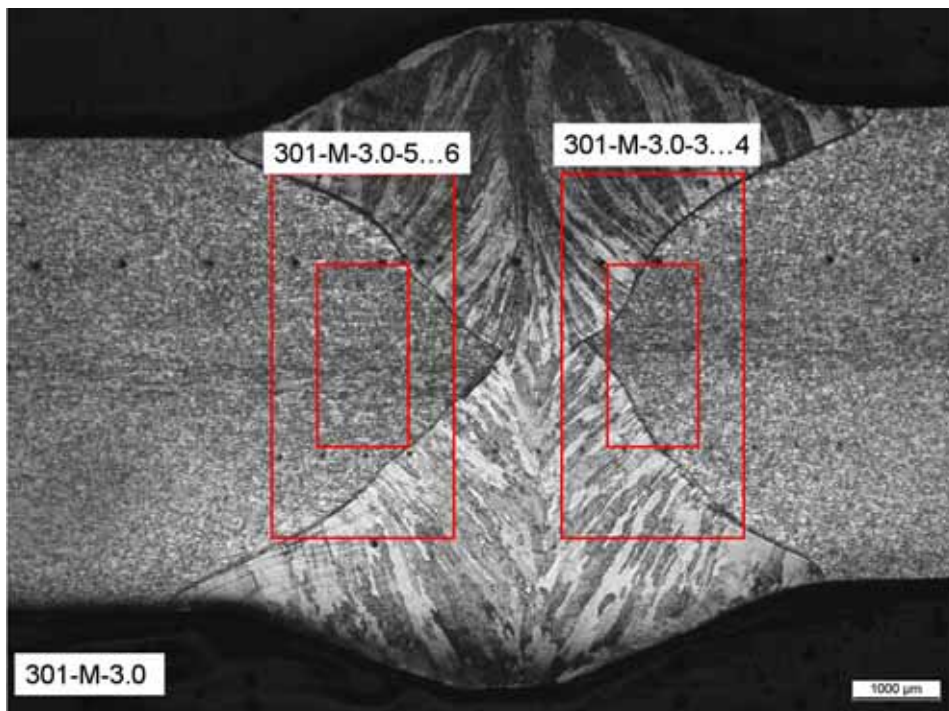


Figure 1. Example of the macrosection of the GMAW multipass welded austenitic EN 1.4318 (AISI 301 LN) steel, 5 mm plate thickness. Extraction of the  $1 \times 2$  mm<sup>2</sup> size flat-bar specimens (in realistic scale): inner rectangular lines: specimen's measuring gauge dimensions; outer rectangular lines: specimen-end dimensions. Right-hand side: specimen sampling the grain-coarsened HAZ immediately adjacent to the fusion boundary (with some weld metal included); left-hand side: specimen sampling the outer HAZ (without any weld metal involved) [2].

### 3. Methods

The optical “Aramis” monitoring system applied in the present study includes two cameras, a tensile testing machine and a computer in which the software for data acquisition and processing is installed. The tensile testing machine is used as in traditional tensile tests. The system takes pictures of the specimen at fixed intervals and it uses these pictures to measure strain components (in x-, y-, and z-directions). Test specimen is painted gray with a plain mat color.

The system adds a grid on top of the specimen in processing of the pictures (4–6 squares in vertical direction in miniature specimen). The position of each square in the grid is determined by tracing certain pixels inside the square. The system specifies the pixels by a color variation. At the beginning of the analysis squares are partially on top of each other so that there are no gaps between them at the end of the analysis. The system determines the strain components at each increment by calculation of the displacement at each square in the grid and numerically differentiating the resulting field.

As the “Aramis” system employs two cameras in angle to each other, all three strain components can be determined. This is especially helpful in tests that are made using round-bar specimens. In standard tensile test only the mean value of strain can be attained, whereas the present optical system produces local values of strain. The system also produces a video of all the pictures it has taken. Flawed, or otherwise disturbed, data can be cut down during the analysis. Such flawed data can occur due to fluctuation in lighting conditions especially at the boundaries of the tensile specimen. Displacement velocity used in the present system is usually slower than in standard tensile tests to aid image processing.

The actual tensile test being completed, the data produced by the system is run through a computer script, see Figure 2. This post-processing phase extracts flawed stages and pin points the necking specimen section.

### 4. Results

The following figures (Figures 3–5) present the true stress-strain curves determined for the EN 1.4318 steel multi-pass GMAW weldments using the flat-bar specimens extracted from the weld metal and the HAZ c.f. Figure 2. Comparison between true and engineering stress-strain curves are shown in Figure 6. Figure 7 presents the true stress-strain curve for the DQT HT80 steel base material determined using round-bar specimens.

Characterization of true stress-strain behavior using optical monitoring

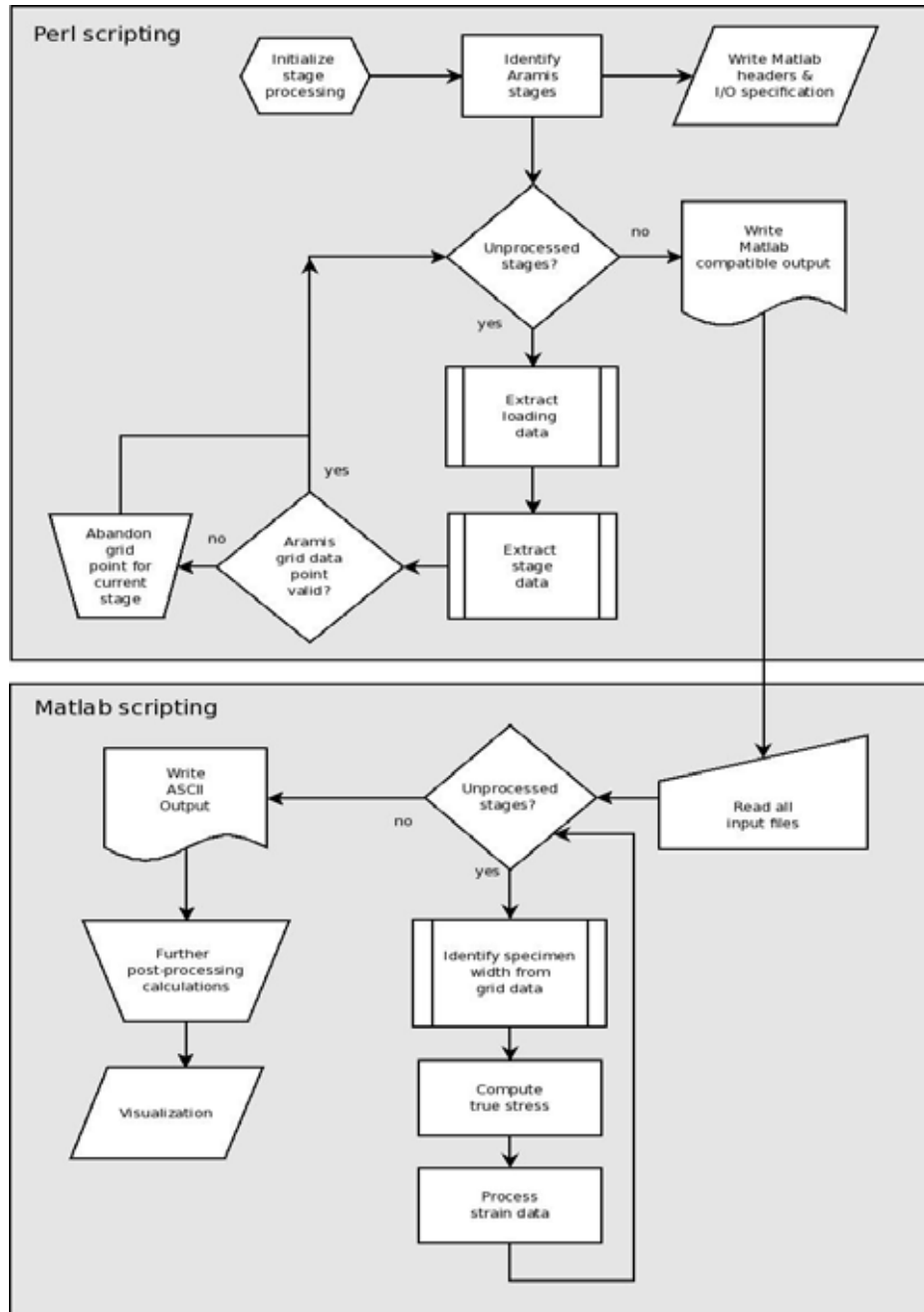


Figure 2. Flow chart of the post processing procedure [2].

Characterization of true stress-strain behavior using optical monitoring

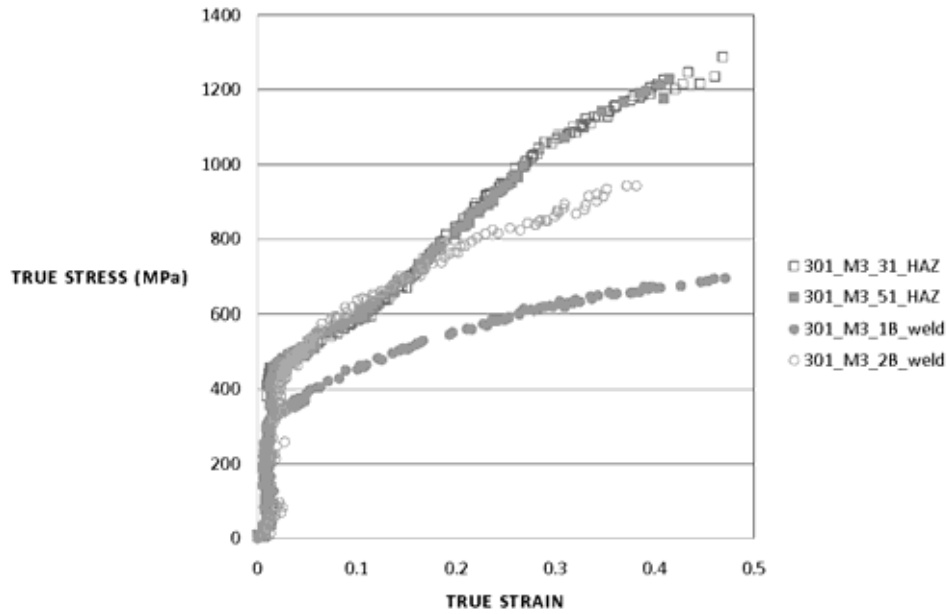


Figure 3. True stress-strain curves for the weld metal and the HAZ – specimen M3 [2].

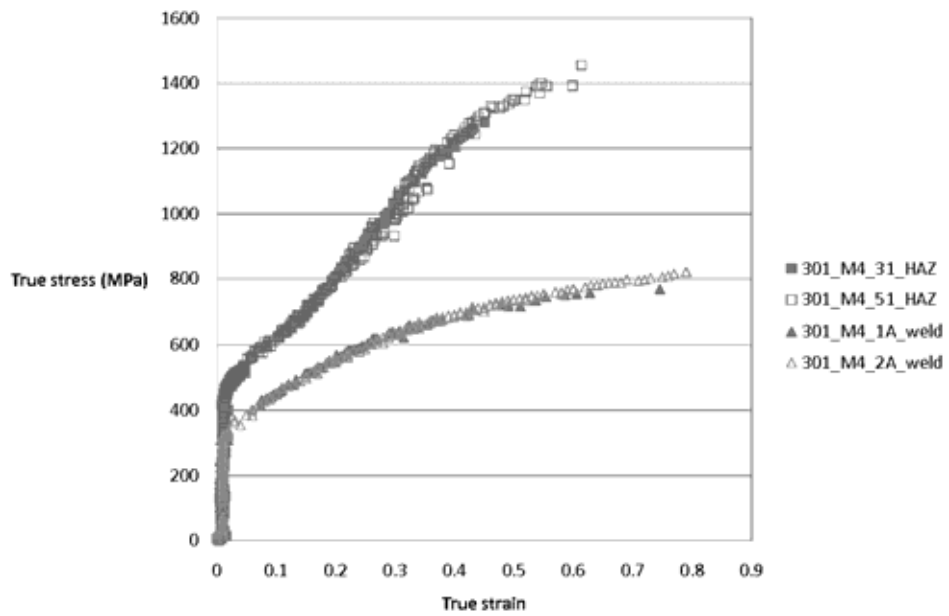


Figure 4. True stress-strain curves for the weld metal and the HAZ – specimen M4 [2].

Characterization of true stress-strain behavior using optical monitoring

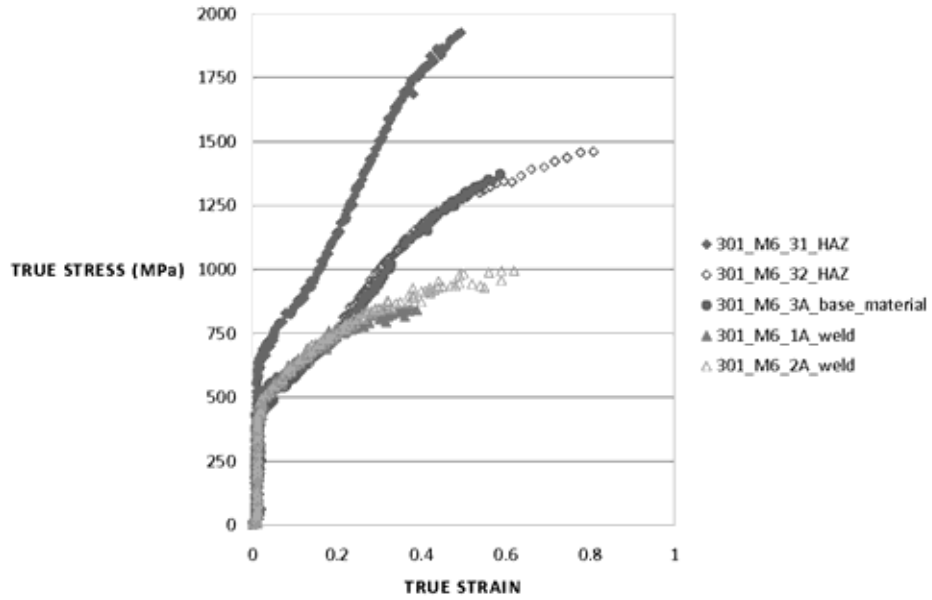


Figure 5. True stress-strain curves for the weld metal and the HAZ – specimen M6 [2].

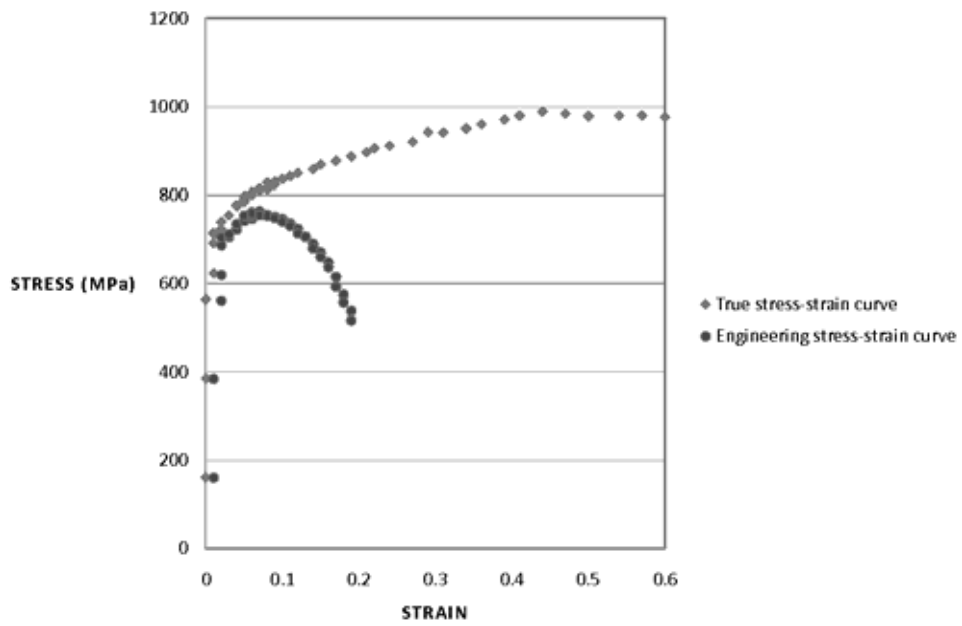


Figure 6. True and engineering stress-strain curves for the HAZ – specimen M4 [2].

Characterization of true stress-strain behavior using optical monitoring

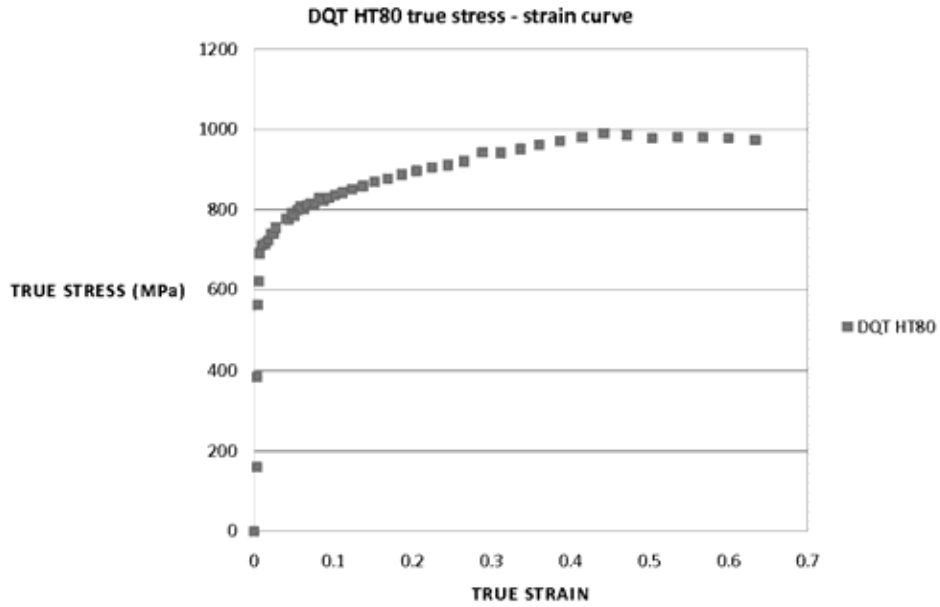


Figure 7. True stress-strain curve for the DQT HT80 steel: round-bar specimens. [4]

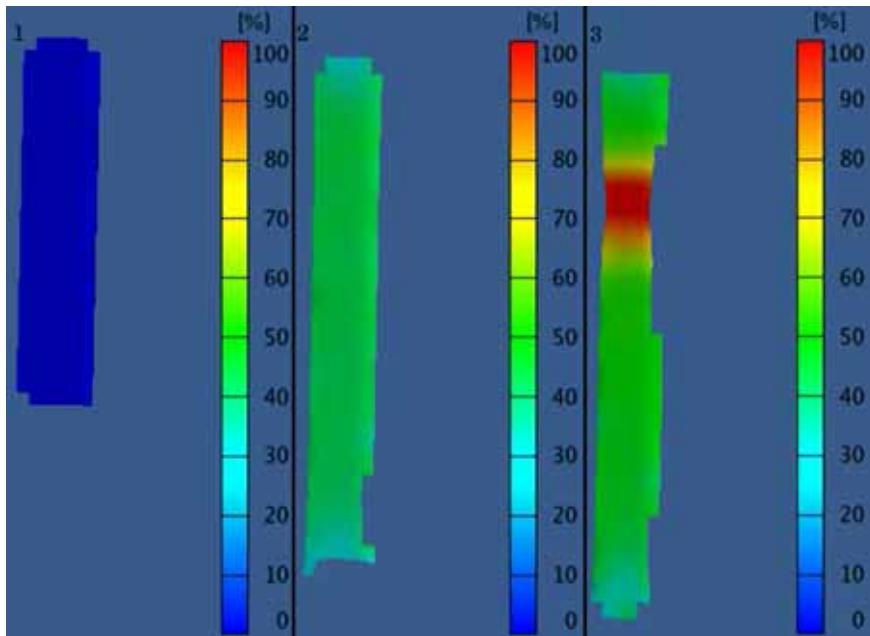


Figure 8. Images from "Aramis" video output: 1 at the beginning of test, 2 at the end of the elastic area, and 3 at end of the test.



Figure 8 shows three contour plots of specimen geometry. First contour plot is from the beginning of tensile test, second in the end of elastic region and third in the end of tensile test when reduction of area is the largest before the final specimen breakage.

## 5. Discussion

Fracture mechanics based integrity assessment of mismatching welds and their interfaces are well presented in the FITNET procedure [1]. Estimation procedures for welds with mismatching mechanical properties are one of the most complicated areas of fracture mechanical fitness-for-purpose evaluation. Thus, often various approximating steps need to be undertaken in an effort to perform and complete a specific analysis. Numerical modeling can thereby be based on detailed finite element analyses (FEA) of the structure in question. The experimental characterization needs to be accomplished with the necessary accuracy in order to sample those particular weldment regions displaying the most significant mechanical property mismatch in terms of strength and toughness. Care should be undertaken in the selection of an appropriate testing approach; these typically rely on so-called "small specimen" testing techniques both with respect to mechanical (tensile) properties and fracture mechanical toughness characterization. In evaluation of the crack driving force and in selection of applicable plasticity corrections (failure assessment diagrams), however, one typically needs to utilize pre-existing solutions for the stress intensity factor (SIF), limit load, failure assessment diagram (FAD) etc., or take the long road and derive these parameters on the basis of a FEA. In both cases, the decision on how material properties are treated needs to be made upon and is one of the crucial stages in determining the analysis outcome and the quality of the attained results [5].

The FITNET structural integrity assessment method requires principal material tensile and fracture mechanical properties for carrying out the analysis. Particularly, some form of true stress-strain curve must be specified and fracture mechanical properties need to be specified by one of various available means. Option 1, the standard option, is recommended for use when the mismatch in tensile properties is less than 10%. Option 2, the mismatch option, is able to treat situations where both base and weld metal have an unspecified degree of mismatch. Option 3 is also able to handle mismatch via an equivalent stress-strain curve concept. In FITNET terms, the numerical analyses are option 4

analyses. The FAD is determined on a case-by-case basis for the combination of structure and material over a range of applied loading from linear-elasticity to plastic collapse [5].

Tensile test results obtained for GMAW welds on strain-hardened austenitic stainless steel EN 1.4318 (AISI 301 LN) using miniature flat-bar specimens with the cross-section geometry of  $1 \times 2 \text{ mm}^2$ , are presented in Figures 3–6. The results demonstrate that in all cases the weld metal exhibits undermatching strength, in relation to the tensile properties of the outer HAZs and, finally, the base material (in C850 delivery condition). According to a parallel study [2], local softening in the EN 1.4318 steel (C850) as a result of welding occurred, and progressively advanced, via diffusion controlled mechanism at peak temperatures exceeding  $900 \text{ }^\circ\text{C}$ . Bearing in mind that welding was made using AISI 308 LSi type filler metal with considerably lower strength ( $R_{p0.2} = 370 \text{ MPa}$ ;  $R_m = 620 \text{ MPa}$ ) than the strain-hardened parent steel, it can be concluded that the true-stress strain curves according to Figures 3–6 provide a realistic description of the strength and stress-strain characteristics of the different regions of the GMAW weldments in question. Thus, the local, narrow weld regions with mismatching strength were successfully hit and sampled using miniature size  $1 \times 2 \text{ mm}^2$  flat-bar specimens (c.f. Figure 2).

Figure 7 shows that it is also possible to use round-bar specimens with geometry of  $\text{Ø } 6 \text{ mm}$  diameter size for the determination of the true-stress strain characteristics. The results are comparable with those of miniature flat-bar tensile specimens [4].

One advantage of the present technique is that the initial set up procedure is fast since the test specimen only needs to be painted and no strain gauges are needed. As the present optical monitoring system uses two cameras to record the tensile test this allows one to extract strain data from different parts of the specimen even after the test has already ended. Recorded data can be used to create visually superior videos.

With respect to the present technique, some challenges still exist. These include for instance the necessity for the paint layer to be smooth. In addition, the post-processing procedures lack in some sophisticated features that are needed in advanced fracture mechanical analyses; thus VTT has developed its own code to extract specific data from “Aramis” system output.

## 6. Conclusions

The present “Aramis” equipment enables continuous optical monitoring and complete mapping of localization of deformation in a specimen during the tensile test. Thus, true stress-strain curves with strain hardening characteristics can be successfully obtained using flat-bar specimens as small as  $1 \times 2 \times 8 \text{ mm}^3$ . As shown in Figure 7, the system still has some difficulties of tracking, especially, the boundary grid squares. Fortunately this flaw is simply avoided in the post-processing by removing from the data the stages that differ too much from the previous one.

True-stress-strain curves provide more accurate information than their engineering equivalents for the use in computational fracture mechanics. Determining the inherent properties of various mismatching weldment regions using miniature specimen techniques enables to gain full advantage of sophisticated numerical non-linear modeling techniques that allow the use of continuous material property descriptions. Especially regarding the FITNET procedure, FADs produced from the true stress-strain curves are more accurate; hence safety margins can be smaller when applying FADs to actual structural design.

## 7. Future works

In the following works, the present optical monitoring system is planned to be used in measure the strain rates in a specimen that consist more than one weld zone (i.e., transverse in relation to the weld). These tests would be compared with ones that are done to specimens consisting only one zone (i.e., parallel to the weld). It is considered extremely beneficial to develop analyzes procedures capable of successfully characterizing material properties across multiple zones with only one single specimen. Experiments to analyze specimens that include cracks are also planned.

## 8. Acknowledgements

The present paper belongs to the ‘FRAS’ project within the national “SAFIR 2010” nuclear research programme. Provision of the primary data from the TEKES ‘MIS-MATCH’ project is appreciated.

## References

1. 'FITNET' Fitness-for-Service (FFS) Procedure. Vol. 1. Eds. M. Kocak, S. Webster, J. J. Janosch, R. A. Ainsworth, R. Koers. European Fitness-for-service Network. CEN 2006.
2. Nevasmaa, P., Sirén, M., Alhainen, J., Andersson, T., Elers, L., Muukkonen, T., Somani, M. C. & Karjalainen, L. P. Paikallisen alilujuuden (mis-match) vaikutus muokkaamalla lujitettujen austeniittisten ruostumattomien terästen hitsausliitosten ominaisuuksiin. Espoo: VTT, 2009. VTT Tutkimusraportti VTT-R-06034-09. 50 s. (In Finnish).
3. Slater, S., Priest, A. H., Álvares, J. A., Gallo, C., Polanco, J. A., Saiz, A., Gutiérrez-Solana, F., Ponsot, A., Wallin, K., Laukkanen, A., Demofonti, G., Di Biaggio, M. & Mecozzi, E. An energy balance approach for crack arrest – final report. Luxembourg, 2004. 171 p.
4. Elers, L. The validity of fracture resistance curve characterization methods for extended ductile crack growth. Espoo: VTT, 2008. VTT Research Report VTT-R-10197-08. 58 p.
5. Laukkanen, A., Karjalainen-Roikonen, P., Nevasmaa, P., Andersson, T. & Elers, L. Fracture mechanical fitness-for-purpose assessment of undermatching high strength steels welds. Espoo: VTT, 2009. VTT Research Report VTT-R-01115-09. 45 p.

# Non-contact measurement of oxide thickness with a laser ultrasonic technique

Jonne Haapalainen<sup>1</sup>, Joonas Eskelinen<sup>1</sup>, Tarja Jäppinen<sup>2</sup>,  
Stefan Sandlin<sup>2</sup> and Edward Hægström<sup>1</sup>

<sup>1</sup> Electronics Research Laboratory, Dept of Physics,  
University of Helsinki, Helsinki, Finland

<sup>2</sup> VTT Technical Research Centre of Finland, Espoo, Finland

## Abstract

Non-contact laser ultrasound (LU) method is a potential tool for structural health evaluation in power plants. In this study a LU surface wave method was employed to determine the oxide layer thickness in zircaloy tubes used as cladding of fuel rods in nuclear reactors. Ultrasound excitation was done with a pulsed laser whereas a laser doppler interferometer was used to remotely receive the propagating ultrasonic signals. To show the method's capability results from a 8  $\mu\text{m}$  zirconium oxide layer measurement are presented.

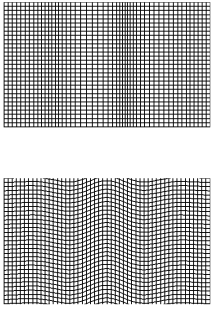
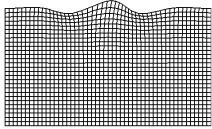
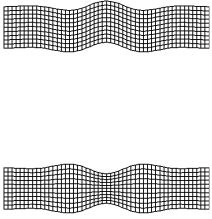
## 1. Introduction

Ultrasonic non-destructive evaluation is widely used in structural health evaluation. It can be used to detect e.g. cracks and corrosion, but it requires typically contact or immersion between the transducer and the sample. Non-contact laser ultrasound (LU) provides means to overcome these limitations e.g. in high temperature or radiative environments. Compared to traditional ultrasound testing, LU provides better spatial resolution and wider frequency bandwidth. We present principles of the LU method and give an example of its use for oxide layer thickness measurement.

## 1.1 Ultrasound

Ultrasound is a propagating mechanical disturbance. The velocity and attenuation of ultrasonic waves are affected by the mechanical properties of the sample. Ultrasound can propagate in multiple modes, cfr Table 1.

Table 1. Different wavemodes employed in ultrasonic testing.

Bulk waves	Surface waves	Guided waves
		
<p>Propagates in bulk material. Reflects from defects in the bulk material.</p>	<p>Propagates along the surface of the material. Can be used for surface characterization.</p>	<p>Propagates along thin surfaces, such as tubes. Velocity depends on the sample geometry and frequency</p>

## 1.2 Laser Ultrasound

Laser ultrasound [1] is used for non-destructive evaluation (NDE) in this study. A short (few nanoseconds) laser pulse is absorbed close to the surface of the sample. Thermal expansion due to heating excites an ultrasonic wave which probes the sample (Figure 1). Broadband, high frequency, (1 ns pulse generates  $\sim 100$  MHz waves) ultrasonic waves can be excited. Moreover, the efficiency to generate different wave modes is good. In metals the normal skin depth of the excitation laser penetration into the sample is a few nm, which provides local excitation (the beam diameter can be as small as  $10 \mu\text{m}$ ). Propagating ultrasonic waves can be detected by measuring the surface displacement (out-of-plane as well as in-plane) of the sample with an interferometric receiver providing a non-contact and remote measurement.

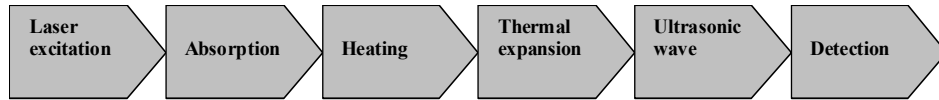


Figure 1. Principle of laser ultrasound testing.

### 1.3 Thickness profiling

Surface waves can be used for thickness profiling of a thin layers [2–4]. Typically surface waves probe a depth which equals their wavelength. If the material parameters changes as a function of depth (for example different layers), varying the wavelength allows probing the layer structure. The material gradient is seen as dispersion (frequency dependent velocity), Figure 2.

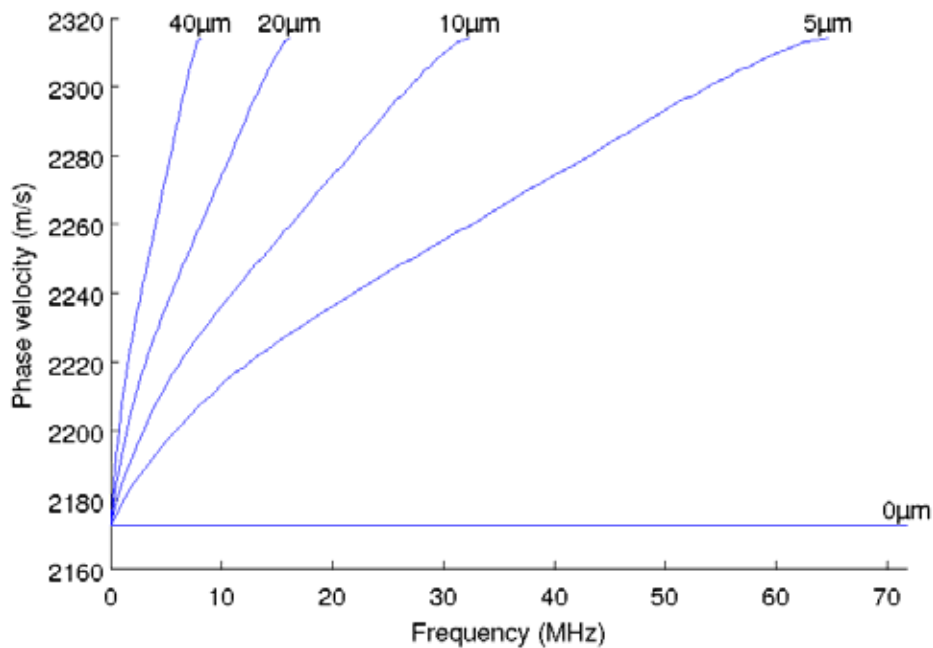


Figure 2. Dispersion of surface wave in a zircaloy tube as a function of covering oxide layer thickness.

## 2. Experiments

We determined the thickness of an oxide layer covering a zircaloy tube sample. The oxide layer was grown in an oven in  $O_2 + Ar$  atmosphere. The layer thickness was also measured destructively with an optical microscope (Figure 3).

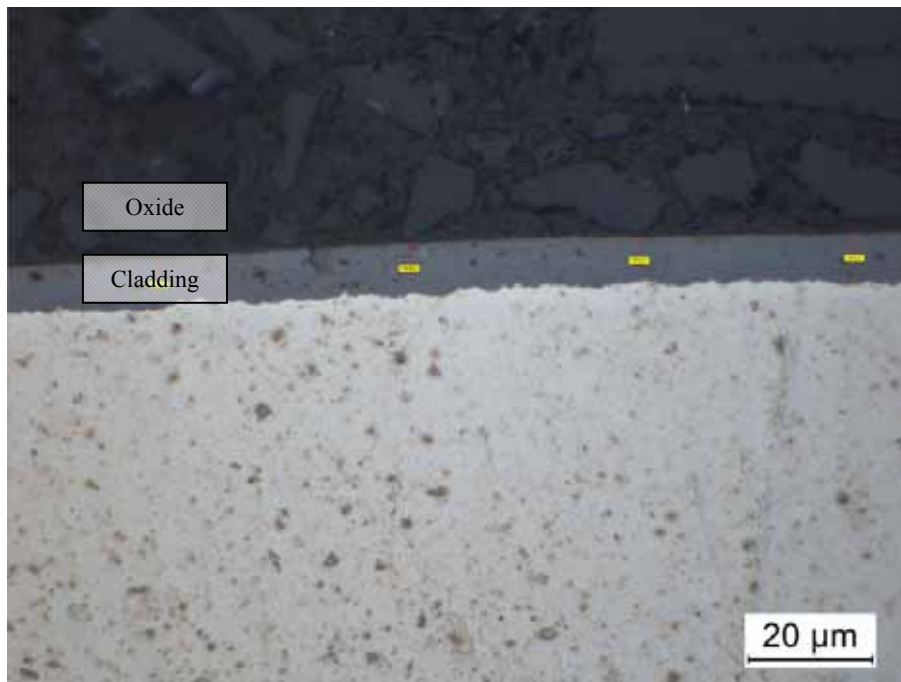


Figure 3. Optical image of the sample showing the cladding, oxide and backing epoxy.

Excitation was done with a Nd:YAG laser emitting a 1 mJ, 1 ns long pulse with a 100 Hz repetition frequency. The excitation beam was scanned with a mirror that was attached to a translation stage. Forty 100 μm long steps were taken for a total of 4 mm measurement distance. Non contact receiving was done with a laser doppler vibrometer (LDV). Each measurement point was averaged 100 times to improve the signal-to-noise ratio (SNR).

A 2D-FFT was next performed on the measured data to determine the phase velocity of the propagating surface waves in frequencies between 9 MHz (limitation of method due to finite thickness of base cladding) and 20 MHz (upper frequency of the receiver). A theoretical fit to the measured dispersion curve was used to determine the thickness of the oxide layer.



### 3. Results

Results of the oxide thickness measurement obtained with both LU and destructive optical methods are presented in Table 2. The root mean square error (RMSE) between the surface wave velocity measurement and the theoretical curve was less than 1 m/s (< 1% of velocity range), which indicates good agreement between the theory and measurement.

Table 2. LU vs. optical measurement of the oxide thickness.

Oven time	Optical measurement	LU measurement
0 h	0 $\mu\text{m}$	0 $\mu\text{m}$
6 h	8 $\mu\text{m}$	6 $\mu\text{m}$

### 4. Conclusions

Principles of LU method for NDE was presented. The proposed LU oxide thickness measurement correlated well with the reference optical measurement for thin samples. The difference between the optical and the LU thickness estimate is probably due to a difference in measurement position and unequal oxide thickness. When the measurement was done on thicker (> 10  $\mu\text{m}$ ) layers, the RMSE between the theory and the measurement exceeded 10 m/s, which is assumed to be due to problems in layer integrity.

Laser ultrasound holds potential for multiple other measurements in the area of NDT in power plants. Possible application areas include:

- Crack detection in power plants [5]
- Changes in elasticity of fuel tubes [6]
- Wall thinning measurements [7].

### References

1. Scruby, C. B. & Drain, L. E. Laser ultrasonics: techniques and applications. Inst of Physics Pub Inc., 1990.

Non-contact measurement of oxide thickness with a laser ultrasonic technique

2. Every, A. G. Measurement of the near-surface elastic properties of solids and thin supported films. *Measurement Science and Technology*, Vol. 13 (2002) 5, pp. 21–39.
3. Windels, F. W., Vanaverbeke, S. & Leroy, O. Thin coating characterization by Rayleigh waves: An analytical model based on normal-mode theory. *The Journal of the Acoustical Society of America*, Vol. 110 (2001) 3, pp. 1349–1359.
4. Hurley, D. C., Tewary, V. K. & Richards, A. J. Surface acoustic wave methods to determine the anisotropic elastic properties of thin films. *Measurement Science and Technology*, Vol. 12 (2001) 9, pp. 1486–1494.
5. Ochiai, I. Development and Applications of Laser-ultrasonic Testing in Nuclear Industry. In *1st International Symposium on Laser Ultrasonics: Science, Technology and Applications*. Montreal, Canada, 2008.
6. Liu, I. & Yang, C. Laser Ultrasound Technique for Nondestructive Characterization of Material Properties in Hydrogen-Charged Zircaloy Tubes. In *1st International Symposium on Laser Ultrasonics: Science, Technology and Applications*. Montreal, Canada, 2008.
7. Murfin, A. S. & Dewhurst, R. J. Estimation of wall thinning in mild steel using laser ultrasound Lamb waves and a non-steady-state photo-emf detector, *Ultrasonics*, Vol. 40 (2002) 1–8, pp. 777–781.

# **On-line flaw growth monitoring in high temperature plant**

Ian Atkinson, KANDE International Ltd, Knutsford, UK

Stephen Kelly, Doosan Babcock, Renfrew, UK

Philip Lay, Doosan Babcock, Renfrew, UK

Colin Brett, E.ON Engineering, Nottingham, UK

## **Abstract**

The operating conditions experienced by power plants place high demands on plant components, and ensuring plant availability without compromising safety or plant integrity can be a significant challenge to operators. On-line measurement of known flaws in plant has the potential to provide plant operators with substantial savings in overall operating costs through the better management of inspection and repair activities. This is particularly true of high-temperature plant, where the preferred inspection techniques for measuring crack growth are unsuitable for on-line application and must be applied during plant shutdown, which can lead to low accuracy and substantial inspection costs, as well as loss of production.

To address such problems, we have been working on the development of in-situ, high-temperature ultrasonic crack growth measurement techniques for several years, and will this year proceed to a trial installation at a UK fossil-fuel plant.

This paper reports the results of a laboratory trial to demonstrate the measurement of fatigue crack growth in a thick-walled ferritic steel pipe section at 615°C. This was part of a programme of tests performed to verify the viability of the transducers and crack-growth measurement techniques, prior to the trial on operational plant.

## 1. Introduction

The operational demands placed on current generation power plants, particularly those in countries where commercial markets in power generation operate, can be severe and ultimately have an adverse effect on plant integrity. For example, thermal cycling associated with load following can lead to fatigue crack growth, while excursions above the design operating temperature can accelerate creep damage. Because such damage can be expected to occur, NDE inspections of vulnerable components are performed periodically with the aim of detecting new flaws.

When in-service flaws are discovered in plant components, it is not always feasible or necessary to replace them immediately. However, in such situations it is important to determine if the flaw is growing and if so, at what rate, so that planning for its management and eventual possible repair or replacement can be undertaken. In the case of cracks in steel components, the preferred way of measuring flaw growth is by periodic ultrasonic inspection during plant shutdown. The cost of such inspections, including NDE services, site preparation and reinstatement, plus the cost of lost production, can be substantial, especially if it becomes necessary to have plant outages specifically to accommodate the flaw monitoring requirement.

Using periodic inspection to measure flaw growth accurately can also be problematic. The variations arising from small differences in measurement location and inspection set-up, combined with random errors in data analysis, can make it difficult to be certain if measured growth is real, or merely a reflection of the uncertainty between repeated measurements. This can lead to the situation where flaws apparently grow rapidly over one operational cycle and shrink over the next. The avoidance of such problems requires careful inspection design and implementation to minimise both systematic and random errors. In ultrasonic inspection, such improvements may be achieved by the use of permanently installed probes.

For high temperature plant such as power stations, the above problems are likely to be exacerbated for a number of reasons, for example:

- Outage duration may be extended because of the time required for the plant to cool to a temperature at which the work can be performed without risking harm to personnel or damage to inspection equipment.
- Surface preparation to remove high temperature oxidation products that adversely affect ultrasonic coupling can also remove reference marks and

change the surface form, making it more difficult to obtain accurate repeat measurements.

- In-service cracks may be subjected to compressive stresses at ambient temperatures, making them more difficult to detect and measure accurately.

High temperature in-situ monitoring with permanently attached probes would avoid these problems:

- Continuous access to accurate information on flaw size makes shutdown specifically for inspection unnecessary. In addition, it enables the operator to build up detailed information on flaw growth rates, which will help to inform decisions such as when to repair or replace affected components.
- Once probes have been installed, further surface preparation is unnecessary and hence uncertainties of probe position and component shape are eliminated and measurement accuracy is increased.
- Measurements are made under the load conditions that are driving the flaw growth and hence crack closure is unlikely to be an issue.

Until recently however, it has not been practical to perform long-term in-situ ultrasonic measurements on high-temperature plant due to the lack of transducers with the required sensitivity and the robustness necessary for long-term application in an operational environment subject to both thermal cycling and temperature extremes. In this paper we report on work performed by KANDE International, Doosan Babcock and E.ON to develop a capability for measuring fatigue crack growth in ferritic steel, thick-walled pipes at temperatures around 600°C.

## **2. Background**

The work reported in this paper is a continuation of work started in an earlier collaborative project known as ULTRASMART (Ultrasonic Scanning and Monitoring at Running Plant Temperatures) (1, 1). Under the ULTRASMART project, KANDE developed a robust, high temperature ultrasonic probe capable of working at temperatures greater than 600°C for extended periods of time. In September 2007 three prototype transducers were installed on a steam-pipe at E.ON's Ratcliffe-on-Soar power station (Figure 1), one measuring wall

## On-line flaw growth monitoring in high temperature plant

thickness and the other pair in a Time-of-Flight Diffraction (TOFD) configuration suitable for crack growth measurement.



Figure 1. High temperature probe installation at Ratcliffe in 2007.

Due to the exploratory nature of the study, these probes were installed well away from any weld or known flaws, so as to avoid any problems arising from adverse effects associated with the installation procedure. At the time of writing these probes are still working after operating for more than 11 500 hr at 565°C and experiencing more than 70 plant starts.

Because of the encouraging results obtained, it was decided to proceed to a trial installation on a known flaw in 2010. It is planned that this installation will be made on a defective weld that is scheduled to be replaced in 2012, as this will provide an opportunity to obtain confirmation of the measured flaw size by destructive examination.

The planned trial is a considerable commitment for all the parties involved and in order to reduce the risks and uncertainties associated with it, laboratory studies have been performed to demonstrate and verify the performance of the transducers, the welding procedures for transducer attachment and the measurement technique itself. The results of the latter study are reported below.

### 3. Experimental Work

#### 3.1 Specimens

The experimental work reported here was performed on fully representative 2¼Cr steel pipe sections removed from power plant service. To minimise interface losses and any materials compatibility issues, the transducer delay lines and the welding consumables used were also made of 2¼Cr steel.

The flaw type selected for the trial is a steam-line circumferential bore crack (Figure 2). These are fatigue cracks that initiate at the inner surface, close to the circumferential welds that join the pipe sections, and propagate in the through-wall direction as a result of the stresses generated by thermal cycling as the plant is stopped and started, according to the demand for power.

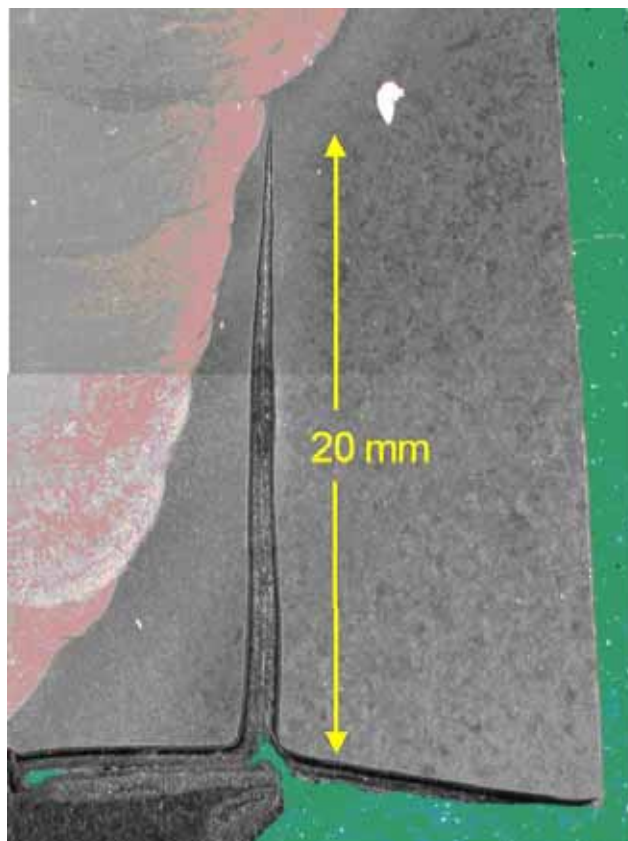


Figure 2. Section through a steam-line circumferential bore crack.

For the laboratory trial of the proposed inspection technique, the aim was to simulate the case of a steam-line bore crack by measuring the growth of a fatigue crack in a specimen subjected to cyclic loading at high temperature. The specimen used was 464 mm long by 100 mm wide with a wall thickness of approximately 62 mm. A full-width starter notch was machined across the middle of the inner surface of the specimen and was approximately 3 mm deep at the specimen centreline.

### **3.2 Inspection technique**

The technique selected to monitor the growth of these cracks is a variant of the two-probe TOFD technique, in which a beam of ultrasound from a transmitter probe impinges on the crack and forward diffracted signals from the crack tip are detected by a receiver probe symmetrically positioned on the opposite side of the weld.

In conventional TOFD inspection, a pair of probes is scanned on the component surface, and the movement of the probes relative to the flaw gives rise to characteristic arc-shaped signals that are used to identify the flaw and determine the flaw extent. In the case of in-situ monitoring, probe movement is not possible and therefore the characteristic arc-shaped signal shapes cannot be obtained. Instead it is necessary to monitor the signals obtained over time, in order to discriminate between the signal from a growing crack, which will change over time and signals from other sources such as backwall reflection or gas pores in the weld, which will not. To collect the required data, KANDE has adapted its USBox UT system to collect data periodically over an extended time interval and to display it as a two dimensional image in which one axis represents flaw depth, and the other axis represents the time elapsed since the start of data collection.

### **3.3 Transducers**

The transducers used for the trial reported here had 6.3 mm diameter circular elements generating longitudinal mode ultrasonic beams with a nominal resonant frequency of 5 MHz. The transducer delay lines were approximately 40 mm long by 20 mm diameter and made of 2¼Cr steel. In order to give 45° angled longitudinal beams in the test specimen and in preparation for attachment by welding, the delay lines were machined to 45° knife-edges. Mineral insulated semi-rigid coaxial cables were used to carry signals to and from the probes.



### 3.4 Transducer attachment

In preparation for transducer attachment, pads of 2¼Cr weld metal were deposited on the outer surface of the specimen at the intended probe locations and heat treated to control material hardness and prevent embrittlement close to the flaw location.

The transducers were subsequently welded onto these pads (Figure 3) using a welding procedure developed by Doosan Babcock. A probe centre separation (PCS) of 104 mm was selected to give maximum sensitivity approximately 10 mm from the bore surface of the 62 mm (nominal) wall thickness pipe and to provide good coverage of the inner half of the pipe wall at the crack position.



Figure 3. High temperature probes welded onto specimen in TOFD arrangement.

## 4. Experimental Setup and Results

The specimen was mounted in a 600 kN materials testing machine for cycling under compressive load in a four-point bend arrangement. It was heated using a resistance heating element and insulated using multiple layers of ceramic blanket insulation (Figure 4). Thermocouples welded to the side of the block, were used for temperature control and monitoring.



Figure 4. Specimen in 4-point bend rig at completion of test with insulation partly removed to show heating element arrangement.

The specimen and transducers were heated from ambient temperature to 615°C before fatigue cycling was started but UT data was recorded every 30 s throughout the full duration of the experiment. The resulting record is shown in Figure 5 and explained in detail below.

The specimen was initially set to reach a temperature of 585°C and allowed to stabilise at this temperature overnight. The reduction in ultrasonic velocity with increasing temperature can be seen in the increased arrival time of the ultrasonic

signals at the left-hand side of the image and the horizontal lines seen in the central portion of the image correspond to the period at 585°C. The temperature was then increased to 615°C, which can be seen as a further small increase in the arrival time of all the visible signals.

After the temperature had stabilised at 615°C, cyclic loading was commenced, shortly after which crack growth was observed (at approximately 20 hours elapsed time in Figure 5). Load cycling then continued for approximately 80 minutes, with a reduction in applied load after 60 minutes to slow the crack growth rate. After cycling was halted the specimen was held at 615°C for 30 minutes before data recording was stopped.

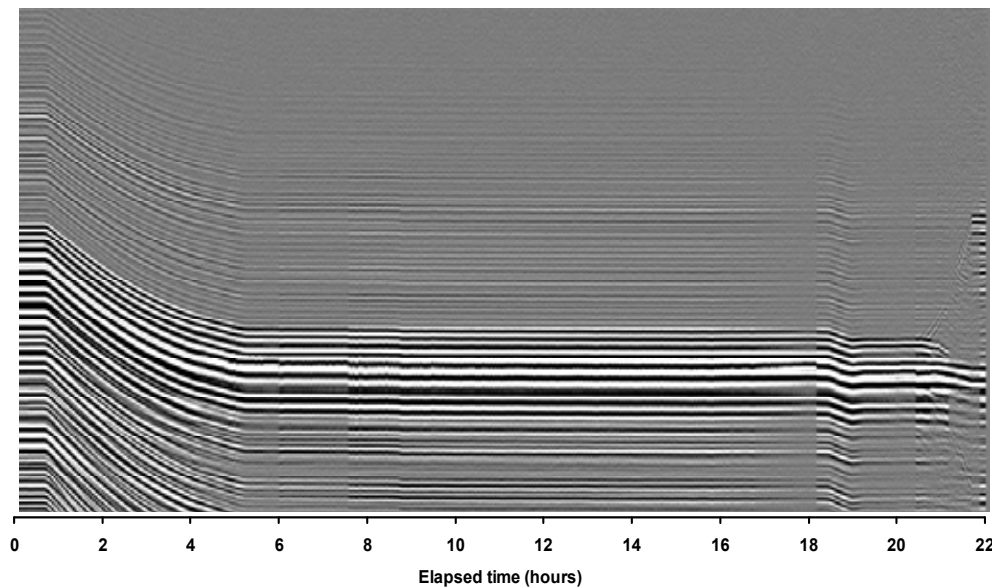


Figure 5. UT data from monitoring trial.

The signals from the tip of the growing fatigue crack are more clearly seen in Figure 6. This detail extracted from Figure 5 covers a period of approximately 90 minutes and shows the weaker signal from the crack tip diverging from the higher amplitude starter notch and backwall reflection signals, giving a steeply inclined line rising across a background of nearly horizontal lines.

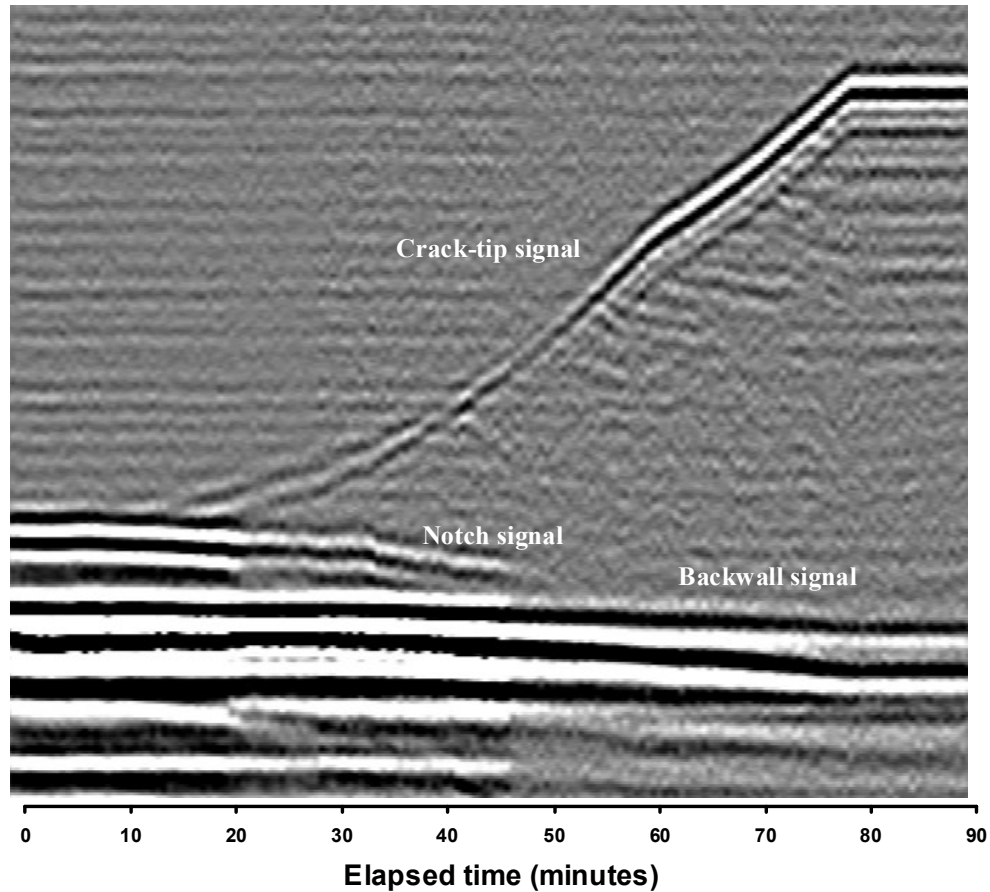


Figure 6. Crack growth detail.

In addition to the inclined line representing the crack tip signal, Figure 6 shows several other points of interest:

- The ‘inclined line’ signal increases in amplitude as the crack tip grows towards the axis of the ultrasonic beams.
- The ‘inclined line’ curves upwards, due to the crack growth rate increasing as the load is applied to a reducing ligament.
- The visible decrease in the slope of the curve after approximately 60 min. indicates where the peak load was reduced to slow the growth rate.
- As the fatigue crack starts to grow, the starter notch signal does not disappear completely but reduces in amplitude and curves increasingly

'downwards'. This indicates that the notch is wide enough to provide a target that reflects some portion of the beam back to the receiving probe until all available paths are interrupted by the increasing large fatigue crack.

- As the crack height increases, the backwall reflected signals are also increasingly interrupted and hence the backwall signal reduces in amplitude and tends to slightly longer range.
- The horizontal signals at the right-hand side of the image show where cyclic loading was stopped and the specimen held at 615°C before recording was stopped.

Due to a number of uncertainties, of which ultrasonic velocity at the measurement temperature, probe separation and wall thickness at the point of measurement are the most significant, absolute crack size is difficult to determine accurately. However, measurement of the crack growth, which is a differential measurement where both initial and final depths are subject to the same systematic errors, should be reasonably accurate provided the total growth is not too large a proportion of the overall wall thickness. Hence, by assuming that:

- The longitudinal velocity in 2¼Cr steel at 615°C is  $5.45 \pm 0.1$  mm/μs (2).
- The specimen is  $62 \pm 2$  mm thick at the position of measurement.
- The effective PCS is  $98 \pm 5$  mm.

It can be estimated that the observed growth under cyclic loading, measured from the tip of the starter notch, in the through-wall direction, was  $16 \pm 1$  mm.

The actual crack depth has not yet been confirmed by destructive examination but Figure 7 shows the result of a magnetic particle inspection of the fatigue crack at the edge of the specimen, performed after completion of the test. This indicates crack growth of approximately 20 mm at the edge of the block, which is reasonably consistent with the result obtained from the UT measurement made on the specimen centreline.

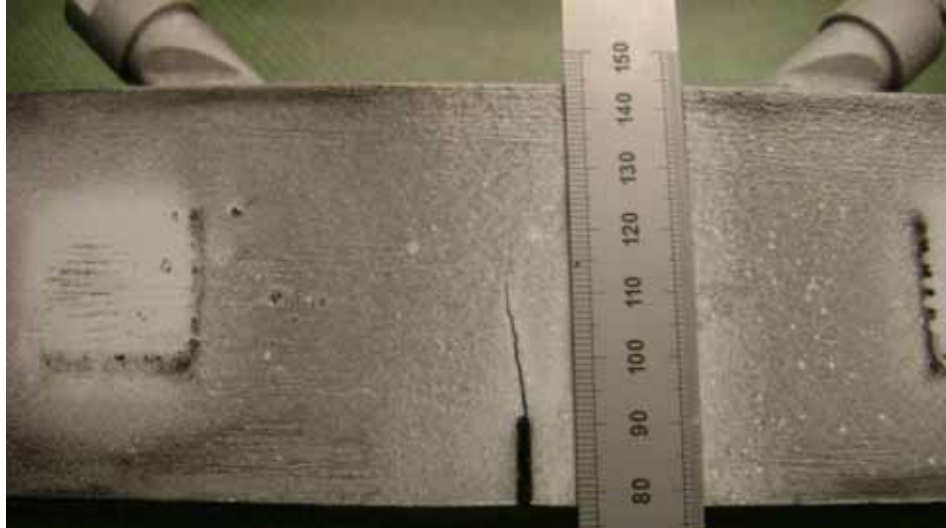


Figure 7. Fatigue crack detail after completion of test.

## 5. Discussion and Conclusions

The experimental trials undertaken clearly demonstrate the feasibility of detecting and measuring crack growth at 615°C using a two probe TOFD ultrasonic technique.

The diffracted signals obtained were substantial and had a good S/N ratio. This gives us confidence that accelerated ageing of the transducer, which is an unavoidable result of high temperature operation, should not degrade the performance to the point where the diffracted signals are too weak to be detected, in the expected lifetime of the installation. This is supported by earlier experimental work and by the previous Ratcliffe trial where the probes have operated for more than two years without significant reduction in output.

Similarly, the signal levels obtained suggest that the higher temperature operation is also likely to be feasible. Results obtained in earlier work lead us to believe that performance should remain good up to at least 650°C and that there may be some capability at temperatures as high as 730°C, with the caveat that both sensitivity and lifetime are expected to reduce increasingly rapidly as the operating temperature increases towards the circa 800°C Curie Temperature of the transducer material.

Whilst it is clear that accurate crack growth measurement is feasible under the constant temperature conditions used in this trial. Under plant operating conditions, where thermal cycling is driving flaw growth and the cycling rate is both slow and variable, accurate monitoring is likely to be more difficult.

Probably the most significant difficulty will arise from the sensitivity of the ultrasonic velocity to relatively small changes in temperature. This may make it difficult to differentiate between changes due to crack growth and changes due to temperature variation. One way of addressing this problem would be by processing the data to correct for the effects of temperature variation, with temperature either being measured directly or estimated from the backwall echo position. While the processing required for this is similar to that used in tools already available for TOFD data enhancement, its application would not necessarily be straightforward in practice, and it may be better to avoid the issue altogether, by collecting data each time the plant passes a set temperature, rather than collecting data at fixed intervals. This approach has the further advantage that the recorded data could then be scaled directly in terms of the number of thermal cycles, rather than in elapsed time, and hence any flaw growth recorded would be more likely to appear as a linear feature, of the type seen in the trial data. KANDE is currently adapting its monitoring systems to implement this mode of operation.

It is also worth noting that although small amounts of crack growth can be detected and measured with accuracy using fixed probes once the flaw signal has been identified in the B-scan image, there will be some minimum amount of growth that has to occur before the signal can be unambiguously identified. Accurate positioning of the crack tip by conventional inspection techniques prior to the installation of the fixed probes should help to reduce the uncertainty associated with signal identification, and correlation based signal processing techniques could also be applied, to help identify small changes between consecutive signals before they become apparent to the naked eye.

## References

1. Atkinson, I., Gregory, C., Kelly, S. P. & Kirk, K. J. Ultrasmart: Developments in ultrasonic flaw detection and monitoring for high temperature plant applications. Proceedings of CREEP8 Eighth International Conference on Creep and Fatigue at Elevated Temperatures. San Antonio, Texas, 22–26 July, 2007.

On-line flaw growth monitoring in high temperature plant

2. Kelly, S. P., Atkinson, I., Gregory, C. & Kirk, K. J. On-line ultrasonic inspections at elevated temperatures. IEEE International Ultrasonics Symposium, UFFC. New York, September 2007.
3. Andrews, K. W. Testing at high temperatures. In: Szilard, J. (Ed.) Ultrasonic Testing – Non-conventional testing techniques. Wiley, 1982.



# **Experience on the periodic wet bar diagnosis of water-cooled generator stator windings**

Hee-Soo Kim and Yong-Chae Bae  
Korea Electric Power Research Institute  
Daejeon, Republic of Korea

## **Abstract**

In this paper, of various integrity evaluation methods for water-cooled stator windings, it is verified that a wet bar diagnosis method is most sensitive. Generally, there are vibration characteristics test, leak test, and water absorption test, as mechanical integrity evaluation methods for water-cooled stator windings. When a generator-rotor is extracted, mechanical integrity evaluation for water-cooled stator windings are carried out by using all of them. In spite of our continuous efforts, critical accidents frequently occurred and tremendous economic cost is paid for stator winding repair. Fortunately, it is confirmed that integrity is evaluated more clearly by analyzing capacitance change and voltage applied into windings among various integrity evaluation methods for water-cooled stator windings.

## **1. Introduction**

It is expected that the mean life of a generator is approximately 20 years. The unique design of the water-cooled generator produces more power per unit size than a conventionally cooled generator. As a result, increased electromagnetic forces act on the stator windings and the bar restraining system in the slot and end-winding are designed to accommodate these increased forces. Deterioration of any part in the bar restraining system may lead to accelerated wear of stator

winding insulation and damage to cooling water circuits. It is important that slot and end-winding restraining systems be well maintained in accordance with standard recommendations.

Figure 1 shows a structure of generator stator windings and Figure 2 shows the flowchart for mechanical integrity evaluation of generator stator windings. As mechanical integrity evaluation methods, there are vibration characteristic test, leak test, and water absorption test. As based on the test results, i) vibration characteristics of windings are changed so the resonance is prevented or ii) leakage parts are found so they are repaired or iii) wet bars are repaired or replaced within 1 year.

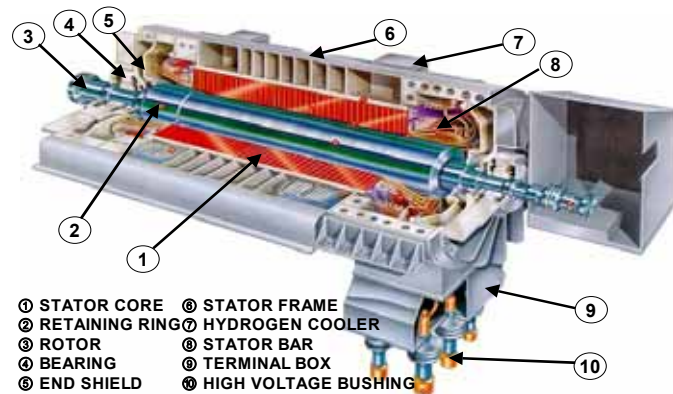


Figure 1. Structure of generator stator windings.

There have been a number of instances of stator winding cooling system water leaks. Generally, operation of the generator has not been impacted, and it has been possible to correct the condition without major maintenance. However, there have been instances of stator winding insulation failures where water penetration of the stator bar insulation, either at the series loop or in the actual groundwall, has been a factor in the failures. In some instances, evidence suggests that mechanical damage to the groundwall may have contributed to the hipot failure. There is, however, no doubt that the presence of water was a significant factor in each of these failures. As a result of these experiences, it is evident that more attention is required to eliminate water leaks which affect the stator bar groundwall insulation, particularly on the stator bar end arms. Even extremely small water leaks can be detrimental if allowed to persist. This is

particularly the case if the stator water pumping unit is left in operation during maintenance outages when the generator is degassed. Under these circumstances the pressure differential provides the greatest impetus for water to be forced through a leak site into the groundwall. Regardless, capillary action may cause water to leak from a bar even though hydrogen pressure is maintained higher than the cooling water pressure. If water leaks occur, they generally develop in the region of the series or phase connections. Stator bars are stringently tested for leaks prior to assembly, and the entire winding is tested twice after assembly to further ensure winding integrity. Leaks which occur in service develop as a result of normal operating conditions, and often take a long time to occur.

The diagnosis methods which are applied in wet bar diagnosis are similar to GE's capacitance mapping method but have some different characteristics. The capacitance diagram method can display the distribution of capacitance of each bar while other stochastic diagnosis methods such as normal probability plot and box plot can diagnose the wet bar among many bars. As well, the new developed diagnosis methods are applied to analyze wet bars for 500 MW generator stator windings.

Figure 3 summarized results of field tests reported to GE. The data represents approximately 50% of the tests done from January 1991 through July 1993. As shown in Figure 3, it is confirmed that the recommended tests are enough to detect leaks. Also, it is confirmed that mechanical testing is more conservative than electrical testing. Similarly, Figure 4 shows the cooling water leakage accidents by EPRI and water leakage accidents are increased rapidly in power plants which is operated more than 14 years.

It is known that water absorption test is an effective diagnosis method to distinguish wet bars by measuring the capacitance of insulator. Basically, the difference of dielectric constant between water and insulator is used. However, it is truly difficult to test and diagnose the condition of an insulator because of the structure of stator windings and complexity of the insulator. Actually, the capacitance between copper and insulator is very low and it is not enough to diagnose wet bars by the stochastic process.

Now, South Korea has more 30 units which are operated and constructed in the mid-90's. Of those units, if some units are outaged suddenly by these mechanical problems, it is expected that a ripple effect on the electric power system has a severe shock.

Experience on the periodic wet bar diagnosis of water-cooled generator stator windings

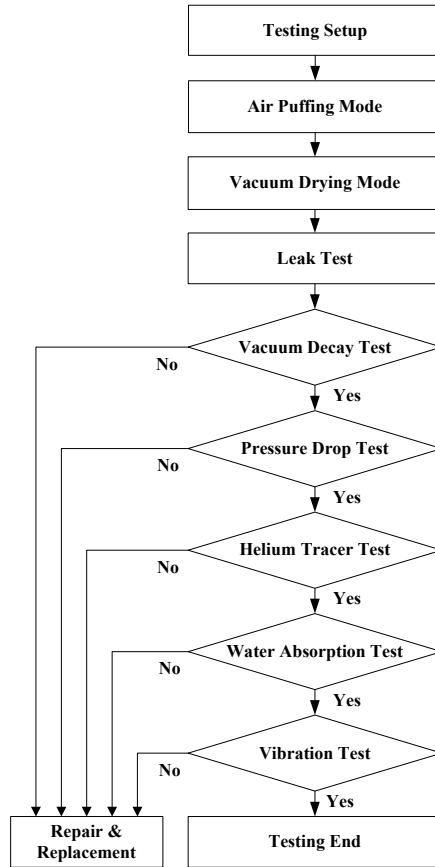


Figure 2. Mechanical integrity evaluation test for generator stator windings.

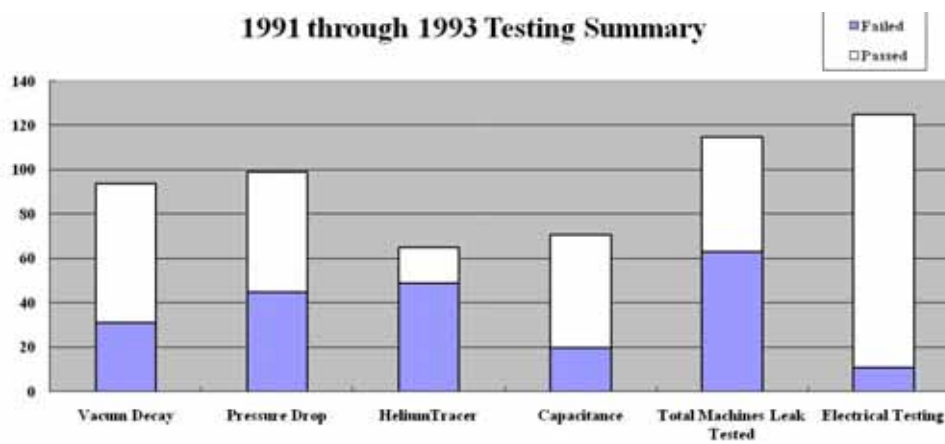


Figure 3. 1991 through 1993 testing summary.

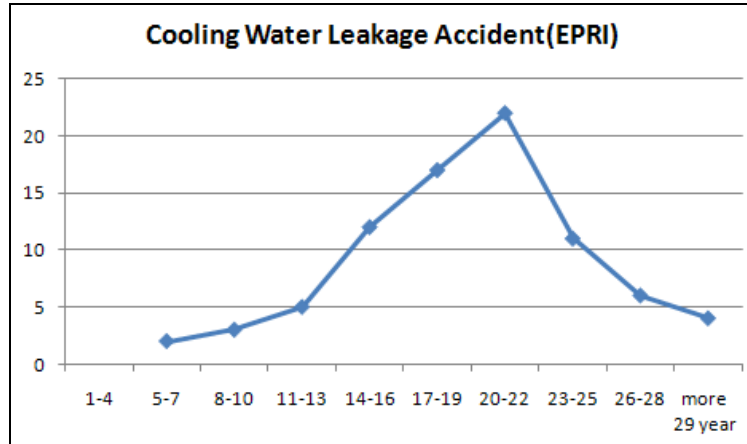


Figure 4. Cooling water leakage accident due to operation time

In this paper, the mechanical integrity evaluation methods are described. Especially, it is shown that the water absorption test is most sensitive of them. But the capacitance value has an order pico-Farad(pF). For this reason, it is easy to make a serious mistake, for example, if you simply decide the wet bar by comparing the amplitude of 5 pF with 8 pF algebraically. Accordingly, it is needed to raise the reliability of wet bar diagnosis by developing several stochastic diagnosis methods.

## 2. Water absorption test

The principle of the water absorption test for stator bars is that it is to measure the capacitance between sensor(+) and copper(-) to press the sensor to the mica surface. A condenser is used to store the electricity. If voltage is applied to the two parallel metal plates, an amount of electricity is stored in this plate, which is called capacitance. If the electric charges are charged in the storage battery as shown in Figure 5, the charges are distributed within the plates. The electric flux is perpendicular to the plates and a uniform magnetic field is formed to a parallel shape. The capacitance of the parallel plate storage battery is equal to equation (1) where C is capacitance,  $\epsilon_r$  is permittivity of a dielectric substance,  $\epsilon_0$  is permittivity constant in vacuum condition, A is area of sensor and d is distance between copper and sensor.

$$C = \epsilon_0 \epsilon_r \frac{A}{d} [\text{F}] \quad (1)$$

Capacitance can be increased in generator stator windings in only two cases.

- (1) When the area of sensor(A) is wide or the distance of poles(d) is short,
- (2) When a material which permittivity is bigger between a sensor and copper is added.

In case (2), a new material for which permittivity is big cannot be added. Also, the area of sensor and the distance between the poles are constant. Accordingly, the capacitance can be increased if only the water which is leaked inside bars exists. With a reference, the permittivity of water is 20 times the permittivity of mica which composes the bar. The water absorption test is to use the above mentioned physical phenomena. In evaluating whether wet bars are present or not, the stochastic diagnosis methods are used with capacitance of windings. It should not be determined through quantitative comparison of the capacitance of bars simply because of the small quantity in the water absorption test. Therefore, as long as the comparable data are numerous, the judgment errors for wet bar can be heightened.

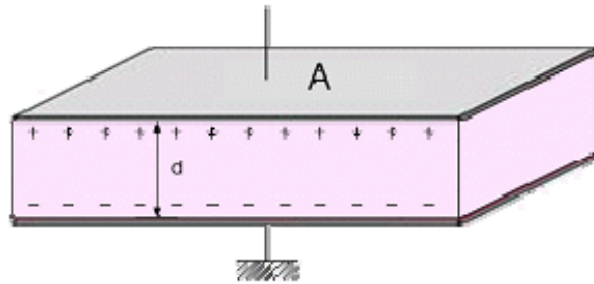


Figure 5. Capacitance for parallel plate storage battery.

Figure 6 shows the structure of stator end winding. The measurable positions are the end winding parts of the turbine end side and collector end side. Among them, until now, they could only be measured in the position which is bent from the core part. The capacitance cannot be measured as other zones are covered by insulation paint or is tied by binders.

If all the windings are absorbed uniformly due to leak of coolant water, it will be diagnosed that they are normal in the stochastic methods. But, it is going to be a long shot. Accordingly, in this paper, these stochastic diagnostic methods are applied under the assumption that the water absorption of the water-cooled stator windings is generated under manufacture defects or continuous operation.

For the water absorption test, the rotor must be removed and the surface of bars is cleaned, and then 3-phases are grounded. Finally, the capacitance of winding can be measured. The upper, inner, and outer sides can be measured in the top bar, and the inner and outer sides can be measured in the bottom bar as shown in Figure 6.

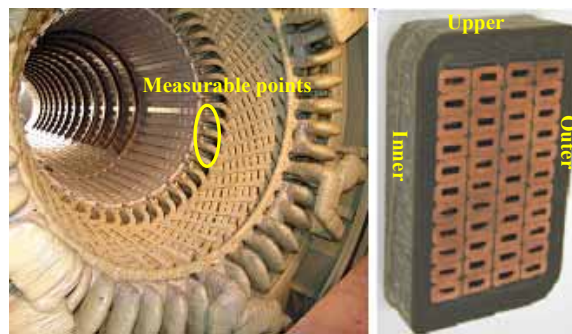
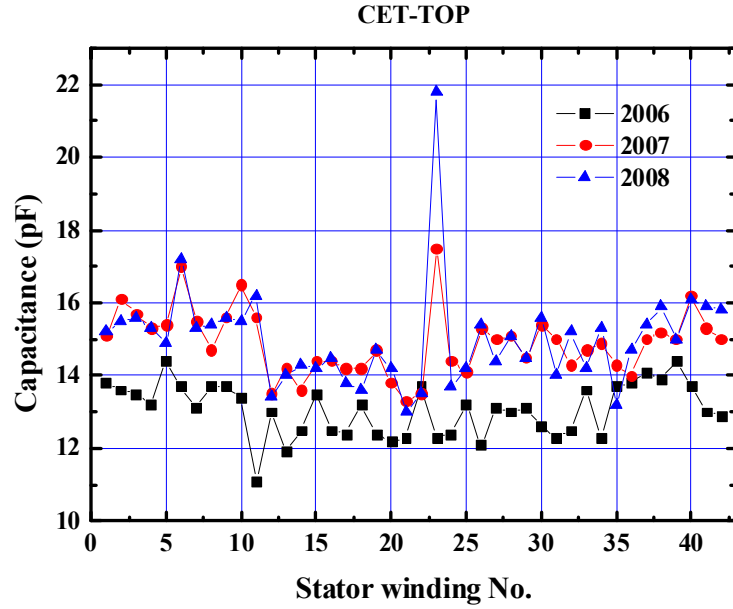


Figure 6. Only measurable points for capacitance measurement & section of winding.

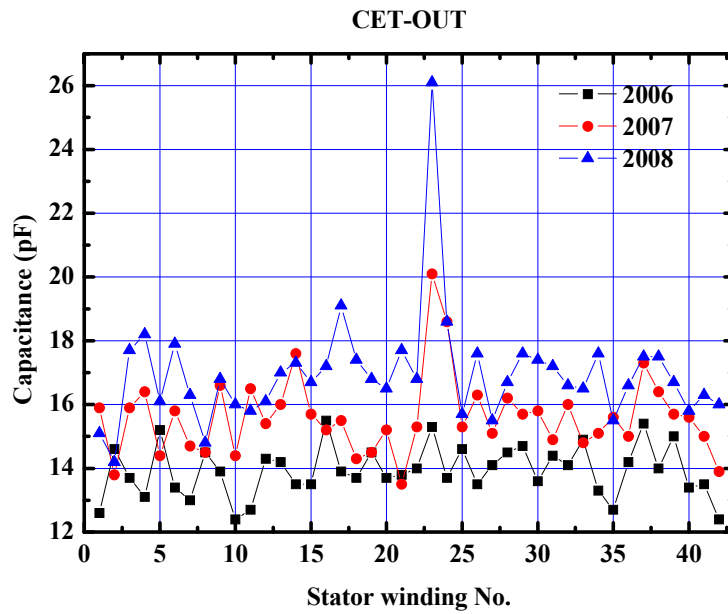
### 3. Wet bar diagnosis

#### 3.1 Case I

This generator is operated over more 15 years and is 500 MW class generator. Figure 7 shows the water absorption test results which are measured in 2006, 2007, and 2008 year respectively where CET-TOP is an upper part of top bar of collector end side and CET-OUT is an outer part of top bar of collector end side. 2006 and 2007 data are measured before sudden outage and 2008 is measured after sudden accident. It can be known that phase voltage is 12.7 kV and 10.8 kV is applied in No. 23 winding and the capacitance of No. 23 winding of stator has been increased gradually. Figure 8 shows the stochastic wet bar diagnosis results in 2007, and Figure 9 shows the stochastic wet bar diagnosis results in 2008 year respectively. It is known that abnormal data don't exist in 2006 year but the capacitance of 23 winding of stator is higher than other windings in 2007 and 2008 year. Especially, it is increased extraordinarily in 2008 year. That is to say, it is beyond the 3 sigma limit in 2007 year. But after insulation breakdown accident, it approaches 5 sigma limit in 2008 year. In stochastic wet bar diagnosis, if it is more than 3 sigma limit, it means suspected wet bar and if it is more than 5 sigma limit, it means wet bar.



(a) CET-TOP

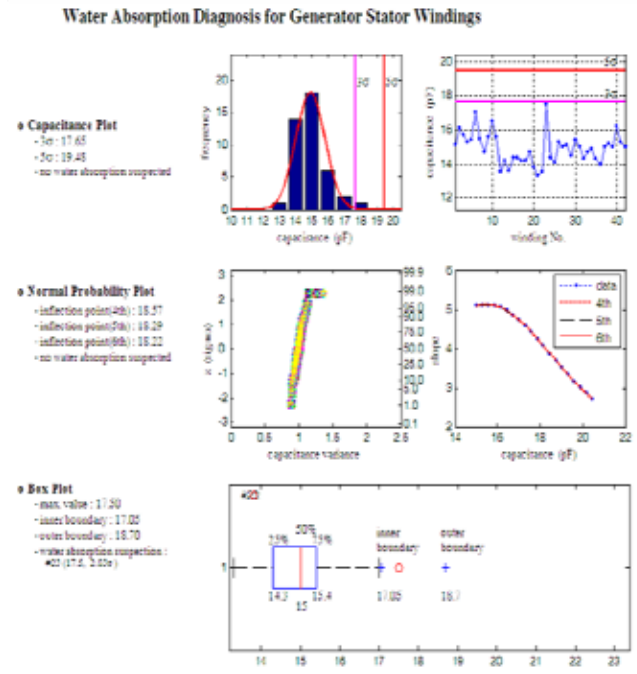


(b) CET-OUT

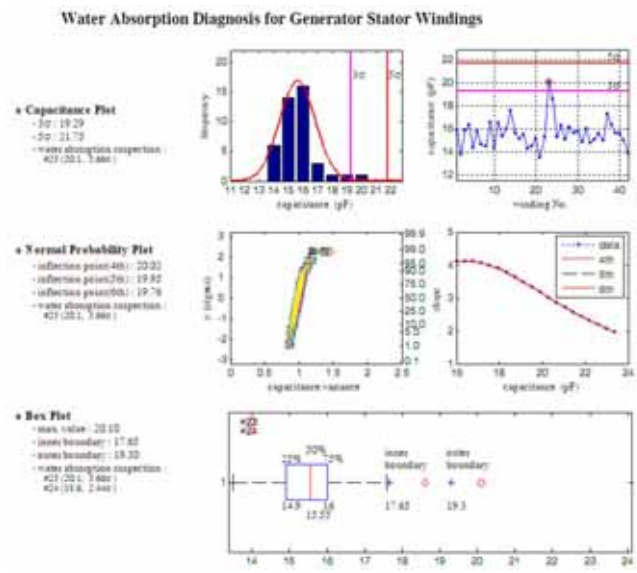
Figure 7. Capacitance trend change due to operation time.



Experience on the periodic wet bar diagnosis of water-cooled generator stator windings



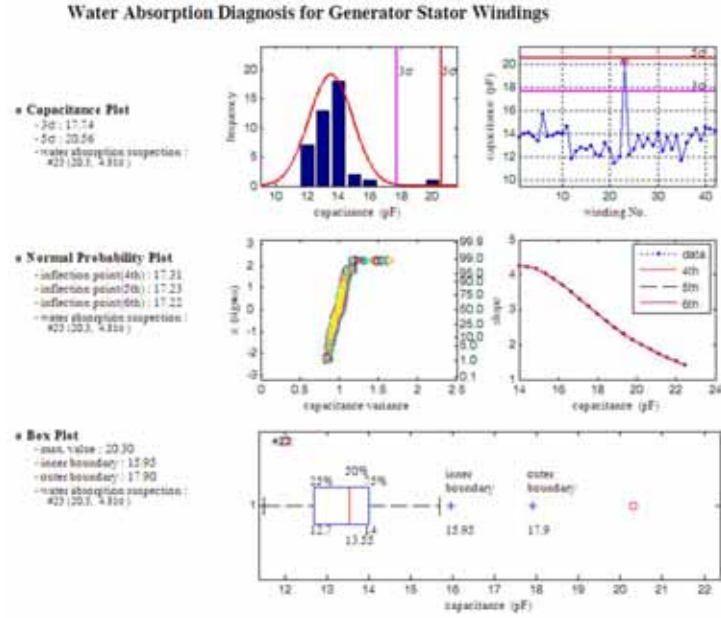
(a) CET-TOP



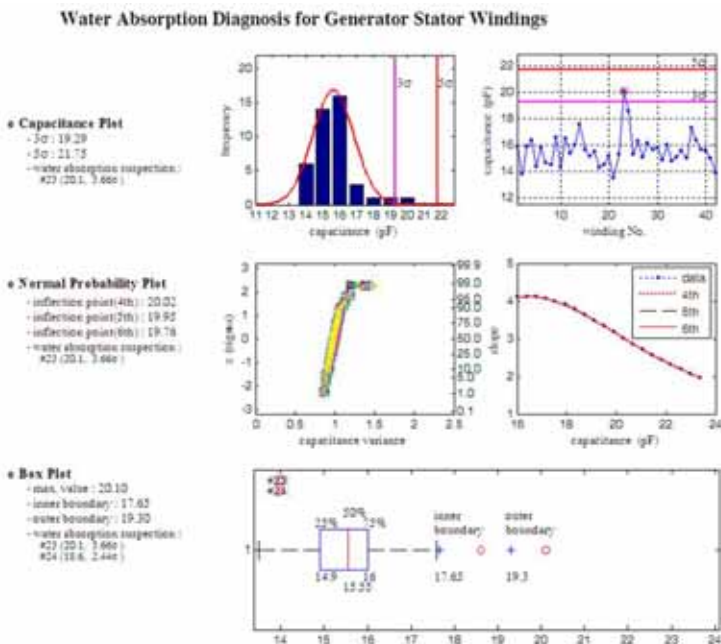
(b) CET-OUT

Figure 8. Wet bar diagnosis results of 2007 year.

Experience on the periodic wet bar diagnosis of water-cooled generator stator windings



(a) CET-TOP



(b) CET-OUT

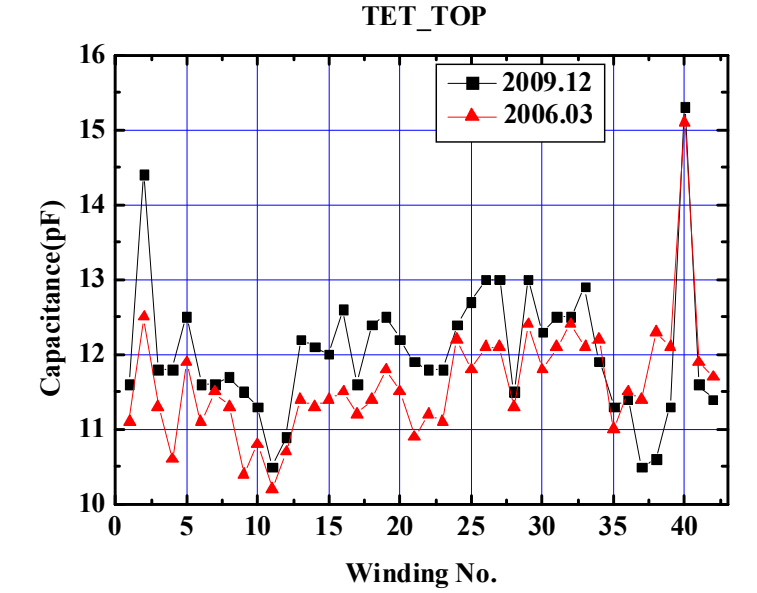
Figure 9. Wet bar diagnosis results of 2008 year.

### 3.2 Case II

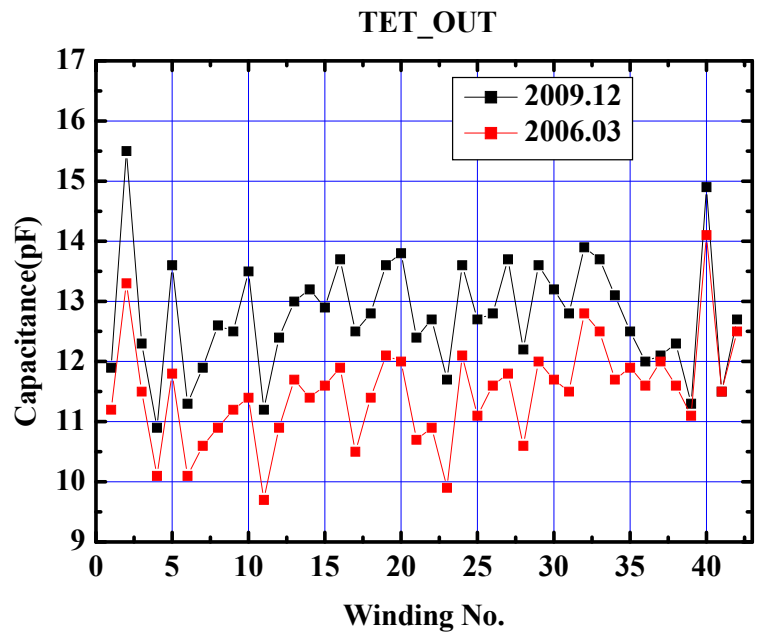
This generator is also operated over 25 years and is 500 MW class generator. Figure 10 shows the water absorption test results which are measured in 2006 and 2009 year respectively where TET-TOP is an upper part of top bar of turbine end side and TET-OUT is an outer part of top bar of turbine end side. Actually, capacitance of No. 2 winding of collector end side was higher than No. 2 winding of turbine end side in 2006. In those days, spare bars were absent so winding was not replaced. As a stopgap measure, they were repaired by using vacuum pressure impregnation method. In spite of that, as shown in Figure 10, it can be confirmed that capacitance of No. 2 winding of turbine end side in 2009 year has been increased in comparison with capacitance of 2006 year. From the above results, it can be predicted that cooling water was leaked in No. 2 winding of turbine end side which was repaired in 2006 year. Figure 11 shows the stochastic wet bar diagnosis results for TET-TOP and TET-OUT in 2006 year respectively. Also, Figure 12 shows the stochastic wet bar diagnosis results for TET-TOP and TET-OUT in 2009 year respectively. In the stochastic diagnosis, capacitance of No. 2 winding of turbine end side isn't higher than 3 sigma limit. But it is confirmed that capacitance of No. 2 winding was increased remarkably irrespective of other bars in 2009 year. Unlike No. 23 winding as mentioned before, equal phase voltage are applied but as sharing voltage of No. 2 winding is 2.7 kV, it is still lower than No. 23 winding. And sharing voltage of No. 40 winding is 4.5 kV.

Figure 13 shows the precise wet bar diagnosis test. Generally, cooling water is leaked in clip-to-strand which water is supplied. Accordingly, water leaks begin from clip-to-strand, that is to say, as shown in Figure 13(a), No. of 26, 27, 28, 29, 30 are start points of water leaks. Therefore, if No. 2 and No. 40 windings are wet bars, capacitances of No. 3, 8, 13, 18, 23, 28 of Figure 13(b) and 13(c) must be heightened in comparison with other numbers. To my surprise, it can be known that the above results agree to our thought well. After all, in order to confirm if they are wet bars, insulation materials are removed and bubble test is carried out as shown in Figure 14. It can be confirmed that No. 2 and No. 40 windings of turbine end side must be wet bars from Figure 14. As spare bars are not prepared until now, vacuum pressure impregnation method is applied for water absorption suppression. Because this generator has been operated for about 30 years, spare bars will be prepared or going to be rewound soon.

Experience on the periodic wet bar diagnosis of water-cooled generator stator windings



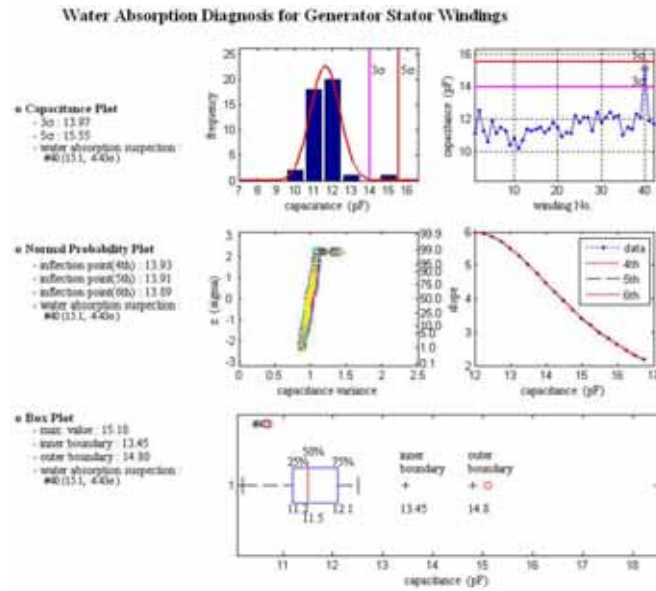
(a) TET-TOP



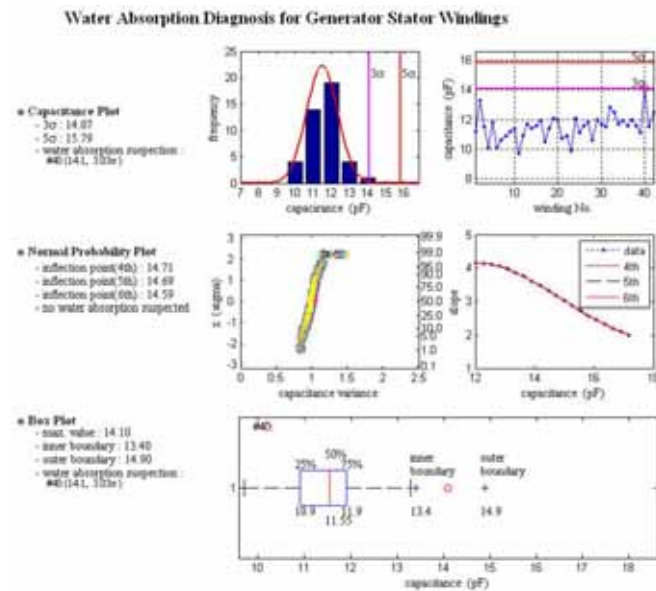
(b) TET-OUT

Figure 10. Capacitance trend change due to operation time.

Experience on the periodic wet bar diagnosis of water-cooled generator stator windings



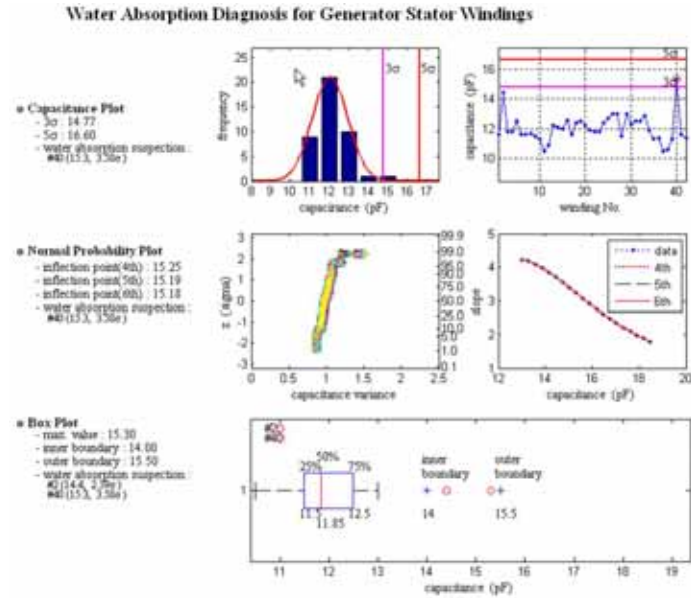
(a) TET-TOP



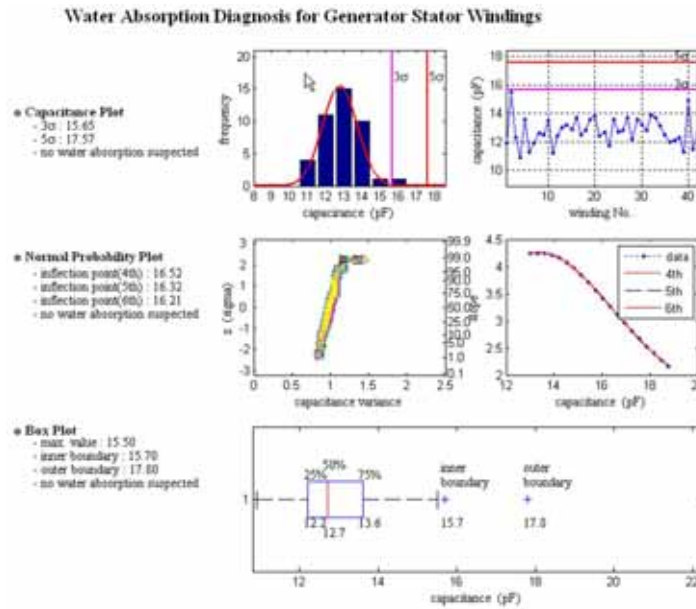
(b) TET-OUT

Figure 11. Wet bar diagnosis results for turbine end side in 2006 year.

Experience on the periodic wet bar diagnosis of water-cooled generator stator windings



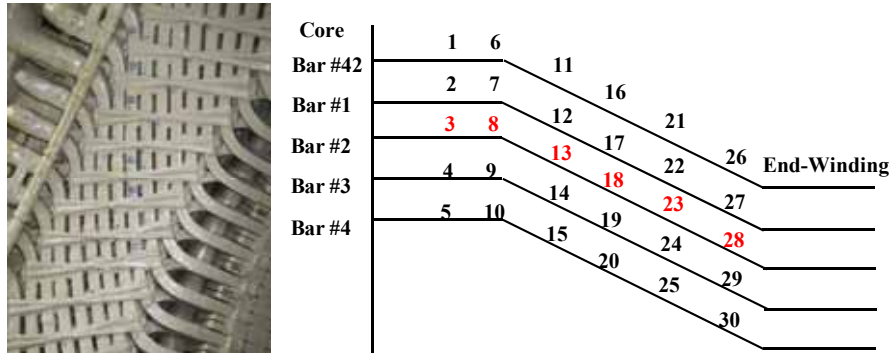
(a) TET-TOP



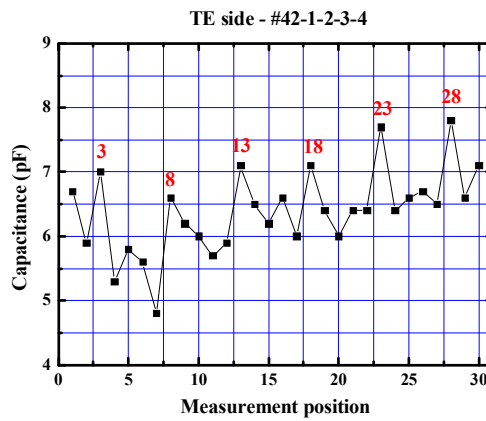
(b) TET-OUT

Figure 12. Wet bar diagnosis results for turbine end side in 2009 year.

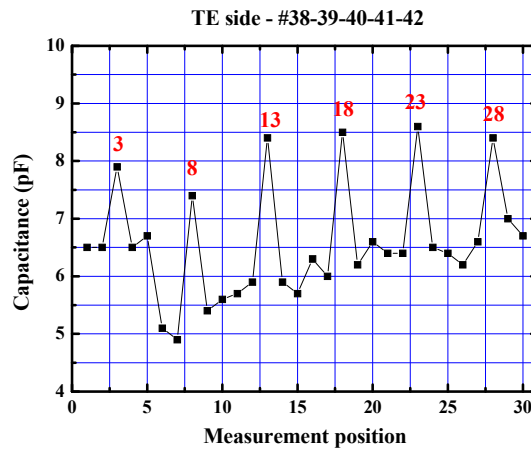
Experience on the periodic wet bar diagnosis of water-cooled generator stator windings



(a) capacitance measurement position for precise diagnosis



(b) wet bar diagnosis results for No. 42, 1, 2, 3 and 4



(c) wet bar diagnosis results for No. 38, 39, 40, 41 and 42

Figure 13. Precise capacitance measurement and wet bar diagnosis.

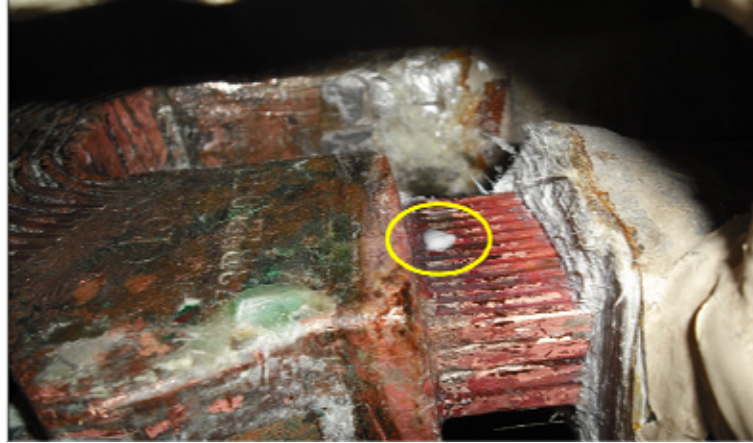


Figure 14. Bubble test for leak point detection.

## 4. Conclusions

During overhaul period, leak test and vibration characteristic test are carried out for generator stator windings. In addition, water absorption test which was developed independently by KEPRI is carried out periodically.

Especially, winding repair due to vibration characteristic change and leak test result is not a great difficult work. But the countermeasures due to wet bar diagnosis have no choice but to replace winding unfortunately. In addition, it is so difficult to determine replacement of winding through the stochastic wet bar diagnosis too. That is because capacitance of bar insulation has very small value[pF] and there may be errors of stochastic diagnosis. Accordingly, precise water absorption test and more reliable stochastic wet bar diagnosis are needed.

In this paper, 2 cases for wet bar diagnosis are described. It is verified that all the diagnosis indicate wet bars well. From this paper, the importance of periodic wet bar diagnosis can be confirmed.



## References

1. Stanton, D. J. Diagnosing and repairing water leaks in stator windings. GE company review. Schenectady, New York, 1992.
2. Inoue, Y. et al. Technology for detecting wet bars in water-cooled stator winding of turbine generators. IEEE IEMDC, June 2003, pp. 1337–1343.
3. Kim, H. S. & Bae, Y. C. Wet bar detection by using water absorption detector. J. of Mechanical Science and Technology, 2008. Vol. 22, pp. 1163–1173.
4. Kim, H. S. & Bae, Y. C. An experimental study on the dryness judgement criterion for water-cooled generator stator windings. Trans. ASME-B, 2010. Vol. 34, No. 2, pp. 137–143.
5. Kim H. S. et al. A study on the water absorption diagnosis method through capacitance measurement for generator stator windings. 2006's KSPE Spring Annual Meeting, pp. 285–286.

# **A breakthrough in ultrasonic detection and sizing of partially closed cracks?**

Stefan Sandlin  
VTT Technical Research Centre of Finland  
Espoo, Finland

## **Abstract**

Ultrasonic testing is one of the most efficient methods available for finding and sizing of cracks in structural components such as for example nuclear reactor circuits. However, some fatigue or stress corrosion cracks (SCC) may be closed or partially closed due to the presence of residual stresses pressing the crack surfaces against each other. In these cases the ultrasound may pass through the closed crack almost without any reflection or scattering. Water or oxide in the crack may also influence the transparency of the crack. This means that the crack may be invisible to ultrasound and, hence, the crack may not be found at all or its size may be seriously underestimated. This may lead to catastrophic failure of the component. Tohoku University in Japan has developed a method in which cracks are monitored both at the insonifying frequency  $f$  and at the subharmonic frequency  $f/2$  using a phased array for focused reception of ultrasound and a  $\text{LiNbO}_3$  single-crystal transmitter for generation of intense ultrasound. The subharmonic ultrasound is generated only at the closed parts of the crack. The method therefore combines normal phased array testing with phased array testing at subharmonic frequency. A commercial version of the equipment for research is under development by a Japanese company. This imaging method is called subharmonic phased array for crack evaluation (SPACE). Different nonlinear ultrasonic methods for evaluation of closed cracks have been proposed for decades (based on superharmonics), however, SPACE seems to include several new innovative ideas and it seems to have the best potential for becoming a standard method for inspection of nuclear reactor

circuits for closed cracks. Subharmonics have a better signal to noise ratio than superharmonics because subharmonics are generated only at closed cracks while superharmonics are generated also in transducers, liquid couplers and electronics. We therefore mainly restrict ourselves to the description of the subharmonic SPACE method in this work. A more traditional sizing method using phased arrays is, however, briefly presented as reference.

## 1. Introduction

Ultrasonic testing is one of the most efficient methods available for finding and sizing of cracks in structural components such as for example nuclear reactor circuits. However, some fatigue or stress corrosion cracks (SCC) may be closed or partially closed due to the presence of residual stresses pressing the crack surfaces against each other. Water or oxide in the crack may also influence the transparency of the crack. In these cases the ultrasound may pass through the closed crack almost without any reflection or scattering. Defects in diffusion joining and friction stir welding may also exhibit poor ultrasonic reflection or scattering properties. This means that the crack or joint defect may be invisible to ultrasound and, hence, the crack may not be found at all or its size may be seriously underestimated. This may lead to catastrophic failure of the component.

Traditional ultrasonic systems operate in linear mode; i.e. the received scattered ultrasound from defects lies in the same frequency range as the insonifying ultrasound. The amplitudes of waves diffracted or reflected at a crack tip or a crack surface are determined by the acoustic impedance mismatch between the material and the air gap. For tight cracks the acoustic impedance mismatch may be negligible. In nonlinear testing, defects behave as active radiation sources of new frequency components rather than as passive scatterers in conventional ultrasonic inspection (Solodov & Busse, 2007). The nonlinear techniques are therefore sensitive to closed fatigue or SCC cracks. In non-classic nonlinearity cracks may be observed by acoustically activated contact clapping in cracks. The nonlinear modulation frequencies caused by clapping of the crack interfaces often unveil flaws with higher contrast and more reliably than higher harmonics (Pfleiderer, 2006). A minimum amplitude of the insonifying ultrasound is needed for generation of subharmonics; this is illustrated by Yamanaka et al. (2004) by saying “if we find subharmonic waves when increasing the input wave amplitude, there is a partly closed crack, hidden in the object”.

Tohoku University in Japan has developed a method in which cracks are monitored both at the insonifying (or fundamental) frequency  $f$  and at the subharmonic frequency  $f/2$  using a phased array for focused reception of ultrasound and a  $\text{LiNbO}_3$  single-crystal transmitter for generation of intense ultrasound. The method therefore combines normal phased array testing with phased array testing at subharmonic frequency (Ohara et al. 2007). A commercial version of the equipment for research is under development by a Japanese company (Yamanaka, 2009). This imaging method is called subharmonic phased array for crack evaluation (SPACE). Different nonlinear ultrasonic methods for evaluation of closed cracks have been proposed for decades (based on superharmonics), however, SPACE seems to include several new innovative ideas and it seems to have the best potential for becoming a standard method for inspection of nuclear reactor circuits for closed cracks. Subharmonics have a better signal-to-noise ratio than superharmonics because subharmonics are generated only at closed cracks while superharmonics are generated also in transducers, liquid couplers and electronics. Further, the attenuation of the subharmonic waves is much lower than that of the fundamental wave and the superharmonic waves. At best the amplitude of the second harmonic wave is of the order of a few percent of the fundamental one (Kawashima et al. 2006). We therefore mainly restrict ourselves to the description of the subharmonic SPACE method in this work. The method is illustrated by imaging of closed fatigue cracks in an aluminium specimen (A7075) and an austenitic stainless steel specimen (SUS316L). Further, the method is also illustrated by imaging of SCC cracks in two other stainless steel specimens (SUS304). According to Ohara et al. (2008) SPACE can measure crack depths with an accuracy of approximately 1 mm. As will be seen, the combination of subharmonic wave detection and phased array technique seems to lead to substantial improvement beyond the present state-of-the-art in sizing and detection of closed cracks. The Japanese scientists have also tested a phased array based on laser interferometry; unfortunately the paper dealing with this topic is mainly in Japanese language. On the application side, localization and sizing of closed or partially closed fatigue and SCC crack in nuclear power plant components was already mentioned. Another important application could be detection of flaws in dissimilar metal joints. These joints can be made by for example diffusion bonding, explosion welding, clad welding, brazing etc. A flaw at the interface between two different metals may be difficult to observe using ultrasonic techniques as there is a strong reflection also from a perfect interface.

In nonlinear ultrasonic technique this kind of flaws become active radiation sources of subharmonic ultrasound and the SPACE method is therefore expected to be effective in quality evaluation of these kinds of joints.

## 2. Goal

The goal of this work was to summarize the published work on the use of subharmonic ultrasound for detecting and sizing of closed cracks or other tight defects. The work is intended to form the basis for a possible further detailed experimental and theoretical evaluation of the technique.

## 3. Fundamental principles

Detection of ultrasonic diffraction from the tip of a partially closed crack has been the “traditional” technique for sizing of this kind of cracks. The diffraction is illustrated in Figure 1. Parts of the crack which are in contact will also cause diffraction and these signals have been detected by special phased array transducers. However, the detection of the crack tip diffraction is often difficult

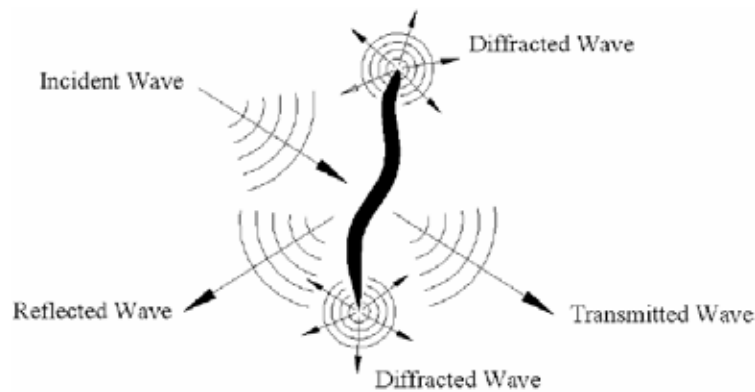


Figure 1. The generation of diffracted waves at crack tips (Gilmour et al. 2009).

(Dupond et al. 2004). The use of subharmonic ultrasound offers a mean for further improvement of the sizing of closed cracks. In this chapter the basic principles of detecting and sizing of closed cracks using subharmonic phased array technique are outlined. The properties of subharmonic ultrasound is the main topic of this chapter, but as the phased array technique plays an important

A breakthrough in ultrasonic detection and sizing of partially closed cracks?

role in the measurement technique using subharmonic ultrasound we also briefly present the phased array technique.

### **3.1 Nonlinear ultrasound**

Nonlinear ultrasound has been expected to become a primary technique of detecting and evaluating closed cracks since the publishing of the pioneering work by Buck, Morris and Richardson in 1978. Nonlinear ultrasound is based on the detection of superharmonic waves ( $2f$ ,  $3f, \dots$ ), subharmonic waves ( $f/2$ ,  $f/3, \dots$ ), ultra-subharmonic waves, frequency pairs etc. generated by the interaction of large amplitude ultrasound with closed cracks, where  $f$  is the central frequency of the insonifying wave. The theory of nonlinear ultrasound is quite complicated; therefore only a brief phenomenological presentation will be given below. The reader who is interested in a deeper and more theoretical description of nonlinear ultrasound in non-destructive evaluation is referred to for example the doctoral thesis by Pfleiderer (2006). The thesis is in German language and written at University of Stuttgart.

### **3.2 Subharmonic ultrasound in non-destructive evaluation**

Although subharmonic waves have better selectivity for closed cracks than superharmonic waves, the measurement of closed crack depths in the thickness direction has not been realized before the SPACE-system (Subharmonic Phased Array for Crack Evaluation) was developed at Tohoku University in Japan (Ohara et al. 2008). Further, the signal-to-noise for superharmonics is not very high because these waves are also generated in for example in piezoelectric transducers and liquid media causing background noise. Subharmonics, on the other hand, are generated only at closed crack surfaces. The intensity of subharmonic waves is higher than that of superharmonic waves (Yamanaka et al. 2004). Subharmonic waves are also less attenuated as they travel through the material. Because of these reasons we only concentrate on the subharmonic technique in the following. For the following brief and simplified description we assume that  $\omega_1$  is the frequency of the intense insonifying ultrasound (fundamental frequency),  $\omega_R$  is the resonance frequency of the crack and  $\omega$  is the frequency of the subharmonic ultrasound. According to Ohara et al. (2008) the subharmonic wave is generated through a resonance phenomenon, called

subharmonic resonance (SR), between the fundamental wave  $\omega_I$  and Rayleigh waves travelling along the crack surfaces as illustrated in Figure 2. The generated subharmonic wave radiates out mainly through the crack tips. The amplitude of the fundamental wave needs to reach a minimum value at the closed crack before subharmonic waves can be generated. Figure 3 illustrates that there is an optimal relation between the input frequency  $\omega_I$  and the resonance frequency of the crack  $\omega_R$ , i.e. when  $\omega_R = \omega_I/2$  the displacement amplitude of the generated subharmonic wave will have a maximum (Figure 3 a). If this condition is not fulfilled the displacement amplitude will drop (Figure 3 b). However, according to Yamanaka (2006) the resonance peak is broad enough to facilitate practical inspections using subharmonic ultrasound. Cracks of different lengths can therefore be evaluated using a single input frequency. Nevertheless, a variable frequency transmitter is highly desired to cover a wide range of crack lengths. The SR is a resonance phenomenon in the entire crack. However, SPACE images indicate that subharmonic waves are generated not only at the crack tip but also at other parts of the crack. To explain this feature Ohara et al. (2008) propose a new concept of localized subharmonic resonances (LSRs). The SPACE image is therefore built up of several LSR sources along the crack as schematically shown in Figure 4. Ohara et al. further conclude that LSR will take place with large probability at the edge of a long, closed crack. This is a practical advantage of SPACE.

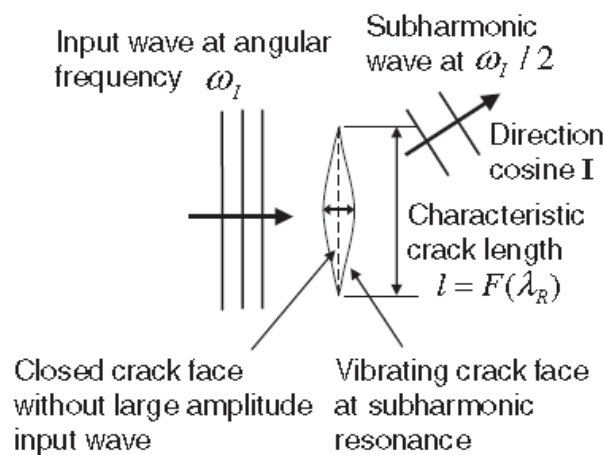


Figure 2. The input wave periodically opens the closed crack and subharmonic waves are generated by subharmonic resonance (Ohara et al. 2008).

A breakthrough in ultrasonic detection and sizing of partially closed cracks?

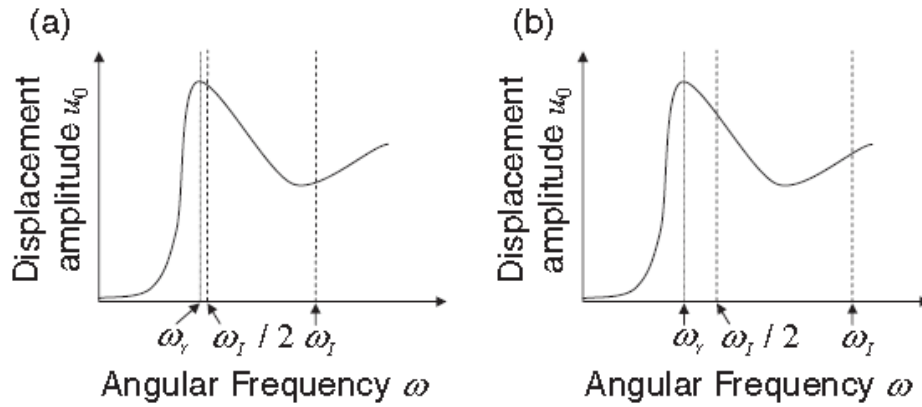


Figure 3. Generation of subharmonic ultrasound at a crack. The displacement amplitude of the subharmonic wave will have a maximum when the input frequency  $\omega_1$  divided by two is equal to the resonance frequency  $\omega_R$  of the crack as in (a). In (b) the input frequency is larger and the generation of subharmonics is less efficient (Ohara et al. 2008).

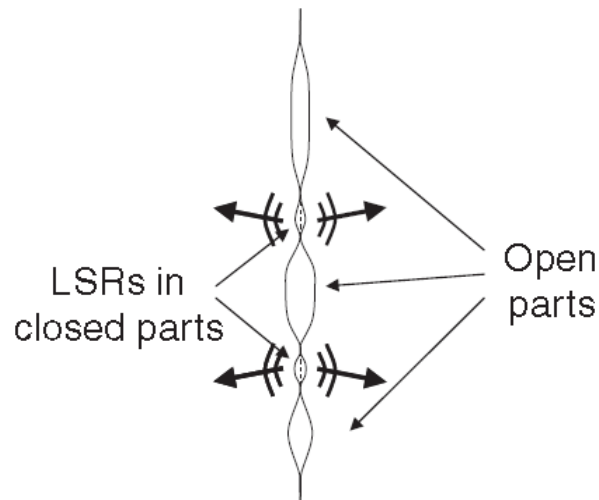


Figure 4. Localized subharmonic resonances (LSRs) will produce subharmonic waves at the closed parts of the crack (Ohara et al. 2008).



### 3.3 Phased array

Phased array probes use an array of probe elements, all individually wired, pulsed and time-shifted on both pulsing and receiving. The elements are usually pulsed are groups of 8 to 32 elements during an inspection. Using this technique it is possible to scan without moving the probe, to change the probe angle and to change the focus. In Figure 5 these techniques are called electronic scan (E-scan), sectorial scan (S-scan) and depth focusing (dynamic depth focusing). Combinations of these are also possible (Davis & Moles, 2006). The use of time-delays mimics for example wedges and lenses in traditional ultrasonic testing.

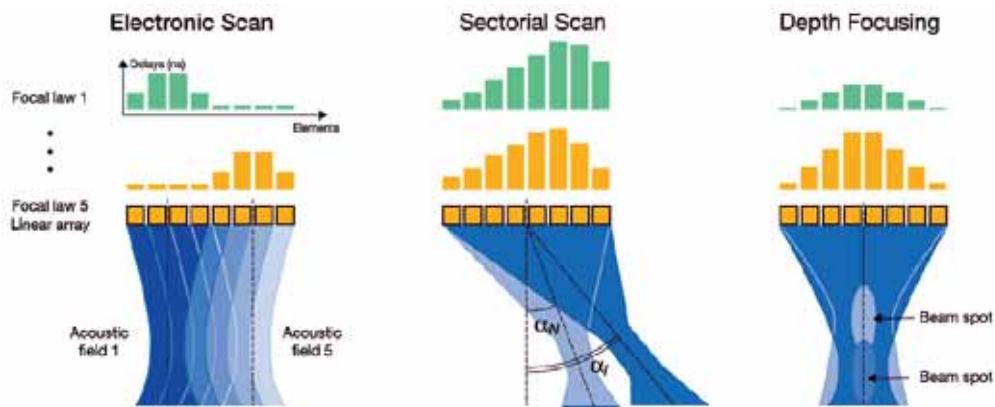


Figure 5. The principles of an ultrasonic phased array probe. Scanning, probe angle sweep and choice of focal depth can be done by selecting individual time-delays for the elements as shown in the upper part of the picture (Davis & Moles, 2006).

Dupond et al. (2004) in France have used a special large aperture phased array transducer (diameter 100 mm and 121 elements) for partially closed crack detection based of diffraction at the crack tip or other diffracting points along the crack. They used 45° shear waves at a frequency of 4.5 MHz. The ultrasonic beam is swept over the crack from the back wall to the tip by scanning and by changing the focal length of the transducer as shown in Figure 14. Dupond et al. did not utilize subharmonic waves. A short comparison of this technique with the SPACE method will be given in the discussion.

### 3.4 The SPACE equipment

A schematic view of the SPACE equipment is seen in Figure 6. Large amplitude ultrasound is generated by a  $\text{LiNbO}_3$  single-crystal transmitter and the scattered fundamental and subharmonic waves are received by a phased array using a digital filtering technique. A sectorial scan is also shown in Figure 6 (Yamanaka et al. 2006). Figure 7 is from a brochure by Tohoku University and illustrates the inspection principle of a welded tubular part.

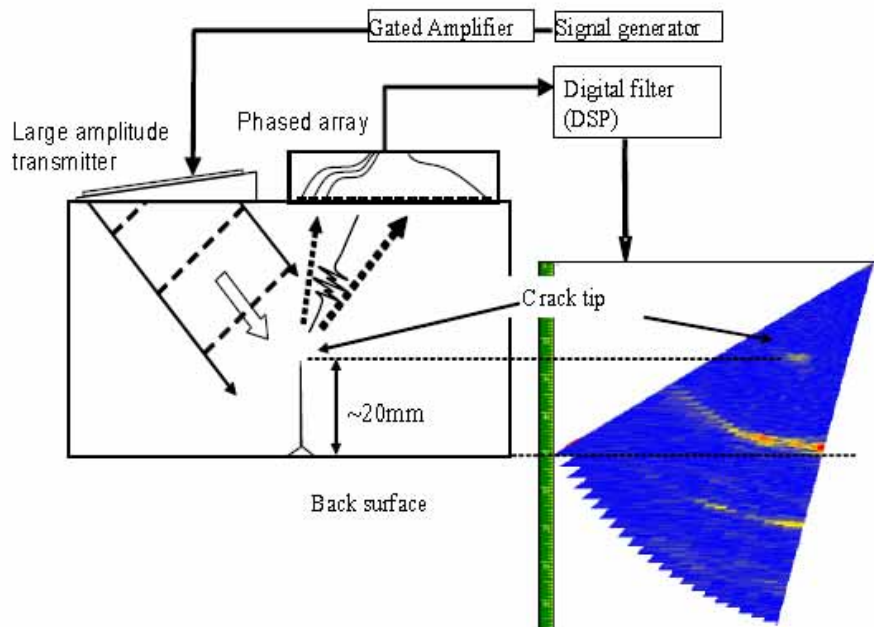


Figure 6. A schematic view of phased array method for imaging of a closed crack tip using subharmonic ultrasound. A sectorial scan of the crack area can be seen to the right (Yamanaka et al. 2006).

A breakthrough in ultrasonic detection and sizing of partially closed cracks?

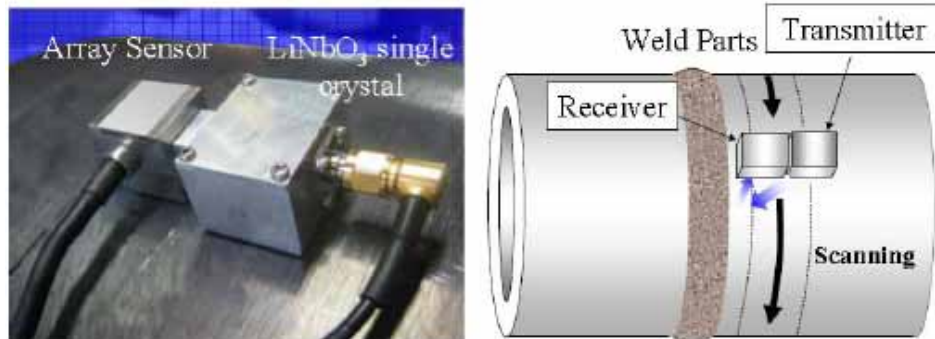


Figure 7. The array sensor and the LiNbO<sub>3</sub> single crystal transmitter. To the right a schematic picture showing SPACE inspection of a welded part (the pictures are from a brochure by Tohoku University).

#### 4. Detection and sizing results

Ohara et al. (2007) used an aluminium specimen with a fatigue crack and two stainless steel specimens, one with a fatigue crack and the other with a SCC crack to evaluate performance of the SPACE equipment. In the fatigue crack specimens the crack opening and closure was controlled by three point bending as shown in Figure 8. All specimens had approximately the same dimensions. A 7 MHz three-cycle burst was used as input signal from the LiNbO<sub>3</sub> transmitter. The transmitter voltage was set to 139 V (peak-to-peak) for the aluminium specimen and to 262 V (peak-to-peak) for the stainless steel SUS316 specimens. This corresponds to wave amplitudes at the crack of 17 nm and 7 nm respectively. These values were selected to be above the subharmonic generation threshold. The corresponding voltage for the stainless steel specimens SUS304 was 220 V (peak-to-peak) giving a displacement amplitude of 10.3 nm (peak-to-peak) at the crack. In another article Ohara et al. (2009) give a brief description of the crack sizing process.

A breakthrough in ultrasonic detection and sizing of partially closed cracks?

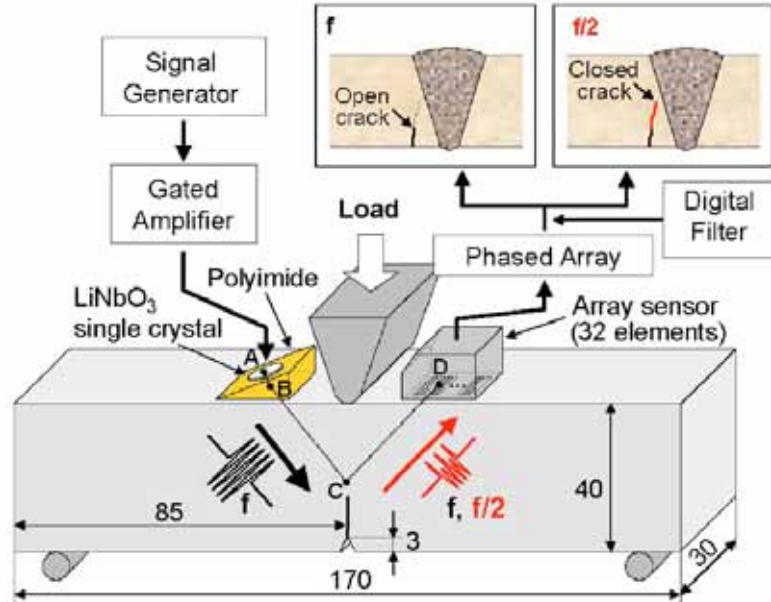


Figure 8. Three point bending was used to control the opening and closure of fatigue cracks. The dimensions are in mm (Yamanaka, 2007).

#### 4.1 Imaging of a fatigue crack in aluminium (A7075)

Figure 9 shows crack sizing results for an aluminium specimen. At fundamental frequency the crack tip was observed only when it was (primarily) open (a). On the other hand, at subharmonic frequency the crack tip is clearly observed when the crack tip is closed (e). In case (b) when the crack is primarily open a very weak subharmonic signal can still be seen just below the crack tip, this seems to indicate that some small parts of the crack are still closed and thus favouring some generation of subharmonic waves. The actual location of the crack tip is illustrated by photographs (c and f) in Figure 9.

A breakthrough in ultrasonic detection and sizing of partially closed cracks?

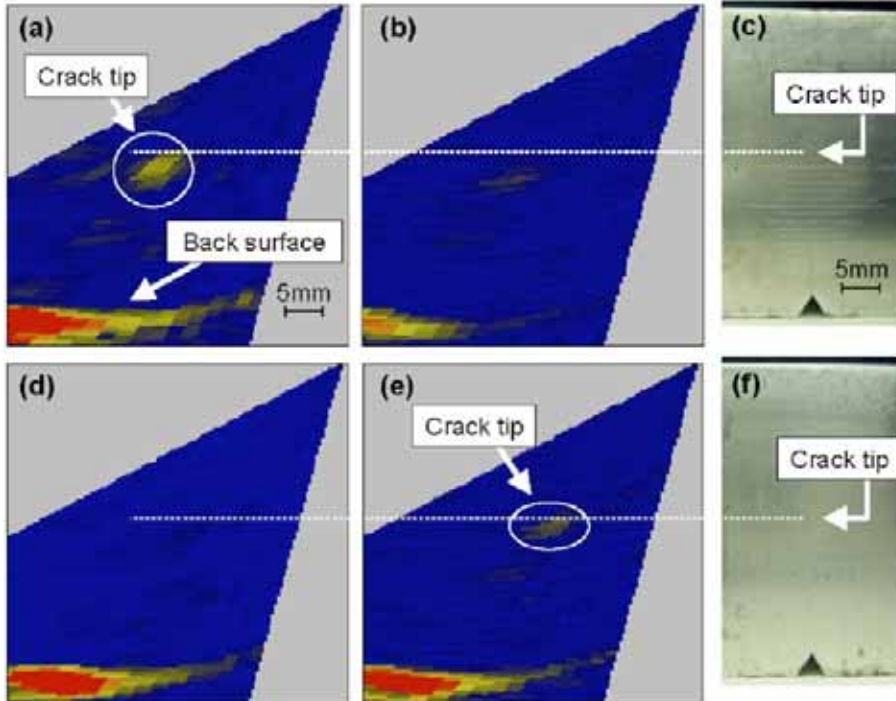


Figure 9. Phased array images of a crack tip in an aluminium specimen (A7075). The crack tip is open in a) and b) while it is closed in d) and e). Images a) and d) are taken at fundamental frequency while b) and e) are taken at subharmonic frequency. The closed crack tip cannot be observed at fundamental frequency d) but it is clearly observed at subharmonic frequency e) (Ohara et al. 2007).

## 4.2 Imaging of a fatigue crack in stainless steel (SUS316L)

In Figure 10 the sectorial scans (a, c and e) are taken at fundamental frequency, while b, d and f are taken at subharmonic frequency. The crack opening increase from almost closed for the topmost scans to almost open for the bottom scans, due to the increase of bending stress from 19 MPa to 84 MPa and finally to 112 MPa.

Some details from Figure 10:

In pictures (a) and (b) the bending stress was 19 MPa.

(a) Sectorial scan at fundamental frequency f. Only the notch is clearly visible, this indicates that the crack is mainly closed

A breakthrough in ultrasonic detection and sizing of partially closed cracks?

- (b) Sectorial scan at subharmonic frequency  $f/2$ . Both the crack tip and the middle part are visible indicating that the subharmonic wave can image closed cracks.

In pictures (c) and (d) the bending stress was 84 MPa.

- (c) Sectorial scan at fundamental frequency  $f$ . The middle parts become visible indicating that the crack is more open and that the middle part is the boundary between the open lower part and the closed upper part.
- (d) Sectorial scan at subharmonic frequency  $f/2$ . Both the crack tip and the middle parts are still visible although with decreased intensity. This indicates that these parts are still partially closed.

In pictures (e) and (f) the bending stress was 112 MPa.

- (e) Sectorial scan at fundamental frequency  $f$ . No part of the crack is visible indicating that the crack tip is still closed. It is surprising that there is no diffracted signal from the border between the open part and the closed tip. A possible explanation might be that this border is zigzaging and thereby giving very weak scattering of the fundamental wave in the direction to the phased array. As the experimental setup is that of Figure 8 the incident fundamental wave is reflected to the left from the open crack and nothing will reach the phased array.
- (f) Sectorial scan at subharmonic frequency  $f/2$ . The middle part has disappeared (i.e. this part is open), but the tip is visible indicating the uppermost part of the crack is still closed and generates subharmonic waves.

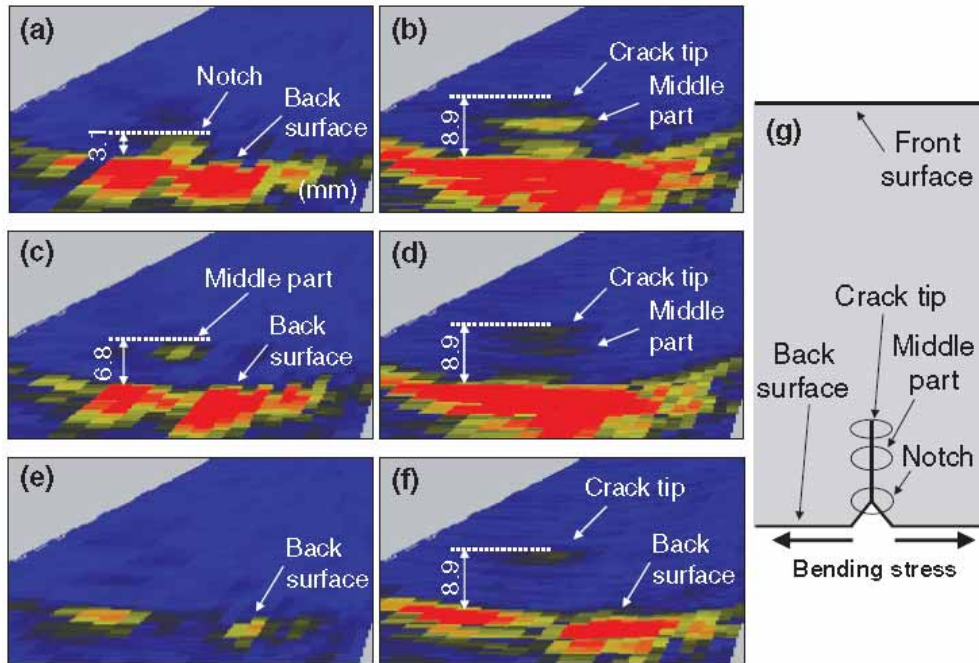


Figure 10. Images of a fatigue crack in stainless steel (SUS316L). Fundamental and subharmonic images (a, b) at nominal bending stress of 19 MPa. Corresponding images (c, d) and (e, f) for nominal bending stresses of 84 MPa and 112 MPa respectively (Ohara et al. 2008).

### 4.3 Imaging of SCC-cracks in stainless steel (SUS304), specimen 1

For the two stainless steel specimens SUS304 the transmitter voltage was set to 220 V (peak-to-peak) giving a displacement amplitude of 10.3 nm (peak-to-peak) at the crack. The central frequency of the fundamental wave was 7 MHz. In the specimen in Figure 11 (c) branched SCC cracks have grown from the initial fatigue crack. In the fundamental image (a), branched SCCs, B and C are observed on both sides of the tip of the fatigue crack. This suggests that B and C were primary open. Another SCC at A was observed above the tip of the fatigue crack in the subharmonic image, although A was slightly visible also in the fundamental image, this shows that A was primarily closed. The crack depth was measured to be 13.8 mm from Figure 11. According to metallurgical measurements on etched cross-sections the deepest SCC was 13 mm.



A breakthrough in ultrasonic detection and sizing of partially closed cracks?

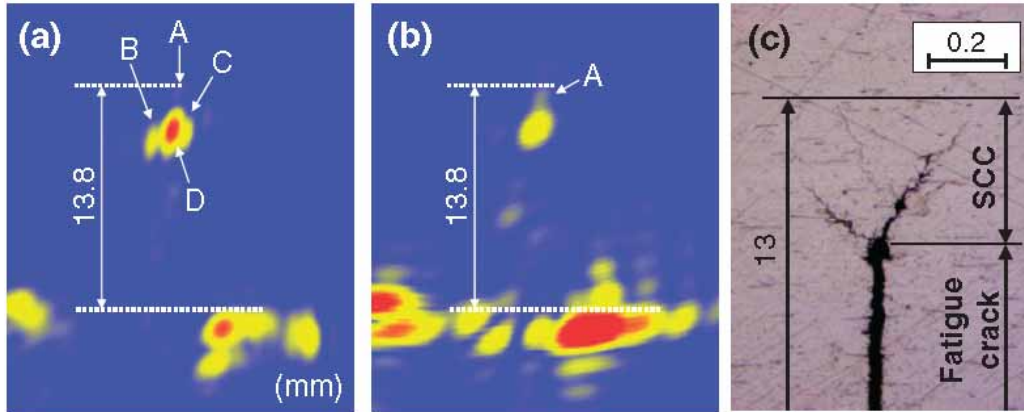


Figure 11. Fundamental (a) and subharmonic (b) images of stainless steel specimen 1 containing SCC cracks. (c) a picture of the etched cross-section (Ohara et al. 2008).

#### 4.4 Imaging of SCC-cracks in stainless steel (SUS304), specimen 2

The measurement settings for this specimen were the same as for specimen 1 above. In Figure 12 the tip of the branched SCC labelled A was observed in the fundamental image (a) suggesting that A was open. On the other hand the root of the SCC labelled A and two other branched SCCs labelled B and C were observed in the subharmonic image (b). This shows that these parts were primarily closed. The crack depth was measured to be 13.5 mm from the fundamental image and 15.2 mm from the subharmonic image. Metallurgical measurement from etched cross-sections showed that the deepest part of the crack was 16 mm.



A breakthrough in ultrasonic detection and sizing of partially closed cracks?

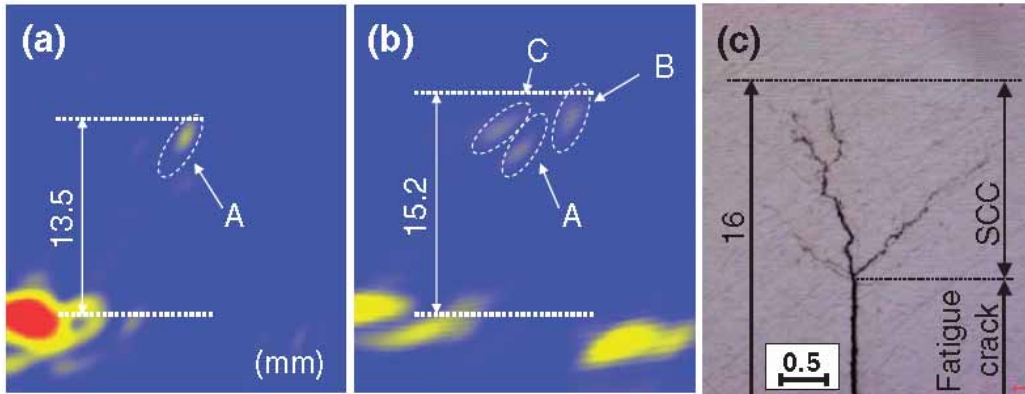


Figure 12. Fundamental (a) and subharmonic (b) images of stainless steel specimen 2 containing SCC cracks. (c) a picture of the etched cross-section (Ohara et al. 2008).

#### 4.5 The measurement accuracy

Ohara et al. (2008) examined the measurement accuracy of SPACE by comparing the true and measured depths of closed fatigue and stress corrosion cracks as shown in Figure 13. They demonstrated that the subharmonic images indicated the correct crack depth with an accuracy of approximately 1 mm. Particularly in the fatigue cracks, the subharmonic images significantly reduced the measurement error compared to the fundamental images. The subharmonic and fundamental images indicated almost the same crack depth for stress corrosion cracks in specimen 1, and the reduction in measurement error was less than 2 mm in specimen 2.

A breakthrough in ultrasonic detection and sizing of partially closed cracks?

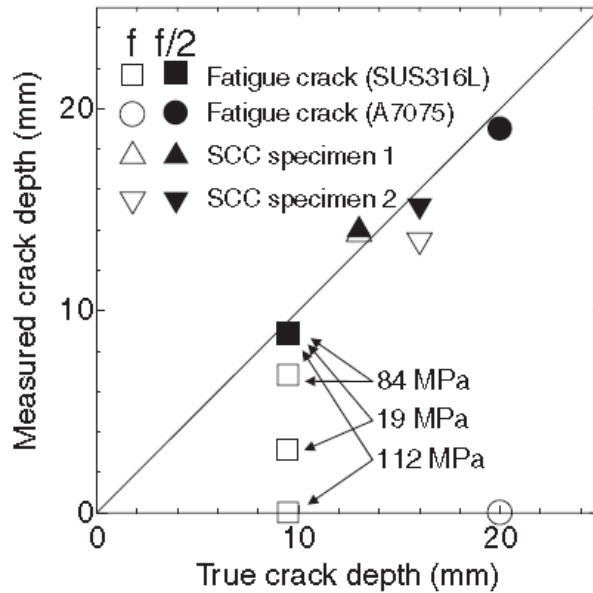


Figure 13. Comparison of measured and true crack depths for fatigue and SCC cracks. The black markers refer to results obtained using subharmonic frequency  $f/2$ . In two cases the crack tip was not observed at all (measured crack depth zero) at fundamental frequency  $f$  (Ohara et al. 2008).

#### 4.6 Sizing results using more conventional methods

In this section we briefly present a more traditional closed crack evaluation done in France (Dupond et al. 2004) as reference for the above SPACE results. The French used pulse-echo technique in immersion mode as illustrated in Figure 14. The specimen was stainless steel (304L). They used a standard focused transducer (SFT) and a 121 element phased array (PA); the main transducer characteristics are summarized in Table 1. The closure stress applied (by four point bending) to the crack caused an underestimation of the crack height for both transducers as shown in Figure 15. For the standard focused transducer the error is about 4 mm while the error for the phased array is 1.5–2.0 mm.

A breakthrough in ultrasonic detection and sizing of partially closed cracks?

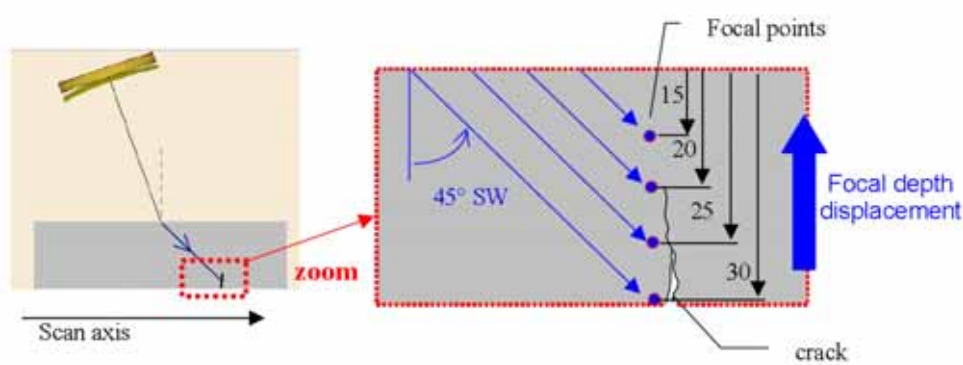


Figure 14. The principle of inspection according to Dupond et al. (2004). The crack closure was controlled by four point bending.

Table 1. The main transducer characteristics (Dupond et al. 2004).

Transducer	Type	Frequency (MHz)	Wave	Angle (°)	Active element diameter (mm)	Focal beam diameter at 25 mm (mm)
SFT	Mono (immersion)	4	Shear	45	50	1.7
PA	PA (immersion)	4.5	Shear	45	100	0.8

Satyanarayan et al. (2007) tested the performance of a 64 element phased array at 5 MHz on mild-steel pipe with wall thickness of 10 mm and three circumferential notches of depths 3-, 5-, and 7 mm. The notches simulated inner surface breaking cracks; no realistic cracks were used in this work. They used the phased array to mimic conventional ultrasonic angular transducers with different angles (i.e. they used the phased array with pre-set angles of 30, 35, 40, 45, 50, 55 and 60 degrees) and some of their experimental sizing results are summarized in Tab. 2 together with the percent errors. The percent errors are about 3% for the 7 mm notch and they will of course increase for smaller notches reaching over 13% for the 3 mm notch at transducer angles 55 and 60 degrees (these two are not shown in Table 2).

A breakthrough in ultrasonic detection and sizing of partially closed cracks?

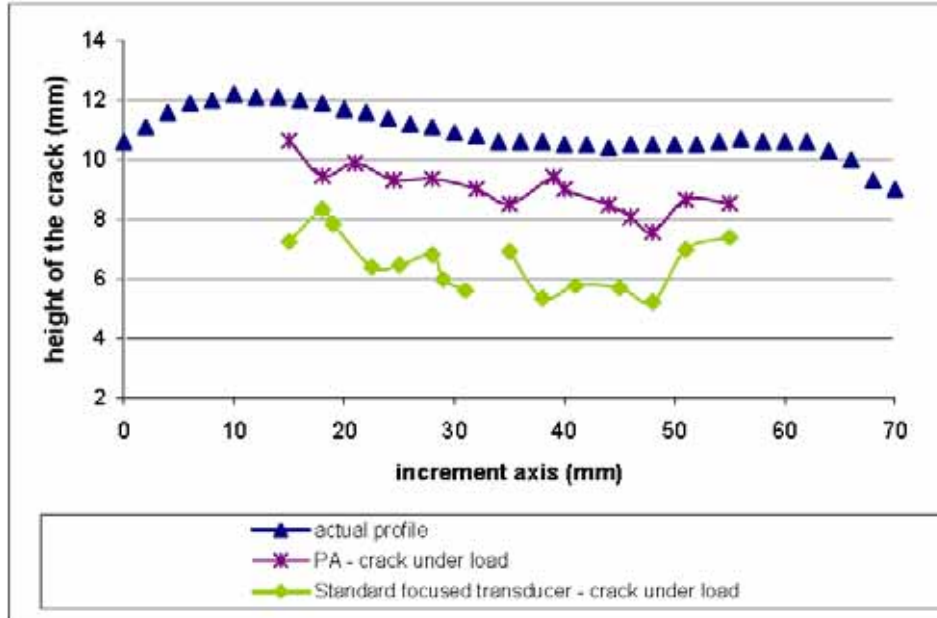


Figure 15. Destructively (actual profile) and ultrasonically obtained crack height for a partially closed crack. The large aperture phased array (PA) gives a better result than the standard focused transducer (Dupond et al. 2004).

Table 2. Sizing errors using different transducer angles on a mild-steel pipe with a wall thickness of 10 mm. Notches of depths 3-, 5-, and 7 mm mimic inner surface breaking cracks (Satyanarayan et al. 2007).

Actual depth (mm)	Estimated depth (mm): $\theta = 30^\circ$ (% error)	Estimated depth (mm): $\theta = 35^\circ$ (% error)	Estimated depth (mm): $\theta = 40^\circ$ (% error)	Estimated depth (mm): $\theta = 45^\circ$ (% error)	Estimated depth (mm): $\theta = 50^\circ$ (% error)
7	6.8 (+2.85)	6.7 (+3.13)	6.8 (+2.85)	6.7 (+3.13)	6.8 (+2.85)
5	4.8 (+4.0)	4.9 (+1.99)	4.8 (+4.0)	4.8 (+4.0)	4.7 (+5.99)
3	2.8 (+6.66)	2.8 (+6.66)	2.7 (+9.99)	2.8 (+6.66)	2.7 (+9.99)

## 5. Summary and discussion

In this report we concentrated mainly on the use of subharmonic ultrasound for detecting and sizing of closed or partially closed cracks (such as stress corrosion cracks and fatigue cracks) in nuclear power plant components or in other critical engineering structures. The subharmonic NDE-technique has been developed at Tohoku University (Japan) by professor Yamanaka and his group during the last years and it is called SPACE (Subharmonic Phased Array for Crack Evaluation). The technique is based on generating an intense ultrasonic wave with central frequency  $f$  using a  $\text{LiNbO}_3$  single-crystal transmitter. When this insonifying (or fundamental) wave interacts with a closed or partially closed crack scattered waves of central frequencies  $f/2$  (subharmonic) and  $f$  (fundamental) are generated. These waves are detected using a phased array together with a filtering technique. Other kinds of waves, such as superharmonics, are also generated, but these are generally of low intensity and tend to disappear in the noise. The intensity of the subharmonic wave may be comparable to that of the fundamental wave, further; the subharmonic wave is less attenuated compared with the fundamental wave and superharmonics because of the lower frequency. According to the articles cited in this report subharmonic waves are only generated at closed parts of a crack; they are therefore very useful in detecting and sizing of these. For subharmonic generation the amplitude of the fundamental wave should exceed a certain material dependent threshold and the frequency should fit into a certain frequency range. However, according to the cited articles, this frequency range is not very critical. Based on these reported observations it seems that the Japanese scientists have developed a method that substantially improves the detectability and sizing of closed cracks. In a comparison between ordinary phased array and SPACE the main advantage of the latter is that some closed crack tips which are not observed at fundamental frequency are quite clearly observed at subharmonic frequency. According to the Japanese researchers the equipment for making subharmonic measurements can be integrated into ordinary phased array instrumentations. Further, the Japanese researchers have also developed a scanning laser interferometric detection system which can replace the piezoelectric phased array. The laser detection technique will expand the frequency bandwidth of the system and make the array configuration more flexible: The laser array will be especially useful in imaging of cracks with complex shapes, such as stress corrosion cracks (Yamamoto et al. 2008). Unfortunately this paper is mainly in Japanese

A breakthrough in ultrasonic detection and sizing of partially closed cracks?

language. Professor Solodov at University of Stuttgart was also contacted during this work to get his opinion about the potential of nonlinear ultrasonics in NDE (see Chapter 6).

## **6. Conclusions and recommendations**

Based on the studied articles about the SPACE method it seems that the Japanese scientist have presented a method that makes an important progress beyond the state-of-the-art in detecting and sizing of closed or partially closed cracks. This regardless of the fact that the sizing process itself could have been described more in detail and compared to the sizing process used in normal phased array technique. The reasons for the progress beyond the state-of-the-art are mainly:

1. Closed crack tips that cannot be observed at all at fundamental frequency are observed at subharmonic frequency.
2. According to the articles cited in this work subharmonics are generated only at closed cracks whereas superharmonics are generated in transducers, liquid couplers, electronics etc. Therefore the subharmonic wave provides increased selectivity in identification of closed cracks.
3. Sizing using the subharmonic wave gives crack depths closer to the metallurgical measurements from etched cross-sections than sizing using the fundamental wave.
4. By comparing phased array images produced at subharmonic and fundamental frequency it is possible to identify closed and open parts of a crack.
5. The intensity of the subharmonic wave is much higher than that of the superharmonic waves, thus giving a better signal-to-noise ratio.
6. The attenuation of the subharmonic wave is less than that of the fundamental wave due to the lower frequency.

Because the SPACE method is new some problems may be encountered, especially in future field applications. Here we try to identify some of these potential problems:

1. Transfer of intense ultrasound to the inspected component and choice of the needed amplitude.

A breakthrough in ultrasonic detection and sizing of partially closed cracks?

2. Choice of the optimal fundamental frequency for optimal generation of subharmonic waves.
3. The influence of oxide and/or water in the crack on the detection and sizing performance.
4. The mechanism of subharmonic generation is not “crystal clear” yet (Solodov, 2009).
5. The influence of possible unbroken ligaments on the ultrasonic signal.
6. Spurious indications due to leakage of the fundamental wave into the measured subharmonic signal.

Besides these concerns regarding practical applications we conclude that the performance of SPACE in sizing closed cracks (fatigue and SCC) in stainless steel and aluminium specimens has been demonstrated. Detecting tight flaws in electron beam welds, friction stir welds, diffusion bonds, explosion joints etc might also be interesting applications. Detection of flaws in dissimilar metal joints may be added to the list. University of Stuttgart also has quite an experience in working with nonlinear ultrasonics and with subharmonics (and ultra-subharmonics) in particular (Solodov, 2009). Solodov recommends further investigations of this emerging field of ultrasonic NDE. According to Solodov the ultrasonic sensitivity to small tight cracks may be further increased by including ultra-subharmonics into the analysis. Because of this and the obvious potential of the SPACE method it is recommended that the real capability of this method is experimentally evaluated on specimens with suitable tight cracks. Information about specimens with realistic artificial flaws can be found in for example the doctoral thesis by Kemppainen (2006).

## **Acknowledgements**

This work was done within the project “Monitoring of the structural integrity of reactor circuit” (RAKEMON), which is a part of the program SAFIR2010, Finnish national research program on NPP safety 2007–2010. Some helpful e-mail discussions with Professor Kazushi Yamanaka (Tohoku University) and Professor Igor Solodov (Stuttgart University) are gratefully acknowledged.

A breakthrough in ultrasonic detection and sizing of partially closed cracks?

## References

- Buck, O., Morris, W. L. & Richardson, J. M. 1978. Acoustic harmonic generation at unbonded and fatigue cracks. *Appl. Phys. Lett.* Vol. 33, No. 5, pp. 371–373.
- Davis, J. M. & Moles, M. 2006. Resolving capabilities of phased array sectorial scans (S-cans) on diffracted tip signals. *Insight*, Vol. 48, No. 4. 7 p.
- Dupond, O., Bredif, P., Poidevin, C. & De Nathasn, N. 2004. Advanced phased array transducer for detection of closed crack tip diffraction. Internet Address, 2009-08-31: [http://www-civa.cea.fr/home/liblocal/docs/PubliOff/Dupond\\_etal\\_ICNDE\\_2004.pdf](http://www-civa.cea.fr/home/liblocal/docs/PubliOff/Dupond_etal_ICNDE_2004.pdf).
- Gilmour, T. H. (Ed.) 2005. In-service non-destructive estimation of the remaining fatigue life of welded joints. Internet Address 2009-08-31: <http://www.shipstructure.org/pdf/444.pdf>.
- Kawashima, K., Murase, M., Yamada, R., Matsushima, M., Uematsu, M. & Fujita, F. 2006. Nonlinear Ultrasonic Imaging of Imperfectly Bonded Interfaces. *Ultrasonics*, 44. Pp. 1329–1333.
- Kemppainen, M. 2006. Realistic artificial flaws for NDE qualification – a novel manufacturing method based on thermal fatigue. Helsinki University of Technology, Laboratory of Engineering Materials. 93 p. Internet Address 2009-11-27: <http://lib.tkk.fi/Diss/2006/isbn9512282631>.
- Ohara, Y., Mihara, T., Sasaki, R., Ogata, T., Yamamoto, S., Kishimoto, Y. & Yamanaka, K. 2007. Imaging of closed cracks using nonlinear response of elastic waves at subharmonic frequency. *Appl. Phys. Lett.* 90.
- Ohara, Y., Yamamoto, S., Mihara, T. & Yamanaka, K. 2008. Ultrasonic evaluation of closed cracks using subharmonic phased array. *Jpn. J. Appl. Phys.*, Vol. 47. No. 5. Pp. 3908–3915.
- Ohara, Y., Endo, H., Mihara, T. & Yamanaka, K. 2009. Ultrasonic measurement of closed stress corrosion crack depth using subharmonic phased array. *Jpn. J. Appl. Phys.*, Vol 48. 6 p.



A breakthrough in ultrasonic detection and sizing of partially closed cracks?

- Pfleiderer, K. Frequenzkonversion aufgrund nichtlinearer akustischer Phänomene: Grundlagen und Anwendung zur defektselektiven zerstörungsfreien Prüfung. Institut für Kunststoffprüfung und Kunststoffkunde der Universität Stuttgart. 120 p.
- Satyanarayan, L., Sridhar, C., Krishnamurthy, C. V. & Balasubramaniam, K. 2007. Simulation of ultrasonic phased array technique for imaging and sizing of defects using longitudinal waves. *International Journal of Pressure Vessels and Piping* 84. Pp. 716–729.
- Solodov, I. & Busse, G. 2007. Elastic wave nonlinearity for monitoring of localized damage in engineering materials. 19th International Congress on Acoustics, Madrid, 2–7 September 2007. 6 p.
- Solodov, I. 2009. Private communication.
- Yamanaka, K., Mihara, T. & Tsuij, T. 2004. Evaluation of closed cracks by analysis of subharmonic ultrasound. *Insight*, Vol. 46, No. 11, pp. 666–670.
- Yamanaka, K., Sasaki, R., Ogata, T., Ohara, Y. & Mihara, T. 2006. Time domain analysis of subharmonic ultrasound for practical crack sizing. *Review of Quantitative non-destructive Evaluation*, Vol. 25. pp. 283–290.
- Yamanaka, K. 2009. Private communication.
- Yamamoto, S., Ohara, Y., Mihara, T. & Yamanaka, K. 2008. Application of laser interferometer to subharmonic phased array for crack evaluation (SPACE). Tohoku University. Pp. 198–203.

# Development of nondestructive techniques for fuel cladding evaluation in hot cell

Tarja Jäppinen and Stefan Sandlin  
VTT Technical Research Centre of Finland  
Espoo, Finland

## Abstract

In nuclear light water reactors (LWR), an effective heat transfer from the fuel through the fuel cladding to the water in the reactor is essential. Furthermore, the cladding should prevent the radionuclides in the fuel from contaminating the reactor circuit. During service the cladding suffers from damage by corrosion, microstructural changes, hydrogen pick-up, creep etc.

Regular nondestructive evaluation in a hot cell is a relatively new complement to laborious destructive evaluation of in-service degradation of irradiated material. In this work the possibilities of laser ultrasonics and eddy current techniques in hot cells are presented. The main emphasis is on oxide thickness measurements and on detection of cracks and delaminations for oxide layers of tubular or planar fuel cladding materials. The detectability of hydrogen concentration in the cladding wall is also discussed.

## 1. Introduction

A brief review and applications of ultrasonics and eddy current techniques for nondestructive evaluation (NDE) of materials degradation due to irradiation are presented in this work. One important advantage of nondestructive examinations is that the same fuel rod can be reinserted in the reactor for further irradiation and re-examined again

There is a limited space available in a hot cell. Also the components to be examined are radioactive. Therefore the nondestructive evaluation measurements

should be completely remotely controlled and the amount of material such as sensors, scanners, cables inside the cell should be minimal.

Ultrasonic Rayleigh waves are widely applied for measuring the thickness of oxide layers on metals. In the case of oxide on zirconium alloy fuel cladding, the thicknesses of interest range from few micrometers to few tens of micrometers. Oxide thicknesses can also be measured using the eddy current lift-off effect. Radiation damage and hydrogen pick-up will change the density and the elastic modulus of the alloy and therefore ultrasonics should have sensitivity to these changes. Furthermore, the electric conductivity of the alloy changes due to radiation damage and hydrogen pick-up. It should therefore be possible to estimate the damage by eddy current measurements [1]. Edsinger et al. have issued a patent on measurement of hydrogen concentration in zirconium alloys in the fuel pool of nuclear power plants based on eddy current technique [2].

## 2. Fuel cladding damage

This section briefly considers those damaging processes that may be of interest for hot cell NDE measurements or otherwise influence the performance of these measurements. Figure 1 illustrates some damaging processes that occur in fuel rods during service [3]. In a fuel rod cladding tube the wall thickness is usually about 0.6 mm and the tube diameter is about 10 mm. The outer surface of the cladding undergoes corrosion which changes the heat transfer properties and reduces the wall thickness and leads to pick-up of hydrogen in the zirconium alloy. It is generally said that thickness of the oxide should stay under 100  $\mu\text{m}$ .

Hydrogen concentrations in excess of the solubility limit lead to precipitation of hydrides which degrade the strength and ductility of the cladding. Further, as the burnup increases there will be an increasing amount of pellet-cladding mechanical interaction due to gap closure by fuel swelling, cladding creep down (due to difference between internal gas and external coolant pressure) and differential thermal expansion between pellets and cladding. The complete or partial disappearance of the gap between the fuel pellet and the cladding will have influence on especially the performance of ultrasonic guided wave inspection as these wave modes are plate waves. According to Edsinger et al. [2] an average concentration across the cladding wall of the order of 600 ppm leads to measurable hydrogen embrittlement. However, the hydrogen concentration across the wall is not uniform. The concentration at the outer surface of the cladding may be ten times higher than at the inner surface. At the end of the fuel

rod life the corrosion rate as well as the hydrogen uptake accelerates rapidly [4]. However, zirconium alloys are said to be protected against hydrogen ingress by the surface oxide film. Also the presence or absence of cracks or pores passing through the oxide film into the metal/oxide interface is a key factor in determining the hydrogen uptake. [4] These statements may have important consequences for the detailed NDE assessment of cladding integrity in hot cells.

Further, because of the pellet-cladding interaction the geometry of the tube will change and this will have consequences for both eddy current and laser ultrasonic inspection. In laser ultrasonic inspection these changes in geometry may influence on the efficiency of ultrasonic generation and detection as well as on the distance travelled by the ultrasound. The geometry variation of the sample surface causes tilting of the eddy current probe and probe alignment is needed. The severity of these phenomena should be assessed and required precautions should be taken.

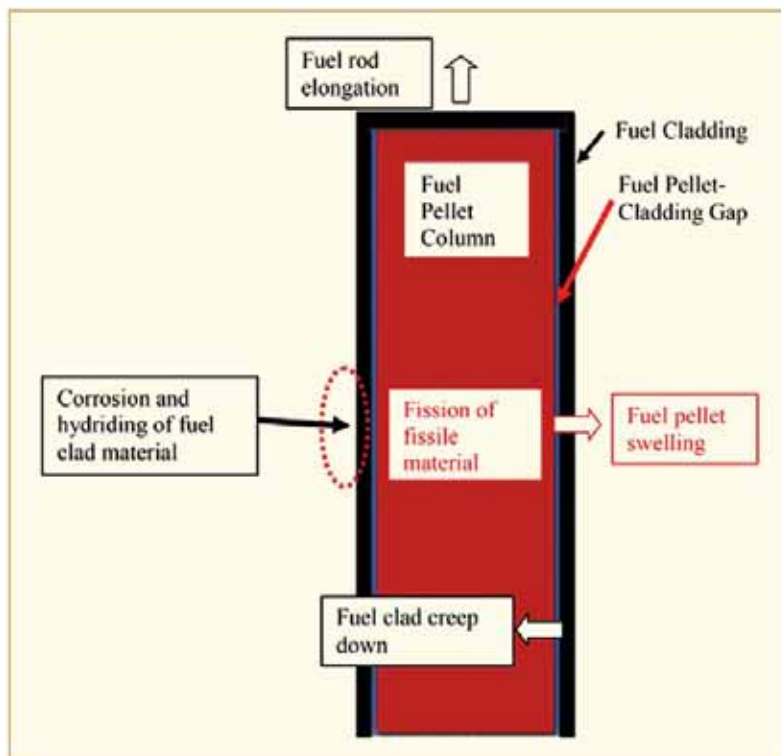


Figure 1. Schematic illustration of the different processes occurring in a fuel rod during irradiation [3]

Figure 2 illustrates the oxide growth along a fuel rod with Zircaloy-4 cladding after three irradiation cycles and after an estimated burn-up of 65 GWd/tU. The oxide thickness was measured axially along four trajectories on the rod separated circumferentially by 90 degrees. The average was calculated from trajectories taken every 30 degree [5]. Figure 3 from the same reference shows the hydride morphology on a cross-section of the same fuel rod as in the previous figure. The hydrides are mostly just below the oxide layer. The hydrogen content was measured by hot vacuum extraction and ranged from 50 ppm to 1200 ppm. Some cracks can be seen in the oxide layer.

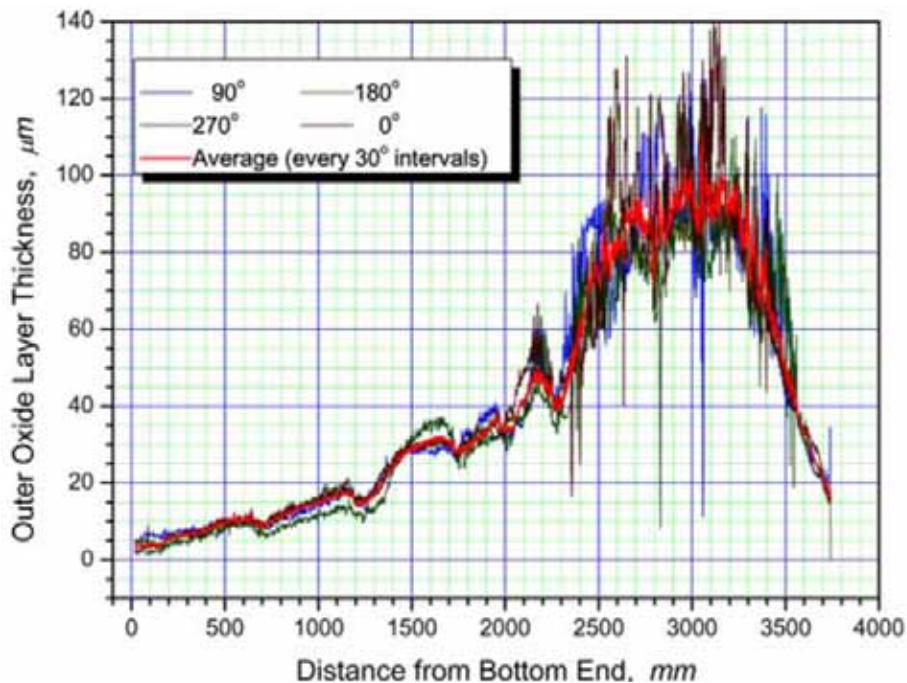


Figure 2. Oxide thickness on a Zircaloy-4 fuel cladding tube after a fuel burn-up of about 65 GWd/tU using eddy current measurement [5]

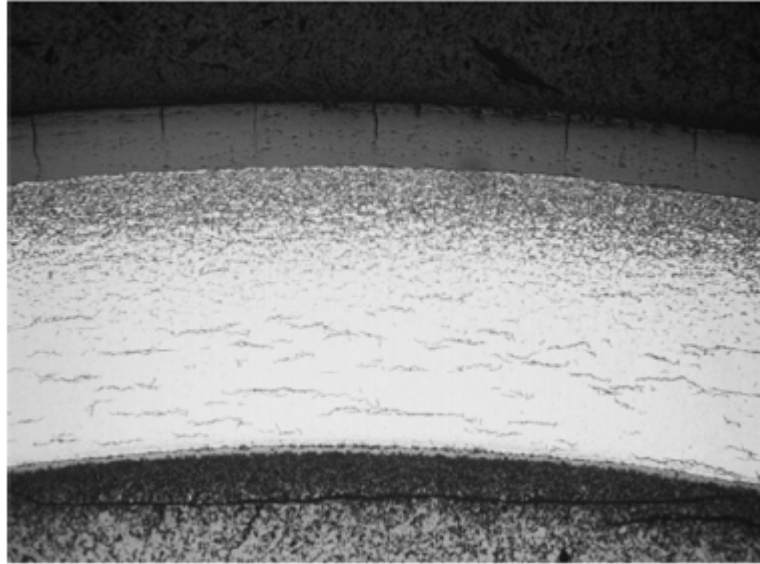


Figure 3. Hydrides can be seen in the Zircaloy-4 cladding just below the oxide layer. Some vertical cracks can be seen in the oxide layer [5]

### 3. Challenges in the hot cell environment

The radioactive environment in the hot cell gives an extra challenge to the nondestructive measurements. In common, it is recommended that no electronic equipments shall be placed inside the hot cell or they must be shielded with lead. Since the walls of the hot cells are thick, approximately one meter in thickness, the cable distance from the measuring probe to the device is long. Most nondestructive measuring methods (e.g. high frequency ultrasound using electrical transducers or eddy current) need a preamplifier near the transducer. In most of the cases also the preamplifier needs to be located outside the radiation protective walls of hot cell.

The radioactive radiation from the samples is impacting also on the transducers. The gamma dose level needs to be taken into account in designing the probes, cables and optical fibres and assure that the probes are resistant to the radiation.

The operator cannot go inside the hot cell. The samples and equipments inside the hot cells are therefore handled with remotely controlled arms. The movement of these arms is limiting the usability of the probes and samples and causes restrictions in the testing methods. For example the measuring probes need to be

well implemented in a cassette that will just be inserted to the manipulator inside the hot cell and be ready to use.

## **4. NDE methods for hot cell applications**

Two nondestructive methods to evaluate the oxide thickness on fuel claddings are discussed more in this section. The methods are laser ultrasonics (LU) and eddy current (EC) technique. Some estimates of the possibility of using these methods for measuring hydrogen concentration and hydride distribution are also given. The eddy current and laser ultrasonic techniques are expected to be complementary to each other. Laser ultrasonics has the advantage of being completely non-contact since both ultrasonic wave generation and detection are done using laser beams. These can be brought into the hot cell using optical fibres. For both laser ultrasonics and eddy current techniques a scanning mechanism is needed to scan the EC probe or optical fibres over the inspected specimen.

### **4.1 Laser ultrasonics**

Figure 4 shows a schematic view of a laser ultrasonic inspection system for testing tubes [6]. Ultrasonic waves are excited with one pulsed laser beam and the propagating surface (Rayleigh or Lamb) or bulk waves are detected by another laser beam using interferometric techniques. The technique is fully noncontact (it can therefore be applied to hot and moving components, velocity up to 5 m/s [6]) and the measurement beams can be scanned along and around the tube. Further, the ease of changing the generation and detection spot geometries according to wave type to be measured, the large bandwidth and the absence of coupling medium give advantages over traditional ultrasonic techniques. By analysing the dispersive (the frequency dependence of ultrasonic velocity) properties of surface waves and/or guided waves (Lamb) the properties of surface layers and the integrity of the tube wall can be assessed.

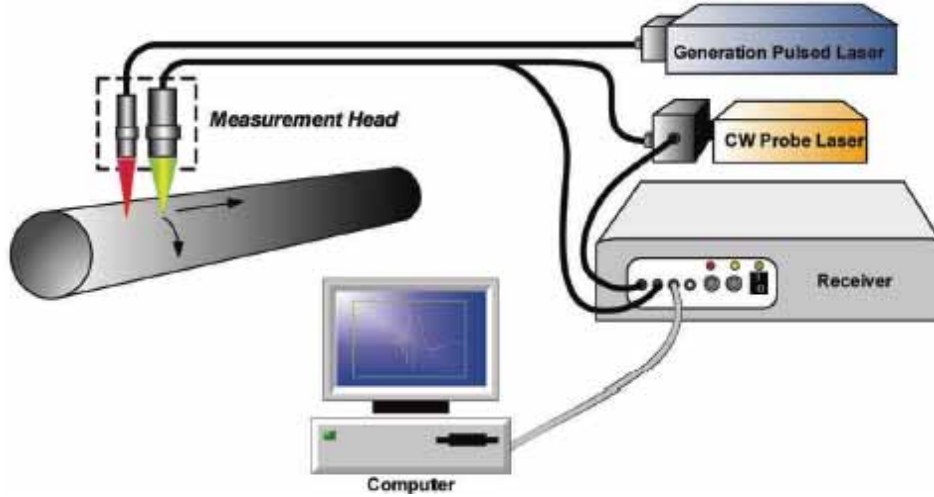


Figure 4. Inspection of a tube by a laser ultrasonic system [6]. Ultrasonic waves are excited and received in a fully noncontact manner using laser beams. The measurement heads are scanned over the tube surface.

#### 4.1.1 Current laser ultrasonic applications

Kruger et al. [7] have applied the LU technique to simultaneously obtain the elastic properties, density and thickness of thermal spray coatings (WC-Co). They also used the technique to detect cracks (perpendicular to the coating) in the coating and coating delamination. The thickness of the thermal spray coatings ( $> 200 \mu\text{m}$ ) was much larger than thickness range of zirconia on fuel cladding, but the properties of the thermal spray coatings, like their special lamellar structure, inhomogeneous composition and the presence of discontinuities like pores and cracks makes the work of Kruger et al. interesting also for the development of the application of LU to characterization of zirconium alloy fuel claddings. Kruger et al. determined the coating thickness, density and elastic modulus by comparing measured ultrasonic dispersion curves to theoretical curves and their results are shown in Figure 5.



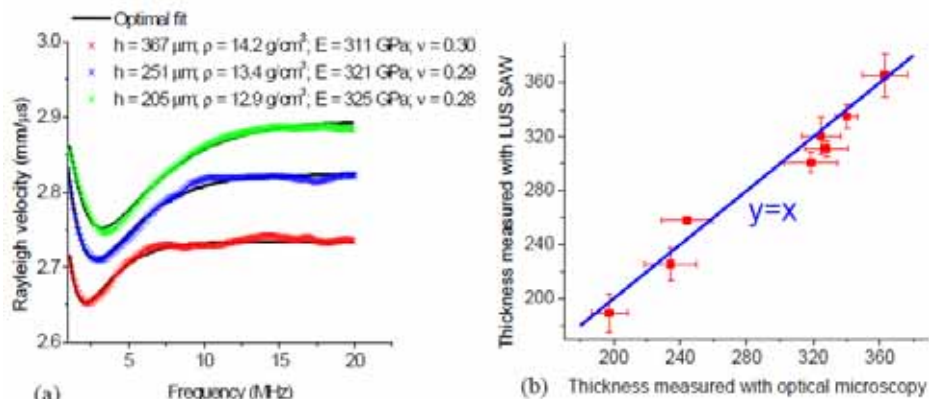


Figure 5. Determination of coating thickness ( $h$ ), density ( $\rho$ ) and elastic modulus ( $E$ ) from measured and theoretical dispersion curves (a) and a comparison of the obtained thickness values to thickness values measured with optical microscopy [7].

Kruger et al. scanned a steel specimen with WC-Co coating with laser generation and detection spots separated by 0.5 mm [7]. The presence of cracks will block the propagation of surface acoustic waves. The measurement of a waveform parameter like the amplitude of the Rayleigh wave can easily identify zones with and without cracks. In Figure 5 (left) the distance between peaks is found to be the same as the distance between the vertical cracks measured by metallography from the sample cross-section.

If there is complete delamination between the coating and the substrate, the coating will vibrate like a membrane when excited by the generation laser. This vibration can be readily detected with a system responding at sufficient low frequencies. Signals obtained from a WC-Co coating in a region where there is good adhesion show a clear difference from signals from a region where the coating is detached as shown in Figure 6. In the tested sample, there were large oscillations at about 200 kHz in the signals from the detached area.

Development of nondestructive techniques for fuel cladding evaluation in hot cell

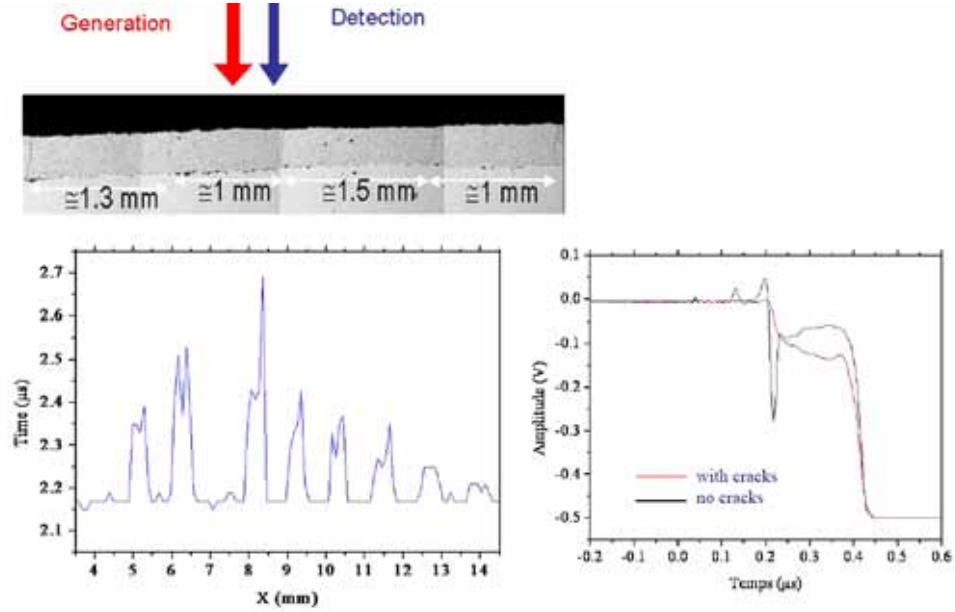


Figure 6. Laser ultrasonic detection of cracks in a WC-Co coating layer. Left, upper picture, cross-sectional view of the sample with the generation/detection scheme and (lower left) the variation of a waveform parameter along the sample. Right, the variation of the vibrational amplitude in a region with partial delamination between the coating and the substrate [8].

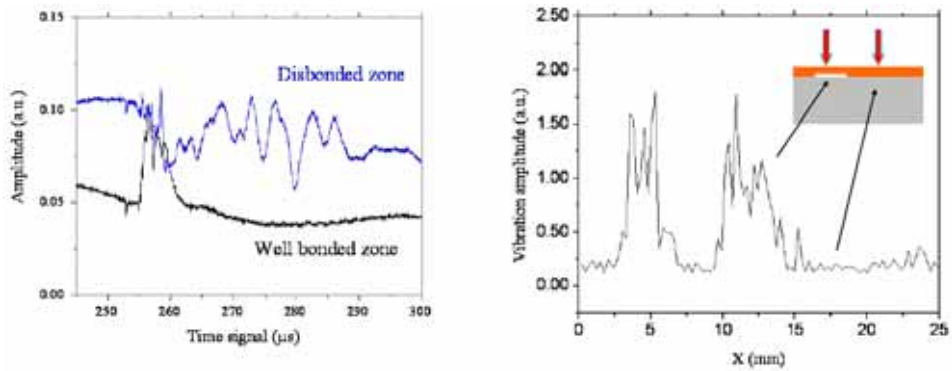


Figure 7. Laser ultrasonic detection of delamination. The signal from the delaminated region is clearly different from the signal from a well bonded zone [8].

#### 4.1.2 Characterization of hydrogen content

Hydrogen embrittlement is one of the major mechanisms responsible for the degradation of ductility of Zircaloy cladding materials. Currently the characterization of hydrogen concentration (HC) very often relies on destructive methods that are time-consuming and costly. Yang and Huang [9] present an ultrasound based non-destructive method for determination of HC in Zircaloy claddings. This method is based on low frequency acoustic microscopy (AM) rather than laser ultrasonics as shown in Figure 8. However, the same authors have ongoing work for determining HC also using laser ultrasound, if successful, this new work will make the technique more suited for hot cell applications as laser ultrasonics is a non-contact method and the need for immersion will therefore be eliminated.

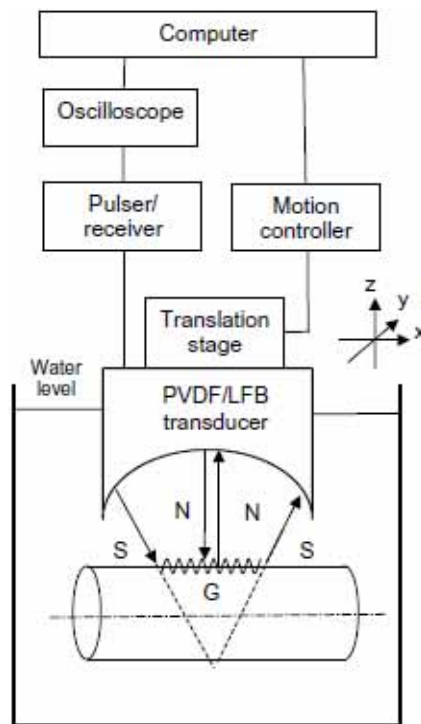


Figure 8. Use of acoustic microscopy (AM) for characterization of hydrogen content in zirconium alloy claddings. The central frequency of the transducer is slightly less than 4 MHz [9].

The underlying principle of the AM technique for HC assessment is to detect the change in ultrasonic wave speed caused by hydrogen in the Zircaloy cladding.

The ultrasonic waves propagating in the cladding are dispersive, meaning that the ultrasonic waves have wave speeds depending on their frequency. Two acoustic paths are important in Figure 8. The first path is the downward acoustic ray N; this ray is reflected from the specimen as the upward ray N. In the second path, an oblique acoustic ray S from the transducer excites a guided wave G travelling along the sample. This wave radiates back to the transducer through the ray S. The phase velocity of the guided wave G carries the information of the mechanical properties that is related to the HC. Due to different ultrasonic wave speeds of waves propagating along NN and SGS, an alternating constructive and destructive interference signal can be detected when the transducer is scanned vertically (z-direction). By analysing the alternating period in the vertical scan, the phase velocity of the guided wave G can be determined. An elaborate Fourier-based signal processing scheme can be used to analyse the periodic phenomena and extract the dispersion spectra of the guided waves. A total scanning distance of 5 mm with 200 steps is used to obtain the dispersion spectra. The phase velocity of the fundamental anti-symmetric Lamb mode  $A_0$  is used for a correlation with HC in the cladding.

## 4.2 Eddy current techniques

Single frequency eddy current measurements are routinely used for oxide thickness measurements on zirconium fuel cladding tubes in hot cells. Small diameter pencil probes are usually applied. The frequency of the eddy current driving current is usually between 1 and 3 MHz. At these frequencies the electromagnetic wave does not penetrate through the wall of the zirconium tube.

The probe response is mainly dependent on the lift-off, i.e. the oxide induced separation between the tip of a probe and the metal surface. This method usually gives reasonably good results if the oxide layer is non-magnetic. The EC lift-off measurement technique is illustrated in Figure 9 where the EC probe is a coil driven by an AC current. The electromagnetic field generated by the coil will create eddy currents in the metal nearby the probe tip and these currents in turn induces a new AC current in the coil thereby changing the impedance of the coil. The coil impedance will depend on the electrical conductivity and permeability of metal under the probe, on the thickness of the metal, on the frequency of the driving AC current and on the distance between the probe tip (lift-off) and the metal surface. Therefore the measured impedance can be correlated to the thickness of the oxide layer and to the wall thickness.

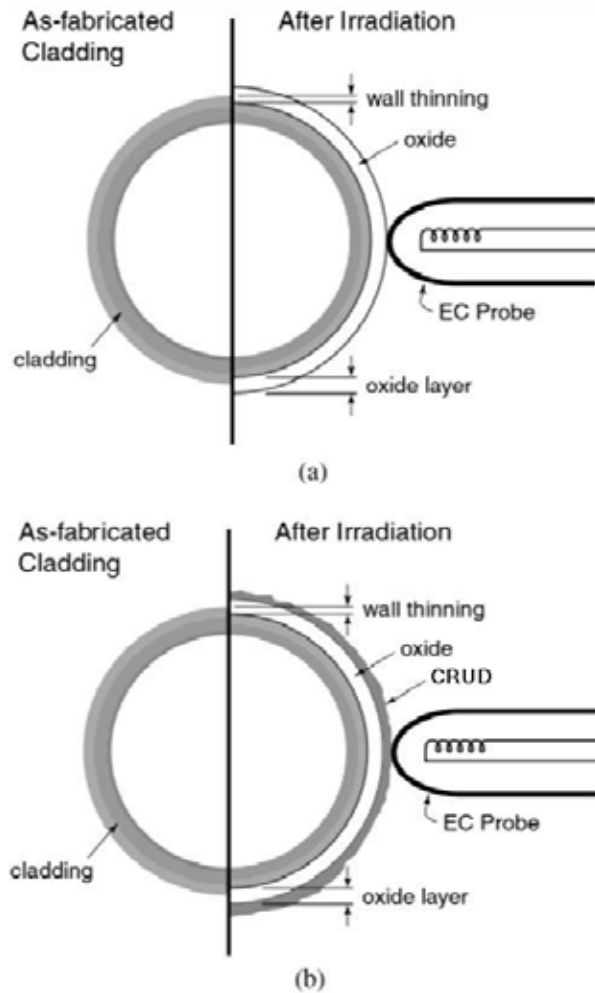


Figure 9. The principle of the eddy current oxide thickness measurements (a) Cladding tube with white oxide layer only (b) Cladding tube with white oxide layer and grey CRUD layer [10]

In the Figure 9 the left hand side shows a cross-section of the zirconium tube in as-fabricated condition. The right hand side shows a cross-section of the tube after irradiation. The thickness of metallic tube wall has been decreased and an oxide layer has been built up on the outer surface of the tube. In the lower right part of the picture there is a deposit (CRUD) layer on the surface of the oxide layer. The deposit not only causes an extra lift-off, it may also significantly change the EC response due to its ferromagnetic nature [10].

A reference tube is needed to enable coating thickness measurement. A thin isolating tape or a plastic foil is usually passed around the tube to simulate oxide layers of different thickness.

For the evaluation of the cladding health a lower frequency should be applied. The lower frequency should be of the order of 500 kHz to achieve 0.6 mm penetration depth which is the wall thickness of the tube. The low frequency eddy current technique can be used for wall thickness measurement but it is also sensitive to the inner surface defects (cracks) and major inclusions in the zirconium wall.

Also measurements with two frequencies can be applied to achieve the results from the tube oxide and the cladding health at the same time. Also when the tube wall thickness is not known a two frequency technique should be applied

The future reactor types bring new geometries to be inspected. The geometry of the sample is giving a probe manipulator a variety of different challenges. In the Figures 10 and 11 there are two different eddy current measuring set ups, one for flat sample and the other for tubular sample.

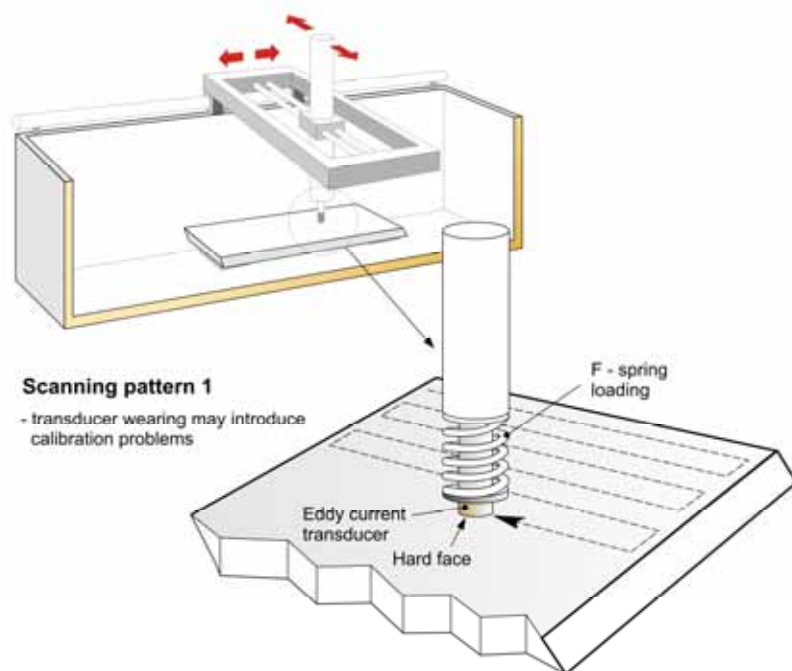


Figure 10. A schematic setup for planar sample eddy current measurements.



Figure 11. An eddy current measuring setup for tubular sample.

## 5. Conclusions

Eddy current techniques are widely used in the hot cell environments, as their tolerance to radiation has been tested in real service. However, the accuracy of the oxide thickness measured with EC should be improved.

Laser ultrasonics is much more rarely used in the field of nuclear NDE applications. The recent results in the developing laser ultrasonics suggest that the method is promising also for hot cell environments.

## 6. Summary

NDE techniques for nondestructive evaluation of materials degradation due to irradiation are presented. Two methods, laser ultrasound and eddy current, are more specifically discussed.

There is a limited space available in a hot cell and the components to be examined are radioactive. Therefore the NDE measurements should be completely remotely controlled and the number of apparatuses inside the hot cell should be minimal. This will restrict or limit the handling of the equipment.

Eddy current measurements based on the lift-off technique and laser ultrasonics are proposed as promising future techniques for oxide measurements of the irradiated fuel cladding.

## References

1. De, P. K. John, J. T., Banerjee, S., Jayakumar, T., Thavaimuthu, M. & Raj, B. Assessment of hydrogen levels in Zircaloy-2 by non-destructive testing. *Journal of Nuclear Materials*, Vol. 252 (1997), pp. 43–54.
2. Edsinger, K., Yagnik, S. & Johnson, D. P. Method and apparatus for measuring hydrogen concentration in zirconium alloy components in the fuel pool of a nuclear power plant. Patent No.: US 7,388,369 B2, 2008.
3. Rudling, P. & Patterson, C. Fuel material technology report. Volume IV. ANT International, Skultuna, Sweden, 2009.
4. IAEA 1998. Waterside corrosion of zirconium alloy in nuclear power plants. IAEA-TECDOC-996. 313 p.
5. Kim, S.-K., Bang, J.-G., Kim, D.-H., Yang, Y.-S., Song, K.-W. & Kim, D.-S. Mechanical property evaluation of high burn-up nuclear fuel cladding using the ring tensile test. *Met. Mater. Int.*, Vol. 15 (2009) 4, pp. 547–553.
6. IOS Intelligent Optical Systems. Inc. Brochure.
7. Kruger, S., Lévesque, D. Bescond, C., Lima, R., Maple, B., Campagne, B., Blouin, A. & Monchalain, J.-P. Laser-ultrasonic evaluation of thermal spray coatings. 1st International Symposium on Laser Ultrasonics: Science, Technology and Applications. 16–18 July, 2008. Montreal. Canada.
8. Kruger, S., Blouin, A., Lévesque, D. & Monchalain, J.-P. Laser-ultrasonic evaluation of thermal spray coatings. Presentation.
9. Yang, C.-H. & Huang, M.-F. Characterization of hydrogen concentration in Zircaloy claddings using low-frequency acoustic microscope with a PVDF/LFB transducer. *Journal of Nuclear Materials*, Vol. 335 (2004), pp. 359–365.
9. Yagnik, S. K., Johnson, D. P. & Kervinen, J. A. Eddy Current Measurements of Corrosion and Metal Loss in Zircaloy Cladding with Ferromagnetic CRUD. *Nuclear Technology*, Vol. 147 (2004), pp. 291–300.









Series title, number and report code of publication

VTT Symposium 265  
VTT-SYMP-265

Author(s) Pertti Auerkari & Juha Veivo (eds.)		
Title <b>Baltica VIII</b> <b>Life Management and Maintenance for Power Plants. Vol. 2</b>		
Abstract BALTICA VIII. International Conference on Life Management and Maintenance for Power Plants, Helsinki–Stockholm–Helsinki, May 18–20, 2010. This is one of the two volumes of the proceedings of the BALTICA VIII Conference. The Conference aims to review recent experience, new technology and views on future development for supporting successful, safe and productive operation of power plants. The triannual BALTICA Conference offers an updated state-of-the-art review on the life management and maintenance of thermal power plants. The themes in BALTICA VIII include e.g. consequences of nuclear revival with issues of the life cycle, new insights into tools and methods for life management and improvements in managing the assets under constraints such as aging, cycling, new fuels and increasing fraction of low to zero emission systems, and recent experience on example cases from new and ageing plants.		
ISBN 978-951-38-7593-2 (soft back ed.) 978-951-38-7594-7 (URL: <a href="http://www.vtt.fi/publications/index.jsp">http://www.vtt.fi/publications/index.jsp</a> )		
Series title and ISSN VTT Symposium 0357-9387 (soft back ed.) 1455-0873 (URL: <a href="http://www.vtt.fi/publications/index.jsp">http://www.vtt.fi/publications/index.jsp</a> )		Project number 71111
Date May 2010	Language English	Pages 308 p.
Name of project Baltica VIII		Commissioned by
Keywords thermal power plant, nuclear plant, boiler, turbine, condition, life, fuel, maintenance, inspection, monitoring, risk, reliability, material, damage, corrosion, fatigue, creep, degradation		Publisher VTT Technical Research Centre of Finland P.O. Box 1000, FI-02044 VTT, Finland Phone internat. +358 20 722 4520 Fax +358 20 722 4374

